UNIVERSITÀ DI PARMA

UNIVERSITÀ DEGLI STUDI DI PARMA

DOTTORATO DI RICERCA IN
" SCIENZE DEL FARMACO "

CICLO XXXV

DEVELOPMENT OF *EX VIVO* MODELS FOR SMART SCREENING OF NOVEL COLLOIDAL OCULAR FORMULATIONS

Coordinatore:

Chiar.mo Prof. Marco MOR

Tutore:

Chiar.ma Prof.ssa Silvia PESCINA

Co-Tutore:

Paolo GASCO

Dottorando:

Felipe M. GONZÁLEZ-FERNÁNDEZ

Anni Accademici 2019/2020 – 2021/2022

UNIVERSITÀ DI PARMA

UNIVERSITÀ DEGLI STUDI DI PARMA

PhD COURSE IN

" DRUG SCIENCES "

XXXV CYCLE

DEVELOPMENT OF *EX VIVO* MODELS FOR SMART SCREENING OF NOVEL COLLOIDAL OCULAR FORMULATIONS

Coordinator:

Prof. Marco MOR

Supervisor:

Prof. Silvia PESCINA

Co-Supervisor:

Paolo GASCO

Candidate:

Felipe M. GONZÁLEZ-FERNÁNDEZ

Academic Years 2019/2020 – 2021/2022

Preface

Data hereby presented have been collected over the course of the PhD project corresponding to Early Stage Researcher 13 of the ORBITAL (Ocular Research by Integrated Training and Learning) Innovative Training Network funded by the European Union's Horizon 2020 Research and Innovation Programme under the Marie Skłodowska–Curie Actions grant agreement number 813440.

Research activity was carried out at the University of Parma, Department of Food and Drug, under the supervision of Prof Silvia Pescina and at Nanovector S.r.l., Torino, under the supervision of Paolo Gasco. In addition, two secondments were completed at the South East Technological University, Ireland under the supervision of Dr Laurence Fitzhenry (04.10.2021-22.12.2021) and at Ocupharm Diagnostics S.L. (Universidad Complutense de Madrid, Facultad de Óptica y Optometría), Spain under the supervision of Dr Gonzalo Carracedo (14.09.2021-01.10.2021; 11.07.2022-31.07.2022).

Contents

PREFACE ..... **I**

LIST OF ABBREVIATIONS ..... **V**

CHAPTER 1. INTRODUCTION **1**

1.1. Ocular Drug Delivery 1
1.2. Ocular inflammation and corticosteroids 5
1.3. Predicting nanoparticle performance in biorelevant conditions 6

CHAPTER 2. AIM OF THE THESIS **9**

CHAPTER 3. DEVELOPMENT OF LIPID-BASED NANOCARRIERS FOR OCULAR DRUG DELIVERY **11**

3.1. Introduction 11
3.1.1. Lipid-based nanocarriers for ocular drug delivery 12
3.1.2. Nanoparticle optimization through Design of Experiments (DoE) 14
3.1.2.1. Statistical Design of Experiments (DoE) 15
3.1.2.2. Two-Level Factorial Designs 18
3.1.2.3. Plackett-Burman designs 19
3.1.2.4. Optimisation Designs 20
3.1.2.5. A particular approach: Mixture Designs 24
3.1.2.6. Data Analysis and Model Application 25
3.2. Development of Dexamethasone Acetate NLC (DexAc-NLC) 27
3.2.2. Materials and Methods 27
3.2.2.1. Materials 27
3.2.2.2. Lipid solubility screening 28
3.2.2.3. Oil-solid lipid mixture characterization by Differential Scanning Calorimetry 28
3.2.2.4. Surfactant screening 28
3.2.2.5. Hot stage polarized light microscopy 29
3.2.2.6. NLC preparation and characterization 29
3.2.3. Results and Discussion 30
3.2.3.1. Lipid Screening 31
3.2.3.2. Surfactant screening 34
3.2.3.3. DexAc-NLC preparation and characterization 38
3.2.3.4. NLC optimization with DoE 39
3.3. Development of Dexamethasone NLC (Dex-ieNLC) 47
3.3.1. Materials and Methods 47
3.3.1.1. Materials 47
3.3.1.2. Dexamethasone solubility in the selected excipients 48
3.3.1.3. Preparation of ieNLC 48

3.3.1.4. Physicochemical characterization: size, PDI, zeta potential and pH 48
3.3.1.5. ieNLC lyophilization 48
3.3.1.6. Morphology analysis: FEG-SEM 49
3.3.1.7. In vitro cytotoxicity 49
3.3.2. Results and Discussion 50
3.3.2.1. Characterization of Dex-ieNLC 50
3.3.2.2. ieNLC lyophilization 51
3.3.2.3. Characterization of ieNLC Morphology: SEM and FEG-SEM 52
3.3.3.4. In vitro cytotoxicity 54
3.4. Development of Dexamethasone Microemulsions 57
3.4.1. Materials and Methods 57
3.4.1.1. Materials 57
3.4.1.2. Selection of tyloxapol-surfactant mixtures 58
3.4.1.3. Selection of the adequate polysorbate 60- tyloxapol ratio 58
3.4.1.4. Microemulsion region identification 58
3.4.1.5. Polarized light microscopy 59
3.4.1.6. Microemulsion region characterization: Design of Experiments 59
3.4.1.7. Dexamethasone solubility studies 59
3.4.1.8. In vitro cytotoxicity 59
3.4.2. Results and Discussion 60
3.4.2.1. Selection of tyloxapol-surfactant mixtures 60
3.4.2.2. Ratio tyloxapol/polysorbate 60 selection: optical transmittance 63
3.4.2.3. Microemulsion region identification 65
3.4.2.4. Microemulsion region characterization through DoE: Size, (PDI) and EE% mathematical modelling 66
3.4.2.5. In vitro cytotoxicity 74

CHAPTER 4. DEVELOPMENT OF AN *EX VIVO* MODEL BASED ON FRESHLY EXCISED PORCINE WHOLE EYES 76

4.1. Introduction 76
4.1.1. State of the art of ocular of *ex vivo* ocular models 76
4.1.2. Porcine *ex vivo* tissues: differences and similarities to the human eye 77
4.1.3. Additive manufacturing in pharmaceutical sciences: 3D printing 79
4.2. Materials and Methods 82
4.2.1. Materials 82
4.2.2. 3D modelling, photogrammetry, and 3D printing specifications 82
4.2.3. Porcine eyes 83
4.3. Results and Discussion 83
4.3.1. Investigations on porcine ocular anatomy 83
4.3.2. A formulation applicator for porcine eyes: the Ocudonor device 84
4.3.2.1. Ocudonor v1: the Poly(methyl methacrylate) Prototype 84
4.3.2.2. Ocudonor v2: the FDM Prototype 85
4.3.2.3. Ocudonor v3: the SLS Prototype 86
4.3.2.4. Ocudonor v4: the MSLA Prototypes 86
4.3.3. A container for whole ocular bulbs: the Ocutainer device 89
4.3.4. Ocudonor and Ocutainer whole-eye *ex vivo* setup 93
4.3.5. Eye dissection and tissue retrieval: S, Ch and Vitreous 96
4.3.6. Vitreous handling 96

CHAPTER 5. *EX VIVO* EVALUATION OF LIPID-BASED NANOCARRIERS 99

5.1. Introduction 99
5.2. Materials and Methods 101
5.2.1. Materials 101
5.2.2. Nile red-loaded NLC 101
5.2.3. Spectroscopy studies 101
5.2.4. *Ex vivo* porcine ocular tissues 102
5.2.5. Validation of an DexAc-Dex extraction method from porcine sclera and choroid 102
5.2.6. Validation of Dex extraction method from porcine vitreous and retina 102
5.2.7. Permeation and Retention experiments on isolated Sclera and Sclera-Choroid 103
5.2.8. Retention experiments on whole porcine eye 104
5.2.9. Multiphoton Microscopy studies 105
5.2.10. HPLC Analysis 105
5.2.11. Data Processing 106
5.2.12. Statistical Analysis 106
5.3. Results and Discussion 106
5.3.1. Validation of extraction methodologies from ocular tissues 106
5.3.1.1. Sclera and Choroid: DexAc and Dex extraction validation 106
5.3.1.2. Vitreous body and retina: Dex extraction validation 107
5.3.2. DexAc-NLC *ex vivo* evaluation 107
5.3.2.1. Permeation and retention on isolated Sclera and Sclera-Choroid 107
5.3.2.2. Spectroscopic studies of NR-NLC 110
5.3.2.3. MPM on isolated sclera 112
5.3.3. Dex-ieNLC *ex vivo* evaluation 117
5.3.3.1. Permeation and retention on isolated Sclera-Choroid 117
5.3.3.2. Retention on whole porcine eye (Ocudonor-Ocutainer) 118
5.3.4. Dex Microemulsions *ex vivo* evaluation 120
5.3.4.1. Permeation and retention on isolated Sclera-Choroid 120
5.3.4.2. Retention on whole porcine eye (Ocudonor-Ocutainer) 122

CHAPTER 6. CONCLUSIONS 123

REFERENCES 126

ACKNOWLEDGMENTS 146

List of abbreviations

AMD	Age-related Macular Degeneration
ANOVA	Analysis of Variance
ARPE-19	Arising Retinal Pigment Epithelium
BBDs	Box–Behnken Designs
CAD	Computer Aided Design
CCDs	Central Composite Designs
Ch	Choroid
CMAs	Critical Material Attributes
CPPs	Critical Process Parameters
CQAs	Critical Quality Attributes
CTAB	CetylTrimethylAmmonium Bromide
Dex	Dexamethasone
DexAc	Dexamethasone Acetate
DLP	Digital Light Processing
DLS	Dynamic Light Scattering
DMEM	Dulbecco's Modified Eagle's Medium
DMSO	Dimethyl Sulfoxide
DoE	Design of Experiment
DR	Diabetic Retinopathy
DSC	Differential Scanning Calorimetry
EDX	Energy Dispersive X-ray Spectroscopy
EMA	European Medicines Agency
EPS	Expanded Polystyrene
FBS	Foetal Bovine Serum
FDA	Food and Drug Administration
FDM	Fused Deposition Modelling
FEG-SEM	Field Emission Gun Scanning Electron Microscopy
GMS	Glycerol MonoStearate
GRAS	Generally Recognized As Safe

HBSS	Hanks' Balanced Salt Solution
HEPES	4-(2-hydroxyethyl)-1-piperazineethanesulfonic acid
HLB	Hydrophilic–Lipophilic Balance
HPLC	High-Performance Liquid Chromatography
LOD	Limit of Detection
LOQ	Limit of Quantification
MPM	MultiPhoton Microscopy
MSLA	Masked Stereolithography
MTT	3-(4,5-dimethylthiazol-2-yl)-2,5-diphenyl tetrazolium bromide
MW	Molecular Weight
NLC	Nanostructured Lipid Carrier
NR	Nile Red
PBS	Phosphate Buffered Saline
PDI	PolyDispersity Index
PEG	PolyEthylene Glycol
PLA	Polylactic Acid
QbD	Quality by Design
QbT	Quality by Testing
RA	Risk Assessment
RPE	Retinal Pigment Epithelium
S	Sclera
SCh	Sclera and Choroid
SEM	Scanning Electron Microscopy
SHG	Second Harmonic Generation
SLA	Stereolithography
SLN	Solid Lipid Nanoparticle
SLS	Selective Laser Sintering
TPEF	Two-Photon Excited Fluorescence
TPGS	Tocopherol Polyethylene GlycolSuccinate
USP	United States Pharmacopoeia

Chapter 1

Introduction

This chapter includes previously published material available as:

González-Fernández, F.M.; Bianchera, A.; Gasco, P.; Nicoli, S.; Pescina, S. Lipid-Based Nanocarriers for Ophthalmic Administration: Towards Experimental Design Implementation. *Pharmaceutics* 2021, *13*, 447. https://doi.org/10.3390/pharmaceutics13040447

González-Fernández, F.M.; Delledonne, A.; Nicoli, S.; Gasco, P.; Padula, C.; Santi, P.; Sissa, C.; Pescina, S. Nanostructured Lipid Carriers for Enhanced Transscleral Delivery of Dexamethasone Acetate: Development, *Ex Vivo* Characterization and Multiphoton Microscopy Studies. *Pharmaceutics* 2023, *15*, 407. https://doi.org/10.3390/pharmaceutics15020407

1.1. Ocular Drug Delivery

The human brain has evolved over millennia to favour the processing of visual stimuli over other sensory modalities. The eyes, and thus, vision, play an important role in human cognition, learning, and perception from the very first weeks of life. Accordingly, vision usually is identified as the most valuable sense that patients are afraid to lose [1,2].

In contrast, recent estimations account for 2.2 billion people being globally affected by vision impairment or blindness. Current lifestyles regarding dietary habits or sedentarism, combined with a constantly ageing population, forecast an increase in chronic ocular diseases such as glaucoma (from 76 to 95.4 million), age-related macular degeneration (from 195.6 to 243.3 million) or diabetic retinopathy (from 103 to 129.8) for 2030. These conditions increase their incidence with an ageing retina, and longevity of the population in industrialised countries is only expected to increase. Furthermore, other ocular infections might also lead to visual impairment, especially if left untreated [3-8].

To date, several drug classes have been investigated to treat these conditions, but their efficacy is influenced by effective ocular delivery, which remains a challenging task [9]. For this reason, despite being easily accessible, the eye preserves its integrity by constantly hindering the access of xenobiotics, including drugs, through a series of static, dynamic, and metabolic barriers which vary depending on the administration route [10].

It has become commonplace to distinguish two ocular segments: the **anterior segment**, which is mostly exposed and visible, and the **posterior segment**, inside the ocular orbit, as shown in Figure 1.

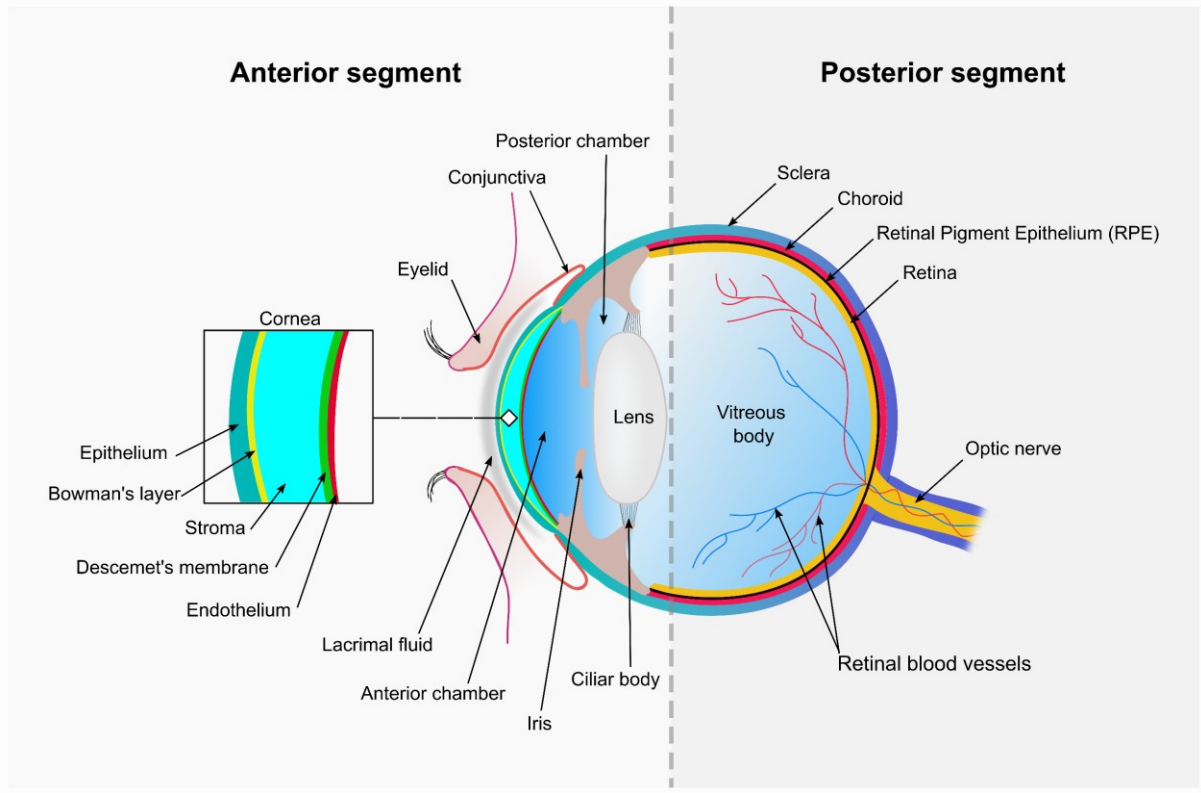

Figure 1. Schematic representation of the ocular anatomy.

An imaginary line (dotted grey vertical line in Figure 1) divides the ocular structures into the two segments. The anterior segment contains the cornea (detailed within the Figure 1 insert), iris, ciliary body and both anterior and posterior chambers. The aqueous humour fills the anterior and posterior chambers, while most of the posterior segment is filled by a hyaluronan-rich gel known as vitreous humour. The posterior segment contains the retina, the neural tissue responsible for visual sight, and is delimited by the sclera, similar in composition to the corneal stroma. The choroid is a highly vascularised tissue separated from the retina by a monolayer of hexagonal pigment-containing cells: the retinal pigment epithelium (RPE) [11].

Based on the target tissue, several **administration routes** are available [10]. **Topical administration** commonly addresses diseases affecting the anterior segment of the eye, such as keratitis, conjunctivitis, or glaucoma. Eye drops account for 70% of prescriptions due to their ease of use, high patient acceptability and cost-effectiveness [12]. The ocular surface is covered by 7–9 µL of lacrimal fluid, which presents an external lipidic layer and two consecutive hydrophilic layers with a predominantly aqueous and mucous nature, respectively. Administration of a single formulation drop activates reflex blinking and is quickly washed away through nasolacrimal drainage and tear turnover. Non-specific absorption trough the conjunctiva, which covers the eye surface and the interior of the eyelids except the cornea (Figure 1), further reduces the remaining formulation available for trans-corneal absorption [13].

The cornea, as detailed in Figure 1, is a highly differentiated tissue containing a lipophilic external epithelium and an internal endothelium separated by a thicker hydrophilic stroma [14,15]. This hydrophobicity gradient and an elevated presence of inter-cellular tight junctions within the epithelium hinder simple drug diffusion, which consequently relies on substance molecular weight and the hydrodynamic radius [9,16]. Less than 5% of the initially applied dose reaches the aqueous humour in the anterior chamber (Figure 1). In this region, several convective flows such as the aqueous humour circulation or the uveal turnover further reduce drug availability [17].

Unfortunately, the anterior segment does not generally benefit from **systemic administration** that, on the contrary, could eventually reach the posterior segment. However, the observed drug levels after oral or intravenous administration are normally non-productive due to the presence of two blood–retinal barriers. The first, known as the outer blood–retinal barrier, is mainly composed of the RPE: a melanin-rich monolayer, intimately adhered to the fenestrated choriocapillaris and able to restrict drug distribution into the retina (Figure 1). The second, known as the inner blood–retinal barrier, is composed of fine capillaries embedded in the retina, presenting a tightly closed endothelium that impedes drug access through the paracellular route [18]. Despite these barriers, some treatment options relying on intravenous administered drugs, such as photodynamic therapy, are used in current clinical practice [19].

Intravitreal injections directly address the posterior segment of the eye, targeting the vitreous body and, ultimately, the retinal region, where degenerative diseases such as diabetic retinopathy (DR) and age-related macular degeneration (AMD) exert their damage [20]. Both low-molecular-weight (*i.e.*, corticosteroids) and high-molecular-weight compounds such as biologicals (*i.e.*, bevacizumab, ranibizumab, pegaptanib) are currently administered by intravitreal injection. Multiple side effects due to the

invasiveness of the procedure have been reported, such as endophthalmitis, cataract or retinal detachment [21-23]. Diffusion in the vitreous body is strongly dependent on the molecule hydrodynamic radius and the presence of a surface charge, which also determines the residence time. Large hydrodynamic radii hamper drug mobility, while the presence of cationic surface charges allows for interaction with the negatively charged collagen and hyaluronan present in the vitreous humour, increasing in both cases drug permanence and reducing dosing frequency [24,25]. This behaviour has also been identified for nanoparticles and, as an example, it has been reported that large (up to 300 nm) anionic liposomes diffuse better than smaller (*approx*. 50 nm) cationic liposomes [26]. Elimination occurs towards the anterior segment (aqueous humour) through the blood–retinal barriers and, to a lesser extent, by biotransformation. As a result, larger molecules (*i.e.*, proteins) remain up to several days, while small molecules show half-life values ranging from several minutes to 10 hours, thus requiring a sustained release to maintain therapeutic levels [18,27,28].

Recent approaches based on **periocular routes** (subconjunctival, sub-Tenon's, retrobulbar, peribulbar and intrascleral) are less invasive than intravitreal injections, respecting the immunological privilege of the inner eye and allowing for formulation deposition at different locations of the posterior segment [29-31]. Drug absorption occurs *via* the trans-scleral pathway and faces three static barriers, namely sclera, choroid and RPE, although systemic absorption cannot be negligible [32,33]. The sclera, similar in composition to the corneal stroma, with a high water and collagen content, shows better permeation to hydrophilic, neutral, or negatively charged molecules with low molecular radii. Similar molecular properties have demonstrated to offer better permeation across Bruch's membrane (the innermost layer of the choroid) and the choroid itself. On the other hand, the RPE favours the passage of more lipophilic molecules [34,35]. In addition, several dynamic barriers (*i.e.*, conjunctival, episcleral or choroidal clearance and uveoscleral outflow) and metabolic barriers (mainly cytochrome P-450 and lysosomal enzymes in the RPE) further impede drug access to the neuroretina [36]. Literature presents several examples of ophthalmic nanosystems suggested for periocular administration that confirm the growing interest for this topic [37-41].

Thus far, although extensive research has been carried out, good ocular bioavailability remains a challenge, especially in the most patient-friendly topical administration route [42].

1.2. Ocular inflammation and corticosteroids

Inflammation can occur as a strong response to pathogens or tissue injury or in other cases, as a more variable reaction to basal homeostasis disruption due to tissue stress (which leads to malfunction), the latter identified as para-inflammation [43]. Aging is a main contributor to oxidative stress accumulation in the chorioretinal tissues, disrupting tissue functionality. Tissue changes due to aging have been reported at the neuroretina, RPE or Bruch's membrane which might lead to chronicity of the para-inflammation [44,45]. Under those circumstances, metabolic and oxidative stress are usually recognized as the starting point for age-related retinal diseases such as DR, glaucoma, or AMD [46].

Corticosteroids, firstly used in ophthalmology in the fifties, still have nowadays a fundamental role in the management of ocular inflammation [47]. Triamcinolone acetonide, fluocinolone acetonide and dexamethasone, amongst others, usually represent the first-line treatment of inflammation related to conjunctivitis, non-infectious uveitis, macular oedema, AMD, and DR [48].

Dexamethasone (Dex), a potent glucocorticoid, has demonstrated not only to downregulate the expression of multiple proinflammatory chemokines and cytokines, but also to inhibit retinal neovascularization. Nonetheless, its high lipophilicity hinders effective therapeutic doses when applied topically and several approaches have been proposed over the years [49]. Water soluble derivatives, such as dexamethasone sodium phosphate, have been developed to obtain more concentrated eye drops, while more lipophilic prodrugs, such as dexamethasone acetate (DexAc) have been selected to promote drug permeation across corneal epithelium [50-52]. Furthermore, to effectively address the back of the eye, dexamethasone-loaded implants (Ozurdex®) are administered intravitreally [47].

Several examples of research studies involving dexamethasone-loaded nano- and microsystems are available: from liposomes [53,54], micelles [55,56] and nanostructured lipid carriers (NLC) [57,58] to nanowafers [59,60] and microparticles [61]. On the contrary, only a few number of studies involve dexamethasone acetate, as in the case of poly(D,L-lactide-co-glycolide) nanoparticles intended for intravitreal injections [62,63], cationic nanoemulsions [64], nanofibers for intravitreal injections [65], and polymyxin B–coated NLC containing DexAc for the treatment of the infection-related eye surface inflammation [66]. These approaches, based on nano or micro-systems, are believed to improve the therapeutic success by i) reducing the frequency of administration with the possibility of a prolonged and sustained release, ii) lowering the invasiveness of the administration routes (*i.e.*, periocular administration routes) and iii) limiting the side effects by effective drug targeting at low dosage levels [67].

1.3. Predicting nanoparticle performance in biorelevant conditions

Developing novel ophthalmic nanocarriers requires a large amount of preclinical safety and efficacy testing before arriving to clinical phase trials. In this sense, it is required to develop high throughput testing platforms that mimic at best the biorelevant conditions and thus allow for a rapid screening of the best formulation candidates. High correlation between preclinical and clinical performance is also a desirable characteristic.

In vitro drug release studies represent the first approach on drug delivery testing, as also described in the United States Pharmacopoeia (USP) for semisolid (ointments) or solid formulations (contact lenses, implantable devices). Some of these tests are implemented for evaluation of novel colloidal drug delivery systems, but often the required testing conditions hinder effective translation of the obtained data into clinical results. In 2011, during a workshop on Dissolution/*In Vitro* Release Testing of Novel/Special Dosage Forms the ophthalmic formulations were included among the "*dosage forms requiring more work before a method can be recommended"* [68]. In fact, the dissolution and release tests described by both the European and the US Pharmacopeia essentially refer to oral dosage forms and therefore they are not properly suitable for ophthalmic formulations. The composition of the dissolution media is different from ocular fluid and its volume is excessive to mimic the ocular delivery conditions. For this reason, even non-compendial setups are accepted, if previously validated [69], and several examples have been proposed in literature for the *in vitro* release studies of ophthalmic products [70,71].

Some attempts have been made on finding a correlation between the *in vitro* release studies of semisolid formulations and *ex vivo* trans-corneal permeation data, but nonetheless in its infancy and far away from *in vivo* predictability [72]. What is more, adequate *in vitro-in vivo* correlation models for drug delivery to the posterior segment of the eye, is still far from being a reality [73-75].

Predicting *in vivo* drug permeability, and thus nanoparticle performance, requires more biomimetic platforms which include from the simplest isolated ocular cells to whole tissue sections or organs. In fact, small changes in nanoparticle composition alter the barriers to drug delivery and thus quick screening platforms that allow for an easy identification of best excipients composition are required [76].

Typical ***in vitro*** approaches are based on cultured cells from diverse ocular tissues from animal or human donors. With an adequate setup, a large amount of information can be retrieved with a relatively low workload, with good biomimetic results, especially

if primary human cells are selected. When considering test for posterior segment of the eye, and the periocular routes related to it, bidimensional cellular cultures lack the natural three-dimensional complexity of the eye, especially the internal outflows which are responsible for drug clearance and avoid therapeutical doses near the retina. These tests allow nonetheless for quick cytotoxicity assays that evaluate excipient and drug compatibility with a specific ocular tissue [77]. By adequately culturing diverse cellular lines (reproducing the natural hydrophobic and lipophilic layers of the mechanical barriers of the eye) permeation across one or multiple cell layers can also be evaluated further mimicking the permeation and retention that would occur in a three-dimensional ocular bulb [78]. Thus far, some available cellular cultures include primary corneal epithelial cells or spontaneously arising retinal pigment epithelium (ARPE-19), amongst others [79,80].

A second level of screening can be obtained by not using single cellular lines but, ***ex vivo*** tissues of ovine, bovine, or porcine origin. Using whole organs, as in the case of the eye [81]; isolated tissues, like conjunctiva [56]; cornea [82], sclera and choroid [83] and/or tissue sections, for example the epi-off cornea [82] adds the complexity of the natural extracellular matrix and pluricellular arrangements of different cellular types. These tissues can be obtained as a by-product of the meat production industry, but require more complex setups, and thus the throughput is lower when compared to *in vitro* screening. *Ex vivo* tissues can also be retrieved from rabbits, but this approach lacks the premise of improving animal welfare since they are not a by-product of other industries [84]. Transportation and manipulation of the excised tissues from the abattoir are of utter importance. Considering delivery to the posterior segment, sclera, choroid Bruch's membrane or RPE can be isolated in various combinations and the permeation and retention of the drug and nanocarrier can be evaluated [85,86]. The use of human excised sclera has also been reported, but tissue availability is very low [87]. A further analysis on the state of the art of *ex vivo* ocular models and porcine ocular anatomy will be presented in Section 4.1.

In vivo studies are usually the last step before the clinical testing and mammalian species as rodents, rabbits, or even primates are preferred. Rodent models of several age-related retinal diseases are currently available, and rabbits allow to collect adequate pharmacokinetic data [88]. However, rodents and rabbits present a different blinking pattern, ocular geometry and dimensions are smaller while vitreous viscosities are increased. In addition, scleral permeability is higher, which might lead to overestimation of nanoparticle performance in later clinical trials [18]. Nonetheless good correlation, *i.e.*, for intravitreal drug clearance between rabbit and human, has been identified for some drugs [89].

Animal housing is time consuming and very cost-intensive, which raises the question if the cost-benefit of performing *in vivo* studies at a large scale with multiple nanoparticle candidates, especially considering that interspecies translation is still not clear, can be considered the best approach. Under these circumstances, a stepwise approach based on *in vitro* and *ex vivo* formulation screening is an adequate approach for more efficient research with improved animal welfare.

To summarize, the data collected in the past decades through the different approaches can serve as a starting point for developing advanced *in silico* models. This approach will ultimately allow to create highly predictive mathematical models and simulations that predict animal and human *in vivo* performance which might facilitate a real interspecies translation with significantly reduced animal experimentation [89].

Chapter 2

Aim of the Thesis

Overcoming the ocular barriers is still a challenging task despite the increasing research efforts over the last decades. Therapeutical approaches based on colloidal nanocarriers have demonstrated their adequacy in this field, with some examples reaching commercialisation status. These treatments only regard diseases affecting the anterior segment of the eye, while the available therapeutics for the posterior segment are still highly invasive. In the recent years, association of nanosystems and less-invasive periocular administration routes has been postulated as a possible strategy to treat these conditions. In addition, preclinical research still lacks robust screening setups which efficiently identify the most promising nanoparticulate systems in biorelevant conditions. These setups would not only improve animal welfare but also potentially boost market access of a new generation of colloidal nanocarriers.

The research work hereby presented was conducted within the framework of the ORBITAL (*Ocular Research By Integrated Training And Learning*) Innovation Training Network, an international consortium funded by the European Union's research and innovation funding programme Horizon 2020 under the Marie Skłodowska-Curie Actions. The ORBITAL-ITN project aims to develop innovative technologies to treat diseases of the posterior segment of the eye.

The present thesis has pursued **three** different **aims**.

The **first**, presented in Chapter 3, was the development of lipid-based nanocarriers intended for the delivery to the back of the eye and loaded with corticosteroids (namely, dexamethasone acetate or dexamethasone). Particularly, starting from pre-formulative studies for adequate ocular-compatible excipients selection, nanostructured lipid carriers and microemulsions were prepared and physiochemically characterized in terms of nanoparticle size, PDI, pH, drug loading and stability. In addition, a novel

approach based on design of experiments (DoE) was applied to create mathematical models that predict these physicochemical characteristics to be able to fine-tune the colloidal nanocarriers for the intended administration route. The selected formulations were further evaluated for their *in vitro* cytotoxicity on a retinal pigment epithelium (ARPE-19) cell line.

The **second** aim, detailed in Chapter 4, was the development and validation of an *ex vivo* setup based on whole porcine eyes for the improvement of preclinical studies in the ophthalmic field in accomplishment of the 3Rs (Replacement, Reduction and Refinement) in animal experimentation. After a preliminary characterization of porcine eyeballs, a 3D printing approach allowed to manufacture two devices (Ocudonor and Ocutainer) for a setup in which retention experiments of liquid (or even semisolid and solid) formulations at a controlled temperature and humidity for up to 18 hours on freshly excised porcine ocular bulbs can be performed. In addition, a methodology for tissue manipulation and drug quantification from the vitreous body was validated.

The **third** and final aim, discussed in Chapter 5, was the *ex vivo* evaluation of the developed formulations. Initially, a classical approach based on isolated porcine sclera and choroid mounted on Franz-type diffusion cells was followed to study drug diffusion and retention. Multiphoton microscopy was utilized for evaluation of the fate of the NLC once in contact with isolated porcine sclera. In a final step, the best performing NLC and microemulsion were further investigated in the novel *ex vivo* whole-eye setup.

Chapter 3

Development of Lipid-Based Nanocarriers for Ocular Drug Delivery

This chapter includes previously published material available as:

González-Fernández, F.M.; Bianchera, A.; Gasco, P.; Nicoli, S.; Pescina, S. Lipid-Based Nanocarriers for Ophthalmic Administration: Towards Experimental Design Implementation. *Pharmaceutics* 2021, 13, 447. https://doi.org/10.3390/pharmaceutics13040447

González-Fernández, F.M.; Delledonne, A.; Nicoli, S.; Gasco, P.; Padula, C.; Santi, P.; Sissa, C.; Pescina, S. Nanostructured Lipid Carriers for Enhanced Transscleral Delivery of Dexamethasone Acetate: Development, ***Ex Vivo*** Characterization and Multiphoton Microscopy Studies. *Pharmaceutics* 2023, *15*, 407. https://doi.org/10.3390/pharmaceutics15020407

Data were partially presented as poster at the 31st Annual Conference of the European Society for Biomaterials (ESB 2021):

González-Fernández, F.M.; Nicoli, S.; Gasco, P.; Pescina, S. Novel application of hot stage polarized light microscopy for the production of nanostructured lipid carriers via warm microemulsion templates. (PS1-12-377). https://esb2021.org/wp-content/uploads/ESB-2021_AbstractBooklet-.pdf

3.1. Introduction

Nanotechnology has seen an exponential growth in the past decades, leading to the development of multiple versatile drug carriers in the range of 10–1000 nm, such as liposomes, polymeric micelles, or solid lipid nanoparticles [90]. Encapsulation into nanoparticles with a high specific surface area allows for increased drug stability and solubility, while maintaining a low side-effect profile [91].

Poorly water-soluble drugs with a strong therapeutic potential have especially benefited from nanoencapsulation, being postulated as a promising tool for circumventing the various ocular barriers. In fact, extensive research in the field has demonstrated an increase in drug bioavailability and residence time at ocular target tissues [92]. As a result, some products are already present in the market, such as Restasis® [93], Ikervis® [94] or Cequa® [95].

During the end of the last century, several nanoparticulate systems based on lipid matrices (also termed lipid-based nanocarriers) have emerged, such as micro- or nanoemulsions, solid lipid nanoparticles (SLN) or nanostructured lipid carriers (NLC), amongst others (*i.e.,* liposomes) (Figure 2).

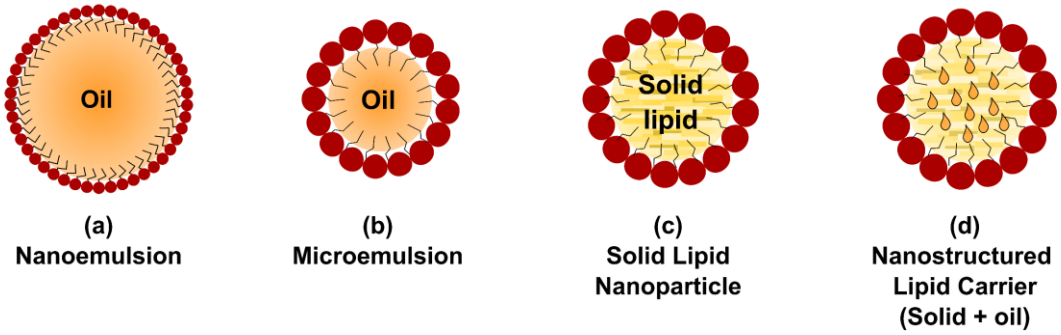

Figure 2. Schematic representation of different lipid-based nanocarriers. Nanoemulsions (a) and microemulsions (b) both present a liquid oily core, but differ in their thermodynamic stability, the former being subject to typical emulsion instabilities, while the latter are thermodynamically stable. Solid lipid nanoparticles (SLN) (c) present a rigid lipid matrix with poor drug-loading capability, which is improved by partial substitution with an oil, leading to the so-called nanostructured lipid carriers (NLC) (d).

Compared to other extensively studied nanocarriers based on polymers, their manufacturing process can be easily scaled-up and, by adequate selection of the production approach, the usage of organic solvents (*i.e.,* chloroform) can be avoided. Moreover, the physiological lipids that form the matrix commonly benefit from the denomination of Generally Recognized as Safe (GRAS) from the regulatory agencies [96,97]. When applied topically, for example, the lipid core is believed to act as a drug depot in the lipid layer of the tear film, while the presence of a non-ionic surfactant is demonstrated to enhance corneal penetration [98]. The low nanoparticle size also accounts for the translucent/transparent appearance to the naked eye, increasing patient acceptance. Regarding the formulation, it has been reported that a size reduction under 90 nm allows for better stability of the colloidal dispersion since gravitational phase-separation is prevented by Brownian motion [99,100].

3.1.1. Lipid-based nanocarriers for ocular drug delivery

Oil-in-water nanoemulsions are colloidal dispersions of an oil, stabilised with a surfactant, that appear as nanometric spheres with a typical nanoparticle size under

100 nm [100]. They are obtained by means of high mechanical shear, remaining as a thermodynamically unstable colloid. Poorly water-soluble drugs such as dorzolamide, terbinafine or acetazolamide have already been formulated as ophthalmic nanoemulsions with positive results [101-103]. A clobetasol propionate nanoemulsion for inflammation after cataract surgery has recently completed a phase III trial [104], while cyclosporine [93,94] and difluprednate [105] nanoemulsions are already on the market.

Different from nanoemulsions, **microemulsions** exhibit thermodynamic stability and reduced nanoparticle average sizes, appearing optically transparent. In fact, oil-in-water microemulsions are defined as lyotropic phases obtained by spontaneous self-assembly and not by mechanical shear, resulting therefore in a thermodynamically stable system [100]. The system remains unaltered if no chemical and/or microbiological degradation occurs and is reversible after agitation or heating/cooling processes [106]. Multiple ocular therapeutics have been loaded into microemulsion systems, such as cyclosporine, dexamethasone, or pilocarpine [107].

Lipids that appear solid at room temperature can also emulsify if heated over their melting point, while further solidification of these globules can lead to the formation of the so-called **solid lipid nanoparticles (SLN)**. Several production methods have been proposed, including high-pressure homogenisation followed by sonication or melt emulsification [97]. SLN present a solid lipid core that protects chemically labile molecules and allows for the possibility of controlled release of both lipophilic and hydrophilic drugs, maintaining a good cost-effectiveness profile [108,109]. Nonetheless, some drawbacks such as high water-content (77–99%), poor drug loading and early drug expulsion have been reported [97].

Solid lipid matrices typically show different polymorphic transitions over time [110]. As a result, densely packed crystalline lattices are progressively formed, and drug interpenetration between fatty acid chains is hindered, leading to premature expulsion [111]. Non-homogeneous matrices that combine long- and medium-chain acylglycerols have been demonstrated, for instance, to increase drug-loading capacity by creating spaces between the different-length fatty acid chains [112,113].

Modifying the lipid polymorphism, and thus improving drug stability, can also be achieved by addition of a liquid lipid to the solid matrix, leading to the so-called **nanostructured lipid carriers (NLC)** [114,115] It has been postulated that the added oil can remain as small droplets that solubilise most of the drug and are protected by the surrounding solid matrix. In other cases, depending on oil and solid lipid miscibility, a new amorphous matrix with improved polymorphic behaviour is believed to be formed [116]. The number of therapeutics that have been successfully incorporated

into SLN and NLC has grown in the past decades and cover several ocular disorders such as inflammation (indomethacin, sodium diclofenac) or infections (ofloxacin, azithromycin, acyclovir, or ketoconazole) [117,118].

Some limitations have been identified regarding the ability to obtain consistent nanoparticle populations. The relatively simple manufacturing processes and the low number of excipients required contrast with the high sensitivity of the production process to small variations. In fact, during nanotherapeutics production, any change in the manufacturing process can result in significant deviation from the quality attributes required for the nanoparticle population [119]. In addition, when the ocular administration route is considered, new challenges arise in the development of efficient nanoformulations. Precise control of key parameters such as average size, polydispersity or surface charge becomes fundamental to effectively overcome physical and mechanical barriers. At the same time, a compromise between colloidal system stability, ocular compatibility (pH, osmolarity) and excipient toxicity must be achieved [120].

3.1.2. Nanoparticle optimization through Design of Experiments (DoE)

Many scientists suggest that identification of critical operator-controllable independent variables could help overcome the aforementioned variability issue [121]. Multivariate analysis tools, based on statistics, allow to understand the simultaneous contribution of various factors in altering final formulation characteristics [122]. The development of mathematical models that predict nanoformulation specifications has been proposed as tool for optimisation [123-125].

The classical **quality-by-testing (QbT)** regulatory framework ensures final product adequacy through inflexible manufacturing steps and testing on bulk materials and both intermediate and final products. Batch quality failure is usually not clearly understood, nor investigated for its cause [126].

In the last years, regulatory agencies such as the European Medicines Agency (EMA) and the U.S. Food and Drug Administration (FDA) have started to recommend a change in classical quality assurance methods, moving forward to the so-called **quality by design (QbD)**. This term has been defined by the International Conference on Harmonization in its guidelines as "*a systematic approach to development that begins with predefined objectives and emphasizes product and process understanding and process control, based on sound science and quality risk management*" [127].

In opposition to traditional systems, QbD allows to unveil the relationships between manufacturing variables and critical, patient-oriented quality product attributes. The

production remains consistent and robust but is also flexible to changes. In fact, end-product testing becomes almost secondary since process control and exhaustive identification of possible variability sources are the actual quality assurance. As a result, batch release may be quicker since constant testing might not be required [128].

Early adoption of a QbD perspective, also in initial research stages, already sets the first steps to a successful patient-focused product. The identification of critical material attributes (CMAs) of bulk materials and critical process parameters (CPPs) allow to control key parameters of the production process that, through proper adjustment, can lead to the desired product. All possible sources of variability should be under control, and the risk assessment (RA) activity at the beginning and end of the process allows for systematic identification of possible hazards and the risks associated with them [129].

Quality-by-design approaches increase research efficacy, benefiting both manufacturers and regulatory agencies. The former reduces the time and cost of research, and the latter benefits from a wider and more robust understanding of the production process that could ease market approval of complex nanoparticulate systems [130]. Patients also benefit from QbD since a new generation of therapeutics, based on nanocarriers, could easier access commercialisation, improving actual therapeutic options. As a result, early adaptation of QbD approaches might lead to effective translation of years of research into innovative marketed nanotherapeutics.

3.1.2.1. Statistical Design of Experiments (DoE)

Assessing the influence of CMAs and CPPs affecting the final product can be performed using univariate or multivariate analysis techniques. In univariate analysis, all factors are set at a baseline level, and each time, a single factor is changed to different levels, analysing the result of this change on the final product. This classical one-factor-at-a-time plan eventually identifies the most important factors (or **main effects**) but fails to account for possible synergisms/antagonisms between the factors (**factor interactions**). In addition, the best factor setting that leads to an optimal product is not guaranteed to be properly elucidated. A more efficient approach to unveil these critical interactions, of utmost interest within the QbD framework, is the so-called statistical design of experiments (DoE) [131].

Design of experiments (DoE) is a multivariate statistical tool that allows to identify relationships between **factors** influencing a process and the observed outputs. This is accomplished through a series of predefined and structured experiments (or **runs**) by which different combinations of the input variables of interest are explored, recording the observed changes on measurable characteristics of the final product (**responses**).

A statistical analysis of the obtained results leads to develop mathematical equations that describe the contribution of each variable to the changes observed in the response under study [132].

In the context of a production process, CMAs and CPPs are independent variables denoted as factors and can have a quantitative or qualitative nature. Quantitative factors are continuous and thus are set within a numerical range (*i.e.*, concentration of an excipient or homogenisation temperature); qualitative variables, such as lipid nature or type of supplier, are defined as categorical factors. The response outputs are selected among critical quality attributes (CQAs) of the final product [133].

The measured response (y) is, consequently, the overall sum of the effects due to single factors (main effects), interactions between the factors and the experimental noise. The resultant regression model equation considering, for example, two quantitative factors (*i.e.*, A and B) can be expressed according to the general formula:

$$y = \beta_0 + \beta_1 x_1 + \beta_2 x_2 + \beta_{12} x_1 x_2 + \epsilon \quad (1)$$

where x_1 represents factor A, x_2 represents factor B and x_1x_2 represents the two-factor interaction (AB). The ϵ term represents the experimental error, the β_0 indicates the intercept and the beta parameters (β_1 and β_2) are the coefficients to be determined through the experimental design. The existence of the $\beta_{12}x_1x_2$ term indicates that factors A and B contribute in a synergistic (if the sign is positive) or antagonistic (if the sign is negative) manner to modify the response [134].

Response equations can be graphically represented creating 3D plots and their respective 2D contour plots (Figure 3).

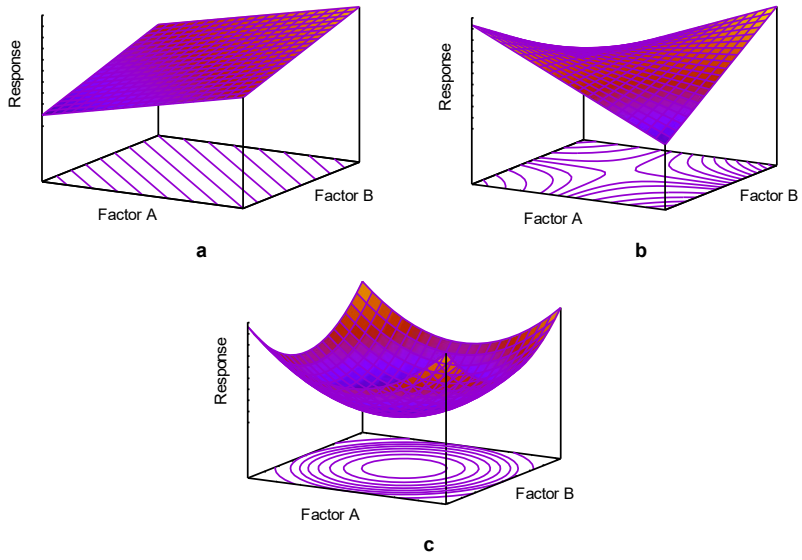

Figure 3. Three-dimensional response surfaces and their respective bidimensional contour plots following (a) a linear or first-order function and (b) a second-order equation. Inclusion of quadratic terms in the function allows to detect maximums or minimums of the response (c). Models calculated with Gnuplot software.

The simplest linear, first-degree polynomial is depicted in Figure 3a. In this way, it is easy to determine how a change in any factors (Factor A or Factor B in Figure 3) produces a change on the response surface. Progressive inclusion of higher-order terms into the polynomial leads to model curvature (Figure 3b, 3c). For optimisation purposes, usually quadratic (Figure 3c) or rarely cubic terms might need to be included to find a proper fit of the model to the observed response. If more than two factors are studied, graphical representation can only be achieved by fixing a constant value for the other factors studied [134,135].

During the initial planning stages, a wide number of factors should be suspected of contributing to response modification. It is important to underline that, nonetheless, following the Pareto rule, only 20% of the factors are considered to contribute to 80% of the observed output. Different approaches allow to select these *vital few* factors (usually 2–4) from the initially considered *trivial many* factors [136]. Factor screening for detection of these vital few factors is sometimes performed following a classical try-and-error methodology, but a special group of experimental designs, known as screening designs, offers a quicker and more efficient approach with low experimental work. Their reduced experimental workload comes with the drawback of limited statistical power: while screening designs can estimate active main effects, they fail to correctly assess factor interactions and model curvature [133,137].

Considering ocular drug delivery, the mean nanoparticle size (Z-average value) and polydispersity index (PDI) are typical CQAs found to be optimised in experimental

designs [138]. Generally, particles of ≤ 200 nm are considered to offer adequate permeation and mobility through ocular barriers, while small particles, around 20 nm, are quickly cleared out, as demonstrated in periocular administration [29,139]. Therefore, populations with a narrow particle size distribution (PDI < 0.2) and a Z-average value under 200 nm are also desired. The zeta potential accounts for the degree and sign of electrostatic forces between nanoparticles, which affect their stability and aggregation behaviour. Regarding colloidal stability, high absolute values (*approx.* ± 20 mV) are of interest, since lower values might be overcome by attractive forces between particles, leading to formulation instability [140,141]. In addition, following a topical administration route, the presence of a cationic surface charge is believed to improve residence time by interaction with the negatively charged corneal epithelium and the mucins from the tear fluid and the conjunctiva [142-144]. High drug loading and entrapment efficiency are also desirable variables to be optimised through DoE. The former accounts for the maximal percentage of a drug that can be encapsulated into the nanoparticles, while the latter quantifies the efficiency of this loading process during formulation production [130].

CPPs can also be considered in the experimental design. In this sense, some Authors have included both the number of high-pressure homogenisation cycles and the pressure at which they are performed as variables under study [145]; other Authors have included the storing temperature since it might modify long-term stability [146].

3.1.2.2. Two-Level Factorial Designs

Two-level factorial designs are of use when only two values for each factor are studied. Considering k = the number of factors studied, 2^k possible combinations between factors and levels are explored. As an example, if three factors are taken into consideration (k = 3), the number of possible combinations is eight and so are the number of experiments (or *runs*) that can be performed [133]. Two-level full factorial designs do not require intensive statistical analysis, and thus, they are an accessible first approach to design of experiments, and some examples have been recently reported to prepare ophthalmic lipid-based nanocarriers.

Dexamethasone-loaded nanostructured carriers intended for topical administration were obtained [147]. In a first step a high drug entrapment efficiency was achieved (*approx.* 88%) through drug solubility in lipid-screening tests, followed by crystallinity studies (differential scanning calorimetry (DSC)) of the matrices, which allowed Authors to select optimal components for NLC formulation. In a second step, the concentration of the drug, the surfactant and the total lipid amount were selected as independent variables to be studied at two levels in a 2^3 full factorial experimental design with four responses to be optimised. All the selected variables, especially

surfactant concentration, showed a contribution to particle size, while lipid concentration did not affect the entrapment efficiency. The best formulation significantly improved dexamethasone solubility and ensured a high corneal retention of the drug when tested *ex vivo*. On this basis, NLC were then functionalised with a mucoadhesive polymer (hydroxypropyl methylcellulose) that could improve nanoparticle adhesion to the mucosal surface. Two further responses related to nanoparticle population distribution by volume were included in a three-factor, two-level full factorial design that led to eight unique formulations. Studies on human corneal epithelial cell layers demonstrated good biocompatibility, while a depot-like effect on the corneal surface was observed in an *ex vivo* corneal porcine model [148].

Following a 2^4 full factorial design flurbiprofen-loaded NLC were developed [146]. In this study a fourth factor, namely storage temperature (either at room temperature or at 4 °C), was included as a CPP, and their influence on the particle mean size, PDI and zeta potential was assessed. The optimised formulation demonstrated good physicochemical stability and high tolerance for eye instillation on both *in vitro* and *in vivo* assays.

These examples should be addressed with caution since the Authors have studied the quantitative factors at only two levels, inevitably forcing the response to follow a linear model, and no curvature of the response surface can be addressed.

3.1.2.3. Plackett-Burman designs

Plackett–Burman experimental designs represent a very economical option for initial screening of many factors. They are not intended for creating a proper response surface but to identify which of the studied single factors and factor combinations actively contribute to modify the response under study. These designs are usually called “screening designs” since they are usually followed by a second experimental design where the factors are studied at, at least, three levels, so a curved response surface can be obtained if required [149]. The number of experiments to perform corresponds to the first multiple-of-four higher than the number of factors to be screened. As an example, for eleven factors set at two levels each, a full factorial design would require 2^{11} = 2048 experimental runs, while Plackett–Burman designs with only twelve experimental runs are able to adequately estimate main effects. Consequently, this design presents a high level of confounding [150]. Recently the development of ibuprofen-loaded NLC intended for topical ophthalmic administration has been reported. In this study, seven initially considered variables were quickly screened following Plackett-Burman design with only 12 experimental runs and only three of them were detected to be actively contributing to modifying the responses under

investigation. The optimisation of NLC was then obtained following a Box–Behnken design [151], as described later in Section 3.1.2.4.

3.1.2.4. Optimisation Designs

Since screening designs only explore two levels of each factor, these designs allow one to model only linear functions (Figure 4a).

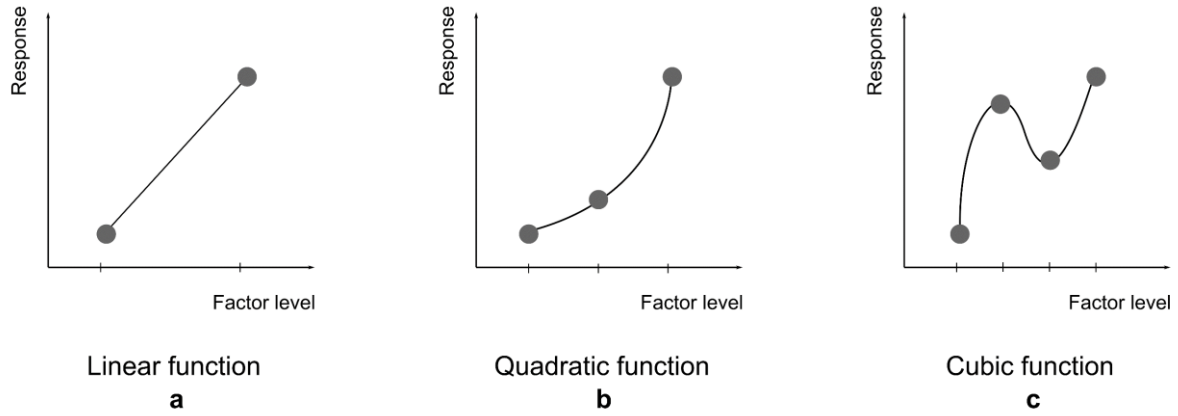

Figure 4. Graphical representation of the possible response function and the number of levels required for its estimation. Two-level factorial designs presuppose a linear response (a), while the inclusion of intermediate points permits one to calculate the possible curvature in the response (b, c).

Optimisation designs (also known as response surface methodologies), on the other hand, explore at least three levels of each factor and thus can more accurately address any lack of linearity by creating polynomials that contain quadratic (Figure 4b) and/or cubic terms (Figure 4c). The number of available experimental designs in this category is elevated, resulting in different possible valid approaches to the same optimisation quest [150]. In this Section a summary of the different optimisation approaches, with examples for lipid-based nanocarriers will be presented.

Three-level full factorial designs adequately estimate non-linear effects, but with increasing factors, the required experimental work increases exponentially. As an example, considering only four factors, a minimum of 81 runs ($3^4 = 81$) is required if all the possible combinations are studied [152,153]. Three-level full factorial approaches remain of interest only if two or three factors are under study, as demonstrated by the available literature [154-157]. Youshia *et al*. [154] developed lipid-based nanocarriers loaded with the anti-glaucoma drug methazolamide containing a heterogeneous solid lipid matrix where the Compritol® 888 ATO (glycerol behenate)-to-cetostearyl-alcohol ratio and also the surfactant concentration (Tween® 80) were selected as factors in a 3^2 full factorial design. Mixed-lipid matrices have been demonstrated to increase drug loading since the heterogeneous composition modifies crystallisation behaviour (See Section 3.1.1.). Including the ratio between lipid components as a factor to be studied

allows to determine the optimum matrix composition to improve entrapment efficiency. Statistical analysis of the results revealed how increasing concentrations of the solid aliphatic alcohol allows for larger dissolution of slightly hydrophilic compounds such as methazolamide. No visual irritation and an increased pharmacological response were demonstrated after *in vivo* topical administration of the optimised formulation in albino rabbits when compared to a methazolamide solution. The presence of stearylamine, a surface-charge modifier, confers a positive charge, enhancing mucin interaction and ultimately increasing the retention time of the formulation. Similar results have been achieved with cetyltrimethylammonium bromide (CTAB), which Fangueiro and colleagues [155] used to confer a positive charge to a lipid nanoparticle with a water/oil/water structure containing Softisan® 100 (lipid mixture), Lipoid S75 (soybean phosphatidylcholine) and Poloxamer 188. A three-factor three-level full factorial design demonstrated that the lecithin concentration in the formulation (Lipoid S75) was the key factor affecting nanoparticle size and the PDI ($p < 0.05$). Surface functionalisation with CTAB was studied after nanoparticle optimisation at varying concentrations of CTAB, analysing *in vitro* cytotoxicity due to CTAB addition. The optimised formulation containing CTAB (0.5% of the lipid phase) was stable over time and biocompatible, as demonstrated with Alamar blue assay in the human retinoblastoma cell line. Although blank formulations were tested, results appear promising for their use in ocular delivery. In fact, epigallocatechin gallate, a useful antioxidant agent in the treatment of several ocular diseases, was successfully loaded into the nanoparticles in a further publication of the same research group [158].

Other examples of the use of three-level factorial design are proposed for the development of brimonidine tartrate nanoemulsion [156] and bimatoprost-loaded SLN [157].

Central composite designs (CCDs) are based on classical two-level full factorial designs to which new intermediate points have been added, called also star points. Depending on the number of star points and their position withs respect to the initial two factor levels, up to three different CCDs typologies have been proposed [150].

Several examples of CCDs applied to lipid nanoparticle optimisation are reported in the literature. Particularly, Yadav and colleagues [159] recently proposed a new approach for the treatment of age-related macular degeneration based on atorvastatin-loaded solid lipid nanoparticles intended to be topically administered. Preliminary studies allowed them to demonstrate that the concentration of all the four formulation components (lipid matrices and co-/surfactants) affected the responses under study. A central composite design concluded that the two responses of interest, particle size and entrapment efficiency, can be expressed as second-order functions of two

independent variables: the Compritol® 888 ATO/Phospholipon® 90H and the Poloxamer 188/polyethylene glycol (PEG) 400 ratios. The optimal formulation was obtained based on the criteria of minimising particle size while maximising entrapment efficiency.

In a series of publications, González-Mira and colleagues explored the application of rotatable CCDs for anti-inflammatory flurbiprofen-loaded NLC optimisation. After a preliminary two-level full factorial design study [146], adequate lipid excipients were selected based on drug solubility and ocular compatibility criteria [160]. The three-factor, five-level rotatable CCD allowed, with only 16 experimental runs, them to create a regression model for each of the four responses under study. The obtained optimised formulation showed promising physicochemical and colloidal characteristics for ocular administration, and ocular safety was assessed through the *in vivo* Draize test. Collected data allowed them to formulate new flurbiprofen-loaded NLC [161], where cetostearyl alcohol, previously used as a solid lipid matrix, was substituted with Compritol® 888 ATO and further response was optimised which quantifies formulation sedimentation or creaming over the storage period (15 days, room temperature).

Another example is provided by triamcinolone acetonide, a corticosteroid with both anti-inflammatory and antioedema action, included into NLC [162]. Nanoparticles, prepared for targeting the posterior segment of the eye by topical administration, were developed following an initial 2^4 full factorial design, augmented afterwards with eight star-points and two centre points to ensure adequate quadratic term estimation. The resulting optimised formulation demonstrated nanoparticles with a spherical shape, with a particle size lower than 200 nm and a negative surface charge. Triamcinolone acetonide was entrapped into the amorphous matrix consisting of Precirol® ATO 5 and squalene with Lutrol® F68 as a surfactant. In a second publication [163], long-term stability was assessed, and *in vivo* studies on mice demonstrated that the same nanoparticles loaded with Nile red (a fluorescent dye used instead of triamcinolone acetonide) can be detected at the posterior segment after topical administration.

Natural antioxidant agents, such as curcumin or quercetin, have also been selected to produce ophthalmic NLC [145,164].

Box–Behnken Designs (BBDs) were firstly introduced in the early 1960s [165]. This design allows to avoid combinations of factors at their extreme values, which might be useful, for example, when optimising processing parameters such as pressure and temperature that cannot reach extreme value combinations [166] and has been identified as a limitation in CCDs. Another advantage is the reduced number of experimental runs. As an example, for three factors under study, CCDs would require

a minimum of 20 runs and possibly new extreme factor settings, while a BBD requires only 15 experimental runs and combinations of factor extremes are avoided. Nonetheless, this advantage disappears when the number of factors considered is higher than four [150,167].

A good number of examples are available in the literature for the optimisation of lipid-based nanocarriers [151,168-173].

The first study here presented shows a sequential approach in which Rathod and colleagues [151] started with an initial Plackett–Burman experimental design (see Section 3.1.2.3.) to develop ibuprofen-loaded NLC. Seven initial factors (amongst others, surfactant type and concentration, lipid concentration, homogenisation speed and time) were quickly screened in only 12 experimental runs by assessing their influence on three responses: particle average size, PDI and zeta potential. Only three factors demonstrated to influence the responses under study, which were further modelled *via* a Box–Behnken experimental design, including the drug entrapment efficiency as a fourth dependent variable. Quadratic effects were observed for three of the responses, while entrapment efficiency demonstrated to be not influenced by the variables under study. A robust optimised formulation, stable over 1 month if stored between 2 and 8 °C, was obtained with up to 3% of effectively loaded ibuprofen that showed no burst release and a sustained release over 12 h.

Following a three-factor Box–Behnken design, Baig and colleagues [168] prepared besifloxacin-loaded cationic nanostructured lipid carriers. Besifloxacin is a practically insoluble fourth-generation fluoroquinolone, approved as suspension by the FDA for the treatment of bacterial conjunctivitis [174]. Three independent variables regarding excipient concentrations were selected for the optimisation of nanoparticle size, PDI and zeta potential in only 17 runs. All three responses were fitted to quadratic models, which demonstrated adequate correlation values and a satisfactory lack-of-fit testing. To further increase drug bioavailability, cetyltrimethylammonium bromide (CTAB) was added for nanoparticle surface functionalisation. Cationic NLC (0.02% CTAB) demonstrated lack of toxicity when tested *in vitro* on porcine fibroblasts. In addition, when fluorescent rhodamine B was chosen as a loading agent, a significant fibroblast uptake was observed.

NLC were also developed for ophthalmic delivery of antimycotic agents such as amphotericin B or natamycin [169-171] or antibiotics such as levofloxacin [172] or gatifloxacin [173].

3.1.2.5. A particular approach: Mixture Designs

Mixture designs consider the studied factors to be the components of a blend [175]. The mathematical perspective of this approach is that the relative proportions between the components of a mixture must sum up to one. This fundamental constraint leads to one limitation: increments in one component leads to diminution in the proportion of at least one of the other components. The measured response, therefore, is not supposed to depend on the quantity of each component (the quantity of mixture) but on the relative proportions between each of them [176]. In addition, the term β_o present in a typical linear model (Equation 1 in Section 3.1.2.1) is not required anymore since all the mixture components must sum up to one. This ultimately leads to more simplified model equations, usually referred to as *canonical* or *Scheffé* polynomials [175].

A natural approach is considering that all factor blends are possible and thus the relative proportions of each component can freely range from zero to one. In this case, boundary designs such as simplex-lattice or simplex-centroid mixture designs propose experimental runs based on single-component mixtures, located on the vertexes, and binary mixtures, located on the edges of the factor space. The overall centroid point contains all mixture components in equal proportions. Axial designs, on the other hand, place the experimental runs inside the simplex region, and only complete mixtures are studied. In pharmaceutical formulations, in most cases, only complete mixtures will be of interest, so research time and model efficiency might be improved by individualising a constrained subregion of interest within the whole simplex. Setting upper and/or lower boundaries to at least one of the components leads to the so-called extreme vertices designs, allowing for a more detailed investigation of the region of interest. It is important to note that in most cases, even though a mixture design should be considered, the same problem can be proposed as a factorial design, as explained by Cornell in [177].

Interpretation of the effects might become difficult if more than three mixture components are present, so it can be helpful to virtually consider similar excipients as a single mixture component. In this sense, lipid-based nanocarrier excipients can be formulated as the components of a pseudo-ternary mixture of water, lipids and surfactants-cosurfactants [178,179]. If some upper and/or lower boundaries are known for one or more of the components, constrained mixture designs allow to explore only a subset of the design space [180]. In case the number of factors is elevated, screening mixture designs allow to select the vital few contributing to the responses under study [181]. Similarly, process variables can also be included in the so-called mixture-process variable designs. Moreover, it is possible to create mixture-amount designs, where the amount of mixture is also considered a factor under study [177-179,182].

Shah and colleagues [183] developed a nanoemulsion-based vehicle for moxifloxacin ocular delivery following a mixture design. The pseudo-ternary mixture consisted of water, oil (ethyl oleate) and a mixture of surfactants (Tween® 80 and Soluphor® P). The only response to be optimised in the mixture design was the nanoemulsion particle size. The second-order model demonstrated that the relationship between the proportion of water and surfactants did not affect the particle size, and drug loading reached 0.5% w/w. The resulting optimised formulation, stable upon dilution, guaranteed antibiotic therapeutic concentrations in the aqueous humour when administered *in vivo* to albino rabbits.

3.1.2.6. Data Analysis and Model Application

The obtained response values for each experimental run must undergo the critical step of data analysis, which has been mainly simplified with current available DoE software [184]. The overall aim is to obtain a regression model that accurately predicts the response by conferring an adequate regression coefficient to each main effect and interaction included in the polynomial. Equally important is to develop the lowest-order model with few terms that still accurately predicts the response. This is achieved by multiple linear regression, which at the same time requires least-squares analysis.

Initial inspection of raw experimental data can serve as a starting point for the next stage of regression analysis. Multiple statistical tools are available: analysis of variance (ANOVA), R-squared (R^2) values, normal probability plots and residual plots, amongst others. The R^2 value is an important indicator of the level at which the obtained model fits the raw data (goodness of fit), and the more its value approaches 1, the better. However, if interpreted alone, it can lead to false conclusions, and a further indicator is required. Predicted-R^2 is an indicator of the model goodness of prediction and accounts for its ability to predict responses for new, previously unexplored factor settings. A model can show high R^2 values while showing negative values for predicted-R^2, indicating that the model has no predictive power, though fitting the initial data (it is predicting experimental noise) [134].

The analysis of variance (ANOVA), in combination with Fisher tests, helps to evaluate model significance and lack of fit, both indicators serving as a statistical validation of the polynomials generated by DoE software. The proposed model is statistically significant if $p < 0.05$ (at a 95% level of significance), and if enough replicates have been included, the lack-of-fit test should be $p > 0.05$, otherwise the model is explaining random noise. Further graphical tools also allow to detect whether any response transformation is required and to check for outliers [133,185]. The obtained polynomial can be plotted, as shown in Figure 3, for a better understanding of factor contribution to the response.

Once the analysis step is concluded with a satisfactory model equation, its validity can be further assessed *via* confirmatory runs. New trials with unexplored factors settings are performed, and the response experimental data are compared to the predicted response of the model.

Finally, current DoE software packages include optimisation tools that use the obtained regression models to find the best factor combination that leads to desired product specifications. The working principle is based on desirability functions that allow one to simultaneously optimise multiple responses [186,187]. The Researcher can select whether each response is desired to be minimised, maximised, or set in a range, and the software proposes multiple solutions (expressed as factor combinations) with predicted responses that meet to in a greater or lesser extent the pre-established criteria. Each solution is assigned a desirability index, which is highly dependent on the severity of the optimisation criteria established by the operator.

3.2. Development of Dexamethasone Acetate NLC (DexAc-NLC)

The Section below describes the initial efforts into developing nanostructured lipid carriers loaded with the anti-inflammatory drug dexamethasone acetate, intended for periocular administration. The results contained in this Section will also serve as starting point for further colloidal nanosystems developed in Sections 3.3 and 3.4, particularly the pre-formulation studies that led to the selection of the excipients. In addition, most analytical methodologies (HPLC, extraction validation, *etc*.) hereby presented will further be used in the other Sections and might not be thoroughly explained again. At the end of this Section, a first attempt to optimize the NLC by statistical design of experiments is also presented. The unconclusive, but promising results also lead to a successful DoE application for the characterization of a microemulsion and will be further discussed in Section 3.4.2.

Corticosteroids are still nowadays a first-line treatment in clinics and maintain a strong research interest due to their high pharmacological impact and their challenging properties regarding ocular drug delivery [49]. Among corticosteroids, dexamethasone acetate has been selected as drug candidate for the development of this project, thanks to its strong clinical rationale. Dexamethasone is usually administered in concomitance with other treatments for retinopathies which usually present with inflammation such as diabetic macular oedema [188]. The main inconvenience is related to the required frequent dosing (when administered topically) or the invasiveness of the route (when administered intravitreally) which breaks the immunological privilege present in the interior of the eye. Nanoparticulate systems with a monodisperse population (PDI $\leq$ 0.2) and an average size below 200 nm capable of a sustained release are believed to overcome the ocular barriers and reduce the frequency of administration. Administration following a periocular route further reduces the risk of undesired complications and allows to place the nanocarrier closer to the site of action (retina) [189]. In addition, DexAc shows a robust analytical method, which is fundamental for the development of an *ex vivo* model where a straightforward analytical process is preferred. This simplicity further eases the application of DoE, as will be discussed in further Sections.

3.2.2. Materials and Methods

3.2.2.1. Materials

Dexamethasone acetate (DexAc; IUPAC [2-[(8S,9R,10S,11S,13S,14S,16R,17R)-9-fluoro-11,17-dihydroxy-10,13,16-trimethyl-3-oxo-6,7,8,11,12,14,15,16-octahydrocyclopenta[a]phenanthren-17-yl]-2-oxoethyl] acetate; MW 434.5 g/mol; LogP 2.65; water solubility 10 µg/ml) [190] was purchased from TCI Europe N.V. (Zwijndrecht, Belgium).

Dexamethasone (Dex; IUPAC (8S,9R,10S,11S,13S,14S,16R,17R)-9-fluoro-11,17-dihydroxy-17-(2-hydroxyacetyl)-10,13,16-trimethyl-6,7,8,11,12,14,15,16-octahydrocyclopenta[a]phenanthren-3-one; MW 392.5 g/mol; LogP 1.9; water solubility 89 µg/ml) [191] and tyloxapol (IUPAC 4-(2,4,4-trimethylpentan-2-yl)phenol; formaldehyde; oxirane) were from Sigma Aldrich (Taufkirchen, Germany). Triacetin (glycerol triacetate) was purchased from TCI Europe N.V. (Zwijndrecht, Belgium). Imwitor® 491 (I491, glycerol monostearate (GMS); ≥ 90% content in monostearate) was kindly gifted by IOI Oleo GmbH (Hamburg, Germany). Ultra-pure water was obtained with an Arium® Comfort equipment (Sartorius, Göttingen, Germany) and all other chemicals were of analytical grade.

3.2.2.2. Lipid solubility screening

A simple method for quick drug solubility screening in both liquid and solid lipid matrices compatible with the ocular route was developed, with modifications from [192]. Briefly, five milligrams of dexamethasone acetate were accurately weighed in transparent glass vials. Aliquots of the selected oils were added at room temperature under magnetic stirring until optical transparency was observed, allowing the system to stabilize for five minutes between each aliquot. For solid lipids, each sample was heated ~5 °C over the melting point and the same procedure was followed. Endpoint was considered when no signs of turbidity were macroscopically observed. Results were confirmed in triplicates.

3.2.2.3. Oil-solid lipid mixture characterization by Differential Scanning Calorimetry

Binary mixtures at different ratios of the selected oil and solid lipid were characterized by Differential Scanning Calorimetry (STAR-e System DSC 1, Mettler Toledo, Columbus, Ohio, USA). To this end, 11 ± 1 mg of material were accurately weighted in 100 µL aluminium crucibles and sealed. DSC apparatus was calibrated with indium calibration standard (for melting point and heat of fusion). Data was obtained following heating ramps from 25 to 90 °C at a 2 °C/min heating rate. Polymorphic events were recorded at 5 minutes, one day, one week and 1 month after solidification of the melts.

3.2.2.4. Surfactant screening

Pseudoternary phase diagrams were constructed with three different ocular compatible surfactants, using a water titration technique. Briefly, initial mixtures containing only lipid mix (40% triacetin and 60% GMS) and a surfactant (in varying ratios, ranging from 9:1 to 1:9 in weight) were accurately weighted in transparent glass vials. The mixtures were heated at 65 °C under magnetic stirring. Aliquots of 10% (with respect of the initial lipid/surfactant weight) ultra-pure deionized water were

progressively added and the macroscopically appearance after stabilization was noted. The mixtures were classified as either macroscopically transparent or not, with no efforts on further characterizing the non-transparent mixtures. Data was plotted using OriginPro® 2019 (OriginLab, Northampton, Massachusetts, USA).

3.2.2.5. Hot stage polarized light microscopy

An optical polarizing light microscope (Nikon Optiphot 2 POL, Nikon, USA) coupled to a stage temperature microscope controller (TP 93 Linkam Scientific Inst., Miami, USA) allowed to confirm microscopical isotropy for the selected candidates of the pseudoternary system lipid mix-tyloxapol-water. A drop of warm sample was deposited on a microscope slide, carefully placing a cover glass. Samples were positioned on the hot stage, preheated at 65 °C, and observed under cross-polarized light immediately, minimizing any possible evaporation. Photomicrographs were taken at 400x magnification.

3.2.2.6. NLC preparation and characterization

A modified method based on previously published work by Cavalli and colleagues [193], with some modifications from [194] was followed. Briefly, the lipid mix, surfactant, and drug were accurately weighted in an 8 mL glass vial with a screw cap and heated under magnetic stirring to 65 °C. After stabilization of the system, 2.25 mL of preheated ultra-pure deionized water was added at the same temperature and the system was stabilized for 5 minutes. The warm microemulsion was dispersed 1:20 in 47.5 mL of cold water (~2 °C) with a sonicating probe at a constant frequency of 30 kHz (Amplitude 100% (180 µm), Cycle 1; UP100H ultrasonic Processor, Hielscher ultrasonics, Teltow, Germany). The dispersed NLC were placed for 10 minutes at -20 °C, followed by 10 minutes in a sonicating bath (Branson 2510 Ultrasonic Bath Sonicator, Branson ultrasonics, Danbury, Connecticut).

After 24 hours the obtained NLC were washed from unencapsulated drug and concentrated by means of a tangential flow cartridge, following manufacturer instructions (Vivaflow® 100kDa, Sartorius, Göttingen, Germany). Samples were characterized for size and zeta potential.

The same procedure was followed for the preparation of Dex-NLC.

Dynamic Light Scattering (DLS)

A Malvern Zetasizer Nano ZS (Malvern Panalytical Ltd., Malvern, UK) was used for nanoparticle size and zeta potential measurement. Measurements were performed at 25 °C, with an incidence angle of 173° (refractive index 1.33; viscosity 0.8872 cP). For the size measurement, samples were diluted 1 to 50 with ultra-pure deionized water.

Size distribution was reported as Z-average expressed as distribution by intensity. For zeta potential characterization, samples were diluted in a 10 mM NaCl solution and measured in a zeta potential cell.

Drug loading

Drug loading was determined after digestion of NLC with tetrahydrofuran (1:5, v/v) at room temperature for 15 min. Aliquots of the digest were diluted 1:10 with an extraction mixture of acetonitrile and water in ratio 65:35 (v/v) and submitted for HPLC-UV analysis.

HPLC Analysis

A HPLC/UV-Vis method allowing for the simultaneous quantification of both dexamethasone and dexamethasone acetate was developed, starting from [56]. Analysis was conducted with an Agilent 1260 Infinity apparatus (Agilent Technologies, Santa Clara, CA, USA). Separation occurred in a reverse phase column Nova-Pak® C18 (4 µm, 3.9*150 mm; Waters, Milford, MA, USA) heated at 40 °C. A mobile phase consisting of an acetonitrile and water mixture in ratio 45:55 (v/v) was pumped at 1 mL/min and detection was performed at 246 nm. Retention times of 2.7 min for dexamethasone and 5.7 min for dexamethasone acetate were observed.

3.2.3. Results and Discussion

The use of lipid-based nanocarriers to address the challenging delivery to the posterior segment of the eye has shown increasing interest in recent years [195]. On this basis, NLC were selected for efficient delivery of dexamethasone, a potent corticosteroid, under its more lipophilic prodrug ester, dexamethasone acetate, to increase its affinity to lipophilic tissues [196].

Pre-formulation studies for selecting adequate excipients are hereby presented. Firstly, solid and liquid lipids that better solubilise DexAc were selected. Then, the polymorphic changes in solid lipid GMS crystallization due to addition of the liquid triacetin were studied. An adequate surfactant, tyloxapol, was selected on the capabilities of rendering macroscopically transparent and isotropic microemulsions at 65 °C, which can serve as templates for NLC production once redispersed 1:20 in cold water. The ratio between lipid mixture, surfactant and water that yield adequate NLC with physicochemical characteristics suitable for the ophthalmic route was identified.

3.2.3.1. Lipid Screening

Drug-lipid solubility screening

DexAc solubility was measured in different lipid excipients, selected based on their ocular compatibility [197,198]. A total of 13 lipid matrices were evaluated and the results are presented in Figure 5.

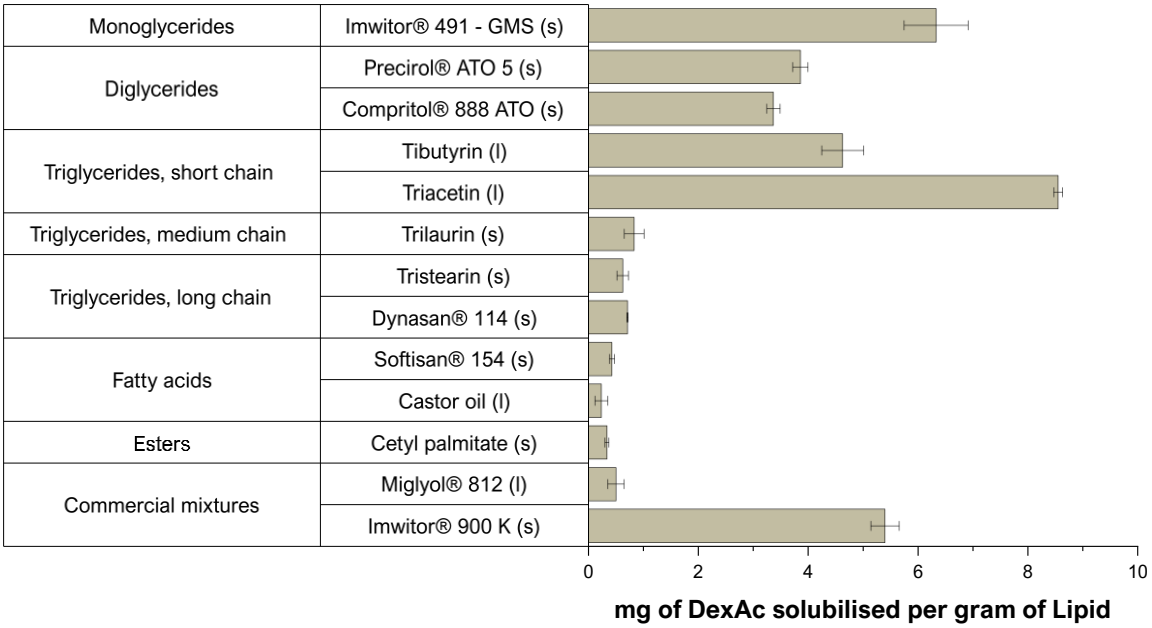

Figure 5. Solubility of dexamethasone acetate in diverse lipid matrices, liquid (l) or solid (s) at room temperature. Mean values are displayed ± standard deviation (n = 3).

The evaluated monoglycerides and diglycerides showed good solubilizing capabilities while for the triglycerides series only the short chain demonstrated adequate results. In fact, within the liquid candidates, exclusively triacetin could be selected since Miglyol® 812 and castor oil performed poorly. Within the solid fats, the best outcomes were observed for C18 diglyceride (Precirol® ATO 5) or monoglyceride (Imwitor® 491 and 900 K). Particularly, Imwitor® 491 is the glycerol ester of stearic acid, thus having an amphiphilic nature. Imwitor® 491 has higher (> 90%) monostearin content than Imwitor® 900 K, which only contains a 40-55 percent of GMS [199-201]. Commercial mixtures rich in diglycerides such as Precirol® ATO 5 or Compritol® 888 ATO, demonstrated lower solubility capabilities than GMS. Both long- and medium-chain triglycerides did not reveal good solubilization capabilities while short chains triglycerides, namely triacetin, demonstrated good DexAc solubilization.

Therefore, the solid lipid (Imwitor® 491 - GMS) and the liquid lipid triacetin were selected based on their individual solubility capabilities for DexAc. GMS could act synergistically with the selected surfactant, due to its amphiphilic nature, thus reducing

the surfactant content for obtaining nanoparticles. Triacetin is a saturated short chain triglyceride with very limited examples in literature of applications in the ophthalmic route, although preliminary data on ocular safety show adequate ocular tolerability [202].

As a preparation for the DSC study, the solubility improvement by combination of GMS and triacetin in different ratios was investigated and is presented in Figure 6.

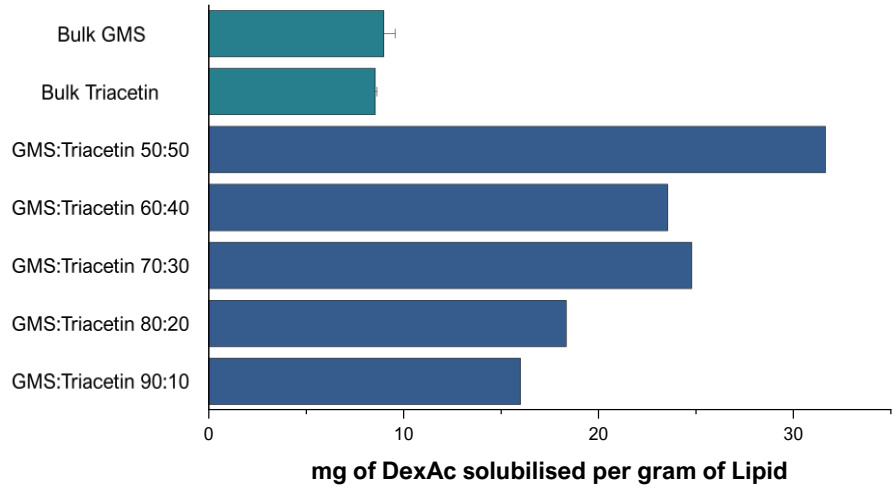

Figure 6. Solubility of dexamethasone acetate (five degrees over the melting temperature, 78 °C in case of Imwitor® 491) in different mixture ratios of Imwitor® 491 (GMS) and triacetin. Preliminary unreplicated data.

Triacetin shows excellent solubilizing capabilities and with decreasing triacetin content, the solubility is also reduced. In any case, adding only a 10% triacetin to the GMS already allows to almost double the solubilizing capabilities (Figure 6).

Oil-solid lipid mixture characterization by Differential Scanning Calorimetry

Classical SLN, composed of only pure solid lipid cores, have been reported to lead to premature drug expulsion, since densely packed polymorphs do not offer free spaces for drug molecules inclusion [203,204]. Unlike SLN, NLC combine long chain with short chain glycerides that not only offer inclusion sites for the drug, but also alter the crystallization behaviour upon solidification. In fact, up to three different NLC types have been identified so far based on the polymorphism observed in the lipidic core. The imperfect-type NLC (Type I) are obtained by combining (spatially different) long-chain and short-chain glycerides which create imperfections in the matrix structure that can accommodate the drug. The amorphous type (Type II) are obtained by adequately mixing lipids that generate matrices that remain in the amorphous state for a prolonged time avoiding crystallization and thus premature drug expulsion. Multiple type NLC

(Type III) are obtained when the lipidic core contains oil compartments (or droplets) where the drug can allocate [116,205,206].

Solid lipids are known to recrystallize in different polymorphs upon cooling of the melt, since the apolar chains can pack themselves in different arrangements. The number of polymorphic species to be observed is related, amongst others, to the lipid nature and the time since solidification. Generally, quick solidification of a melt will lead to amorphous, less stable polymorphs, where the long hydrophobic chains are poorly arranged. Over the time, polymorphic transitions towards a more thermodynamically stable packing are observed, minimizing the free Gibbs energy [207].

The polymorphic behaviour of different ratio mixtures of triacetin and GMS (from 50 to 90% GMS content) were studied at 5 minutes, one day, one week and one month after solidification of the melt when preserved at room temperature. The DSC thermograms are depicted in Figure 7.

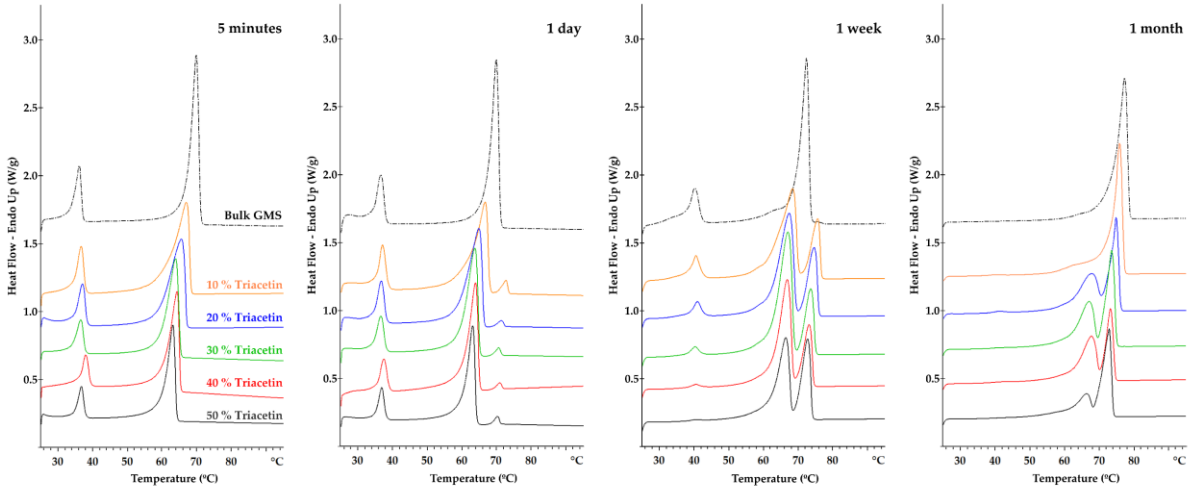

	5 min			1 day			1 week			1 month		
	Peak 1	Peak 2	Peak 3	Peak 1	Peak 2	Peak 3	Peak 1	Peak 2	Peak 3	Peak 1	Peak 2	Peak 3
Bulk GMS	36.5	70.5	*	37.4	70.6	*	41.2	73.1	*	*	*	78
10% Triacetin	37.2	68	*	37.9	67.5	73.1	41	69.5	76.3	*	*	76.5
20% Triacetin	37.8	67	*	37.6	66	72	41.7	68.8	75.5	*	69.7	75.7
30% Triacetin	37.2	64.9	*	37.4	64.7	70.2	41	68.4	74.6	*	68.6	74.5
40% Triacetin	38.7	64.9	*	38.3	64.6	71.5	41	68	74	*	69.3	74.1
50% Triacetin	37.2	63.8	*	37.5	63.8	70.9	*	67.6	73.7	*	67.4	73.6

Reported values correspond to peak temperatures (T_m) in °C.
*No peak was detected

Figure 7. Melting thermograms (from 25 to 90 °C) and polymorphic events recorded 5 minutes, 1 day, 1 week and 1 month after solidification of different lipid melts containing Imwitor® 491 (GMS) with increasing concentrations of liquid triacetin (top) and numeric values for the observed temperature peaks (bottom). Pure GMS as a discontinuous line.

The resolidified pure monoglyceride shows two endothermic melting peaks at 36.5 °C and 70.5 °C during the first hours after re-solidification. The low temperature melting peak (*i.e.*, peak 1 at 1 day) is believed to correspond to a sub-alpha-form, which is not

present after one month storage at room temperature. Previous studies indicate presence of this sub-alpha form until 36 days after solidification but, in our case, it could not be detected already after 30 days. The second peak at 70.5 °C (initial hours) represents the alpha-form, as confirmed by XRD studies elsewhere [208], where it has been reported up to 16 days after solidification. After one month, all the GMS has evolved to a polymorph with a melting peak at 78 °C which might correspond to the more stable beta triclinic cell polymorph, as confirmed in previous XRD studies, where this beta-form starts to be detectable 24 days after solidification of the melt [209-211]. Partial substitution of the bulk GMS with triacetin (≥ 10% ratio) leads to an intermediate peak (denoted as Peak 2) which progressively decreases, but is still detectable after one month. The peak temperature value coincides with that of the alpha-form observed in the initial hours for the bulk GMS, but it appears downshifted by the increasing triacetin concentration. Triacetin (already at 10%) appears to interact with the functional groups of GMS, hindering the tendency of bulk GMS to rearrange into more densely packed lattices (*i.e.*, single peak at 78 ºC after 1 month in the bulk GMS). Addition of 10% triacetin is nonetheless insufficient to maintain this effect after 1 month, while the concentrations of ≥ 20% triacetin still maintain this intermediate peak. On the other hand, if data at 1 week is observed, it appears that increasing triacetin concentrations promote conversely the elimination of the sub-alpha form (*approx.* 41 ºC), an effect also previously reported with similar oil-lipid mixtures [212,213].

The addition of triacetin to GMS has demonstrated to delay complete progression of the solid lipid towards densely packed rearrangements. In fact, less-ordered polymorphs, with lower melting temperatures, still subsist in the lipid matrix after one month when triacetin content is ≥ 20% in the lipid mixture. Considering also the previously obtained data on DexAc solubility, a GMS mixture containing 20% triacetin was selected for further studies.

3.2.3.2. Surfactant screening

Water titration studies for pseudoternary phase diagram construction

Several methods have been proposed to produce NLC, amongst which cold redispersion of warm microemulsions is a straightforward methodology [214]. Oil-in-water (O/W) microemulsions are thermodynamically stable, self-assembled systems with a particulate size under 200 nm mainly composed of a lipid core stabilized by surfactant(s) in an aqueous media. O/W microemulsions obtained with solid lipids at high temperatures (above the melting point of the lipid) have been proposed as templates to produce SLN and NLC by means of rapid solidification of the melted core by redispersion in cold media [215].

This production technique requires quick methodologies to easily identify the best ratios between water, lipid and surfactant that yield adequate warm O/W microemulsions. In this sense, a quick method for screening of surfactants based on water titration techniques, typically proposed for microemulsions at room temperature, was applied at 65 °C with similar results. The progressive addition of water to a lipid-surfactant mixture allows to quickly identify the water-lipid-surfactant mixture that yields colloidal systems that appear transparent to the naked eye, allowing to individualize an initial region in the pseudoternary phase diagram of the components mixture, possible templates for our NLC production.

Three ocular compatible non-ionic surfactants, namely Tween® 20, Tween® 80 and tyloxapol were studied, and the resulting pseudoternary phase diagrams are presented in Figure 8.

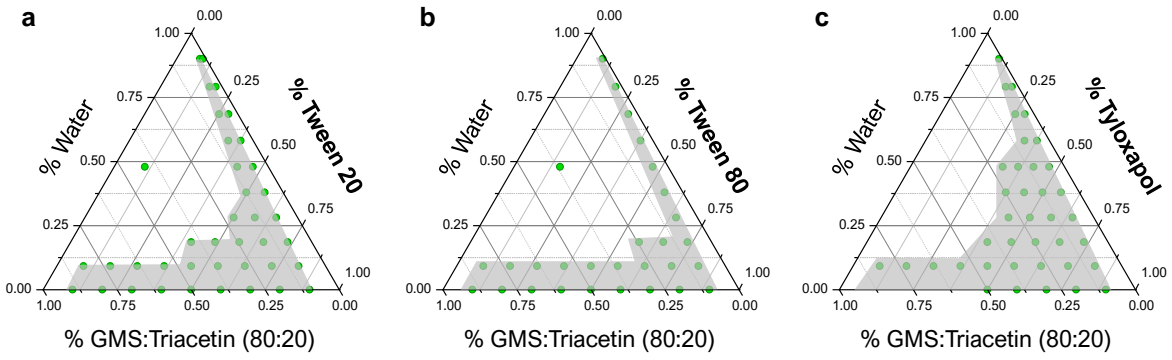

Figure 8. Pseudoternary phase diagrams for the selected water-GMS/triacetin-surfactant mixtures at 65 °C: (a) Tween® 20, (b) Tween® 80 and (c) tyloxapol. Green points represent the studied mixtures that yield macroscopically transparent systems defining an area (indicated in grey) of possible microemulsion templates for the NLC production.

No differences could be observed between polysorbates while tyloxapol yielded a bigger area (indicated in grey in Figure 8) of macroscopically transparent formulations, with a higher number of possible NLC templates candidates. Only when the surfactant-to-lipid percentage was higher than 80%, optically transparent formulations could be observed at water percentages over 50% in the case of both polysorbates. Tyloxapol was able to produce transparent formulations at only 60% of surfactant (with respect to the surfactant-lipid mixture), indicating enhanced stabilization capabilities. Tyloxapol is a non-ionic oligomeric surfactant with an ultra-low micellization point (0.018 mM), in comparison to its corresponding monomeric surfactant (Triton X-100, CMC: 0.22 mM), in combination with higher surface tension lowering abilities, which could be beneficial to produce less-toxic NLC [216,217]. In fact, it is present also in several available formulations due to its good ocular tolerability [218,219].

During the titration studies, a relatively large region of candidate points appeared as gel-like structures when only 20% triacetin was present in the lipid mixture. GMS is an amphiphilic lipid classically used as a surfactant in the food industry. A simple water-GMS mixture exerts a plethora of lyotropic mesomorphs depending on their relative proportions and the working temperature [220,221]. The duality of its behaviour could be helpful to further reduce the surfactant content in the formulation, increasing ocular tolerability. Nonetheless, with the aim of reducing the gel-like region, the same titration for the 60% GMS – 40% triacetin lipid mixture was performed. The results are presented in Figure 9 and demonstrate that reducing the GMS content in the formulation leads to elimination of the gel-like region and to an increase in the number of microemulsion templates.

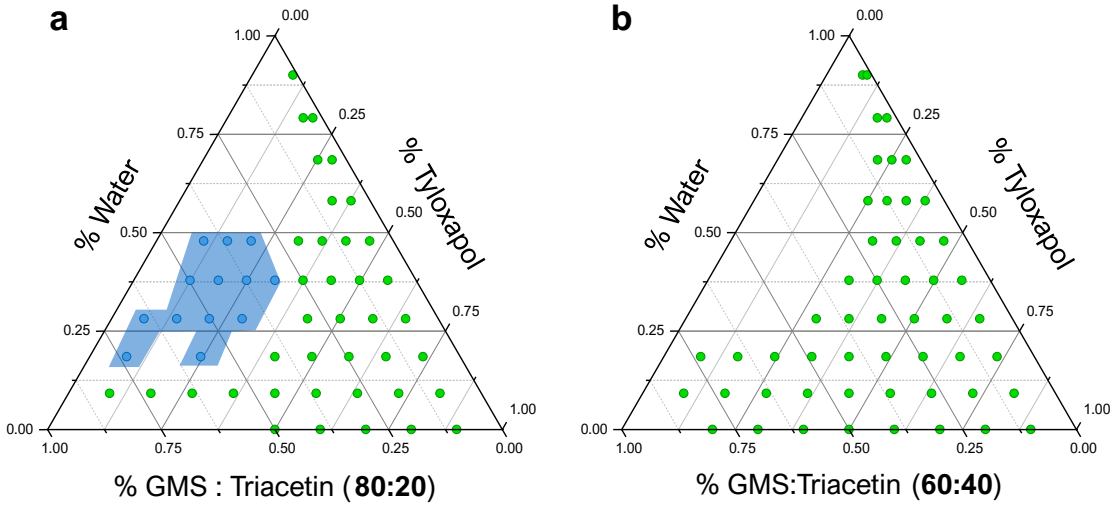

Figure 9. Pseudoternary phase diagrams for the water-tyloxapol-lipid mix pseudoternary systems when lipid mix was composed of (a) 80% GMS:20% triacetin and (b) 60% GMS: 40% Triacetin. Note how the large gel-like region (light blue) in (a) disappeared once GMS content was reduced (b).

The undesired gel-like phases usually occurred at low tyloxapol concentration, where GMS was the predominant molecule, and thus might be acting as jellifying agent [217,222]. In addition, optically transparent microemulsions were spontaneously obtained without cosurfactant addition.

Hot stage polarized light microscopy

Pseudo-ternary mixtures of a lipid, surfactant/cosurfactant and water can lead to multiple systems, depending on the relative proportions of each component, their chemical nature and/or the processing parameters. Well-known systems such as oil-in-water (O/W) or water-in-oil (W/O) emulsions or micro-/nanoemulsions can be obtained. In a similar manner, normal or reverse micelles and more complex systems such as bicontinuous or mesomorphous phases have also been reported [223,224].

Macroscopical transparency is not an absolute indicator of isotropy, which is a fundamental characteristic of a microemulsion [100]. In this sense, the macroscopically transparent candidates were observed under polarized light in order to identify the isotropy/anisotropy of the systems for the pseudoternary system GMS:triacetin (3:2)/tyloxapol/water. The resulting pseudoternary phase diagram summarizing the findings is depicted in Figure 10, in addition to photomicrographs of the observed mesophases.

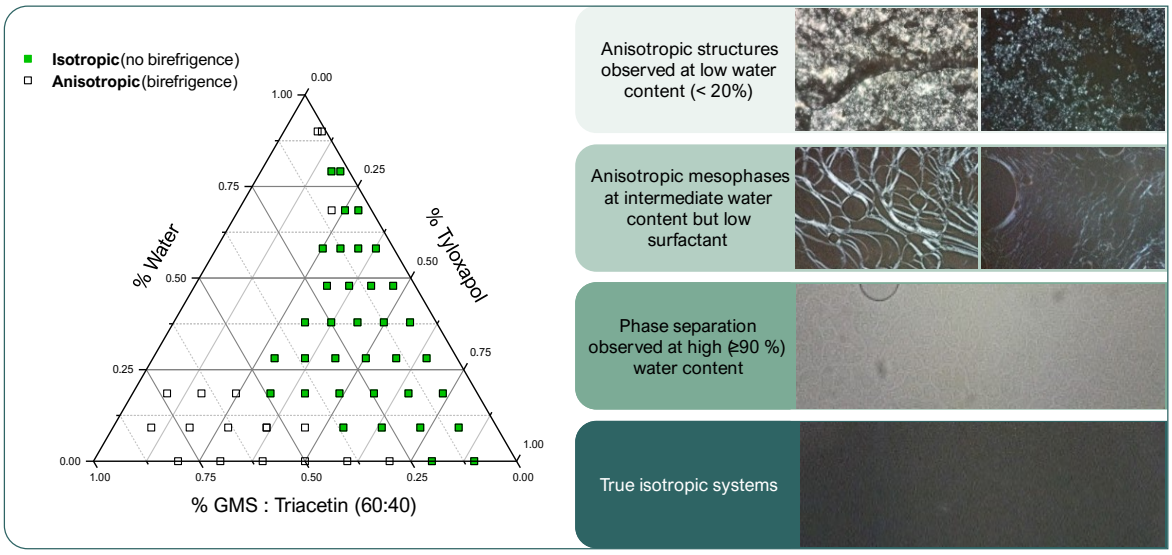

Figure 10. Pseudoternary phase diagram corrected after microscopic characterization under polarized light (left) and different micrographs of the observed anisotropic structures (right).

At low water concentrations, highly birefringent spherulitic-like structures were observed which could be mainly explained due to the presence of unmelted GMS alpha-crystals [225,226]. Above 20% water content, isotropic systems can already be observed at high surfactant concentrations, while with low surfactant concentrations birefringent liquid crystalline mesophases appear. No efforts were made on further characterization of these birefringent mesophases since the focus of interest are isotropic systems which appeared dark under the polarized light. Unexpectedly, some formulations showed a clear phase separation at high water concentrations (≥ 90% water content) which had not been identified previously.

The developed method allowed to reduce the initial 53 candidate points to only 37 possible formulation candidates. Nonetheless, amongst the both isotropic and transparent candidates, different colloidal systems can still exist such as bicontinuous, oil-in-water and water-in-oil microemulsions. Therefore, a final step based on trial and error is required for the NLC production.

3.2.3.3. DexAc-NLC preparation and characterization

Three different regions of the proposed pseudoternary phase diagram were studied to produce NLC using warm microemulsion templates. Particularly, i) a low water microemulsions region, below a 50% water content; ii) a rich-in-water region with a 90% water content in the warm microemulsion and iii) the previously obtained region of isotropic, optically transparent candidates. Percentage of drug was fixed at a 4% with respect to the mass of lipid mix present in each formulation. Table 1 summarizes the main findings.

Table 1. Composition of six selected microemulsion templates, their macroscopical and microscopical appearance and the macroscopic result obtained after 1:20 redispersion in cold water. Note how even if a formulation is both transparent and isotropic can still lead to inadequate redispersion products (L2) and less macroscopically transparent microemulsions can still lead to adequate NLC production (H1). All formulations were loaded at 4% DexAc with respect to their lipid mix content.

Phase diagram region	Code	Lipid mix %	Water %	Surfactant %	Warm microemulsion		Redispersed 1:20 product
					Transparent	Isotropic	
Low water	L1	37.3	37.9	24.8	Y	N	> 1 mm pellets
	L2	12.4	37.9	49.7	Y	Y	> 1 mm pellets
Isotropic	Iso1	11.1	65.7	23.2	Y	Y	Slightly bluish, milky
	Iso2	10.1	60	29.9	Y	Y	Slightly bluish, milky
	Iso3	12	57.7	30.3	Y	Y	Slightly bluish, milky
High water	H1	5	90	5	N	Y	Slightly bluish, milky

As expected, redispersion 1:20 in cold water of the templates with less than 50% water (L1, L2, Table 1) lead to the instant solidification of the redispersing drop, indicating that the external phase of the microemulsion was the lipid. Therefore, isotropy of the system was not enough to predict their suitability.

Three different candidates from the isotropic and transparent region led to adequate DLS results, compatible with the ocular route (< 200 nm Z-Average, desirable PDI of 0.1) confirming initially the adequacy of the formulated hypothesis (Figure 11).

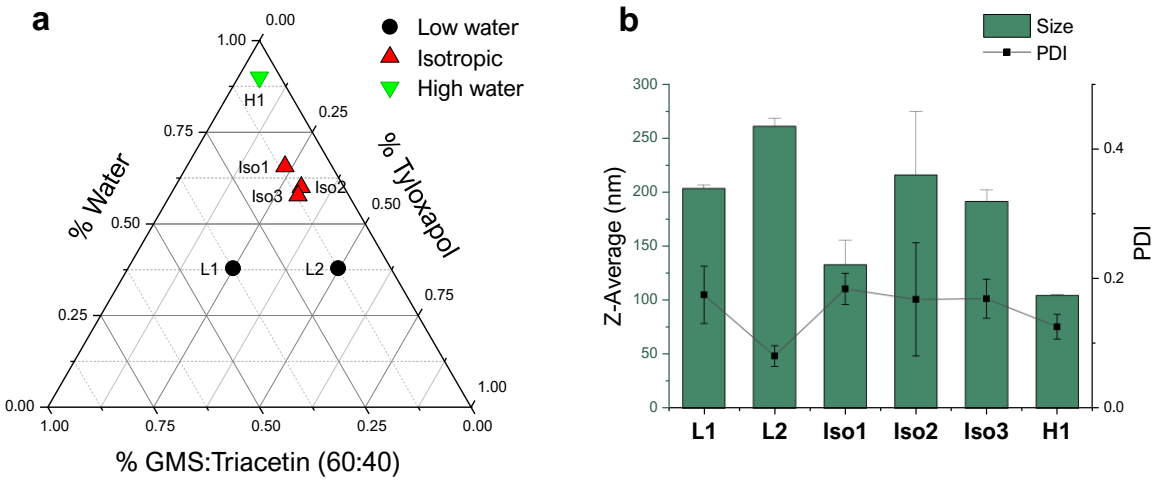

Figure 11. Pseudoternary phase diagram (a) with the composition of the six studied formulation candidates and (b) size and PDI values of the obtained NLC at t = 24 h after production. Data values are mean ± standard deviation (n = 3).

A third region was explored, with high (90%) water content in the warm template which also led to satisfactory results. In fact, high-water-content microemulsions are preferred for the selected method since they allow for better pipetting and thus less drug loss in the preparation process. Small changes in the composition between Iso1, Iso2 and Iso 3 lead to relatively large changes in the nanoparticle size but, on the other hand, an important increase in the water content did not produce any significant changes in the obtained nanoparticles.

Based on the collected results, formulation H1 with a composition of 125 mg tyloxapol, 75 mg GMS, 50 mg triacetin and 2.25 mL water as the warm microemulsion template was selected. This was then redispersed 1:20 in cold water for globule solidification and eventual NLC production. The resulting NLC presented a Z-Average of 104.4 ± 0.8 nm, PDI of 0.125 ± 0.019 and zeta potential of -6.51 ± 0.575 mV and were selected for further studies. Drug loading of the formulation was quantified only after tangential flow filtration of the NLC which also allowed to reconcentrate the NLC previously diluted in the 1:20 dispersion step. Formulation H1 presented a final concentration of dexamethasone acetate of *approx.* 0.2 mg/mL (DexAc-NLC) and, when required, to *approx.* 0.2 mg/mL dexamethasone (Dex-NLC).

3.2.3.4. NLC optimization with DoE

Based on the previous results, it was clear that only a limited number of water/lipid mixture/surfactant relative proportions were adequate to produce NLC. Application of DoE could help furthers delimit this subregion of interest within the simplex (the pseudoternary phase diagram) where all the NLC produced express physicochemical characteristics compatible with the ocular route. The obtained mathematical models

would be able to: i) identify how important responses, such as nanoparticle average size and PDI, behave as a function of the relative proportions between the excipients used; ii) identify the stability/robustness of the production process to small variations that might occur; iii) create fine-tuned nanoparticulate systems with desirable pre-defined characteristics, that is, to obtain the best formulation for our application.

First attempt DexAc-NLC DoE

Since previous work had been based on "systematically" titrating pseudoternary phase diagrams, an approach following the previously described mixture designs introduced in Section 3.1.2.5. was followed. In this sense, a constrained mixture design was proposed, and the subregion of interest was delimited following only lower-bound constraints for an easier candidate point selection process. Three factors were studied, namely: the proportion of water, the proportion of surfactant and the proportion of lipid mixture present in the warm microemulsion. Drug was fixed at a 4% with respect to the solid excipients (surfactant + lipid mixture). The resulting subregion of interest was therefore a simplex within the simplex (a *triangle* inside the *triangle*) delimited by the constraints:

$$0.225 \leq \text{Surfactant}$$
$$0.45 \leq \text{Water}$$
$$0.075 \leq \text{Lipid}_{mix}$$

Following these constraints, the Design Expert software, based on D-optimality criteria, proposed 21 factor combinations to be tested. This included 5 runs for lack-of-fit testing, 5 runs as replicates (to increase the degrees of freedom of the system) and 2 additional centre points, which improve model predictability capabilities (Figure 12).

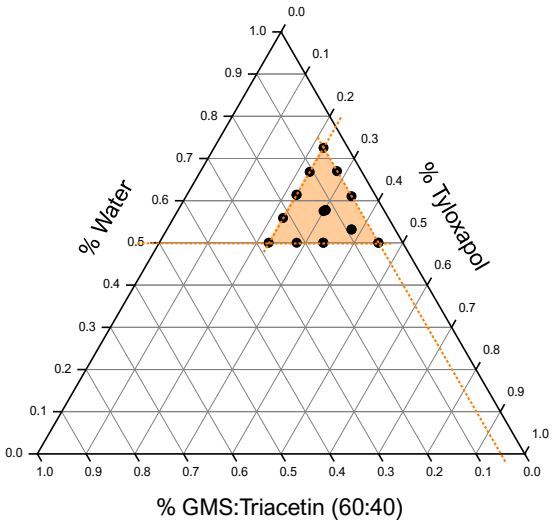

Figure 12. Pseudoternary phase diagram containing the experimental runs (dots) within the subregion delimited by the three lower-bound-constraints set to the three studied factors (orange discontinuous lines) which delimit another simplex triangle.

Experimental runs were blocked into 4 days to detect any possible inter-day differences. The region depicted in Figure 12 did also include some candidate points towards oil-rich mixtures (to *the left)* that were initially not explored in the water titration experiments but fall very close to the limit of non-transparent warm microemulsion which might fail to produce any valuable NLC. Several problems were encountered at this initial stage. Some of the formulations failed when dispersed 1:10 in cold water by either producing large clumps (which could be interpreted as a W/O microemulsion that is being redispersed) or either because they were too viscous to be pipetted and poured on the 1:10 dispersion media (Table 2).

Table 2. Experimental runs and their observed responses in the first DoE applied to DexAc NLC.

#Run	Block (day)	Water (mg)	Imwitor® 491 (mg)	Triacetin (mg)	Tyloxapol (mg)	DexAc (mg)	Redispersible?	Z-Average (nm)	PDI
1	1	400.8	38.5	25.7	135.0	2.6	Y	146.4	0.179
2	1	368.3	58.0	38.7	135.0	3.9	N	-	-
3	1	300.0	99.0	66.0	135.0	6.6	Y	284.3	0.304
4	1	368.3	58.0	38.7	135.0	3.9	N	-	-
5	1	435.0	18.0	12.0	135.0	1.2	Y	186.7	0.186
6	1	335.1	77.9	51.9	135.0	5.2	Y	200	0.618
7	2	401.9	18.0	12.0	168.1	1.2	N	-	-
8	2	300.0	78.4	52.3	169.4	5.2	Y	184.9	0.15
9	2	345.0	45.0	30.0	180.0	3.0	Y	182.2	0.121
10	2	345.0	45.0	30.0	180.0	3.0	Y	182	0.251
11	2	346.4	43.2	28.8	181.7	2.9	Y	164.1	0.098
12	2	346.4	43.2	28.8	181.7	2.9	N	-	-
13	3	346.4	43.2	28.8	181.7	2.9	N	-	-
14	3	300.0	58.7	39.2	202.1	3.9	Y	190	0.239
15	3	300.0	58.7	39.2	202.1	3.9	Y	180.1	0.219
16	3	366.2	18.0	12.0	203.8	1.2	Y	194.6	0.32
17	3	366.2	18.0	12.0	203.8	1.2	N	-	-
18	4	318.8	32.2	21.5	227.5	2.1	N	-	-
19	4	318.8	32.2	21.5	227.5	2.1	Y	196.3	0.355
20	4	300.0	18.0	12.0	270.0	1.2	Y	136.2	0.337
21	4	300.0	18.0	12.0	270.0	1.2	N	-	-

Z-Average and PDI values were acceptable for the formulations that could be redispersed. With 8 missing runs, no further efforts on data regression analysis were made and a second version of the experimental design was proposed.

Second attempt DexAc-NLC DoE

The second subregion of interest studied did not include the formulation candidates that were no dispersible in cold water in the first attempt and included higher water-content areas thus defined by the constraints:

$$0.097 \leq \text{Surfactant} \leq 0.375$$
$$0.575 \leq \text{Water} \leq 0.75$$
$$0.05 \leq \text{Lipid}_{mix} \leq 0.16$$

The proposed extreme vertices design, as depicted in Figure 13 included 21 candidate points, selected also on D-optimality criteria by the software. Also in this case, replicates, lack-of-fit test runs, and centre points were included.

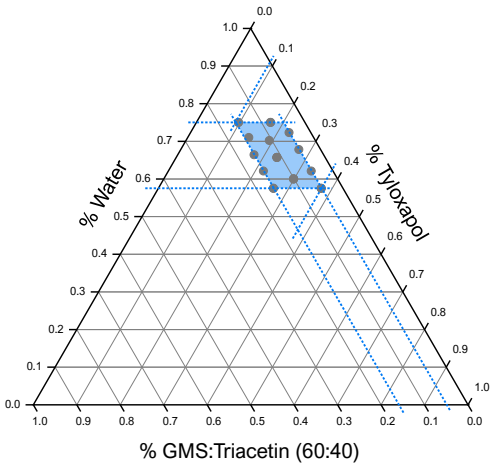

Figure 13. Pseudoternary phase diagram containing the experimental runs (dots) within the subregion delimited by the upper and lower boundaries (blue discontinuous lines) which delimit an extreme vertices design.

The composition of each formulation and the observed responses are presented in Table 3.

Table 3. Experimental runs and their observed responses in the second DoE applied to DexAc NLC.

#Run	Block (day)	Water (mg)	Imwitor® 491 (mg)	Triacetin (mg)	Tyloxapol (mg)	DexAc (mg)	Z-Average (nm)	PDI
1	1	450	28.44	18.96	102.6	1.9	143.0	0.308
2	1	450	55.08	36.72	58.2	3.7	86.1	0.194
3	1	372.6	18	12	197.4	1.2	163.5	0.376
4	1	406.8	18	12	163.2	1.2	153.4	0.133
5	1	360	36.36	24.24	179.4	2.4	139.5	0.103
6	1	450	28.44	18.96	102.6	1.9	109.6	0.148
7	1	360	36.36	24.24	179.4	2.4	268.3	0.277
8	1	372.6	57.6	38.4	131.4	3.8	225.1	0.199
9	1	450	55.08	36.72	58.2	3.7	120.3	0.186
10	1	398.4	57.6	38.4	105.6	3.8	157.6	0.123
11	1	360	36.36	24.24	179.4	2.4	239.0	0.122
12	2	345	57.6	38.4	159	3.8	200.6	0.192
13	2	394.2	39.96	26.64	139.2	2.7	110.7	0.196
14	2	421.2	38.16	25.44	115.2	2.5	133.8	0.175
15	2	394.2	39.96	26.64	139.2	2.7	126.2	0.180
16	2	345	18	12	225	1.2	130.8	0.252
17	2	345	57.6	38.4	159	3.8	181.6	0.144
18	2	426	53.64	35.76	84.6	3.6	105.5	0.110
19	2	345	18	12	225	1.2	163.3	0.307
20	2	394.2	39.96	26.64	139.2	2.7	161.5	0.175
21	2	433.8	18	12	136.2	1.2	168.7	0.200

In this second attempt, the experiments were blocked in only two days to consider any possible inter-day variability into the regression model. A simple observation of the raw data indicates that a good number of formulation candidates present a Z-Average value around the 200 nm value and in some cases in combination with PDIs close to 0.1. The regression analysis for the response Z-Average (nm) is presented in Table 4.

Table 4. Output of the DoE software for the response "Z-Average (nm)" for regression model order selection in the second DoE attempt.

Source	Sequential *p*-value	Lack of Fit *p*-value	Adjusted R^2	Predicted R^2	
Linear	0.0105	0.3977	0.3460	0.0787	Suggested
Quadratic	0.1396	0.5807	0.4563	0.1437	
Special Cubic	0.7770	0.4872	0.4183	0.0556	
Cubic	0.3368	0.5429	0.4524	-3.2703	
Sp Quartic *vs* Quadratic	0.3163	0.6889	0.4916	0.2252	
Quartic *vs* Cubic	0.5429		0.4124		Aliased
Quartic *vs* Sp Quartic	0.6889		0.4124		Aliased

Although enough experimental runs have been performed, increasing the degrees of freedom for higher order models (up to a possible special quartic model) the data can only be fitted to a linear mixture model. This simpler model still indicates a poor fitting, since the Adjusted R^2 is of only 0.3460 and the predicted R^2 remains at a value of 0.0787, which both indicate poor correlation and poor predictability of the model.

The ANOVA Table for the main effects terms (see Section 3.1.2.6. for theoretical background) is presented in Table 5.

Table 5. ANOVA table for the response "Z-Average (nm)" fitted to a linear mixture regression model in the second DoE attempt.

Source	Sum of Squares	df	Mean Square	F-value	*p*-value	
Block	962.11	1	962.11			
Model	20377.43	2	10188.71	6.03	0.0105	significant
[(1)]Linear Mixture	20377.43	2	10188.71	6.03	0.0105	
Residual	28743.64	17	1690.80			
Lack of Fit	16591.50	9	1843.50	1.21	0.3977	not significant
Pure Error	12152.15	8	1519.02			
Cor Total	50083.18	20				

The model is apparently significant (p = 0.0105), and the lack-of-fit is not significant (p = 0.3977), indicating that the model up to a certain point is predicting something more than just random experimental noise

The linear mixture model is plotted in Figure 14 in both two and three dimensions (Figure 14a and 14b, respectively).

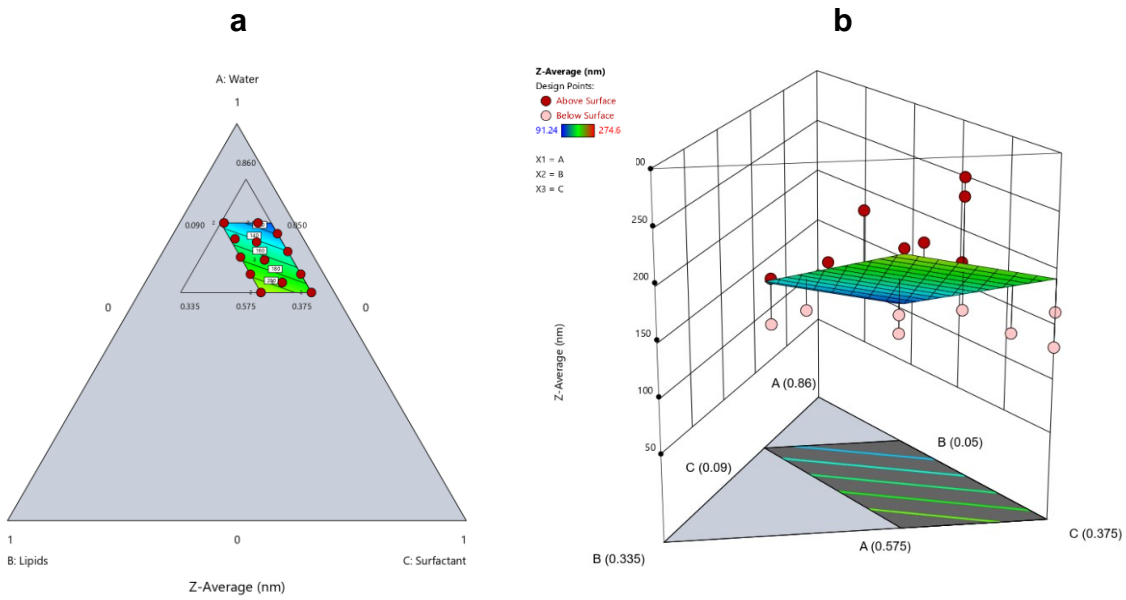

Figure 14. Graphical representation of the linear mixture regression model adjusted to the DoE data obtained for the response "Z-Average (nm)" in the second DoE attempt. The model can only be considered valid within the subregion of interest studied as it can be observed in the bidimensional representation (a) and also the three-dimensional representation (b).

Figure 14b clearly indicates the reason for the poor R^2 values: exact same factor combinations (exact same compositions) deliver sometimes nanoparticle diameters that fall far above the regression plane (red dots) and at the same time far below (pink dots), hence the model inability to fit the values to higher-order models. This can be further appreciated in the Predicted *versus* Observed plot in Figure 15.

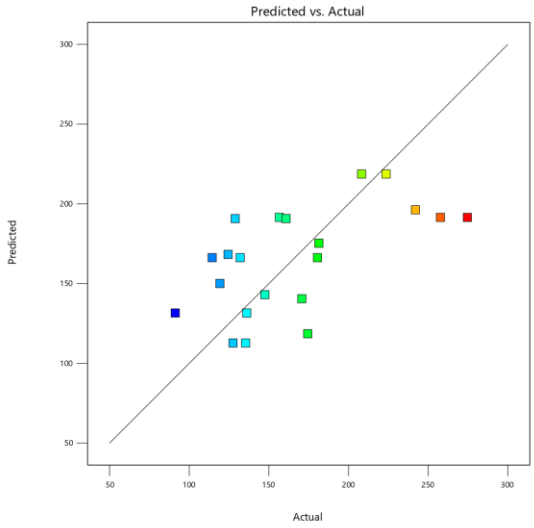

Figure 15. Predicted *vs* Observed plot for the response "Z-Average (nm)" when adjusted to a linear mixture model.

Almost no observed experimental value falls on the line, indicating very poor model predictability.

Regarding the poor results for the Z-Average response, no further efforts were made on analysing the PDI response. An attempt to analyse the responses observed at 7 days was also made, with no improvement in regression models predictability (data not shown).

As introduced before, these results can be explained by analysing, for example, the results observed for the experimental runs number 5, 7 and 11 (Table 3). Although all three formulations have an identical composition, the recorded Z-Average responses are highly variable, being 139.5, 268.3 and 239 nm, respectively. A natural inter-batch variation is to be expected due to random variability of the production and measurement processes. In this case, although strict standardized production procedures were followed, the high variability might rather be explained by a certain level of simplicity in the production method. Several hand-operated steps are required with this technique *(i.e.*, the manual redispersion of the warm microemulsion in cold water) which remain as relatively uncontrollable process parameters, considering the small batch scale production.

The obtained formulations nonetheless indicate that the assumption that clear isotropic systems that can be easily identified with a titration method by macroscopical and microscopical observations render adequate NLC populations, confirming our initial hypothesis. A trial-and-error approach remains nonetheless the "quickest" approach in our case to find the "golden ratio" between excipients for valuable NLC production, when produced with such a hand-operated method.

3.3. Development of Dexamethasone NLC (Dex-ieNLC)

The developed DexAc-NLC presented some limitations once applied on freshly excised porcine sclera and choroid, mainly due to the fact that the *ex vivo* tissues maintain to a certain level their metabolic activity thus bioconverting the released acetate prodrug in dexamethasone and other metabolites which hinders a straightforward interpretation of the permeation and retention data on *ex vivo* tissues (this will be discussed further in Chapter 5).

As discussed at the beginning of Section 3.2., apart from the clinical rationale, the main reason for selection this model drug was based on the premise of a straightforward analytical process that could ease the validation process of the newly developed *ex vivo* model that will be presented in Chapter 4. The dexamethasone acetate prodrug, despite its higher lipophilicity (desirable for a lipid-based nanocarrier) failed to offer easy-to-interpret permeation and retention data. For this reason, the decision to continue the research with plain dexamethasone was taken.

Some pitfalls regarding the DexAc-NLC production process had also been identified, mainly derived from the fact that the warm microemulsion had to be redispersed 1:10 in cold water, which subsequently required a reconcentration step. As a result, Dex-ieNLC were developed and the new production only required a 1:1 dilution ratio in cold water, avoiding therefore the reconcentration step. The ”ie” designation is an arbitrary nomenclature to identify the NLC produced with the methodology presented in this Section.

3.3.1. Materials and Methods

3.3.1.1. Materials

Dexamethasone (Dex; IUPAC (8S,9R,10S,11S,13S,14S,16R,17R)-9-fluoro-11,17-dihydroxy-17-(2-hydroxyacetyl)-10,13,16-trimethyl-6,7,8,11,12,14,15,16-octahydro-cyclopenta[a]phenanthren-3-one; MW 392.5 g/mol; LogP 1.9; water solubility 89 µg/ml) [191], tyloxapol (IUPAC 4-(2,4,4-trimethylpentan-2-yl)phenol; formaldehyde; oxirane) and Triton X-100 (IUPAC 2-[4-(2,4,4-trimethylpentan-2-yl)phenoxy]ethanol) were from Sigma Aldrich (Taufkirchen, Germany). Triacetin (glycerol triacetate) was purchased from TCI Europe N.V. (Zwijndrecht, Belgium). Imwitor® 491 (I491, glycerol monostearate (GMS); ≥ 90% content in monostearate) was kindly gifted by IOI Oleo GmbH (Hamburg, Germany). Saline solution (composition: 9 g/L NaCl) and phosphate buffered saline (PBS; composition: 0.19 g/L KH_2PO_4, 2.37 g/L Na_2HPO_4, 8.8 g/L NaCl; pH 7.4 by adding 85% H_3PO_4) were prepared using ultra-pure water (Arium® Comfort Sartorius, Goettingen, Germany). MTT reagent (3-(4,5-dimethylthiazol-2-yl)-2,5-diphenyl tetrazolium bromide) was purchased from Sigma Aldrich (Taufkirchen,

Germany) and prepared as sterile solution in Hanks' Balanced Salt Solution (HBSS) at a final concentration of 0.5 mg/mL. All other chemicals were of analytical grade.

3.3.1.2. Dexamethasone solubility in the selected excipients

The methodology presented in Section 3.2.2. was followed for analysing the solubility of dexamethasone in the selected lipid matrices.

3.3.1.3. Preparation of ieNLC

ieNLC were produced by a modification of the method described in Section 3.2.2.6. Briefly, 125 mg tyloxapol, 75 mg Imwitor® 491, 50 mg triacetin were warmed to 65 ºC and after 5 minutes, 4.5 mL ultra-pure deionized water was added under magnetic stirring. The warm microemulsion was added dropwise into 4.5 mL ultra-pure deionized water at 4 ºC under sonication (Branson 2510 Ultrasonic Bath Sonicator, Branson Ultrasonics, Danbury, Connecticut), up to 10 minutes. Drug-loaded ieNLC also contained 2 mg dexamethasone added to the initial warm microemulsion while blank ieNLC did not contain any drug.

3.3.1.4. Physicochemical characterization: size, PDI, zeta potential and pH

Nanoparticle size and polydispersity index was measured by triplicate on a Malvern Zetasizer Nano ZS (Malvern Panalytical Ltd., Malvern, UK) by 1:50 previous dilution in water. Zeta potential was obtained by dilution in a 10 mM NaCl solution in water, also by triplicates, on the same instrument.

pH of the formulations was measured on a Beckman Phi 71 pH Meter (Beckman Instruments, Inc, Pasadena, CA, USA) by triplicates.

3.3.1.5. ieNLC lyophilization

Samples of 1 mL Dex-ieNLC were subject to lyophilization using three different cryoprotectants: sucrose, lactose, and D-trehalose dihydrate. Two ratios between solid excipients in the formulation (lipid + surfactant) and cryoprotectant were studied by adding 13.8 mg (excipient to surfactant ratio of 2:1) or 27.7 mg (1:1) of cryoprotectant. The cryoprotectant was added only 24 hours after production of the ieNLC, which had been preserved at 4 ºC to allow for NLC stabilization. The samples were placed in 25 mL brown glass containers with a wide bottom to increase the liquid-air contact surface and frozen at -20 ºC overnight. Samples were lyophilized in a single cycle at a constant temperature of -40 ºC using an Alpha 1-2 LDplus freeze-dryer (Martin Christ GmbH, Osterode, Germany) equipped with a Vacuubrand RZ 6 vacuum pump (Vaccubrand GmbH, Wertheim, Germany). Samples were reconstituted at 50% of the initial water content and cake wettability, size and PDI were analysed.

3.3.1.6. Morphology analysis: FEG-SEM

Initially, undiluted samples were observed on a Benchtop Scanning Electron Microscope (SEM), with Energy Dispersive X-ray Spectroscopy (EDX) (TM4000, Hitachi Technologies, Japan). Blank and Dex-loaded ieNLC were analysed as liquid samples directly placed undiluted (5 µL) on specimen stubs and air-dried overnight while the lyophilizates (Blank ieNLC only) were analysed as powder. Samples were sputter coated with Au before observation.

In a second trial, nanoparticles were observed on a Field Emission Gun Scanning Electron Microscope working at an acceleration voltage of 3.0 kV (FEG-SEM; ZEISS Merlin® FEG-SEM microscope). Samples were diluted 1:100 in ultra-pure deionized water and 5 µL were directly deposited onto SEM specimen stubs and dried in a desiccator 24 h before analysis. No sputter coating was required. Photomicrographs were obtained at 500k magnification.

3.3.1.7. In vitro cytotoxicity

The cytotoxicity on human retinal pigment epithelial cells (ARPE-19) was assessed *via* the MTT assay. ARPE-19 cell line (ATCC-CRL-2302) was purchased from ATCC (American Type Culture Collection, ATCC, Manassas, VA; LGC Italy, Sesto San Giovanni, Italy). Growth medium consisted of Dulbecco's Modified Eagle's Medium (DMEM)/Nutrient Mixture F-12 (DMEM/F12 (1:1) with HEPES (Gibco Life Technologies, Carlsbad, CA), supplemented with 10% foetal bovine serum (FBS) and 1% penicillin/streptomycin (10,000 U/mL, Gibco Life Technologies, Carlsbad, CA). Cells were maintained in a humidified incubator at 37°C and 5% CO_2. Cells were seeded in 96-well plates and cultured for 24 hours.

The diverse treatments consisted of 100 µL of Dex-ieNLC suspension in growth medium at a dexamethasone concentration of 10, 50 and 100 µM. Dexamethasone was solubilised in DMSO and diluted in growth medium to achieve the same drug concentrations and maintaining a maximum DMSO content under 0.05%. Blank ieNLC diluted in medium were also analysed by following the same dilution volumes as their respective drug-loaded formulation counterpart. Solutions of the single excipients in DMSO were also prepared in the same concentration as they would be in the formulation, this is, 13.88 mg/mL for tyloxapol, 8.3 mg/mL for GMS and 5.5 mg/mL for triacetin. For the 24 h experiment, growth medium (with 0.05% DMSO) and a 1% DMSO solution in growth medium were used as positive and negative controls of cell viability, respectively. When the experiment lasted 4 hours, growth medium and a 5% Triton X-100 solution in growth medium were used as negative and positive controls of cell viability loss, respectively.

After 24 or 4 hours contact with the treatments, the wells were washed and 100 µL of the MTT dye were added to each well and incubated for 3 hours. Subsequently, the well content was replaced with 100 µL DMSO for solubilisation of the formazan crystals for at least 10 minutes and preserved from light. Absorbance was measured at 570 nm using a microplate reader. Cell viability was assessed following Equation 2:

$$\% \text{ Cell Viability} = (\text{Test Absorbance}/\text{Positive Control Absorbance}) * 100 \quad (2)$$

3.3.2. Results and Discussion

3.3.2.1. Characterization of Dex-ieNLC

Dex-ieNLC showed a final Dex concentration of 235 ± 20 microg/ml (corresponding to 600 ± 50 µM). Six batches of Dex-ieNLC were produced and their stability at 4 ºC was studied (Figure 16).

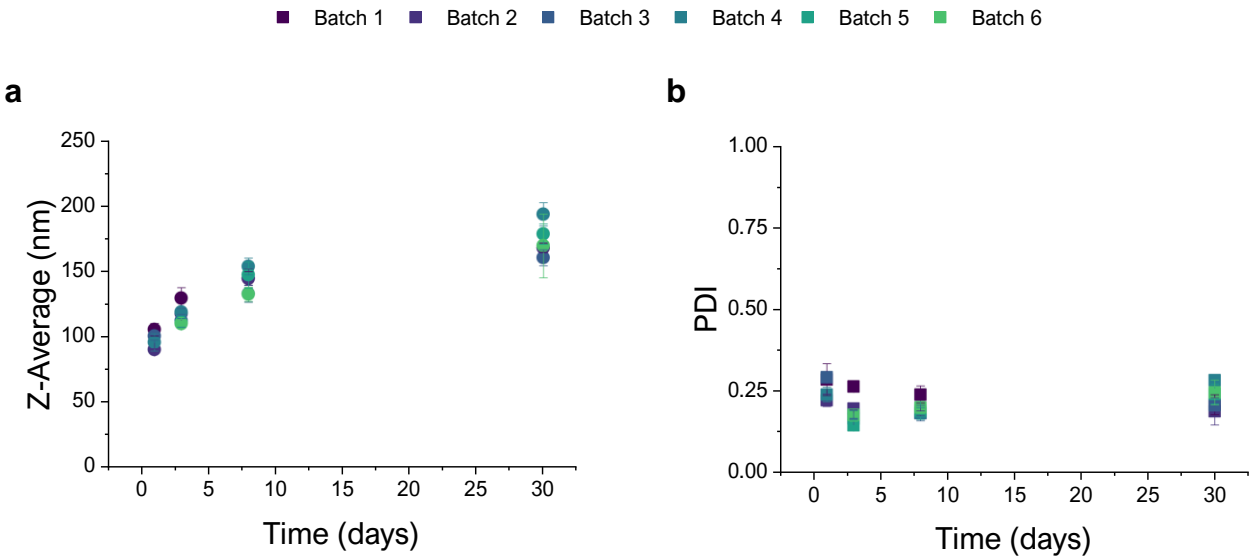

Figure 16. Measured values for (a) Z-Average (nm) and (b) PDI of six batches of Dex-ieNLC when preserved at 4 ºC over 1 month. Data are mean ± SD for each batch.

The freshly obtained Dex-ieNLC expressed at day one a Z-average diameter of 98.2 ± 3.8 nm and a PDI of 0.258 ± 0.023. The populations appeared monodispersed, but in some cases a second mode could be recorded at ≥ 5 µm which might be interpreted as an interference of the apparatus and in any case, represented < 1% of the size distribution by intensity. After one month the nanoparticles expressed a Z-average diameter of 172.9 ± 39.0 nm and a PDI of 0.228 ± 0.026, which indicates a possible nanoparticle aggregation. This is mainly explained by the nearly-neutral surface charge of the ieNLC, as indicated by the zeta-potential values of -2.93 ± 0.25 mV which did not strongly change over one month study (-3.72 ± 0.19 mV).

The drug is nonetheless entrapped inside the ieNLC and remains protected from hydrolysis since the drug recovery after 30-day storage at 4 ºC remained at 100.9% ± 4.0% (*n* = 6 batches).

pH of the formulations is slightly acidic, with a value of 5.82 ± 0.07 which is constant after 1 month storage at 4 ºC (5.71 ± 0.14 after 30 days). The eye can nonetheless tolerate a slightly acidic pH value, although it might produce some discomfort in patients [227]. In any case, this could be further improved in further studies by buffering the suspension for instance with a phosphate buffer at 7.4 and analysing the effect of the salt addition into ieNLC stability over time.

3.3.2.2. ieNLC lyophilization

The stability results presented in Section 3.3.2.1. indicated that a further strategy was required for increasing the long-term stability of ieNLC. Lyophilization was selected as a strategy for increasing long-term stability while also allowing for a further sterilization step of the formulation *i.e.*, by gamma sterilization of the lyophilizates.

Three cryoprotectants at a 2:1 and 1:1 excipient-to-cryoprotectant ratio were studied, namely sucrose, lactose, and D-trehalose dihydrate [228-231]. The results are presented in Table 6.

Table 6. Lyophilization results for Dex-ieNLC with three different cryoprotectants.

Cryoprotectant	Excipient to cryoprotectant ratio	Wettability of the cake	Size (nm) after reconstitution	PDI after reconstitution
Sucrose	2:1	Very poor	363.2 ± 6.2	0.328 ± 0.058
	1:1	Poor	285.1 ± 3.8	0.269 ± 0.049
Lactose	2:1	Good	195.3 ± 7.3	0.206 ± 0.004
	1:1	Very good	204.1 ± 2.9	0.244 ± 0.011
D-Trehalose	2:1	Very poor	283.8 ± 3.0	0.287 ± 0. 029
	1:1	Poor	227.9 ± 3.3	0.242 ± 0.001

The Dex-ieNLC showed a size of 124.6 ± 4.8 nm and a PDI of 0.215 ± 0.030 before lyophilization. All three cryoprotectants produced adequate cakes during the lyophilization process. Reconstitution of the cakes was performed at a 50% percent of the initial water content in order to evaluate possible increase of the drug concentration in the reconstituted formulation. Sucrose and D-trehalose produced cakes with poor wettability after addition of 0.5 mL water. Size and PDI values were also too high, with observed values of 363.2 ± 6.2 nm for the sucrose (2:1) case for example. The best results were obtained when lactose was used and both ratios delivered an easily wettable cake. No statistical differences could be observed when using the two ratios in the nanoparticle size.

Isoosmolarity and isotonicity are desirable characteristics for ophthalmic preparations and addition of a cryoprotectant can alter ocular tolerability. The eye has demonstrated to tolerate NaCl solutions ranging from 0.5 to 1.8 % w/v NaCl, which is 5 to 18 mg/mL. For the ieNLC formulation lactose has demonstrated the best reconstitution values. In addition, lactose is a non-electrolyte and thus high concentrations of 9.75% w/v (or 97.5 mg/mL) are required to reach isoosmolarity with a 0.9% NaCl solution [232].

3.3.2.3. Characterization of ieNLC Morphology: SEM and FEG-SEM

The samples were observed with a benchtop SEM microscope (TM4000, Hitachi Technologies, Japan) in an exploratory phase. Unfortunately, the system setup did not have enough resolution for the expected nanometre size range of the ieNLC, but still delivered precious information about the sample preparation. In fact, depositing the samples undiluted led to an apparent formulation destabilization, which created a lipidic film observable already at low magnification (Figure 17, row a).

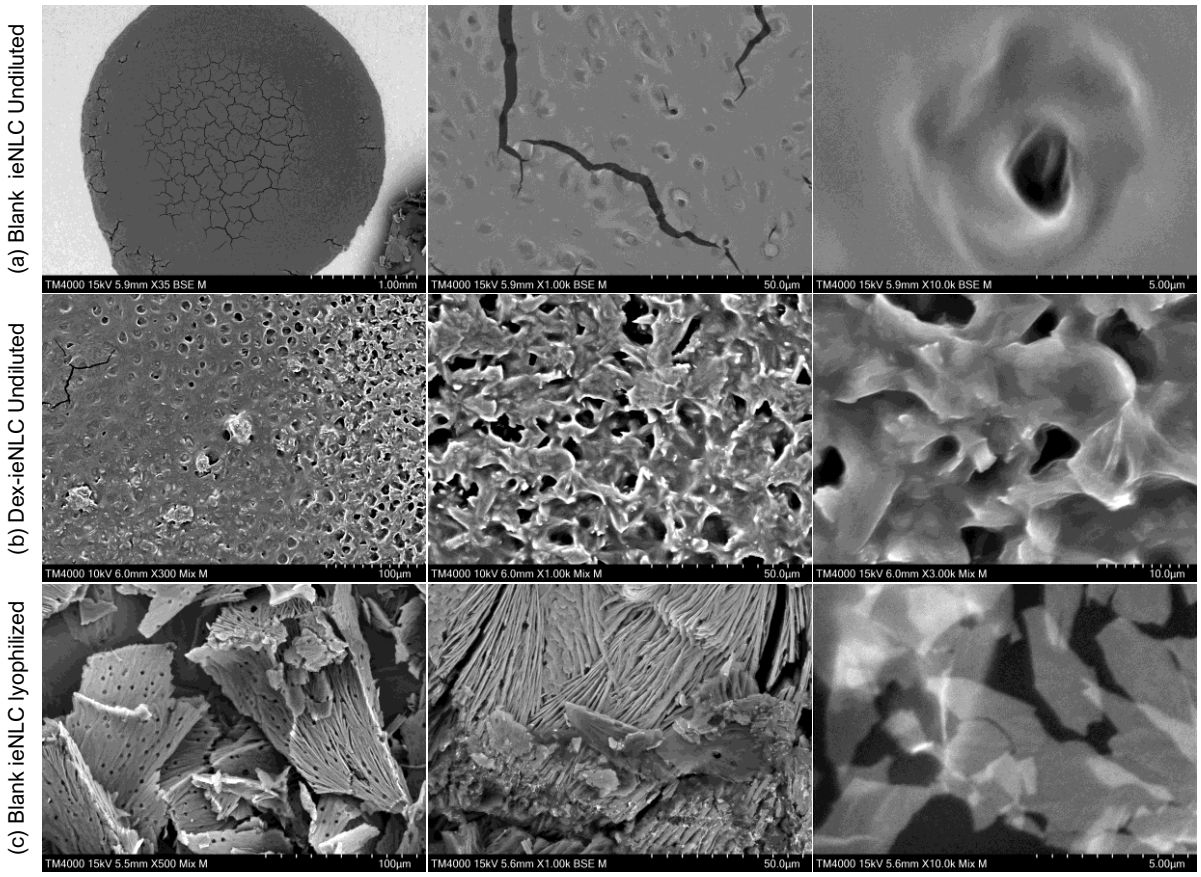

Figure 17. SEM images of liquid air-dried samples of the blank ieNLC (a) or Dex-loaded ieNLC (b) and (c) the lyophilizate powder containing blank ieNLC and lactose as cryoprotectant.

Due to the low resolution of the setup, in the lyophilizates only lactose crystals could be observed (Figure 17, row c), and no ieNLC could be observed; only fragments of

this friable “excipient film” (possibly a lipidic film) remain as the only structure observable at the highest magnification studied (10.0k) (Figure 17, row b).

The developed Dex-ieNLC were further observed with a FEG-SEM apparatus which did not require prior sample metallization and is expected to reach better resolution at high magnification. Only Dex-ieNLC were observed and photomicrographs corresponding to 1:100 diluted samples at different magnifications are presented in Figure 18.

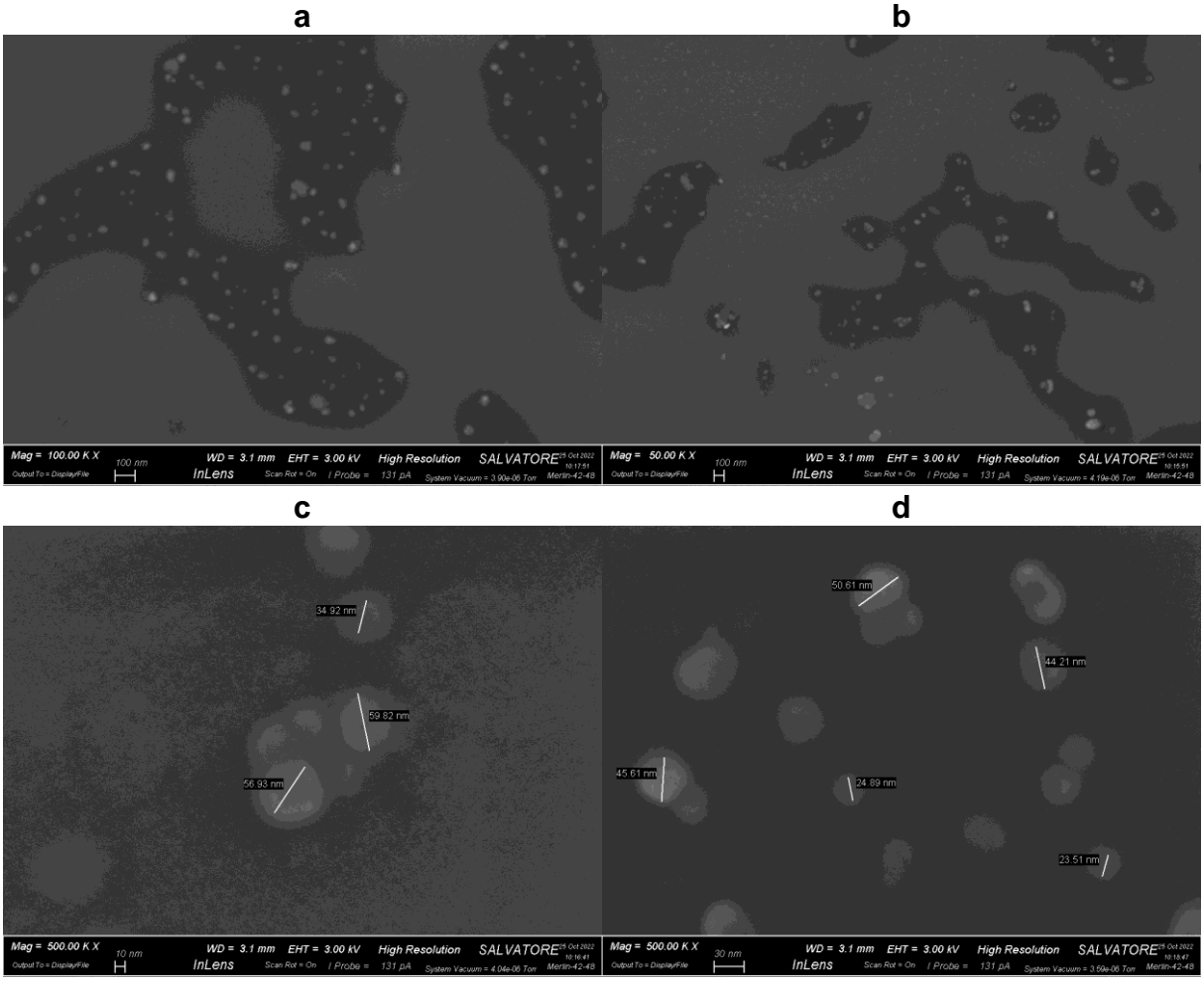

Figure 18. FEG-SEM images obtained at different magnifications of air-dried Dex-ieNLC diluted 1:100.

The FEG-SEM technique allowed to adequately observe the nanoparticles, which appeared sufficiently separated at a 1:100 dilution (Figures 18a and 18b). The spherical morphology was also preserved (Figures 18c and 18d) in contrast to the previous sample preparation which had produced an “excipient film”.

3.3.3.4. In vitro cytotoxicity

In vitro cytotoxicity after a 24 h contact

The formulated Dex-ieNLC were evaluated for their cytotoxicity when in contact with retinal pigmented epithelial cells for 24 hours, the same time considered for the permeation and retention experiments (see Sections 5.2.7 and 5.2.8). The obtained results are presented in Figure 19, where data values have been normalized by the positive, untreated, control, as indicated in Equation 2.

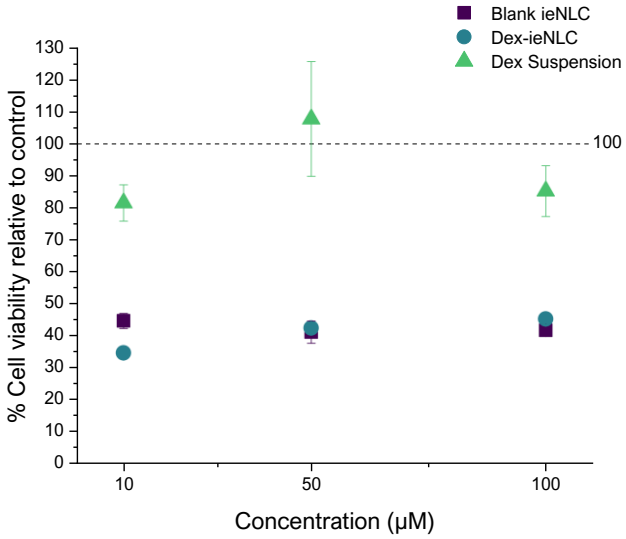

Figure 19. Dose-response curve for the MTT assay on ARPE-19 cells after a contact time of 24 h with blank (drug-free) ieNLC, dexamethasone-loaded ieNLC and a dexamethasone suspension in growth medium at three different drug concentrations. The blank ieNLC were diluted in the same ratio as their drug-loaded counterparts. Data are mean ± standard deviation for n = 6.

The drug suspension in growth medium demonstrated adequate cell viability values (≥ 80%) at all the three concentrations evaluated, which could indicate that the drug alone might not be responsible for the observed loss in cell viability although no proportional correlation between drug concentration and reduction in cell viability could be detected.

In addition, independently of the drug concentration in the ieNLC (and thus also independently on the number of nanoparticles present) cell viability remained below 50%. This could indicate that presence of the ieNLC is interfering with the results, independently of the nanoparticle concentration. This is further confirmed if data for the 100 μM concentrations are compared, as depicted in Figure 20.

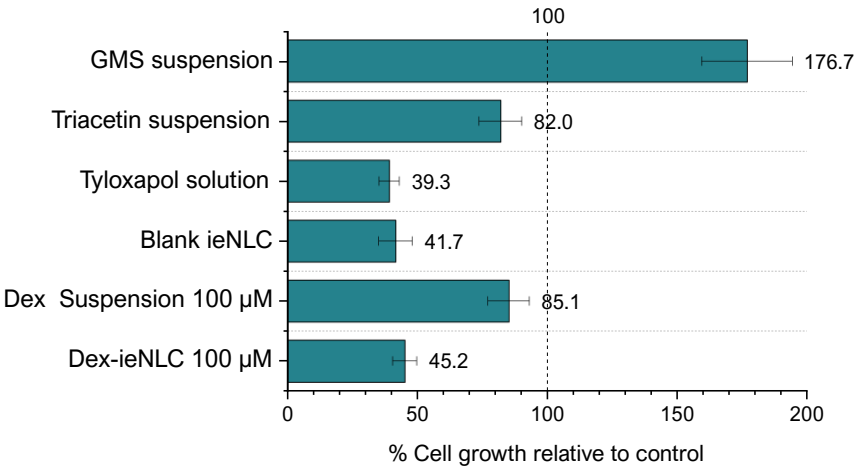

Figure 20. Comparative results of the MTT assay for the 100 µM series after a 24-hours exposition.

The GMS suspension shows a possible interference, since cell viability rises to 176.7%, although when GMS is present as a component of the nanoparticle, cell viability is reduced. Both triacetin alone or dexamethasone alone, do not seem to be interfering with either the analysis or the cell viability, which remains ≥ 80%. The tyloxapol solution in growth medium (at the same concentration that would be present in a 100 µM dilution of ieNLC) does appear cytotoxic after 24 hours.

In any case, the quality of the obtained data is too poor for reaching any conclusions regarding ieNLC cytotoxicity. What is nonetheless clear is that over a 24 h period and at 37 ºC, the formulation is not stable in the growth medium, which can be also observed macroscopically as a lipidic supernatant or turbidity in the wells containing ieNLC (Figure 21).

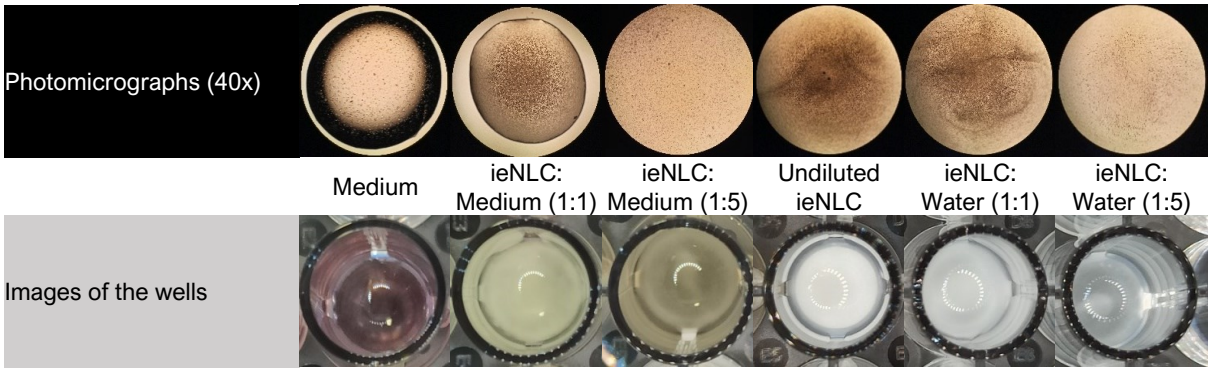

Figure 21. Photomicrographs (top row) and macroscopic images (bottom row) after 24 hours incubation at 37 ºC of Dex-ieNLC at different dilution rates with growth medium or water.

The lipidic “creaming” might hinder adequate gas exchange from the well (*suffocating* the cells) and could also interfere with the MTT reagent which cannot be utilised by the surviving ARPE-19, thus leading to the observed unconclusive results.

At this point, the experiment was repeated with a reduced contact time of four hours in an attempt to reduce the possibility of formulation destabilization.

In vitro cytotoxicity after a 4 h contact

After a 4-hour contact, still a lipidic "creaming" was clearly visible on the top of the wells containing ieNLC, particularly at higher concentrations (that is, 100 and 50 μM, referring to Dex concentration). This phenomenon highly influenced cell viability, as depicted in Figure 22.

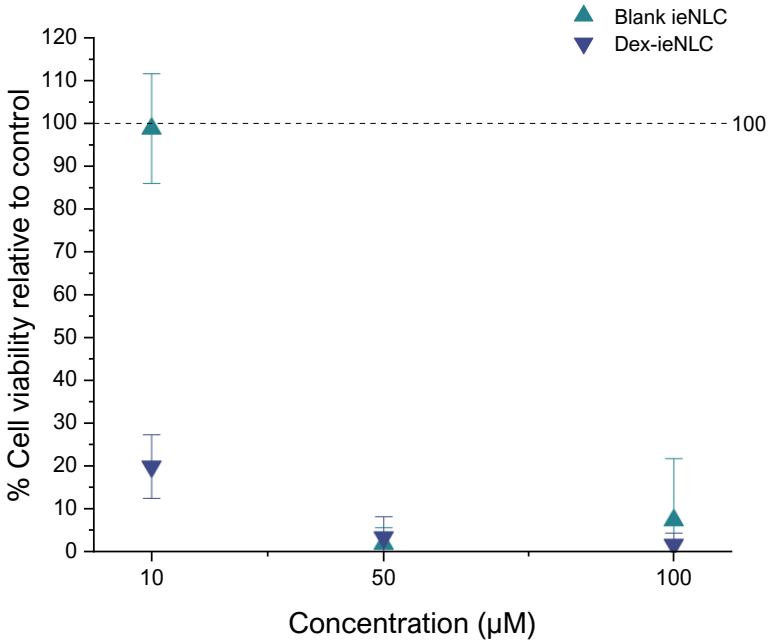

Figure 22. Dose-response curve for the MTT assay on ARPE-19 cells after a contact time of 4 H with blank (drug-free) ieNLC and dexamethasone-loaded ieNLC at three different drug concentrations. The blank ieNLC were diluted in the same ratio as their drug-loaded counterparts. Data are mean ± standard deviation for n = 6.

When the lowest concentration was studied (10 μM), the lipidic supernatant was less evident and the viability for blank ieNLC was comparable to the positive control, while for drug-loaded ieNLC, cell viability remained at a 20% level. Therefore, considering the results obtained for the dexamethasone suspensions in growth medium (Figures 19 and 20), a possible cytotoxicity dependent on the combination between drug and ieNLC cannot be excluded.

3.4. Development of Dexamethasone Microemulsions

The NLC developed in Sections 3.2. and 3.3. were mainly composed of tyloxapol, triacetin and Imwitor® 491. As previously introduced, Imwitor® 491 is a commercial mixture with a ≥ 90% content in glycerol monostearate and represents the only solid excipient in the formulation requiring multiple production steps, subject to variation, which hindered a successful DoE application (as discussed in Section 3.2.2.6). In addition, a further lipid-based colloidal system would allow to obtain comparable data for evaluation of the whole-eye *ex vivo* setup to be presented in Chapter 4. In this sense, the development of a microemulsion with a similar composition, except for the solid Imwitor® 491 will be presented in the current Section.

Tyloxapol has demonstrated in our studies to have strong surface tension lowering capabilities, hence the observed nanometre diameters achieved on the NLC without requiring any typical cosurfactant such as short-chain alcohols [217,233-235]. Thereby it was initially studied the feasibility of using tyloxapol as the only stabilizer of the microemulsion. The results indicated that a cosurfactant might be required and in a series of trials, it has been evaluated up to four molecules that could act as cosurfactants and offer the largest O/W microemulsion regions.

As introduced in Section 3.1.1., microemulsions are lyotropic systems based on self-assembly and thus form spontaneously with hardly any energy input required. The systems are also thermodynamically stable and thus, if adequately formulated, could express a long shelf-time. What is more, with such a simplified production process (where only accurate weighting and brief stirring are required) the chances of a successful DoE application can only increase. In this sense, an approach based on the open-source RStudio software, based on the R programming language was followed.

3.4.1. Materials and Methods

3.4.1.1. Materials

Tween® 60 was purchased from Galeno S.r.l. (Prato, Italy). Transcutol® P (2-(2-Ethoxyethoxy)ethan-1-ol) was kindly gifted by Gattefossè (Saint-Priest, France); Lutrol® L44 (poloxamer 124) was a gift from BASF (Ludwigshafen, Germany) and Span® 80 (sorbitan monooleate) was kindly gifted by Bregaglio S.r.l. (Biassono, Italy). Triton X-100 (IUPAC 2-[4-(2,4,4-trimethylpentan-2-yl)phenoxy]ethanol) was from Sigma Aldrich (Taufkirchen, Germany). All other excipients have previously been described in Section 3.2.2.1..

3.4.1.2. Selection of tyloxapol-surfactant mixtures

The water titration technique presented in Section 3.2.2.4. was followed, but at room temperature. After each water aliquot addition, the microemulsions were left under magnetic agitation for at least five minutes and the obtained system was characterized following the classification system presented in [236,237]. For the tyloxapol-only and Transcutol® P-tyloxapol (1:4) the whole simplex space was studied while for the other surfactant mixtures, only the formulation corresponding to an initial triacetin content of 30% triacetin and 70% surfactant mixture was studied, since it might contain the left boundary (oil-rich formulations) of the microemulsion region.

3.4.1.3. Selection of the adequate polysorbate 60- tyloxapol ratio

A modified method from [238] was followed. Briefly, ten mixtures of polysorbate 60 and tyloxapol at varying ratios (from 0% to 90% tyloxapol content) were prepared to a total mass of 0.5 g and heated at 45 ºC for mixing. Emulsions containing 0.4 ml triacetin, 0.4 mL water (1:1 ratio) and 150 mg of each polysorbate 60-tyloxapol mixture were prepared by vortexing for 30 seconds. The formulations were left at room temperature for two hours.

Transmittance at 638 nm of the systems was measured on quartz cuvettes at room temperature. Transmittance measurements were performed on a Jasco V-570 UV/Vis/NIR spectrophotometer (Jasco Europe Srl, Cremella, Italy). A further macroscopical evaluation at 72 h was performed to detect phase separation.

3.4.1.4. Microemulsion region identification

The water titration technique presented in Section 3.2.2.4. was followed at room temperature. After each water aliquot addition, the microemulsions were left under magnetic agitation for at least five minutes and the microemulsions were only characterized as “Transparent and non-viscous” or “Not transparent or viscous”. The microemulsion region is denoted as the region within the simplex where the transparent and non-viscous systems were observed. Each titration series was named according to the initial compositions reported in Table 7, to which 10% increments of water were added.

Table 7. Initial composition of the microemulsions that were subject to water titration.

Coded name	% Triacetin (w/w)	%Tyloxapol (w/w)	% Polysorbate 60 (w/w)
A	90	8	2
B	80	16	4
C	70	24	6
D	60	32	8
E	50	40	10
F	40	48	12
F’	35	52	13

G	30	56	14
G'	25	60	15
H	20	64	16
I	10	72	18

3.4.1.5. Polarized light microscopy

Microemulsions were investigated for system isotropy using a polarizing light microscope (Nikon Optiphot 2 POL, Nikon, USA). Samples that appeared black, with no birefringent structures under polarized light were considered isotropic and thus confirmed the existence of a microemulsion system.

3.4.1.6. Microemulsion region characterization: Design of Experiments

A constrained mixture design was followed on the previously identified microemulsion region. Code snippets for experimental run design and multivariate regression analysis were written using the opensource RStudio software, with the help of the *mixexp*, *dplyr* and *broom* packages [239-243].

The studied factors were the ratio of the components of the pseudoternary mixture, namely triacetin, water and surfactant mixture (S_{mix}; tyloxapol 80%: polysorbate 60 20%). The analysed responses were nanoparticle size (nm), PDI and maximum amount of Dex solubilized after 24 h at room temperature (mg/mL).

3.4.1.7. Dexamethasone solubility studies

Drug solubility in the selected formulations was determined by adding Dex in excess to 1 mL of each formulation at room temperature for 24 hours under magnetic stirring. Aliquots of 0.5 mL were centrifuged for 10 minutes at 12000 rpm (Scilogex D3024, Cromwell, London, UK) and the supernatant was diluted 1:100 with pure acetonitrile. This was further diluted 1:5 with an extracting mixture composed of acetonitrile-water (65:35, v/v). The final 1:500 diluted samples were submitted for UV-Vis HPLC analysis. Values were obtained by triplicates and are reported as mean ± standard deviation.

3.4.1.8. In vitro cytotoxicity

The cytotoxicity on human retinal pigment epithelial cells (ARPE-19) was assessed *via* the MTT assay. ARPE-19 cell line (ATCC-CRL-2302) was purchased from ATCC (American Type Culture Collection, ATCC, Manassas, VA; LGC Italy, Sesto San Giovanni, Italy). Growth medium consisted of Dulbecco's Modified Eagle's Medium (DMEM)/Nutrient Mixture F-12 (DMEM/F12 (1:1) with HEPES (Gibco Life Technologies, Carlsbad, CA), supplemented with 10% foetal bovine serum (FBS) and 1% penicillin/streptomycin (10,000 U/mL, Gibco Life Technologies, Carlsbad, CA). Cells

were maintained in a humidified incubator at 37°C and 5% CO_2. Cells were seeded in 96-well plates (~ 7000 cells/well) and cultured for 48 hours.

The diverse treatments consisted of 100 µL of Dex-F'80 in growth medium at a drug concentration of 10, 50 and 100 µM of drug. Blank F'80 microemulsions diluted in growth medium were also analysed by following the same dilution volumes as their respective drug-loaded counterparts. A tyloxapol solution at 0.5% w/v, corresponding to the concentration reached when the final Dex concentration is 100 µM, was also tested. Growth medium and a 5% Triton X-100 solution in growth medium were used as positive (untreated) and negative controls of cell viability, respectively.

After a 4-hour contact with the treatments, the wells were washed and 100 µL of the MTT reagent (0.5 mg/mL in HBSS) were added to each well and incubated for 3 hours. Subsequently, well content was replaced with 100 µL DMSO for solubilisation of the formazan crystals for 15 minutes under agitation (150 rpm) and preserved from light. Absorbance was measured at 570 nm using a microplate reader (Spark multimode microplate reader, Tecan Group Ltd., Männedorf, Switzerland). Cell viability was assessed following Equation 2 (3.3.1.6).

3.4.2. Results and Discussion

3.4.2.1. Selection of tyloxapol-surfactant mixtures

The surfactant tyloxapol has demonstrated superior surface tension lowering capabilities and thus, the possibility of formulating a microemulsion without a cosurfactant explored. The ternary phase diagram for the water/triacetin/tyloxapol ternary mixture was created, and the observed structures were sorted following the classification system proposed in [237]. Categorization was based on macroscopical observation to the naked eye where the desirable microemulsions appear completely transparent and form spontaneously under low speed stirring conditions in less than a minute. Other systems appeared less transparent, slightly bluish (Type II) or as opaque, white macroemulsions (Type III). Type IV systems appeared dull and greyish and did not improve over time while in Type V systems a clear phase separation was observable. In some cases, also gel-like phases were observed or, due to a very low water content, a solid sediment was formed. The results are presented in Figure 23a, from which it is clear that tyloxapol only is not able to reach the ultra-low surface tension required for microemulsion production since no quick-forming optically transparent formulations (Type I) could be observed.

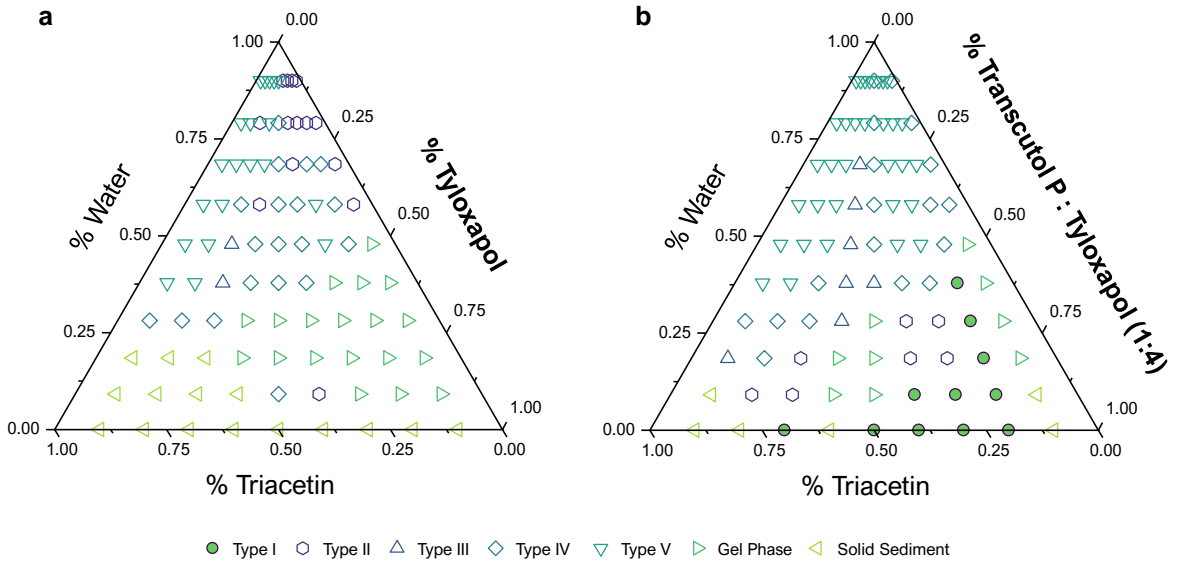

Figure 23. (a) Ternary phase diagram obtained by water titration and macroscopical observation for the water/triacetin/tyloxapol mixture at room temperature where no microemulsion region could be identified and (b) pseudoternary phase diagram of the macroscopical observations for the water/triacetin/S_{mix} system, where S_{mix} is composed of 80% tyloxapol and 20% Transcutol® P.

Transcutol P (diethylene glycol monoethyl ether) is typically used as cosurfactant and has already been utilised in ocular formulations [244,245] and has also demonstrated to transiently increase corneal permeation [246]. An initial trial with 20% tyloxapol substitution with Transcutol® P was studied (Figure 23b) creating a surfactant mixture (S_{mix}). Only a small microemulsion region (Type I) could be identified with optically transparent microemulsions. However, the systems were obtained at low water contents, which is indicative of possible water-in-oil microemulsions that also present high surfactant concentrations which might have poor ocular tolerance.

These initial attempts did not offer any valuable results, and therefore further excipients were selected as cosurfactants, namely: Span® 80, Lutrol® L44 and Polysorbate 60. Span® 80 (sorbitan monooleate) is a non-ionic ocular-compatible surfactant previously used in ocular microemulsions [247]. Lutrol® L 44 is the commercial denomination for the Poloxamer 124, a liquid poloxamer with adequate ocular tolerability [248]. Polysorbate 60 is also typically present in ocular formulations as niosomes or microemulsions, allowing for drug and gene delivery [249-251].

Instead of exploring the whole simplex (and to reduce excipients usage) only one titration series was performed, namely the one starting at a 30% triacetin and 70% surfactant (mixture) to which increments of 10% water were added. The microemulsion region is expected to appear at high surfactant concentrations (≥ 80% surfactant and ≤ 20% triacetin in the initial titration mixture) and thus studying only this titration series

allows to identify the triacetin-rich border of the microemulsion region. The results are presented in Figure 24.

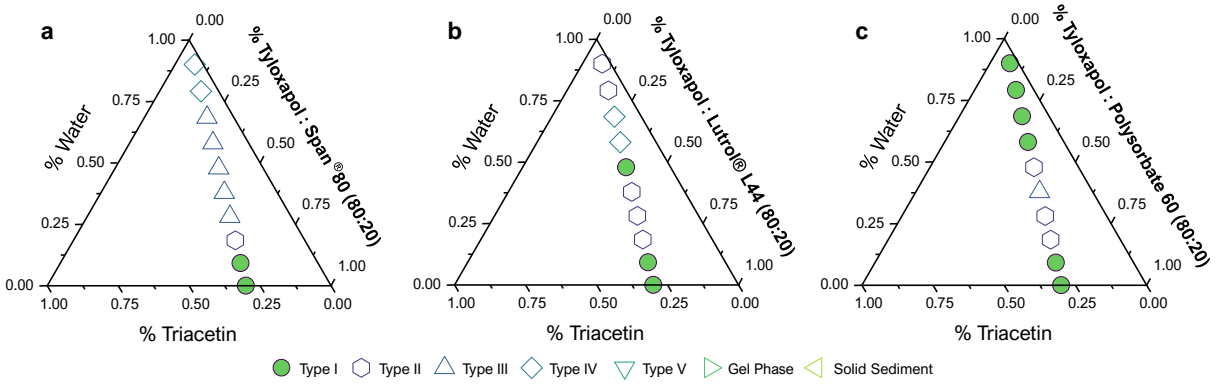

Figure 24. Pseudoternary diagram containing only one titration series (specifically the one staring at a 30% triacetin and 70% S_{mix}) for the S_{mix} composed of 80% tyloxapol and (a) 20% Span® 80, (b) 20% Lutrol® L44 and (c) 20% Polysorbate 60.

Span® 80 showed macroscopical transparency only at 0 and 10% water contents, which indicates that no O/W microemulsion is formed and thus was no longer considered. Lutrol® L44 and Polysorbate 60 did both form microemulsions at ≥ 50% water contents, indicating their eligibility for further studies, with Polysorbate 60 indicating a larger area.

Lutrol® L44 and Polysorbate 60 where further studied by increasing in both cases their percentage in the S_{mix} to 30 and 40% (Figure 25).

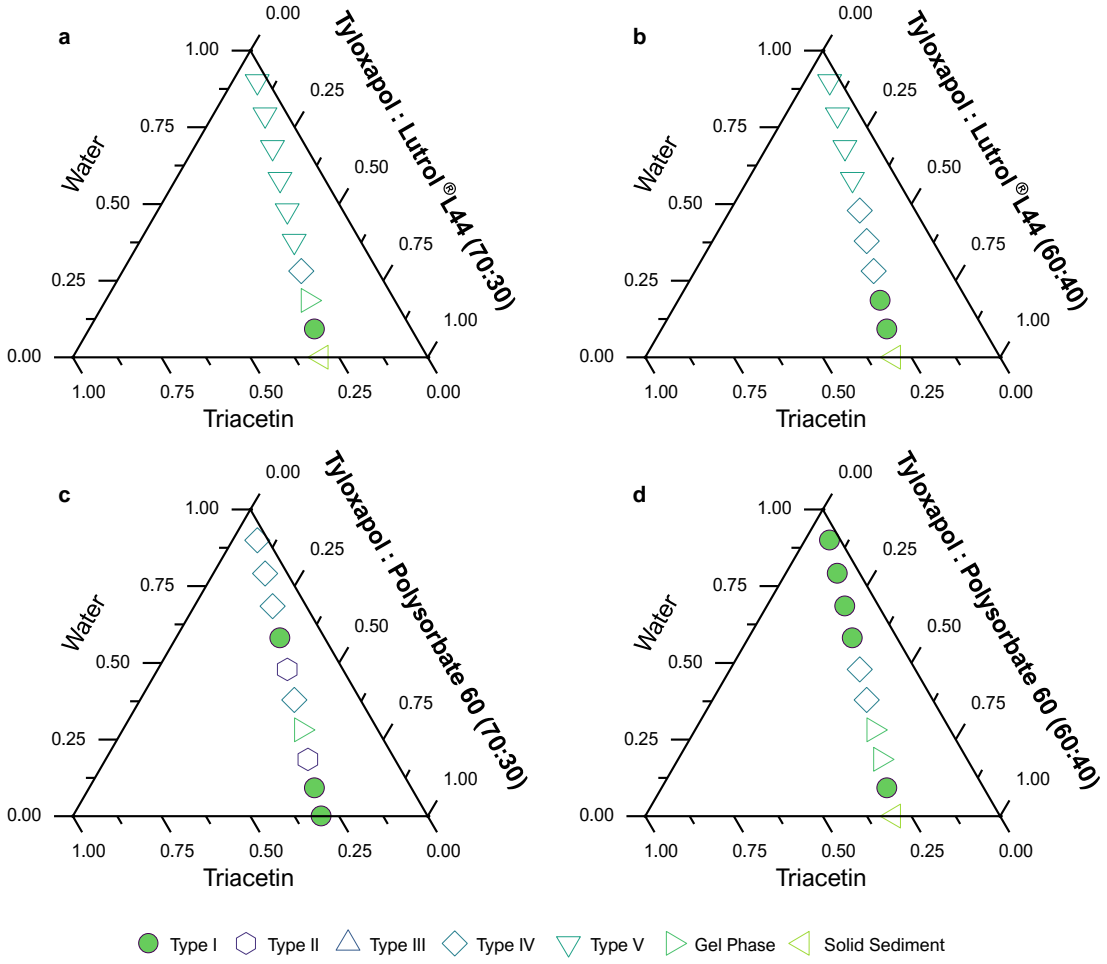

Figure 25. Pseudoternary diagram containing only one titration series (specifically the one staring at a 30% triacetin and 70% S_{mix}) for the S_{mix} composed of 70% tyloxapol and (a) 30% Lutrol® L44, (c) 30% polysorbate 60 and S_{mix} composed of 60% tyloxapol and (b) 40% Lutrol® L44 and (d) 40% polysorbate 60.

These series of trials demonstrated that increasing the relative proportion of Lutrol® L44 in the S_{mix} does not deliver any O/W microemulsion candidates. On the other hand, polysorbate 60 still does show O/W microemulsions with similar results for 40% polysorbate 60 to the previously observed at 20%. The 30% polysorbate 60 S_{mix} surprisingly performed poorer, indicating that further analysis for identifying the best tyloxapol/polysorbate 60 ratio is required.

3.4.2.2. Ratio tyloxapol/polysorbate 60 selection: optical transmittance

The promising results in the previous Section can mainly be explained by the fact that Polysorbate 60 presents a monostearate hydrophobic tail. This apolar tail is identical to the one present in the glycerol monostearate previously used for NLC production, but the polar head is larger thus conferring polysorbate 60 an HLB of 14.9, rather than the observed HLB value of 3.8 reported for GMS [249,252]. Therefore, it

can be hypothesized that the monostearate tail inserts itself on the nanoparticle surface in a similar manner as GMS does in the NLC, but the large hydrophilic portion further contributes to reach the required ultra-low surface tension in the thermodynamically stable microemulsion.

The quick screening approach for finding the best tyloxapol/polysorbate 60 is based on Windsor classification system for multiphase microemulsions [253-255]. In fact, depending on the emulsifying activity of each mixture, the equal parts of non-miscible oil and water will be integrated to a greater or lesser extent into an emulsion. If the required ultra-low surface tension is not achieved, large globules will be present, which reduce the optical transmittance of the system. On the other hand, if a microemulsion is achieved, the nanosized globules do not interfere with the optical transmittance and values close to 100% transmittance will be detected by the spectrophotometer [236,238]. The results of this experiment are presented in Table 8.

Table 8. Transmittance values recorded for tyloxapol/polysorbate 60 mixtures with ranging relative proportions from 0 to 100% and their stability after three days. Screening data, unreplicated.

% Tyloxapol	% Polysorbate 60	% Transmittance (638 nm)	Phase separation after 3 days?
0	100	82.34	Y
10	90	25.50	Y
20	80	51.57	Y
30	70	38.56	Y
40	60	90.28	Y
50	50	83.60	Y
60	40	76.24	Y
70	30	95.70	N
80	20	95.62	N
90	10	89.18	N

The data indicate that polysorbate 60 by itself is unable to solubilize all the triacetin present in the formulation and deliver a microemulsion since haziness was observed and phase separation after 3 days occurred when only polysorbate 60 was present. By increasing the content of the tyloxapol ratio in the S_{mix} an initial reduction in optical transmittance could be detected but values of ≥ 95% transmittance were not obtained until tyloxapol represented the 70% of the S_{mix}. These tyloxapol-rich microemulsions also did not show any apparent phase separation after storage for 3 days at room temperature. Based on these results, studies were continued with an S_{mix} composed of 80% tyloxapol and 20% polysorbate 60 since ± 10% variations do not greatly influence optically transmittance and thus the systems would be stable to any possible small variability during the production process.

3.4.2.3. Microemulsion region identification

The whole simplex was explored, *via* water titration technique, for the pseudoternary system water/triacetin/S_{mix} (tyloxapol 80%: polysorbate 60 20%). The results are presented in Figure 26.

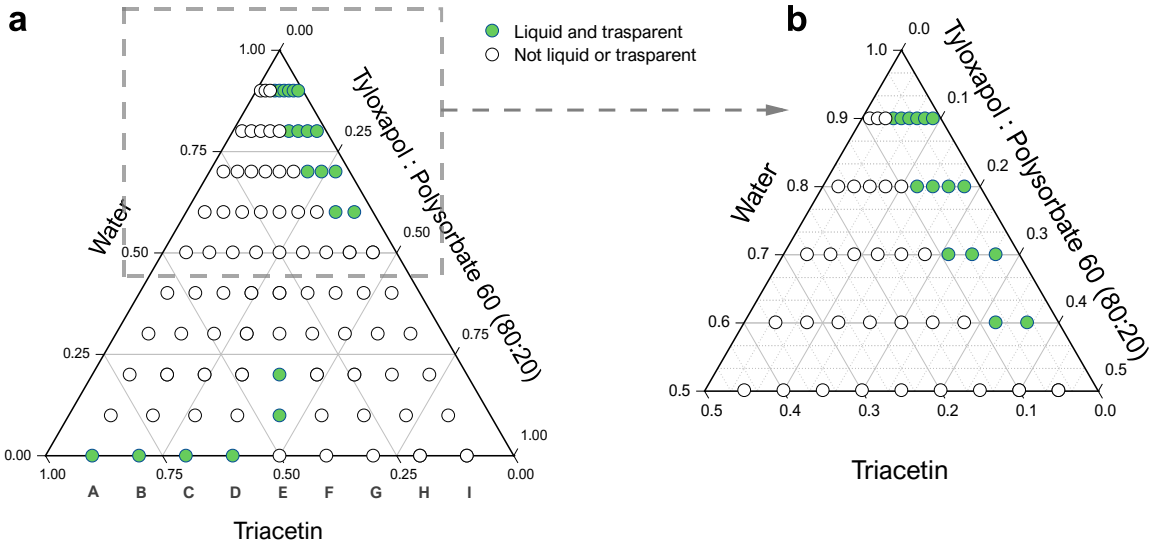

Figure 26. Pseudoternary phase diagram obtained by addition of 10% water increments to the system composed of water/triacetin/S_{mix} (tyloxapol 80%: polysorbate 60 20%). Panel (a) contains the whole simplex, while panel (b) is a zoomed section of the pseudoternary phase diagram for water contents ≥ 50%. The letters "A", "B", "C", (…),"I" indicate the titration series coded name.

In this case, no efforts were made to characterize the non-transparent or highly viscous systems that are not the desired, rapidly forming O/W microemulsions (Type I, according to the previously used classification system). In fact, some titration points appeared liquid and transparent (specially at high lipid contents), but were not considered since the content in water was in any case ≤ 20%, which indicates possible W/O systems (Figure 26a).

A microemulsion region was identified with a "left boundary" (triacetin-rich formulations) falling on the G titration series (*i.e.*, the ratio between Triacetin and S_{mix} is 30:70). The o/w microemulsions occurred at ≥ 60% water contents.

The region was further characterised by repeating the titration with increments of only 2.5% water aliquots and including two new titration series (F' and G') with 35% and 25% triacetin content and 65% and 75% S_{mix} content, respectively. The resulting microemulsion region is depicted in Figure 27.

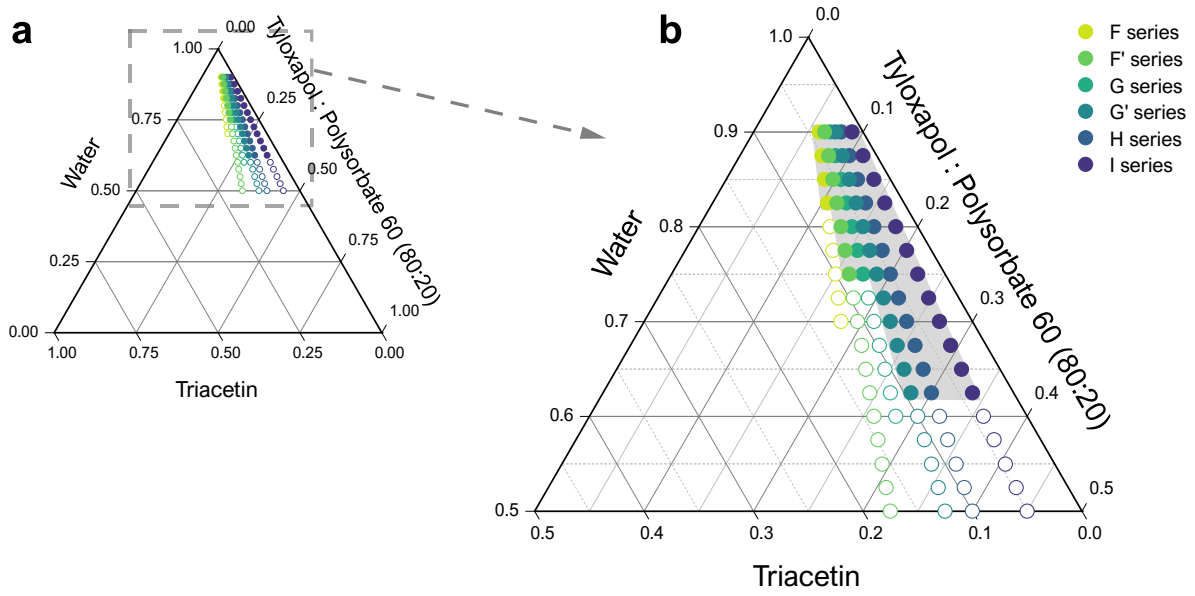

Figure 27. Pseudoternary phase diagram obtained by addition of 2.5% water increments to the system composed of water/triacetin/S_{mix} (tyloxapol 80%: polysorbate 60 20%). Panel (a) contains the whole simplex, while panel (b) contains a zoomed section for ≥ 50% water content. Full points indicate transparent O/W microemulsions while void points indicate non-transparent and/or viscous formulations.

Inclusion of the G' titration series allowed to determine that the microemulsion region further expands to higher triacetin contents (*towards left*) and that the O/W microemulsions require at least ≥ 62.5% water content to adequately form, with increasing water contents required the more the triacetin content increases.

3.4.2.4. Microemulsion region characterization through DoE: Size, (PDI) and EE% mathematical modelling

The identified microemulsion region was characterized following a DoE approach in order to create regression models that predict the microemulsion globules size and PDI and also the maximal amount of dexamethasone that the formulation can solubilise.

Experimental design and runs

Three pseudocomponents of the mixture, namely, relative proportion of triacetin (oil), S_{mix} (composed in 80% tyloxapol and 20% polysorbate 60) and water were defined as factors. Three responses were evaluated: maximal quantity of incorporated dexamethasone, also known as maximal drug loading, expressed as mass concentration (mg/mL), the Z-Average size (nm) of the first peak detected (Peak 1) in DLS and the PDI value.

A constrained mixture design was performed on the previously individuated region of existence of the microemulsion in order to model each response (namely: maximal

drug loading, size and PDI) as a function of the relative proportion of the components of the microemulsion.

The opensource packages *mixexp* and *dplyr* were used for the design and analysis of the experimental runs. The previously identified microemulsion region was mathematically defined by the constraints:

$$0.05 \leq S_{mix} \leq 1$$
$$0.625 \leq \text{Water} \leq 0.90$$
$$0.023 \leq \text{Triacetin} \leq 0.075$$

The *mixexp* package followed the XVERT algorithm [181] for finding the vertices of the constrained region and a D-Optimal design was followed for the candidate point selection. The initial design proposed included 11 experimental points (5 vertices, 5 edge centres and the overall centroid). The design was augmented in order to allow for lack-of fit testing, with 4 axial points that were randomly selected from a list of interior point candidates generated by the *Fillv* function in the mixexp package. In addition, three replicate points were also randomly selected to increase the degrees of freedom of the system. The resulting 18 experimental runs, enough for a quadratic-model fitting, are plotted in Figure 28.

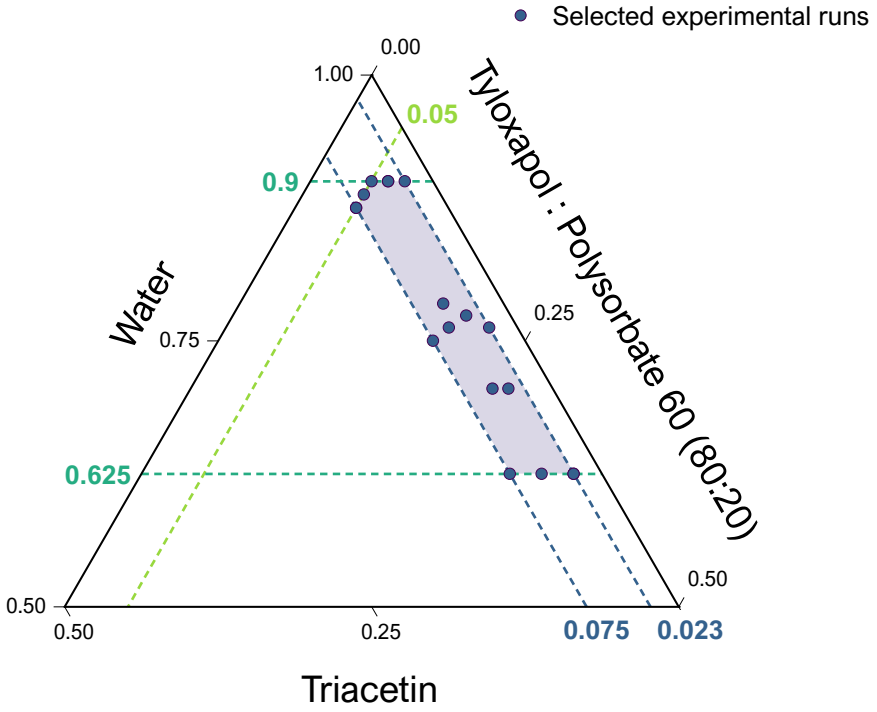

Figure 28. Ternary plot of the experimental runs performed within the constrained region. The coloured dashed lines indicate the lower and upper boundaries for each mixture pseudocomponents which define the constrained region.

The proposed 18 microemulsions were produced in a randomized order and their composition, the results for their maximal solubilising capabilities of Dex (maximal drug loading mg/mL), their size (nm) and PDI are presented in Table 9.

Table 9. Experimental run compositions and the recorded responses for each combination.

#Run	Order	S_{mix}		Triacetin (mg)	Water (mg)	Responses			Peak 1 %
		Tyloxapol (mg)	Tween 60 (mg)			Max Drug loading (mg/mL)	Size (nm)	PDI	
3	1	218.1	54.5	83.6	1143.8	2.87	6.01 ± 1.16	0.180 ± 0.122	96.2
10	2	228.2	57.0	54.2	1160.6	2.98	5.43 ± 0.42	0.250 ± 0.126	98.3
6	3	295.1	73.8	73.7	1057.5	3.78	5.89 ± 5.89	0.310 ± 0.090	96.5
8	4	310.7	77.7	54.2	1057.5	4.03	5.85 ± 0.64	0.880 ± 0.203	84
15	5	60.0	15.0	75.0	1350.0	0.92	6.96 ± 0.31	0.180 ± 0.075	76.9
12	6	422.4	105.6	34.5	937.5	5.01	3.71 ± 0.13	0.440 ± 0.101	99.5
16	7	92.4	23.1	34.5	1350.0	1.31	6.06 ± 0.14	0.920 ± 0.078	46.9
2	8	60.0	15.0	112.5	1312.5	0.90	7.64 ± 0.01	0.240 ± 0.014	92.7
1	9	360.0	90.0	112.5	937.5	4.40	4.52 ± 0.16	0.330 ± 0.079	95.9
18	10	60.0	15.0	93.8	1331.3	0.89	7.01 ± 0.22	0.390 ± 0.070	46.4
7	11	391.2	97.8	73.5	937.5	4.47	3.97 ± 0.11	0.380 ± 0.038	90
11	12	76.2	19.1	54.8	1350.0	1.10	7.32 ± 0.08	0.210 ± 0.022	56.7
13	13	257.4	64.4	34.5	1143.8	3.44	5.95 ± 0.23	0.380 ± 0.049	96.4
17	14	210.0	52.5	112.5	1125.0	2.75	6.41 ± 0.15	0.230 ± 0.003	76.4
9	15	199.0	49.7	73.8	1177.5	2.58	6.41 ± 0.12	0.220 ± 0.087	92.6
5	16	76.2	19.1	54.8	1350.0	1.10	6.77 ± 0.26	0.250 ± 0.079	91.6
14	17	60.0	15.0	112.5	1312.5	0.92	7.88 ± 0.10	0.180 ± 0.012	93.5
4	18	422.4	105.6	34.5	937.5	5.27	3.52 ± 0.09	0.430 ± 0.050	97.4

All 18 candidates resulted into optically transparent microemulsions, and their isotropy was confirmed with the help of polarized light microscopy. Isotropy was confirmed when no birefringent structures or phase separation appeared on the black background. A quick analysis of the raw data indicates that all candidates within the microemulsion region have good solubilising capabilities with values ranging from 0.89 mg/mL up to 5.27 mg/mL. The DLS data confirms the nanometre range of the microemulsion globules from 3.52 to 7.88 nm, when considering the first peak of the distribution curve by intensity since presence of any secondary peaks is already taken into consideration when analysing the PDI, which ranges from 0.180 up to 0.920. No outliers could be identified and thus the data was considered valid for calculation of the regression models.

The experimental results were fitted to the highest model possible. In this sense each response was fitted to linear, quadratic, special cubic and full cubic Scheffé polynomials and Analysis of Variance (ANOVA) was performed within each model level to establish if a higher higher-order model is justified, or the response can be adequately modelled by a lower-order model (Table 10).

Table 10. Results of the ANOVA for each response in order to find the highest order model that fits the observed responses.

Response		Res Df	RSS	Df	Sum of Sq	F	Pr(>F)	Selected model
Maximal Drug Loading	Linear *vs* Quadratic	15 12	0.240 0.102	3	0.137	5.365	0.014 *	Quadratic
	Quadratic *vs* Special Cubic	12 11	0.102 0.102	1	0.000	0.028	0.871	
	Special Cubic *vs* Full Cubic	11 8	0.102 0.048	3	0.054	3.043	0.093	
Size	Linear *vs* Quadratic	15 12	3.331 1.845	3	1.485	3.219	0.061 ·	Quadratic
	Quadratic *vs* Special Cubic	12 11	1.845 1.762	1	0.084	0.523	0.485	
	Special Cubic *vs* Full Cubic	11 8	1.762 0.929	3	0.833	2.390	0.144	
PDI	Linear *vs* Quadratic	15 12	0.599 0.527	3	0.072	0.550	0.658	Linear
	Quadratic *vs* Special Cubic	12 11	0.527 0.521	1	0.006	0.126	0.729	
	Special Cubic *vs* Full Cubic	11 8	0.521 0.296	3	0.225	2.030	0.188	

***(p ≤ 0.001) **(p ≤ 0.01) *(p ≤ 0.05) ·(p ≤ 0.1)

On the other hand, no efforts were made on reducing, by elimination or aggrupation, non-significant terms of the Scheffé polynomials since, due the high intercorrelation between the terms, a non-significance of one term does not imply no influence on the response [256].

Effect of the excipient concentrations on the maximal drug loaded

Solubility studies of dexamethasone in the formulations indicate the maximum amount that can be loaded into the microemulsion globules.

The effect of the ratio of the components on the maximal amount of Dex solubilised after 24 h at 25 ºC was found to be in a wide range of 0.89-5.27 mg/mL despite the highly constrained region. The obtained data was fitted to a quadratic Scheffé polynomial with the values of

$$\hat{y}(x) = 8.11x_1 + 0.16x_2 + 94.44x_3 + 10.79x_1x_2 - 111.15x_1x_3 - 102.95x_2x_3 \quad (3)$$

where x_1 represents the S_{mix}, x_2 the water and x_3 the triacetin relative proportions.

Scheffé polynomials are to be interpreted differently from ordinary polynomial models. The **main effects** (β_1, β_2, β_3…= b_i) **coefficients** are interpreted as the response that would be obtained at the vertices of the simplex, where pure blends of one single component are present [257]. This interpretation is not applicable in this case since

microemulsions require all three components to be present in the mixture in order to form, and thus the regression model can only be used in the constrained region, that is the region of existence of the microemulsion. In any case, the main effects coefficients indicate that the mixture component mostly influencing drug solubility is triacetin (x_3) (*p*-value = 0.00029), and the component mostly hindering solubility is water (x_2), where dexamethasone has poor solubility.

On the other hand, the coefficients of the product terms (β_{12}, β_{13}, β_{23}…= β_{ij}) can be interpreted as a *joint effect* between components that bends the fitted response surface below (if negative sign) or above (if positive) the plane that connects the responses at the vertices (pure blends) [258]. In the present case, the combined effect of a S_{mix}:Water blend (b_{12} coefficient; *p*-value = 0.002) bends the response surface upwards (increasing the maximal drug loading) while the other two joint effects are considered to reduce maximal drug loading by twisting the plane downwards.

The R^2 value is an indicator of the goodness of fit of the model to the obtained data. In order to avoid data overfitting, the adjusted R-squared (R^2_{Adj}) indicates if all the terms included in the model do actually enhance the model (otherwise penalizing the value) in comparison than what is predicted by chance [134]. The closer these values are, the better the fitting. In this case, an adequate fitting was obtained since R^2 = 0.99941 and R^2_{Adj} = 0.99911. The normal probability plots an residuals plots did not show any outliers, with a high predictability in all the range, and the standardized residuals values were maintained lower than an absolute value of three. The model was therefore found to be significant (F-value = 3385.49; *p*-value = 1.18E-18) with a residual standard error of 0.0923 on 12 degrees of freedom.

Effect of the excipient concentrations on the nanoparticle size

Nanoparticle size is considered as the value (nm) observed for the first peak of the DLS analysis since presence of any secondary peak is already taken into consideration in the PDI value.

The measured microemulsion globule diameter varied in a small range between 3.52 and 7.88 nm. The responses were also fitted according to a quadratic Scheffé polynomial with the following coefficients:

$$\hat{y}(x) = -20.927x_1 + 5.382x_2 - 55.718x_3 + 33.475x_1x_2 + 26.482x_1x_3 + 99.742x_2x_3 \quad (4)$$

where x_1 represents the S_{mix}, x_2 the water and x_3 the triacetin relative proportions.

The main effects coefficients indicate the expected value at the vertices of the simplex, but since β_1 and β_2 in this case are negative, the nanoparticle size values

obtained at the vertices of the simplex would also be negative, which is not physically possible. It is important to notice that the obtained regression models are only valid within the constrained region since the data for its constructions was only obtained within that specific area.

The single component S_{mix} (β_1 coefficient, *p*-value = 0.0098) apparently promotes globule diameter increase (*i.e.*, it contributes to globule *formation*) while the water component (β_2 coefficient, *p*-value < 0.001) promotes a decrease and no effect for triacetin is detected (β_3 coefficient, *p*-value = 0.855). The joint effects between pairs of excipients (β_{ij} terms in Equation 4) do all three contribute synergistically to increase the diameter of the globules, bending upwards the response surface.

The R-squared values were R^2 = 0.9972 and Adj-R^2 = 0.9959. The calculated R-squared concluded that all terms in the model are significant and no overfitting was performed, although the initial ANOVA testing did initially not justify the increase to a higher order model (*p*-value = 0.061) from a simple linear model. The overall model was found to be significant with an F-value of 722.69 and *p*-value < 0.001.

Effect of the excipient concentrations on the nanoparticle PDI

The Polydispersity index (PDI) is an adimensional value which is obtained as PDI = (Standard Deviation / Mean Size)^2 [259]. A perfectly monodisperse nanoparticle population expresses a PDI < 0.1, but usually values of 0.2 are acceptable.

Analysing the raw data for the PDI response, the observed mean and standard deviation values were in many cases too high, which hampered the calculation of a good regression model. Considering that all microemulsions were optically transparent, the high PDI values might rather be explained by the calculation methodology of this value in the measurement apparatus which gives a high leverage to interferences recorded in the micrometre range.

The PDI response, as indicated in the initial ANOVA testing, could only be adequately fitted to a linear model since higher order models were not recommended by the test statistics. Even in that case, the R-squared value is only of R^2 = 0.8047 and an Adjusted R-squared = 0.7657 when the data is fitted to the linear Scheffé polynomial:

$$\hat{y}(x) = 0.7499x_1 + 0.5682x_2 - 4.5959x_3 \quad (5)$$

where x_1 represents the S_{mix}, x_2 the water and x_3 the triacetin relative proportions. Even at this low-order model, only the β_2 coefficient for the water was significant ($p < 0.05$). The model can be considered significant (F-value = 20.6; $p < 0.001$), but it can be

expected it will have poor prediction capabilities. This is to be further confirmed with new independent runs at previously unexplored factor combinations.

Contour response surface plots for the adjusted models in the constrained region

The previously obtained response surfaces (Equations 3, 4 and 5) can be plotted in two dimensions creating plots that contain contour lines representing iso-response values, as depicted in Figure 29.

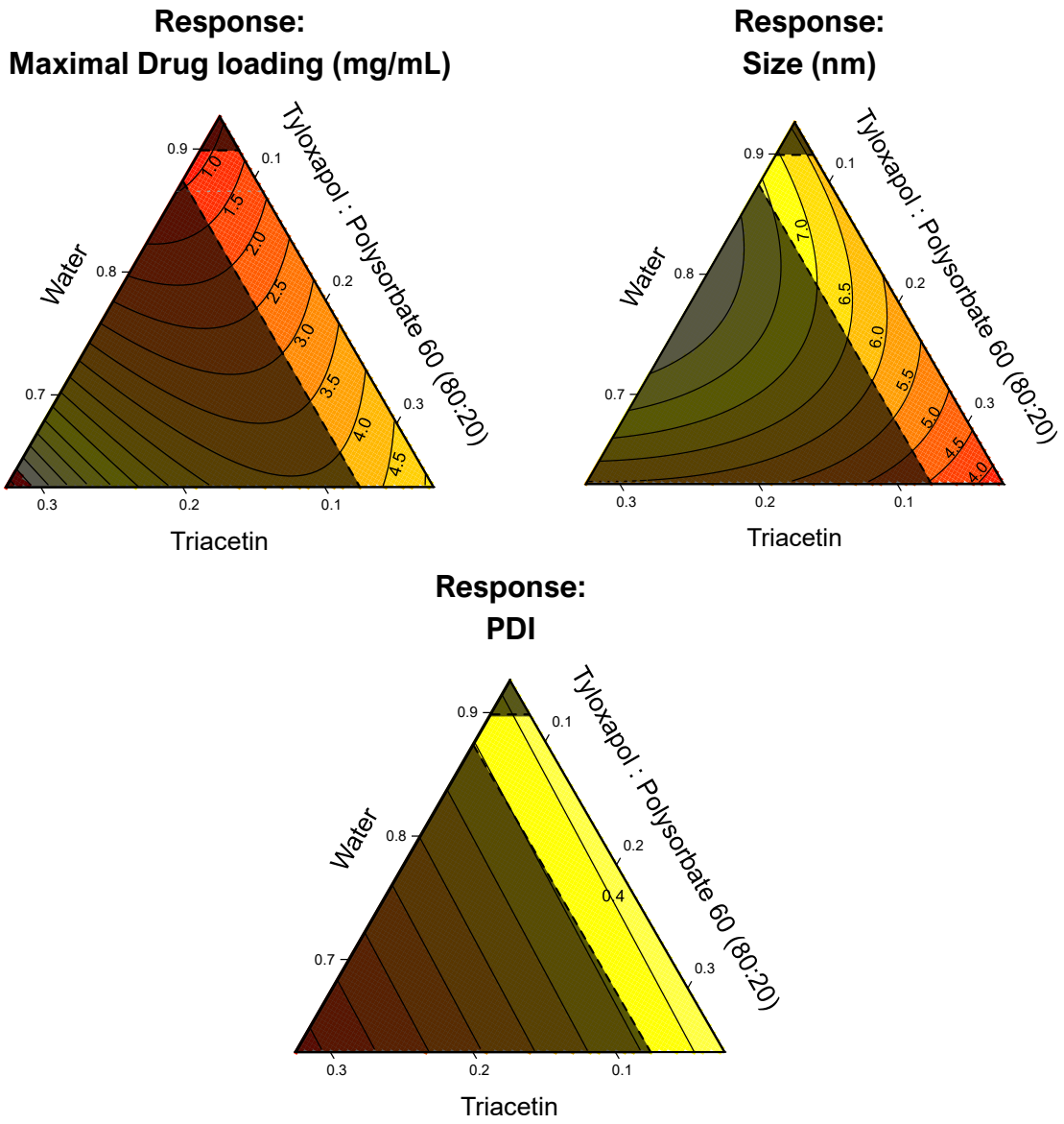

Figure 29. Contour plots of the response surfaces of the fitted models for the three responses of interest (Maximal drug loading (mg/mL); Size (nm) and PDI).

These contour plots are only valid within the constrained region since the experimental values utilised for the regression model calculation were only obtained inside this area, hence the black shading outside the area. In this case, the

interpretation is even simpler considering that pre-formulation studies have indicated that true O/W microemulsions can only be obtained inside this area (see Figure 27) and thus the model predictions outside the constrained region are not valid.

Model confirmation: Residuals plots and new independent observation predictions

Three new formulation candidates, namely F'80, G77.5, F'75, where selected within the constrained region to confirm model ability to predict the response at new factor combinations. The results are presented in Table 11.

Table 11. Experimental run compositions and the recorded responses for each combination.

Name	**Observed** Responses			**Predicted** Responses		
	Max drug loading (mg/mL)	Size (nm)	PDI	Max drug loading (mg/mL)	Size (nm)	PDI
F'80	2.08	6.48	0.14	2.14	6.99	0.23
G77.5	2.62	6.06	0.16	2.52	6.71	0.25
G'75	3.06	6.22	0.25	2.93	6.32	0.28

Name	**Composition**			**% Prediction Error**		
	S_{mix}	Water	Triacetin	Max drug loading (mg/mL)	Size (nm)	PDI
F'80	0.13	0.80	0.07	2.9%	8.0%	69.4%
G77.5	0.16	0.78	0.07	3.7%	10.7%	51.6%
G'75	0.19	0.75	0.06	4.1%	1.7%	10.9%

The prediction error was calculated as the difference between the predicted and the observed values, divided by the observed values, expressed as percentage.

The prediction error was found low for the maximal drug loading (mg/mL) response, indicating that the model can adequately predict the amount of dexamethasone that can be loaded into the microemulsions as a function of its composition for any possible combination within the region of existence of the microemulsion. Particularly, microemulsion allowed to increase Dex solubility between 23 (F'80) and 34 (G'75) times with respect to water.

The prediction error was higher for the response regarding the microemulsion globule size (nm). This variation could be explained partly by the DLS technique used to characterize the globule diameter which adds further variability to the recorded response. This is further supported by the fact that the variations are observed at a decimal level of a nanometre, which in this case cannot be considered to greatly influence the performance once administered onto the eye. PDI already had been fitted to a linear model which had poor fitting and thus the model has also very poor prediction capabilities and thus cannot be used for prediction purposes.

The developed regression models indicate that all the possible microemulsions within the region of microemulsion have good enhancing capabilities of dexamethasone (≥ 0.8 mg/mL). The obtained response surfaces also demonstrate that the variations in size are rather low, and all remain between 7.5 nm and 3.5 nm, which are all compatible with the ocular route too. The PDI cannot be interpreted.

Under these circumstances, the three formulation candidates for further characterization studies were selected on the basis of reducing the S_{mix} component and thus limiting the possible ocular toxicity. Particularly, the previously selected F'80, G77.5 and G'75 microemulsions for model validation were further characterized for their *ex vivo* performance (Chapter 5) and F'80 was also selected for cytotoxicity studies in ARPE-19 cells.

3.4.2.5. In vitro cytotoxicity

The cytotoxicity of microemulsion F'80 was evaluated with retinal pigmented epithelial (ARPE-19) cells for 4 hours. Obtained results are presented in Figure 30, where data values have been normalized by untreated cells (see Equation 2).

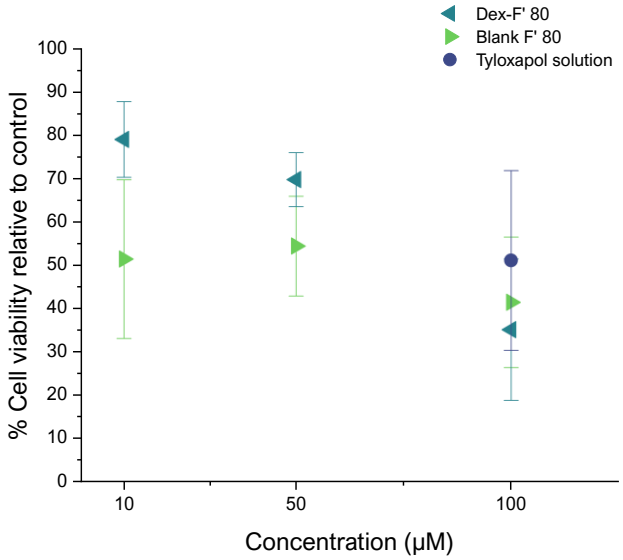

Figure 30. Dose-response curve for the MTT assay on ARPE-19 cells after a contact time of 4 h with blank (drug-free) F'80 microemulsions and dexamethasone-loaded F'80 at three different drug concentrations. The blank F'80 was diluted in the same ratio as its drug-loaded counterpart. The tyloxapol solution corresponds to the tyloxapol concentration obtained when F'80 is diluted for the 100 μM concentration. Data are mean ± standard deviation for n = 6.

Formulations containing Dex at 50 μM and 10 μM have a comparable behaviour, since cellular survival is (69.8 % ± 6.2) % and (79.0 ± 8.7) %, respectively. Differently, at the highest concentration tested, ARPE viability fell to approximately 35%.

Blank microemulsions, independently of the concentration of the excipients, reduced to 50% the cell viability and a similar result was obtained when the tyloxapol solution (at the same concentration that would be present in a 100 μM dilution of F'80) was tested. Unfortunately, data, especially those referring to blank microemulsions, are affected by high variability and therefore their interpretation is difficult.

Chapter 4

Development of an *Ex Vivo* Model Based on Freshly Excised Porcine Whole Eyes

Data discussed in this chapter were partially presented at the "2022 European Association for Vision and Eye Research *Festival", 13-15 October 2022, Valencia (Spain) as:*

González-Fernández, F.M.; Cauzzi, D.A.; Nicoli, S.; Gasco, P.; Pescina, S. Development of 3D-printed devices for the study of transscleral drug delivery on freshly excised whole porcine eyes. *Acta Ophthalmol* 2022*, 100*, https://doi.org/10.1111/j.1755-3768.2022.15545.

4.1. Introduction

4.1.1. State of the art of ocular of *ex vivo* ocular models

***Ex vivo* models** (sometimes still referred as *in vitro*, being the term *ex vivo* misunderstood and considered synonym of *in vitro*) are recognized as robust tools for permeability assays when evaluating formulations intended for topical administration (*i.e.*, isolated skin [260]). The *ex vivo* studies allow Researchers to collect valuable information about the excipient roles in drug release and distribution within tissues, highlighting the barrier effect exerted by biological membranes [219,261,262]. In contrast to *in vitro* assays, where a highly controlled environment like a culture dish is created, the *ex vivo* setups maintain the physiological properties of the tissue at least for a certain time. This allows to obtain crucial information about the barrier effect exerted by the biological membrane against drug diffusion. *Ex vivo* samples are, in principle, easy to isolate and manipulate; the integrity of the membranes is

macroscopically observable and simply assessable and usually no oxygenation or specific supplementation is required.

In the field of ophthalmic drug delivery, *ex vivo* models consist mainly of **isolated ocular tissues**, such as cornea or sclera, from different animal sources (porcine, bovine, ovine or leporine) [263]. The setup conventionally used for permeation and accumulation experiments is the Franz-type diffusion cell [264]. Effective implementation of the 3Rs (Replacement, Reduction and Refinement) in animal experimentation, requires the development and validation of standardized *ex vivo* models that at preclinical level allow to collect robust data from pre-formulative and formulative studies, in view of reducing the ultimately required *in vivo* experiments [265,266]. Over the past years, several *ex vivo* ophthalmic models have been proposed in the literature for isolated tissues such as cornea [267,268] or vitreous body [269,270], amongst others. Few examples of *ex vivo* setups involving **whole ocular bulbs** are available. Artificial perfusion of the enucleated eye for the study of drug distribution within ocular tissues has been studied [81,271], while early attempts on developing a simple *ex vivo* setup involving whole porcine eyes have also been recently reported [272].

4.1.2. Porcine *ex vivo* tissues: differences and similarities to the human eye

Porcine (*Sus scrofa domestica*) ocular anatomy and histology are similar to the human eye in several aspects which mostly justify their superiority as *ex vivo* ocular model and the differences observed with human eyes are of minor importance for the requirements of permeation and accumulation of drugs, as is the focus of this thesis.

The ocular globe is very similar in dimensions with a nasal-temporal diameter of 25.4 mm pig *vs* 24.2 mm human; superior-inferior axis of 24.4 mm pig *vs* 23.7 mm human and almost identical antero-posterior axis length (23.9 mm pig *vs* 24.0 human) which confers an almost spherical shape to human eye, while porcine eye appears as a prolate spheroid [273-275].

In the anterior segment, the porcine cornea is larger in terms of corneal radius and its thickness almost doubles the human one while Bowman's layer cannot be easily identified. Further small differences can be observed in the lens and ciliary body dimensions [276,277].

The insertion points where the ocular vasculature enters or exists the ocular bulb can be used as reference point for manipulating the eye (Figure 31).

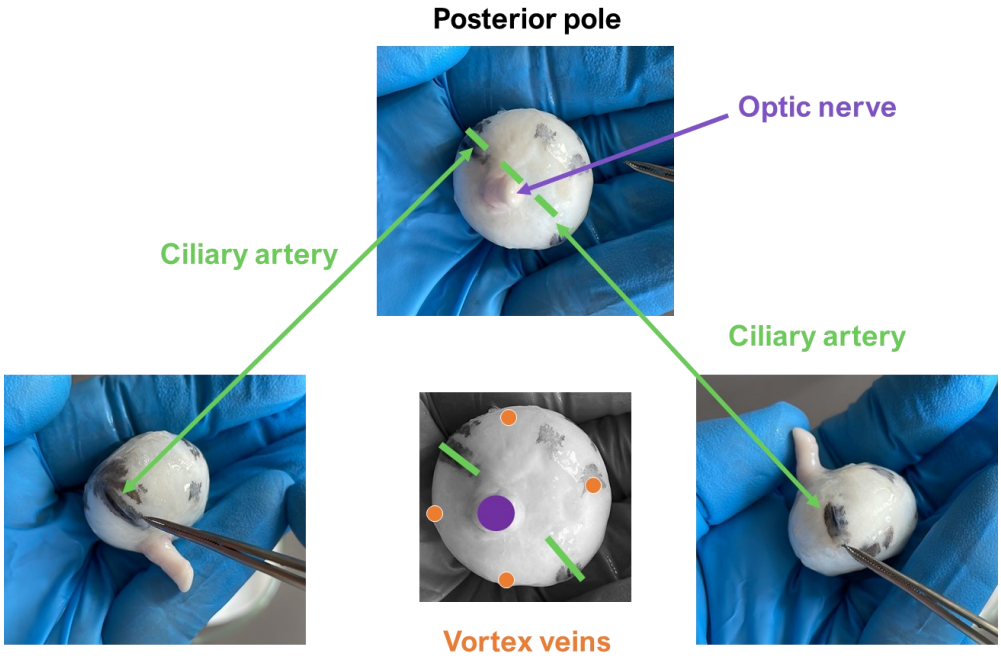

Figure 31**.** Schematic representation of the ocular vascular system of the porcine eye, which can serve as reference points.

The ciliary arteries can be observed on both temporal and nasal sides at the equator level and arriving from the posterior segment, virtually dividing the eye into a superior and an inferior half. Four exits of the vortex veins, one on each quadrant of the bulb, are observable near the equator [278,279].

Scleral thickness is approximately double when compared to human, which in some cases has demonstrated to be threefold more permeable [87,280]. Almost 70% of its content is water, so the scleral surface is sensible to evaporation and special measures must be taken in consideration for its manipulation in the laboratory (see Section 4.3.3.). The remaining 30% are mostly collagen fibres, which appear in more disorganized and thicker bundles in the porcine eye, with some sparse fibrocytes. In addition, porcine sclera differs from human one for the presence of a variable pigmentation ascribable to melanin deposits, completely lacking in human specimens [281]. On the contrary, the presence of melanin within choroid (uveal melanocytes) is a common element for both porcine [83] and human eyes [282]. Melanin is a ubiquitous pigment showing high affinity towards several active ingredients, especially the lipophilic ones, and therefore its role in hindering the drug diffusion can be not negligible [83]. The vitreous body also appears similar in composition and total volume [283].

In the case of the human eye, the retina follows an euangiotic pattern since blood supply arrives from a central retinal artery, while on the porcine eye, the pattern is

holangiotic since they derive from the ciliary arteries. In the human eye, the visual acuity is located in a cone-rich (photoreceptors) area, the fovea, centrally positioned in the circular macula lutea, while on porcine eye it has an elongated form, known as *area centralis* [284,285]. Cellular nature and arrangement are similar to humans and the absence of *tapetum lucidum* further contribute to consolidate its use as ocular model [88].

The porcine eye can retract inside the cranium, due to the presence of a muscle (*retractor bulbi*), which also activates the third eyelid or nictitating membrane, which are not present in the human eye [286]. These differences do not interfere in our case for *ex vivo* studies since they are enucleated.

It is important to underline that the eyeball dimensions or the level of scleral pigmentation vary between breeds, age, sex, and overall size of the animals, which also help to bring the natural variability that would be encountered in human population to a simple *ex vivo* laboratory setup. On the other hand, poorly reproducible results can be obtained sometimes due to this high variability.

Owing to the high similarity, porcine eyes have been successfully used for the evaluation of contact lenses, drug solutions and multiple nanocarrier systems [219,287,288].

4.1.3. Additive manufacturing in pharmaceutical sciences: 3D printing

3D printing is nowadays considered an “umbrella term” for a wide collection of techniques of additive manufacturing. The common nexus is the basis of creating a digital three-dimensional object in a computer aided design (CAD) software, which is then “sliced” in multiple layers which are sequentially printed layer-by-layer creating a physical three-dimensional object. A vast number of 3D printing approaches are currently available in the literature, but in this Section only the techniques of interest for the present thesis will be introduced [289,290].

Material extrusion 3D printing is the simplest and widely used approach. In this category **fused deposition modelling (FDM)** is the simplest example. A solid filament is warmed and then extruded from a nozzle onto a plate, rendering layer by layer the three-dimensional physical object. This technique allows to create hollow structures, with unexpensive materials (*i.e.*, polylactic acid filament, PLA) that on the other hand must be thermoresistant. The 3D printed object has a low definition and, without any post-processing, air- or watertightness cannot be guaranteed since small spacing between layers can be present. Gels or pastes can also be extruded (semi-solid

extrusion) and, in some cases, direct powder extrusion (no filament required) has been reported [291,292].

The second group are the laser-based techniques, which benefit from a high definition and precision of the 3D printed object but require post-processing to eliminate unused excess material. The laser beam can be accurately directed onto a powder bed and the incident beam causes the material to solidify at precise points, creating the layers of the physical object. This technique is called **selective laser sintering (SLS)** and the powder bed typically contains polyamide-12 (also known as nylon) or a mixture of excipient-drug which must withstand the high localized temperatures of the laser. Instead of a powder bed, the material can be a liquid resin that photopolymerizes. The selective photopolymerization can occur by means of a precise moving laser beam (**stereolithography or SLA**), or by projecting single images of a whole layer at once, as is the case of **Digital Light Processing (DLP)** and **masked stereolithography (MSLA).** In DLP, a single-layer digital image is displayed using a projector and only the light of each pixel (called *voxel*) causes resin solidification at that small region while in MSLA the layer images are produced by a LED array that selectively turns on or off at specific wavelengths that photopolymerize each required voxel [293].

The versatility of approaches and materials has translated into an increasing literature of application of 3D printing in the field of ophthalmology and ocular drug delivery [294,295].

Punctal plugs are non-invasive devices inserted in the ocular tear ducts, reducing lacrimal drainage, and thus intended for the treatment of dry eye disease. Xu and colleagues developed dexamethasone-loaded punctal plugs for dry eye disease using a DLP printer. The resulting device was accurately printed, although having only 1 mm diameter, and a sustained dexamethasone release for up to 21 days was achieved when the plug was composed of the biocompatible polyethylene glycol diacrylate [296]. Ophthalmologic patches to be produced in an hospital pharmacy have also been developed by semi-solid extrusion of hydrogels containing hydroxypropyl methylcellulose, mannitol or xylitol and different drugs. Optimization of the ink composition allowed to obtain multiple shapes and patterns with controlled dosing by changing the infill and-or thickness of the patches [297]. Poly(2-hydroxyethyl methacrylate) contact lenses have been recently 3D printed (MSLA) containing various wavelength filtering dyes for colour blindness management. The lenses demonstrated adequate optical and mechanical properties and, when tested by patients, their ability to discriminate colours was improved [298]. 3D printing of contact lenses requires adequate smoothness and superb optical characteristics, which are currently still

under refinement [299]. The fine-tuning possibilities of 3D printing also has allowed to create personalized ocular prosthetics based on a computed tomography-scans of ocular sockets [300-302] or for ophthalmic surgery training purposes [303].

The applications of 3D printing in preclinical research have also been steadily increasing over the past years [304-307]. Chang and colleagues recently developed a simple lab setup to analyses protein adsorption and resorption from ocular contact lenses by creating a posterior eye model with SLA technology which allows to dynamically characterizes protein interaction with two commercially available daily contact lenses [308]. Dixon and colleagues developed two FDM printed devices, that attached either to commercial ocular drops bottles or quartz cuvettes allowing to quantify the oxygen permeability of contact lenses, using cysteamine as an indicator of oxidation. The obtained values with this 3D printed setup demonstrated to be comparable to the ones reported by manufactures for the commercially available contact lenses [309]. FDM has also been used to manufacture an ocular model which simulates the physiological blinking mechanism to evaluate drug release from soft contact lenses [310]. The model was further improved and printed with SLA technology for ensuring watertightness [311]. A novel *in vitro* dissolution model, the Eye Flow Cell, for drug release characterisation of intravitreal implants has also been reported. In combination with a simulated vitreous, composed of agarose (shell) and polyacrylamide (core), the release conditions allowed for a better mimicking of physiological conditions with more accurate results when compared to standard USP apparatuses used for drug release studies [312].

Bioinks containing extracellular matrix components (like collagen) and cells have led to the development of the so-called bioprinting [313]. Corneal stromal substitutes for clinical applications have been developed by FDM printing a bioink composed of sodium alginate, methacrylated type I collagen and corneal keratocytes. Good cell viability was observed still after 1 week and the ability to resemble the corneal anatomy is believed to positively influence cell migration and collagen alignment in further studies [314]. ARPE-19 or porcine RPE cells have also been bioprinted on simulated Bruch's membranes creating viable retinal constructs for research [315,316].

In the present Chapter, a new *ex vivo* whole porcine eye setup is developed and validated for permeation and retention experiments across the trans-scleral pathway. The 3D printing approach is followed in order to obtain a robust setup that a) allows to maintain a liquid and /or semisolid formulation at a defined application point up to 24 hours and b) maintain the ocular bulb at a constant position, and hydration and temperature values.

4.2. Materials and Methods

4.2.1. Materials

Saline solution (composition: 9 g/L NaCl) and phosphate buffered saline (PBS; composition: 0.19 g/L KH_2PO_4, 2.37 g/L Na_2HPO_4, 8.8 g/L NaCl; pH 7.4 by adding 85% H_3PO_4) were prepared using ultra-pure water (Arium® Comfort Sartorius, Goettingen, Germany).

4.2.2. 3D modelling, photogrammetry, and 3D printing specifications

Photogrammetry of the frozen porcine eye was created with the help of Autodesk® Recap Photo (Autodesk® Inc, California, USA).

3D modelling of the eye and all prototypes was performed with the help of the free CAD software Autodesk® Tinkercad and Fusion 360 (Autodesk® Inc, California, USA). The 3D meshes were adjusted and repaired, when required, with the opensource packages MeshLab and Autodesk Meshmixer. High quality renderings for imaging purposes of the 3D models were produced with Autodesk® Fusion 360.

The Ocudonor v2 device was printed on a 3DPR Coobot FDM 3D printer equipped with Polylactic acid (PLA) filament and 0.4 mm diameter nozzle, in collaboration with FabLab Parma (Parma, Italy), part of the worldwide network Fab Charter.

The Ocudonor v3 device was externally produced in a local plastic materials handler (Arteplast Lavorazione Materie Plastiche S.r.l., Parma, Italy) using a selective laser sintering (SLS) printer with grey polyamide 12 powder (no more technical specifications available).

The Ocudonor v4 prototypes were printed on an Elegoo Mars UV Photocuring LCD MSLA printer (Elegoo, Shenzen, China) with eSun Hard-Tough blue resin (Shenzhen Esun Industrial Co., Ltd, Shenzen, China) and Elegoo ABS-like grey Photopolymeric rapid resin (405 nm). Pre-processing and slicing of the 3D models were achieved with the freely available Chitubox® (Guangdong, China) slicing software. Printing settings were adjusted according to manufacturer specifications for each resin.

Printed objects were washed with isopropanol in a sonicating bath for at least one minute and at least two times before being dried cured under UV light (340-395 nm). The Ocutainer was printed on the same MSLA printer with and Elegoo ABS-like transparent Photopolymeric rapid resin (405 nm) and coated with an epoxy resin (SigWong Epoxy Resin Clear Crystal Coating Kit, Sigwong®, China)

4.2.3. Porcine eyes

Porcine ocular bulbs (*Sus scrofa domestica*) were obtained from a local slaughterhouse (Macello Annoni S.p.a., Busseto, Italy), transported under refrigeration in saline solution and manipulated within 4 h upon arrival. Ocular adnexa were carefully removed with surgical Mayo scissors. Eyes were considered “fresh” and consequently suitable for experiments until 7 days from harvesting. The storing until 7 days occurred at +4 °C, in humid chamber. Before storing in the refrigerator eyes were soaked in 0.2% w/v amikacin solution for 10 seconds to clean the surface. To remove possible amikacin residues, eyes were carefully soaked in saline solution just before the experiments. Referring to “frozen eyes” means eyes that have been preserved at -20°C at least for 24 hours.

4.3. Results and Discussion

4.3.1. Investigations on porcine ocular anatomy

Ocular bulbs from *Sus scrofa domestica* are dimensionally and anatomically similar to human eyes as previously described in Section 4.1.2. The main differences observed are in their less-rounded-shape, creating an oblate spheroid with an equatorial radius is greater than the polar radius.

Measurements were obtained from previously published literature [275,317] which were also confirmed by random measurements on available frozen eyes. A three-dimensional and idealized model of the swine bulb spheroid (Figure 32a) was created for the design of the whole-eye *ex vivo* setup with the following measures: nasal-temporal axis 24.6 mm; superior-inferior axis 22.8 mm and anteroposterior axial length of 21.2 mm.

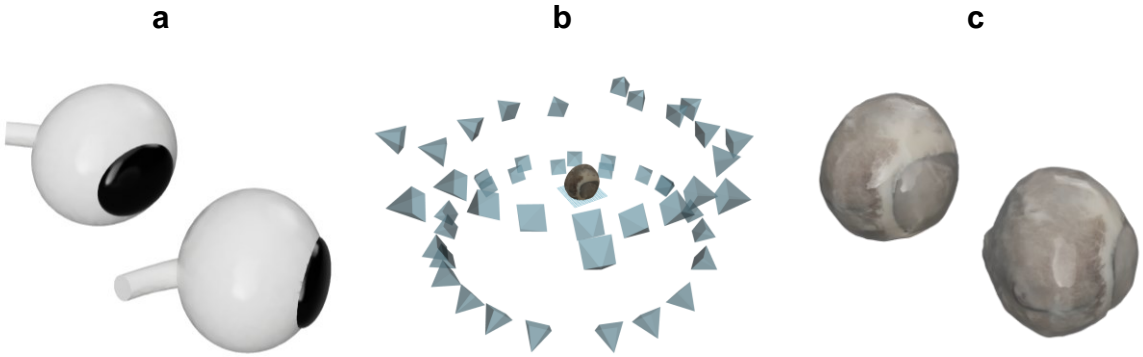

Figure 32. (a) Three-dimensional rendering of an idealized porcine ocular bulb obtained by mean values of measurements available in the literature, (b) representation of the camera positions used in the photogrammetry process of a porcine eye and (c) 3D rendering of a frozen swine eye obtained by photogrammetry.

Photogrammetry is a technique that allows to create three-dimensional objects from multiple bidimensional pictures taken at different position around the object of interest [318]. For this purpose, a frozen swine ocular bulb was mounted on a syringe needle and a total of 47 pictures were taken as depicted in Figure 32b. The images were loaded into the Autodesk Recap Photo software which rendered the three-dimensional object depicted in Figure 32c.

4.3.2. A formulation applicator for porcine eyes: the Ocudonor device

The **Ocudonor device** was developed with the aim to obtain a tailor-made device, with a defined permeation area, to be placed onto the whole-eye and allowing for the contact between formulation and scleral surface throughout the whole time of the experiment, mimicking a periocular administration. The permeation area, circular in shape, corresponds to 0.6 cm^2, the same value for the Franz-cells commonly used for trans-scleral studies. The device is intended to be applied to the equatorial region since sclera thickness varies from the anterior to the posterior region (that is, posterior > limbal > equatorial), and thus the diffusion pathway could vary [280]. The Ocudonor allows for the evaluation of both liquid and semisolid formulations that otherwise would quickly spread onto the ocular spheroidal surface; in addition, also solid formulations can be used.

The major challenge for this task was to achieve a good water-tight adhesion onto the scleral surface with little damage to the tissue. Hessburg-Barron corneal trephines are surgical instrumentation commonly used in corneal transplantation procedures [319]. The device firmly attaches around the cornea thanks to an annular vacuum chamber in which a small negative pressure is applied with the help of a syringe. A similar vacuum annulus is commercially available as medical device for corneal delivery of riboflavin by iontophoresis for the treatment of keratoconus in both human (Iontofor-CXL®, Fidia Farmaceutici S.p.A., Italy) and animals (Iontoforvet®, OPIA Technologies S.A.S., France). This minimally invasive principle of a vacuum annulus was adopted also for the design of the Ocudonor device.

Several prototypes were 3D-modelled and multiple manufacturing techniques were investigated prior to arriving to the final design, as it will be explained in the following Sections.

4.3.2.1. Ocudonor v1: the Poly(methyl methacrylate) Prototype

Our initial prototype did not consider the 3D-printing approach but rather the externalized manufacturing of a Poly(methyl methacrylate) or PMMA device. PMMA is a thermoplastic polymer with low toxicity and sufficiently rigid and durable [320]. The device was designed focusing on simple figures (such as, cylinders, circles) that would

ease the production, and the projections were submitted to the manufacturer (Figure 33).

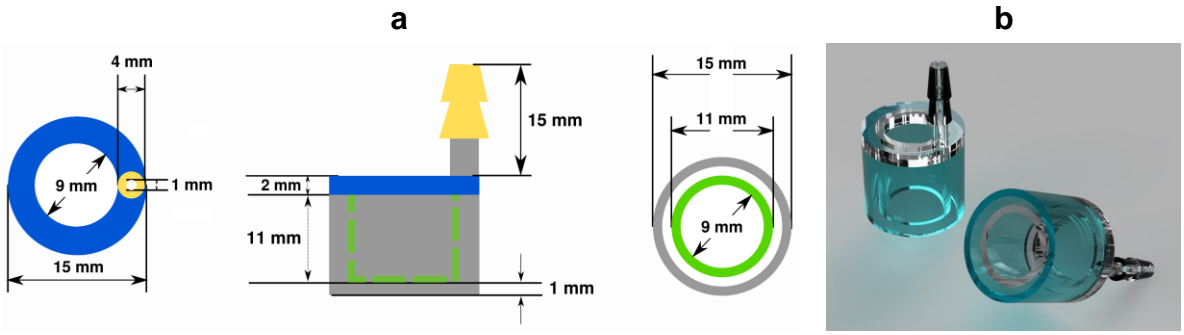

Figure 33. (a) Graphical projections, with measurements, of the first version of the Ocudonor device intended to be manufactured in Poly(methyl methacrylate) and (b) 3D rendering of the prototype which was not produced due to the inability to obtain such small sizes by the manufacturer.

This device was not further investigated since the manufacturer could not guarantee good definition and precision in the production of wall thicknesses of 1 mm.

4.3.2.2. Ocudonor v2: the FDM Prototype

The second prototype was the first approach to 3D-printing, and thus the design could be more intricate to better adapt to the scleral curvature. The device acquired an oval shape that might adapt better to the equator of the spheroid while maintain a defined permeation area (Figure 34).

Figure 34. 3D rendering at different positions of the second version of the Ocudonor device (a) which was printed using the FDM technique in PLA filament (b).

The cylinder ending was not flat, but adjusted to a parabolic surface and the edges were bevelled for adhesion improvement. The tubing exit was now placed on a 45-degree angle for more stability, reducing a possible leverage effect. The main goal nonetheless remained to establish if wall thicknesses of 1 mm could be achieved with good precision with the 3D-printing approach. The design was 3D printed in collaboration with FabLab Parma, part of the worldwide network Fab Charter. The printing resolution of the product remained low due to the high diameter of the extrude (Figure 34b). In addition, without any postprocessing, the device was not airtight and

would not attach to the ocular bulb. It allowed nonetheless to confirm that the 3D printing approach was adequate for our purposes.

4.3.2.3. Ocudonor v3: the SLS Prototype

The prototype presented in Figure 34 was subject to modifications. The permeation area was modified from an oval shape to a circular shape of 9 mm diameter (0.6 cm^2), similarly to the Franz diffusion vertical cells commonly used for trans-scleral diffusion (see 5.2.7.). The prototype was externally printed in polyamide 12 (Nylon 12) using a SLS system which can print 1 mm thicknesses with high resolution. The results are presented in Figure 35.

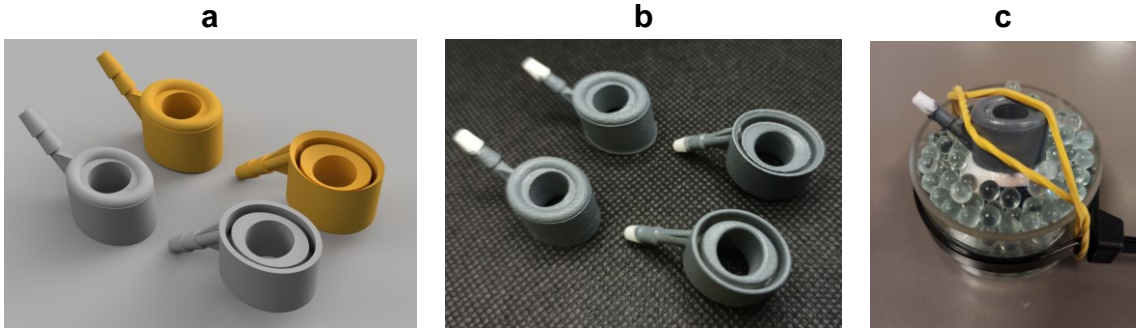

Figure 35. (a) 3D renderings of the third version of the Ocudonor device with a circular permeation area and flat adhesion surface (grey) or curved adhesion surface (yellow) that were printed using the SLS technique in nylon 12 and spray coated (b) but still could not adhere adequately to the ocular surface (c).

Two designs were printed: the first one, in grey (Figure 35a) had a flat ending while the yellow prototype was adapted to the natural curvature of the porcine eye. The high resolution of the prints is appreciable in Figure 35b. Unfortunately, several drawbacks were still encountered at this stage. Despite the high accuracy of the SLS printing technique, the prints are highly porous, and Nylon 12 is a highly adsorbent material (hence its use as textile fibre that greatly absorbs dyes) [321]. In fact, the devices appear grey in Figure 35b because they have been spray-coated with an acrylic spray paint in an attempt of rendering them water- and air-tight. In addition, the production was externalized, which hindered quick adjustments of the prototypes, delivery times were of two weeks, and each printed piece had a considerable cost. The overall setup on a whole porcine eye (Figure 35c) also failed despite the coating, but this could be explained due to the high thickness of the wall between the vacuum chamber and the permeation area.

4.3.2.4. Ocudonor v4: the MSLA Prototypes

The fourth **final version of the Ocudonor** device was designed and printed using an in-house MSLA 3D printer. The low-cost, versatility and high precision of the Elegoo

Mars MSLA printer boosted the creative process by allowing to quickly print multiple prototypes in less than one hour at a low cost. The high definition is reached thanks to a pixel-by-pixel definition or as previously explained, voxel-by-voxel.

A complete redesign of the Ocudonor device occurred at this stage and the prototypes were produced focusing mainly on four challenges: increasing stability of the device once positioned on the ocular surface, maximizing the adhesion to the ocular surface, and minimizing the required post-printing process. The oval shape was dismissed to better adapt to the preferred circular permeation area and the contact area between eye and device was reduced to the lowest to avoid the non-adhesion observed in Ocudonor v3.

To improve stability of the Ocudonor device once positioned over the eye and avoid the leverage effect due to the weight of the silicone tubing that connects to the vacuum syringe, the exit arm for the tubing was studied at both 90º and 45º angle (Figure 36).

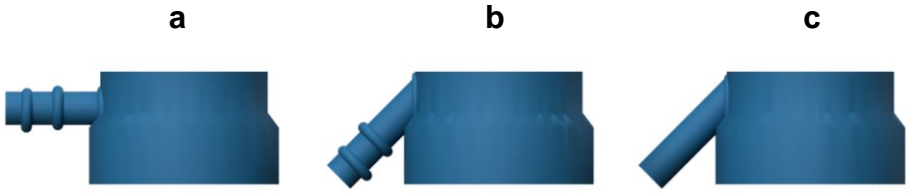

Figure 36. Modifications evaluated to improve stability onto the eye and tubing grip to the device.

In addition, the possibility of adding two rings for improving tubing grip to the device was contemplated, but soon discarded since good grip was obtained without this requirement. The configuration depicted in Figure 36c was therefore selected.

The inner ring that delimits the permeation area was also subject to improvement (Figure 37).

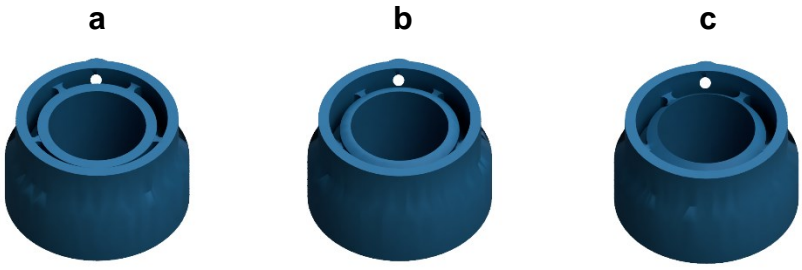

Figure 37. Modifications evaluated to improve adhesion and bevelling of the inner ring in the Ocudonor device.

The vertices were bevelled at three levels from none to a sharp bevel with an intermediate level. A lack of bevel difficulted the grip while a too-sharp bevel risked

damaging the sclera. The best grip, with minimal tissue damage could be obtained with an intermediate, rounded bevelling (Figure 37b).

A critical optimization was regarding the bevel of the outer ring of the vacuum chamber. The contact (shape) of a right angle in the bevel with the tissue would intuitively perform poorly over time (Figure 38a).

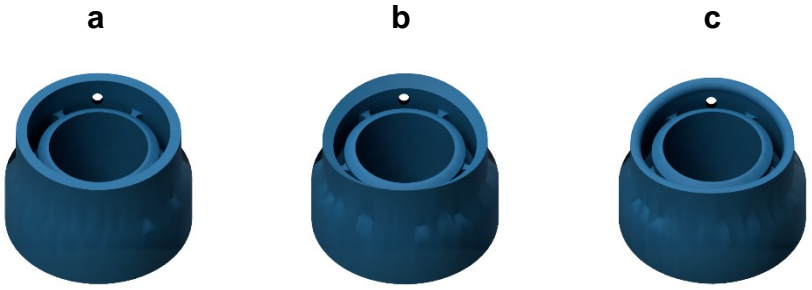

Figure 38. Modifications evaluated to improve adhesion and bevelling of the outer ring in the Ocudonor device.

Therefore, it was rounded and twisted following the natural curvature of the idealized eyeball spheroid depicted in Figure 32 (Figure 38b). This resulted in a sharp bevel, which was rounded up, which delivered the prototype in Figure 38c.

Lastly, since MSLA usually requires printing supports and also an easy detachment from the printing plate, other modifications were considered (Figure 39).

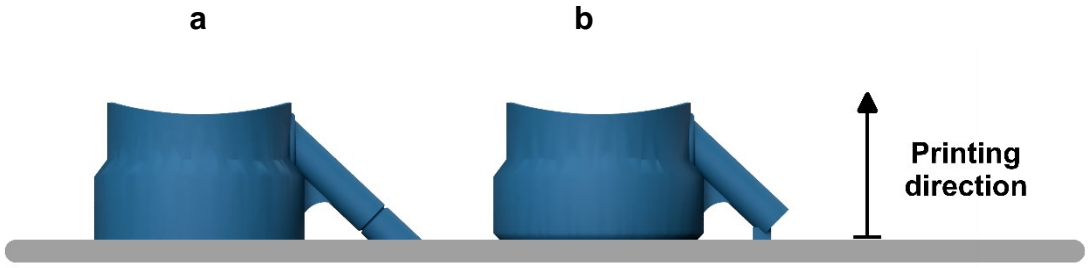

Figure 39. Modifications evaluated for a simpler post-printing processing. In (a) the vacuum arm is prolonged, and the added circular crevice indicates where the excess arm can be cut while in (b) a simple cube that can easily be cut supports the 45º vacuum arm.

The prolongation of the arm with an incision for cutting was found to perform worse than a simple cube that is enough as support for printing the rest of the arm. By printing the design from downwards to upwards, as indicated by the arrow, enough support is ensured and no angles over 30º were reached, in fact the prints did not fail. A bevel for better insertion of the scraper was also added around the outer cylinder.

The final Ocudonor included the best configurations investigated in the prototyping phase. The vacuum arm is positioned at a 45º angle without the double ring. The inner cylinder presents an intermediate bevel that does not damage the sclera while the outer cylinder follows the natural curvature of the eyeball, and the bevel is rounded for better grip and no tissue damage (Figure 40).

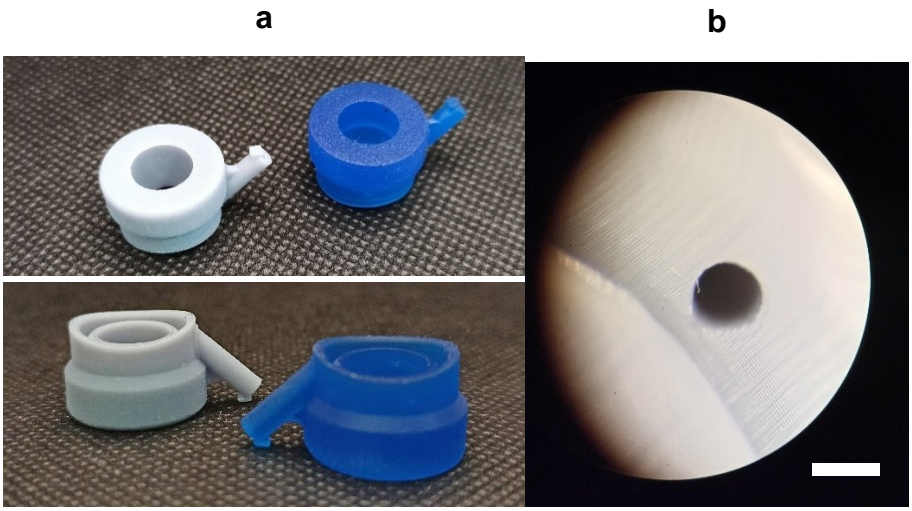

Figure 40. The final prototype for the Ocudonor device (a) and a photo micrograph of the inner tubing (b). The white scale bar represents 1 mm.

The Ocudonor is printed without any extra supports, apart from a small cube that supports the arm which can be easily cut afterwards. The devices are printed in less than one hour and each batch can contain up to 15 devices. A high definition is achieved due to the MSLA 3D printing technique, as observed in Figure 40b.

4.3.3. A container for whole ocular bulbs: the Ocutainer device

The second major challenge to overcome when designing a whole-eye *ex vivo* setup is holding the eye in a given position, while preserving tissue hydration and maintaining constant temperature throughout the whole experiment. With this aim, a first attempt was done using commercially available 6-well polystyrene plates (Corning, Corning, NY, USA). The eye with Ocudonor was placed inside a well and, to avoid free movement, glass beads having a diameter between 2 and 5 mm, were placed around. Plates were then supported by expanded polystyrene (EPS) frames to float inside the water bath set at 37°C and covered with plastic film to prevent dehydration (Figure 41a).

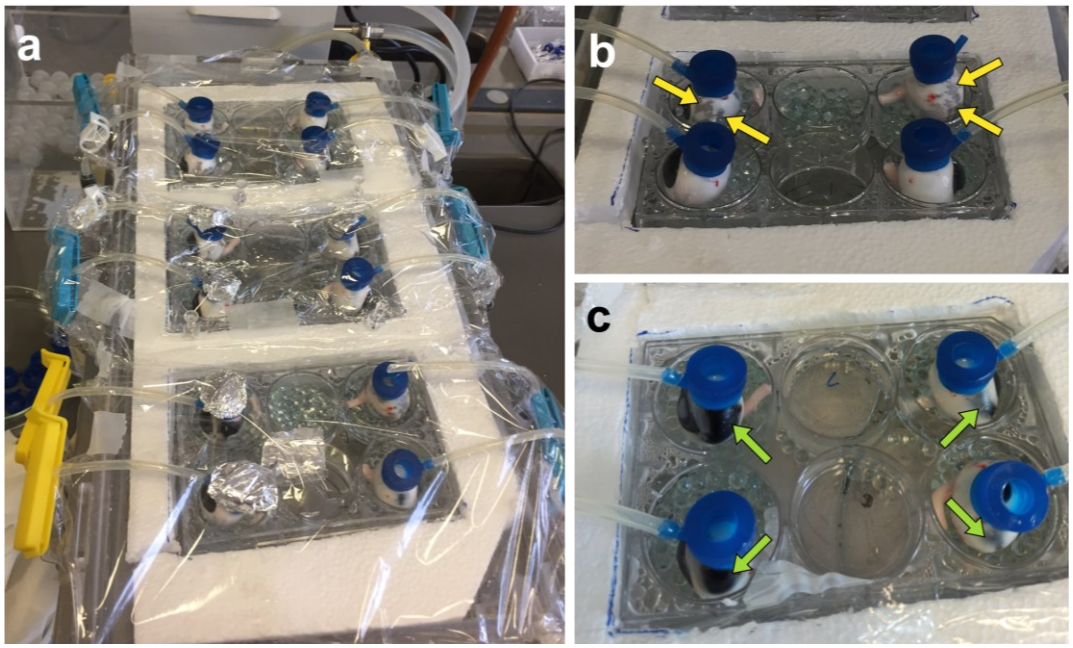

Figure 41. (a) 6-well polystyrene plates floating in water bath (37°C) containing porcine eyes with the Ocudonor device (blue) applied. Glass beads were put around the ocular bulbs to limit free movement. Plastic wrap film was used to prevent tissue dehydration. In panel b) one plate at the beginning of the experiment and in panel c) after 6 hours: yellow arrows in panel (b) indicate the natural pigmentation of the porcine sclera due to the presence of melanin, while green arrows in (c) show the exposure of pigmented choroid as consequence of scleral dehydration.

The presence of dry glass beads did not prevent dehydration, which occurred after few hours: in fact, eyes appeared black, since the loss of water from the sclera has exposed the underlying pigmented choroid (Figures 41b and 41c). In a second attempt, a 20% w/w poloxamer P407 solution in 0.9% NaCl was used. Cold poloxamer solution was poured around the eye and gelation occurred at 37°C so that the portion of the eye inside the well remained embedded in the gel. Unfortunately, even in this case, dehydration was not prevented (Figure 42).

Figure 42. Bulb eyes embedded in a 20% w/w solution of poloxamer 407.

A third attempt was followed by adding ~1 mL of phosphate buffered saline (pH 7.4) to each well containing glass beads. After a few hours, the ocular bulbs appeared macroscopically unchanged, but the setup did not guarantee reproducibility since the leverage effect of the Ocudonor tubing caused the eyes to turn within the glass beads. As a result, some Ocudonors had also detached from the scleral surface.

The lack of robustness with the 6-well plates setup led to the development of a second 3D-printed device: the **Ocutainer**. Each container was designed to have 3 cavities or wells, to easily produce data by triplicates. The initial prototype for each well is depicted in Figure 43a from which several modifications were added until the final design presented in Figure 43b was achieved.

Figure 43. Cross-section of the initial prototype for the Ocutainer device (a) and the final device which includes an insert for the silicone tubing (b). The Ocutainer device ensures that the ocular bulb is maintained in an upright position and the Ocudonor does not detach throughout the whole experiment, hence the crevice in Figure 43a or the specific insert for the tubing in Figure 43b. In addition, the Ocutainer was designed to ensure adequate humidity and temperature rates.

The bottom of each well was initially round (Figure 43a) but in the process of eliminating most of the avoidable printing supports they were increased in thickness and included a flat bottom so it can serve as attachment point to the printer build plate. This final orientation also allowed to eliminate the small reinforcement ring present in the initial design around the top of each well.

The initial prototype of the Ocutainer did not contemplate the requirement of tubing inserts and the tubing would be only clamped in a lateral incision in the container (Figure 43a). This configuration quickly demonstrated to be impractical since the weight of the tubing and the syringe could release the tube from the incision and cause the Ocudonor to detach due to a leverage effect. Further optimization led to the creation of an insert which easily “clicks” on the eye container and firmly keeps the silicone tubing at a 45º angle, in correspondence to the vacuum arm of Ocudonor (Figure 44).

Figure 44. (a) A detailed view of the incisions presents in the lid that allow to accommodate the three inserts and (b) cross-section view of a well in the Ocutainer where the function of the insert for maintaining the Ocudonor in position while allowing free manipulation of the syringe is appreciable.

The syringe can freely be operated without any risk of detaching the Ocudonor during the experiment. The lid does include three lateral incisions to accommodate the inserts (Figure 44a). A cross section of the mounted setup is indicated in Figure 44b.

All the components can be printed in one single batch. Orientation of the device played an important role to avoid failing of the print and detachment from the build plate. Initially, the components were tilted to avoid printing failure and printing supports were therefore required (Figure 45a).

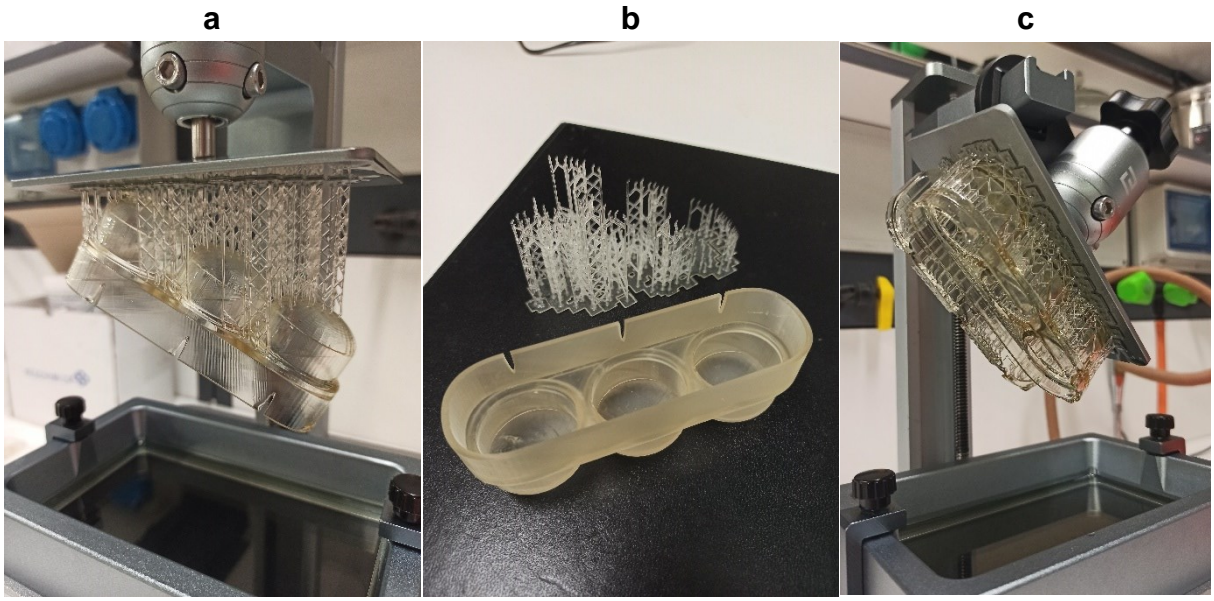

Figure 45. Images obtained right after 3D printing of (a) the initial prototype which required a considerable amount of printing supports (b) and (c) the final device which requires fewer supporting structures and printing time.

These supports are easily detached in the postprocessing step but increased the height of the whole stamp and thus, the required printing time (Figure 45b). Due to the thickening of the curved bottoms of the wells, the eye container could be printed directly onto the build plate. Shorter printing supports were maintained for printing the lid and the laterals of the eye container while the inserts required no supports (Figure45c).

The Ocutainer is intended to be placed in a water bath to maintain constant humidity and temperature rates. Although the MSLA print should be watertight, long exposure times to water could result in material alteration (*i.e.*, appearance of crevices) thus affecting the integrity of the device. Therefore, both the eye container and the lid were subjected to a coating with self-curing epoxy resin and the result is presented in Figure 46.

Figure 46. The final Ocutainer device, including the lid and the three tubing inserts after being coated with an epoxy resin for increased durability.

4.3.4. Ocudonor and Ocutainer whole-eye *ex vivo* setup

The developed Ocudonor and Ocutainer allow to perform trans-scleral permeation experiments on freshly excised whole porcine eyes. The bulbs are cleaned from ocular adnexa and slightly dried with filter paper. Up to three eyes are placed inside the Ocutainer, with the cornea facing the tubing insert so that the eye rests on its equator. The Ocudonor is then placed on the scleral region delimited by the two upper vortex veins (Figure 47a) with the vacuum arm towards the anterior ocular segment following the median plane.

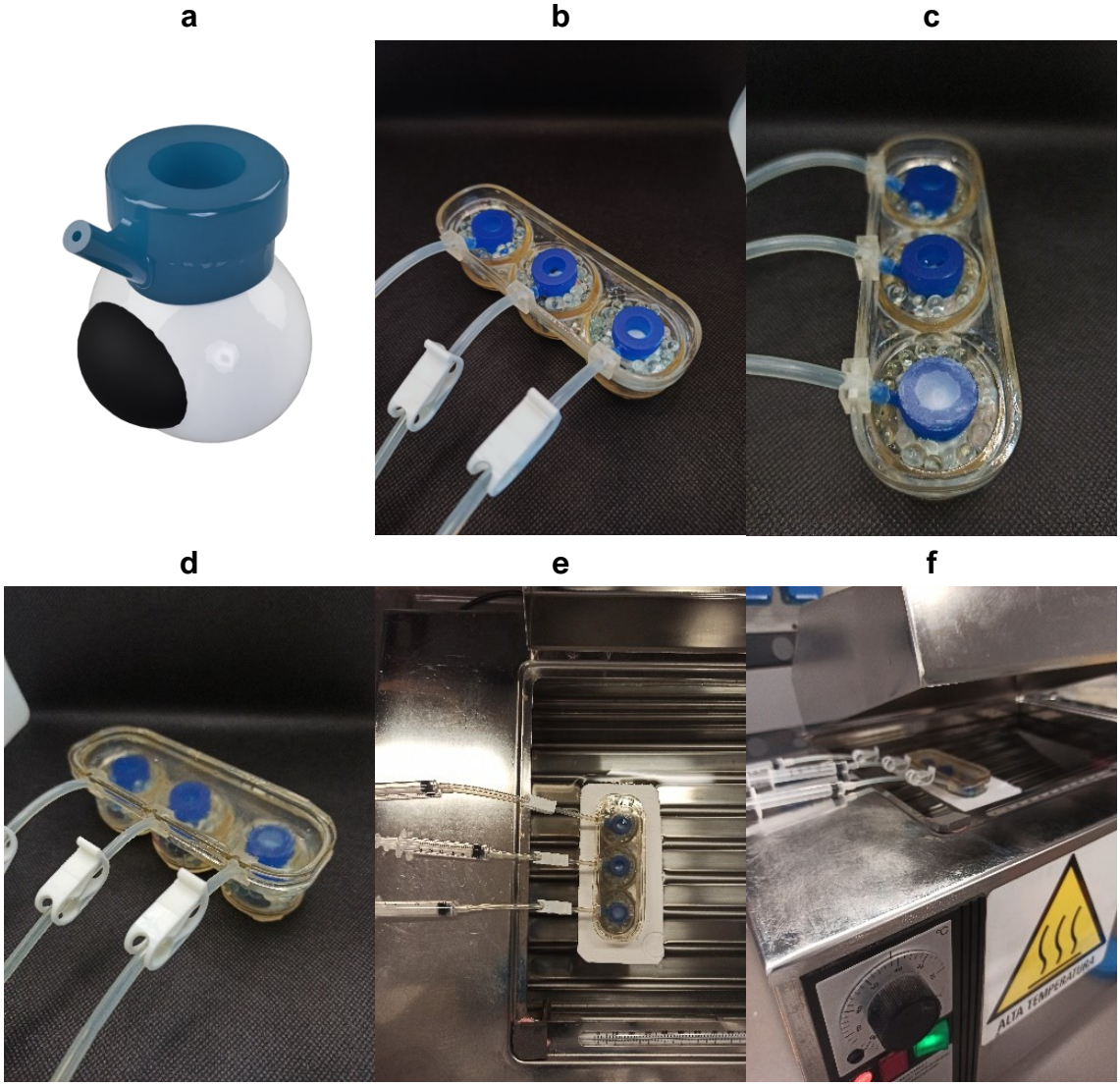

Figure 47. (a) Correct positioning of the Ocudonor onto the porcine sclera, between the two upper vortex veins and with the vacuum arm towards the corneal side; (b-e) steps required for performing a permeation experiment with the Ocudonor-Ocutainer setup.

The silicone tubing is securely fixed inside the insert and the syringe can be operated freely, also when the lid is positioned. Although the term “vacuum” has been used in the description, only a small negative pressure (corresponding to ~ 2.5 mL on a 5 mL syringe) is exerted and maintained through proper tube clamping. To avoid free movement of the eye once inside the well, glass beads having a diameter between 2 and 5 mm, are placed around and approximately 3 mL of phosphate buffered saline (pH 7.4) are added per each well to prevent dehydration (Figure 47b).

The drug formulation is pipetted into the donor compartment (usually 200 µL; up to 500 µL), and the compartment is sealed with parafilm with the help of a thin layer of silicone oil to increase adhesion (Figure 47c). The lid is placed (Figure 47d), and an expanded polystyrene (EPS) frame is set around to allow floatability in the water bath

(Figure 47e). The setup is maintained at 37 ºC in the closed water bath throughout the whole time of the experiment (6 or 18 hours) as showed in Figure 47f. Once the permeation is concluded, the setup is retrieved from the water bath, donor compartments are accurately emptied with a Pasteur pipette and dried with filter paper. The eye is lifted in combination with the still attached Ocudonor and placed on a filter paper inside a Petri dish. Releasing the vacuum clamp allows to detach the Ocudonor and exhibit the permeation area. Figure 48a was obtained when loading Ocudonor with a methylene blue solution (0.5 mg/mL, 200 µL) for 18 hours.

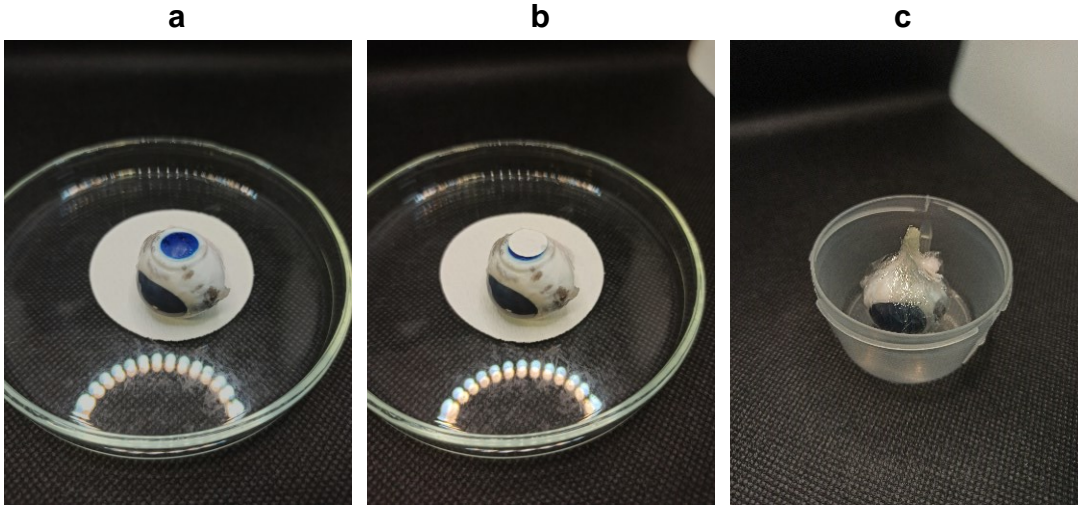

Figure 48. (a) Ocular bulb after an 18-hours permeation experiment with a methylene blue test solution, the permeation area is covered by a filter paper disk (b) and then protected with cling film (c) before preservation at -20 ºC.

The permeation area is covered with a 9 mm filter paper disk (Figure 48b) and the eye is covered with plastic wrap (Figure 48c) before being frozen with the permeation area downwards for at least 24 h at -20 ºC. This ensures an easier tissue retrieval and is also considered to stop any further diffusion of the drug [272].

Water content is a useful parameter for integrity evaluation when considering *ex vivo* tissues since both hydration and dehydration represent a major issue. To confirm the ocular bulbs were adequately hydrated throughout the experiment, six eyes were accurately weighted before and after 24 hours. The eyes appeared macroscopically unchanged, and their weight was 99.4 ± 0.4% with regard to the initial values, clearly indicating no water loss or gain.

Although hydration levels remained constant over a 24-hour period, degradation processes might be accelerated at 37°C. To slow down degradation processes, the present setup should be further optimized by the addition of preservatives, like chlorhexidine or benzalkonium chloride, to the PBS surrounding the glass beads. The addition of new substances must be checked for interferences in terms of barriers

preservation and drug quantification. A more careful evaluation should be done for the addition of antibiotics, not only for analytical interferences, but also for antibiotic resistance issue: therefore, the antibiotics supplementation should be subjected to a real need.

4.3.5. Eye dissection and tissue retrieval: S, Ch and Vitreous

As previously indicated, the eyes are preserved at -20 ºC for at least 24 hours before retrieving the tissues of interest for drug quantification. Still frozen, the eye is cut in two halves, following the horizontal plane at the equatorial line delimited by the ciliary arteries with the help of a pipe cutter. Two halves corresponding to a proximal and a distal hemisphere with respect to the permeation area are obtained (Figure 49).

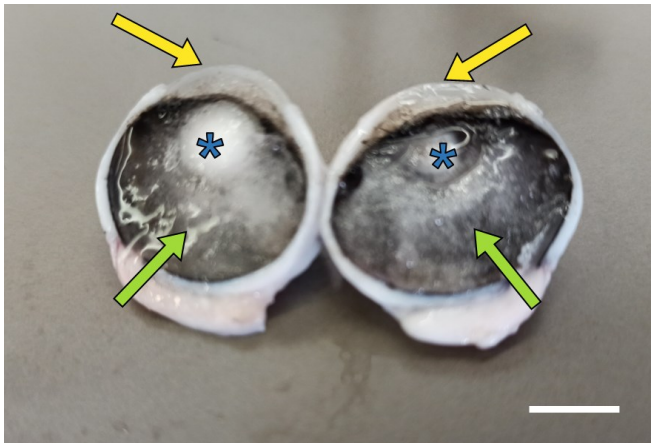

Figure 49. Frozen porcine eye cut into two halves using a pipe cutter. Yellow arrows indicate the cornea, green arrows show the vitreous body, while blue asterisks mark the lens. The white scale bar represents 1 cm.

In the proximal hemisphere, the frozen vitreous is easily lifted, but the thin and fragile retina remains attached and therefore both tissues are analysed together. The permeation area, indicated by the previously placed filter paper disk is punched with a 9 mm diameter punch. This section contains the proximal sclera which was in direct contact with the formulation to which also the choroid is firmly attached. The choroid can be easily peeled with the help of some tweezers from the scleral disk. In the distal hemisphere, the vitreous body and retina are retrieved in the same manner while choroid is removed and analysed entirely. The weight of each tissue is accurately noted.

4.3.6. Vitreous handling

The gel-like consistency of the vitreous body, due to hyaluronan and collagen presence in combination with a high water-content (*approx.* 98%), represents a limitation for tissue handling and consequently, for drug extraction. The gel is not

consistent enough to be manipulated as a semisolid material, while the aspiration with a micropipette is not feasible, since material is not homogeneous (*i.e.*, hyaloid membrane). On the contrary, the manipulation of frozen vitreous body, resembling an ice cube, is advantageous and allows to avoid drug cross contamination between tissues. Once the frozen eye is cut with the pipe cutter, vitreous body is easily retrieved from each ocular half: choroid remains firmly attached to the sclera, most of the retina is adhered to the vitreous body, while RPE can easily be removed with filter paper.

The initial step required for drug extraction is liquefaction of the vitreous body, and thus altering the gel-like consistency. Three different methodologies, based on physical and enzymatic approaches, were explored.

Initially, **cryomilling or cryogenic grinding** was considered. The eyes were firstly frozen at -20°C for at least 24 hours and then transferred into liquid nitrogen for 10 seconds. Vitreous samples, retrieved from the eyes, were manually pulverized inside a steel mortar using a stell pestle, as shown in Figure 50.

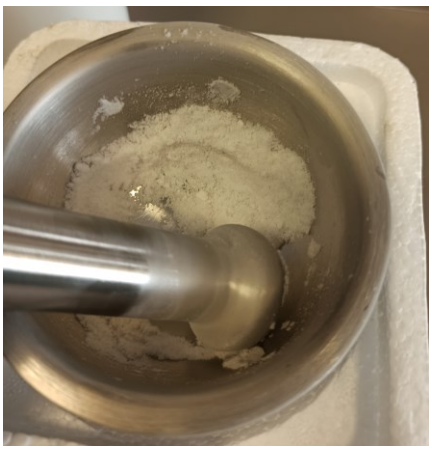

Figure 50. Stainless steel mortar (volume 250 ml; diameter 10 cm) in liquid nitrogen bath (expanded polystyrene box) containing grinded vitreous body, obtained by cryomilling.

To prevent thawing, the mortar was also surrounded by an expanded polystyrene box containing liquid nitrogen at the bottom. The method was not further investigated since it required too many steps and constant freezing. In addition, tissue sample was too small for the mortar size and material loss can occur.

The second and third attempt explored the **enzymatic** vitreolysis. Once thawed, 2 ml vitreous sample were transferred into an 8 mL polypropylene tube. 200 microliters of a 11,000 USP trypsin (Trypsin type I from bovine pancreas, activity 8,550 BAEE units/mg, corresponding to 2,850 USP units/mg; Sigma Aldrich, St. Louis, MO, USA) or 3,300 USP hyaluronidase (Hyaluronidase type II from sheep, activity 1,320 units/mg; Sigma Aldrich, St. Louis, MO, USA) were added to the sample. After a 2 h contact at

37°C, only a slight opacification was observed and the addition of acetonitrile (ratio 50:50) did not produce any collapse of the gel matrix which would otherwise precipitate. In the case of the trypsin, a prolonged contact time (overnight) did not produce better results.

The last attempt contemplated the use of **ultrasounds**. Approximately 2 ml of thawed vitreous were transferred into an 8 mL polypropylene tube. The sample was sonicated with an ultrasonic probe at a constant frequency of 30 kHz (Amplitude 100% (180 µm), Cycle 1; UP100H ultrasonic Processor, Hielscher ultrasonics, Teltow, Germany) for 1 minute. Aliquots of 0.35 mL of liquefied vitreous were withdrawn, transferred into an Eppendorf® tube, and 0.65 mL acetonitrile were added. Sample was vortexed several times during the 2-hours contact. The sample was then centrifuged at 12,000 rpm for 5 minutes and the supernatant appeared as a transparent, non-viscous liquid. Filtration of the 1 mL sample with small diameter (4 mm) regenerated cellulose syringe filters did not exert any noticeable resistance.

Chapter 5

Ex vivo Evaluation of Lipid-Based Nanocarriers

This chapter includes previously published material available as:

González-Fernández, F.M.; Delledonne, A.; Nicoli, S.; Gasco, P.; Padula, C.; Santi, P.; Sissa, C.; Pescina, S. Nanostructured Lipid Carriers for Enhanced Transscleral Delivery of Dexamethasone Acetate: Development, *Ex Vivo* Characterization and Multiphoton Microscopy Studies. *Pharmaceutics* 2023, *15*, 407. https://doi.org/10.3390/pharmaceutics15020407

5.1. Introduction

Classical **fluorescence microscopy** allows for visualization of fluorophores chemically bounded to biological targets which, by adequate excitation, emit a signal that is interpreted to reconstruct images of live or fixed tissues. The intensity of the recorded signal is directly proportional to the excitation energy applied to the fluorophore. This has been identified as a limitation for thick biological samples where in-depth images are hardly obtained at a high resolution due to interferences (such as scattering) despite increasing the intensity of the source (which, on the other hand, might photodamage the tissue) [322].

In the past years, the field of non-linear microscopy has been under development. In non-linear optics, the detected emission is not directly proportional with increasing excitation intensity. Under those circumstances, lower fluorophore concentrations and less-energetic excitation wavelengths allow to obtain better three-dimensional resolution with low photodamage risk. This phenomenon is exploited in **multiphoton microscopy (MPM)**, which is a non-invasive imaging technique for visualization of

fluorescent dyes within biological tissues, that has been recently proposed also in the field of formulations development [323].

The multiphoton microscope works by a non-linear optical process collecting diverse signals such as the two-photon excited fluorescence derived from fluorophores (TPEF) or more complex nonlinear signals inherent to the tissue, such as the second harmonic generation (SHG). TPEF is recorded as the light emitted by dyes excited *via* two-photon absorption (that is the simultaneous absorption of two photons, in contrast with a linear process, in which only one photon is absorbed). The SHG signal is observable only in locally non-centrosymmetric media such as myosin filaments or collagen fibres, thus providing 3D images of the unstained tissue, clearly distinguishable from the dye [324]. MPM is a technique with intrinsic 3D resolution, particularly suitable for the visualization of biological tissues due to its non-invasiveness, limited photodamage and the possibility to obtain in-depth images (up to 2 mm below the sample surface) [325]. MPM has been recently proposed for investigating the skin distribution of PLGA nanoparticles [326] and polymeric micelles [327] after topical application, as well for studying the fate of polymeric micelles in ocular tissues [41].

In this chapter the developed lipid-based formulations, *i.e.*, DexAc-NLC and Dex-NLC (3.2.), Dex-ieNLC (3.3.) and Dex microemulsion (3.4.), were evaluated using *ex vivo* ocular models. Particularly, permeation and retention across and within porcine sclera and choroid were studied by Franz-type cells, while drug distribution within posterior segment was investigated *via* the newly validated setup (Chapter 4).

In addition, the spectroscopic and the MPM techniques have been used for collecting additional information about the NLC behaviour in *ex vivo* conditions. For this purpose, NLC were loaded with Nile red (NR), a lipophilic fluorescent dye with solvatochromic properties (*i.e.*, its spectroscopic behaviour depends on the polarity of the surrounding environment). NLC loaded with the NR were spectroscopically characterized and their behaviour once in contact with porcine sclera was studied using MPM.

5.2. Materials and Methods

5.2.1. Materials

The materials previously described in Section 3.2.2.1. were used. In addition, Nile red (NR; IUPAC 9-(diethylamino)benzo[a]phenoxazin-5-one; MW 318.37 g/mol) was purchased from TCI Europe N.V. (Zwijndrecht, Belgium).

Saline solution (composition: 9 g/L NaCl) and phosphate buffered saline (PBS; composition: 0.19 g/L KH_2PO_4, 2.37 g/L Na_2HPO_4, 8.8 g/L NaCl; pH 7.4 by adding 85% H_3PO_4) were prepared using ultra-pure water (Arium® Comfort Sartorius, Goettingen, Germany). All other chemicals were of analytical grade.

5.2.2. Nile red-loaded NLC

Nile red-loaded NLC (NR-NLC) were produced following the aforementioned methodology (Section 3.2.2.6.), substituting pure triacetin with a 0.1 mg/mg or 0.5 mg/mg solution of NR in triacetin.

Unencapsulated NR was separated by size exclusion chromatography (PD-10 Desalting Columns, Sephadex™ G-25 M, Cytiva, UK). One millilitre of loaded NLC was eluted through the column by stepwise addition of 1 mL volumes of ultra-pure water. A total of eight fractions were collected. Fractions 4 and 5 appeared coloured to the naked eye and were then analysed by DLS for confirmation of NLC presence. Separation efficiency was further checked *via* fluorescence measurements, which provided also spectroscopic properties of fluorescent-NLC (5.2.3).

5.2.3. Spectroscopy studies

Both blank and NR-loaded NLC were spectroscopically characterized to investigate Nile red encapsulation. UV-Vis absorption spectra were acquired with a PerkinElmer Lambda650 spectrophotometer (PerkinElmer, Waltham, USA), while a FLS1000 Edinburgh fluorometer was used to perform fluorescence measurements in solution and aqueous suspension. Fluorescence spectra were collected on diluted samples, with absorbance lower than 0.1 (to avoid inner filter effects) and further corrected for the excitation intensity and detector sensitivity. Absorption spectra of the NLC aqueous suspensions were inevitably convoluted to the scattering signal, which dominated most of the absorption profile. Appropriate long-pass filters have been inserted in the emission path to collect fluorescence spectra of NLC suspensions, to minimize the scattering of the excitation light.

5.2.4. *Ex vivo* porcine ocular tissues

Swine ocular bulbs (*Sus scrofa domestica;* Landrace and Large White breeds, both female and male; 10–11 months of age; 145–190 kg) were obtained from a local abattoir (Macello Annoni S.p.a., Busseto, Italy) and transported under refrigeration in saline solution and manipulated within 4 h upon arrival. Ocular adnexa were carefully removed with surgical Mayo scissors. To obtain tissues for permeation and retention experiments in Franz-type diffusion cell (Section 5.2.7.) the ocular bulbs were opened by means of a perilimbal incision with a scalpel. Anterior ocular tissues, and vitreous body were removed. Retina and retinal pigmented epithelium (RPE) were thoroughly detached with the help of filter paper. The ocular bulb was halved following the line of the ciliary arteries and the half without optic nerve, consisting of sclera with attached choroid or plain sclera, was used. In contrast, intact ocular bulbs were used for drug distribution analysis on whole eyes, as described in Section 5.2.8, using the setup developed in Chapter 4.

5.2.5. Validation of an DexAc-Dex extraction method from porcine sclera and choroid

Circular sections (9 mm diameter) of fresh or thawed (previously stored at -20 °C) sclera and choroid were punched and accurately weighted in 1.5 mL Eppendorf® tubes. 2.5 mg/mL stock solutions of both DexAc and Dex in ethanol 90% (v/v) were prepared and 10 µL were carefully applied onto the isolated tissues, allowing for solvent evaporation. After 30 minutes, an extracting mixture of acetonitrile and water (65:35, v/v) was added (1 mL for the sclera and 0.5 mL for the choroid). Tissues were left in contact with the extracting mixture for 2 hours at room temperature with eventual sample vortexing. Supernatants were taken for HPLC drug quantification. To check the presence of interferences from the tissues, samples of sclera and choroid without drugs (blank samples) were subject to the same extraction procedure.

5.2.6. Validation of Dex extraction method from porcine vitreous and retina

Approximately 2 g of frozen vitreous body, including retina, corresponding to half the vitreous body contained within a porcine eye, were transferred into an 8 mL polypropylene tube. 20 µL of 2 mg/mL Dex in ethanol 90% (v/v) were added. After 30 minutes, the sample was liquefied with a sonicating probe at a constant frequency of 30 kHz (Amplitude 100% (180 µm), Cycle 1; UP100H ultrasonic Processor, Hielscher ultrasonics, Teltow, Germany) for 1 minute. Aliquots of 0.35 mL from the digest were transferred into 1.5 mL Eppendorf® tubes and 0.65 mL of acetonitrile were added. Vitreous was left in contact with the extracting mixture for 2 hours at room temperature with eventual sample vortexing. Samples were centrifuged at 12,000 rpm for 5 minutes

and the supernatant analysed with HPLC for Dex quantification. To check the presence of interferences from the tissue, samples of vitreous and retina without drug (blank samples) were subject to the same extraction procedure.

5.2.7. Permeation and Retention experiments on isolated Sclera and Sclera-Choroid

Isolated sclera or sclera with attached choroid were mounted on Franz-type vertical glass diffusion cells (0.6 cm^2 permeation area, corresponding to 9 mm diameter) with the episcleral side facing the donor. The donor contained 200 µL of the formulations of interest reported in Table 12.

Table 12. Composition of the diverse donors used for permeation and retention experiments on Franz-type cells.

Formulation	DexAc concentration (µg/mL)	DexAc concentration (µM)	pH	Replicates number
DexAc-NLC *(Section 3.2)*	230 ± 20	529 ± 46	n.d.	8
Triacetin *(Section 3.2)*	250	575	n.d.	4
Formulation	**Dex concentration (µg/mL)**	**Dex concentration (µM)**	**pH**	**Replicates number**
Dex-NLC *(Section 3.2)*	141 ± 15	360 ± 37	n.d.	4
Dex-ieNLC *(Section 3.3)*	241 ± 22	614 ± 57	5.82 ± 0.07	8
Triacetin *(Section 3.3)*	210	535	n.d.	4
Microemulsion F'80 *(Section 3.4)*	1000	2547.8	5.75 ± 0.04	3
Microemulsion G77.5 *(Section 3.4)*	1000	2547.8	5.64 ± 0.03	3
Microemulsion G'75 *(Section 3.4)*	1000	2547.8	5.51 ± 0.02	4

n.d. = not determined

The receptor chamber contained a defined volume (*approx.* 4 ml) of a 0.5 mM TPGS solution in PBS (pH 7.4), previously degassed, where solubility at 25 ºC had been determined by triplicates for dexamethasone (103.5 ± 1.8 µg/mL) and dexamethasone acetate (26.4 ± 2.9 µg/mL). Aliquots of 300 µL were taken at predefined times of 0, 2, 4, 6, 20, 22 and 24 h (in the case of the microemulsions no sampling occurred at 20 and 22 h) and replaced each time with fresh medium. Drug

loss due to sampling was corrected during construction of the cumulative profiles. After 24 h, the formulation was removed and discarded, and the scleral surface was accurately washed, to eliminate any formulation residues. Circular sections of 9 mm diameter, consisting of sclera and/or choroid corresponding to the contact area of 0.6 cm^2, were cut, weighted, and placed in an extractive mixture for 2 h (as per validated method in Section 5.2.5.). Drug-free NLC and plain triacetin were used as blanks to exclude possible analytical interferences, while Dex-NLC were tested for comparison purposes.

5.2.8. Retention experiments on whole porcine eye

The developed setup consisting of Ocudonor and Ocutainer, described in Chapter 4, was used for studying the Dex retention within ocular tissues, namely sclera, choroid and vitreous body-retina. The donor compartment contained 200 µL of Dex-ieNLC (Dex concentration 227.98 ± 12.51 µg/mL corresponding to 580.83 ± 31.86 µM), applied for 6 h (n=9) and 18 h (n=6) or of microemulsion F'80 applied for 6 h at the concentration 1 mg/ml, corresponding to 2547.8 µM (n=5).

The procedure previously described in Section 4.3.4. was followed. In brief, ocular bulbs were placed into the Ocutainer and the Ocudonor was secured onto the sclera. The lid was placed and the whole setup was positioned in a water bath at 37°C. After 6 or 18 hours, the formulation was removed, and the scleral surface accurately washed to eliminate any residues. The eyes were retrieved, the permeation area marked with a filter paper disk, and the eye was frozen at -20°C for at least 24 h, protected by cling film.

The frozen eyes were cut in halves following the horizontal plane using a pipe cutter. The hemisphere in contact with Ocudonor and thus with the formulation, was identified as proximal, while the other hemisphere, as distal. Vitreous was easily retrieved from both hemispheres: samples, also including retina, were referred as proximal and distal vitreous, respectively. The RPE was removed with paper filter. Dexamethasone was extracted from vitreous and retina following the procedure presented in Section 4.3.6. (validated in Section 5.2.6.). The permeation area was punched (9 mm diameter) and both the proximal sclera (in direct contact with the formulation) and the proximal choroid (easily peeled off from the sclera) were retrieved. In the distal hemisphere the choroid was collected entirely. The weight of each tissue was accurately noted, and dexamethasone was extracted following the procedure used for Franz-cell experiments (5.2.7.).

5.2.9. Multiphoton Microscopy studies

NR-NLC were put in contact with fresh porcine sclera for 2 h using the Franz-cell setup. After NLC removal and tissue washing, the sclera was punched to obtain 9 mm diameter discs. The distribution of NR within scleral tissue was studied by multiphoton microscopy (MPM). Scleral discs were placed into a customized plexiglass holder and moistened with saline solution to avoid dehydration and to maintain the contact between the objective of the microscope and the tissue.

The equipment consisted of a two-photon microscope Nikon A1R MP+ Upright and a femtosecond pulsed laser Coherent Chameleon Discovery (~100 fs pulse duration with 80 MHz repetition rate, tunable excitation range 660–1320 nm). The excitation beam was focused on the sample by a 25× water dipping objective with numerical aperture (NA) 1.1 mm and 2 mm working distance. The two-photon excited fluorescence (TPEF) and the second harmonic generation (SHG) signals were collected by the same objective and directed by a dichroic mirror to two non-descanned detectors (high sensitivity GaAsP photomultiplier tubes) allowing fast image acquisition. The detectors are preceded by optical filters allowing the simultaneous acquisition of two separated channels: a green channel (506–593 nm) and a red channel (604–679 nm). Imaging overlay of the two channels and image processing was performed by the operation software of the microscope. Images were acquired with 1024 × 1024 pixels definition using 1100 nm as excitation wavelength. A third photomultiplier GaAsP detector, connected to the microscope through an optical fibre and preceded by a dispersive element, was used to record the spectral profile of the TPEF/SHG signal (from 430 to 650 nm with a bandwidth of 10 nm). Laser power and detector gains have been adjusted for different samples and different depths, to acquire enough signal for images and spectra.

5.2.10. HPLC Analysis

A HPLC/UV-Vis method allowing for the simultaneous quantification of both dexamethasone and dexamethasone acetate was developed, starting from [56]. Analysis was conducted with an Agilent 1260 Infinity apparatus (Agilent Technologies, Santa Clara, CA, USA). Separation occurred in a reverse phase column Nova-Pak® C18 (4 µm, 3.9*150 mm; Waters, Milford, MA, USA) heated at 40 °C. A mobile phase consisting of an acetonitrile and water mixture in ratio 45:55 (v/v) was used for the simultaneous quantification of DexAc and Dex, while when Dex was the only analyte, the ratio was 35:65 (v/v). The mobile phase was pumped at 1 mL/min and detection was performed at 246 nm. Retention times of 2.7 min for dexamethasone and 5.8 min for dexamethasone acetate were observed with the first method, while in the second method, dexamethasone eluted at 2.1 min.

Two calibration curves were constructed: one for extraction samples in organic extracting mixture (acetonitrile/water, 65:35, v/v) and one for permeation samples in aqueous phase containing 0.5 mM TPGS in PBS pH 7.4. Both dexamethasone and dexamethasone acetate expressed linearity in the 0.2-10 µg/mL concentration range when present in organic extracting mixture. The limit of quantification (LOQ) was 0.3 µg/mL, when the drugs were present in the aqueous phase. For both drugs and calibration curves, limits of detection (LOD) were ≥ 0.1 µg/mL, precision (expressed as relative standard deviation %) was lower than 2.5% for all studied concentrations while the relative error, indicative of method accuracy, remained in any case under 10%.

5.2.11. Data Processing

The amount of Dex and DexAc permeated across sclera and sclera-choroid (nmol/cm^2) in Franz cell experiments was plotted against time (hour): the slope of the regression line at steady state represents the trans-scleral flux J_{SS} (nmol/cm^2 h). The apparent permeability coefficient P_{app} (cm/s) was then calculated from Equation (6):

$$P_{app} = J_{SS}/C_d \quad (6)$$

being C_d (µM) the concentration of the donor solution. In addition, the lag-time (h) was calculated as the intercept of the regression line at steady state on x axis.

5.2.12. Statistical Analysis

Data were reported as mean ± standard deviation, unless otherwise stated. The differences between values were assessed using Student's t-test and considered statistically significant when $p < 0.05$.

5.3. Results and Discussion

5.3.1. Validation of extraction methodologies from ocular tissues

5.3.1.1. Sclera and Choroid: DexAc and Dex extraction validation

A method for extracting both DexAc and Dex from porcine sclera and choroid was developed and validated. The extracting procedure consisted in soaking fresh tissue samples in an acetonitrile/water mixture (65:35, v/v) for 2 h at room temperature. Both DexAc and Dex were successfully extracted from choroid, while only Dex recovery from sclera was satisfactory (*i.e.*, > 90%), as shown in Figure 51a.

Figure 51. Percentage recovery of DexAc (blue) and Dex (green) from fresh (a) and thawed (b) isolated sclera and choroid. Data were collected by applying either DexAc or Dex to ocular tissues.

The amount of DexAc retrieved from scleral samples was *approx.* 60%, while a significant amount of Dex was detected in the sample. DexAc lowering in favour of Dex formation could be attributed to an enzymatic bioconversion boosted by esterases, which are ubiquitous enzymes expressed in mammal eyes [328]. Particularly, amongst the porcine ocular tissues, sclera shows the higher hydrolysis rate [329]. To verify this hypothesis, the experiment was repeated using frozen and thawed tissues, considering that the freezing process could decrease the esterase activity. As shown in Figure 51b, the amount of DexAc was significantly higher compared to fresh sclera (92.8 ± 2.7% *vs* 61.9 ± 4.6%, respectively) confirming the metabolism. On the contrary, despite esterase expression within choroid, DexAc was not found to be metabolized under the conditions tested. In any case, Dex recovery was always above 90%.

5.3.1.2. Vitreous body and retina: Dex extraction validation

The amount of Dex retrieved form vitreous body + retina is 99.9 ± 4.6%.

5.3.2. DexAc-NLC *ex vivo* evaluation

5.3.2.1. Permeation and retention on isolated Sclera and Sclera-Choroid

Ex vivo permeation and retention experiments were performed using both freshly excised porcine sclera (referred as S) and sclera with choroid (SCh). With the aim to increase dexamethasone acetate concentration, DexAc-NLC was subjected to tangential flow filtration, thus reaching the final concentration of *approx.* 0.2 mg/mL. No dexamethasone was detectable in the formulation. Since, as demonstrated above, dexamethasone acetate undergoes metabolism when in contact with fresh ocular tissues, and dexamethasone is produced, data are presented as total amount (nmol) of both DexAc and Dex.

No detectable concentrations of DexAc or Dex could be observed after 24 h when a reference oily solution of DexAc in triacetin (250 µg/mL corresponding to 575.4 µM) was used as donor for permeation experiments across sclera and sclera-choroid. These results can be explained by the partition coefficient: DexAc finds a favourable

environment within the hydrophobic triacetin, thus the trans-scleral diffusion does not take place.

Permeability coefficients were calculated from permeation profiles reported in Figure 52, applying Equation 6 to the linear portion, defined by the three last timepoints.

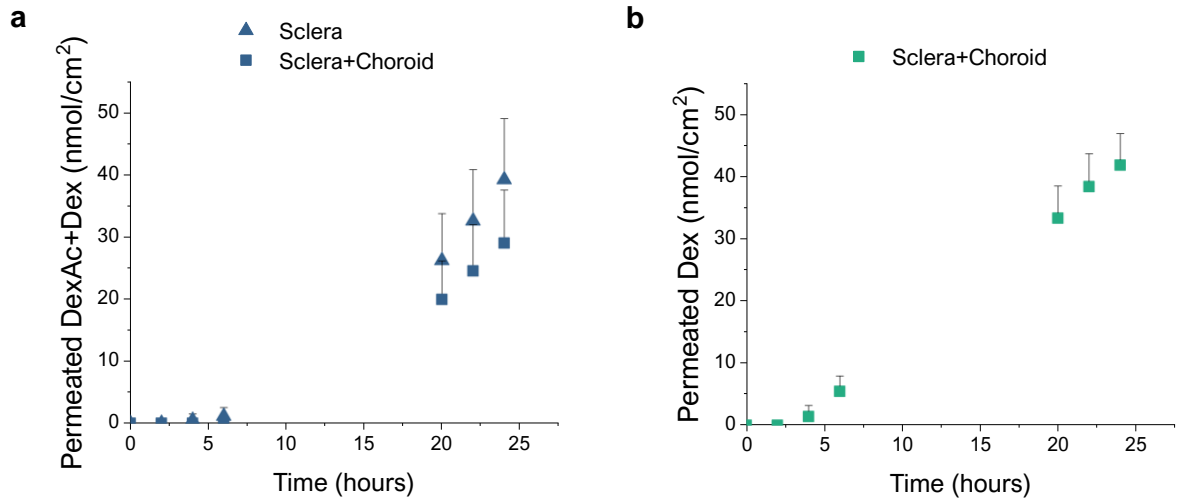

Figure 52. (a) Dex+DexAc permeation profile across S and SCh from DexAc-NLC (donor concentration 230 µg/mL, corresponding to 529.3 µM DexAc). (b) Dex permeation profile across SCh from Dex-NLC (donor concentration 141 µg/mL, corresponding to 360 µM Dex).

Considering the sum of DexAc and Dex, P_{app} was 1.7 ± 0.6 *10^{-6} cm/s for sclera and 1.2 ± 0.4 *10^{-6} cm/s for sclera-choroid. After 24 h of permeation experiment, no statistical differences were detected ($p > 0.05$): choroid presence apparently did not hinder the diffusion of both compounds, as also demonstrated by the lag-time, which was calculated considering DexAc+Dex, and resulted *approx.* 11 h in both cases. The percentages of the permeated drug, in relation to the drug applied, were found to be 22.2 ± 5.6% (S only) and 16.4 ± 4.8% (SCh). Permeability coefficients for DexAc across sclera, to the best of our knowledge, are not available in literature. However, the P_{app} for Dex referred to porcine sclera is 11.1 ± 2.1 *10^{-6} cm/s, one order of magnitude higher than the value observed in our experience [65]. This difference can be easily explained considering the time required for the release of DexAc from NLC, as well as for Dex formation *via* DexAc metabolism. In fact, when a Dex-NLC formulation was applied to SCh (Figure 52b), the obtained P_{app} value was 1.6 ± 0.1 *10^{-6} cm/s, while the lag time is *approx.* 3.5 h. Slight differences in P values, might be attributed to different pig breeds, affecting the biologic variability, as previously reported in [330]. The percentage of permeated Dex in this case was of approximately 35%.

Our findings confirm a relevant role of esterase on DexAc, even on isolated *ex vivo* tissues, as already shown in Figure 51. At the end of the experiment, when studying

the permeation across the sclera, the amount of the prodrug was 2.9-times lower than for the Dex, which is formed by enzymatic process (10.1 ± 3.2 nmol/cm^2 *vs* 29.0 ± 7.6 nmol/cm^2). The underpinning mechanism that might justify this result is that the ester prodrug, due to its high logP of 2.65, will rather be retained inside the intact NLC than diffuse into the highly hydrophilic sclera. Nonetheless, the released DexAc is quickly converted into dexamethasone, a less lipophilic compound (logP = 1.9), which diffuses more easily across the sclera. At the same time, when the double barrier sclera-choroid was present, still a difference was observed, being the amount permeated 5.4 ± 1.8 nmol/cm^2 for DexAc and 23.5 ± 6.9 nmol/cm^2 for Dex, respectively. This outcome confirms that, by selecting the acetate ester prodrug, a sustained Dex release was achieved (in comparison to Dex-NLC) since the limiting step in the process is the enzymatic conversion of the ester prodrug into dexamethasone.

In addition to permeation, retention plays a relevant role in view of a periocular administration. It has been previously demonstrated for compounds having different physicochemical properties that sclera acts as a drug reservoir, allowing for a sustain release over time and ultimately for a reduced frequency of administration [272,331]. Table 13 reports the retention data collected after 24 h of contact between DexAc-NLC and Dex-NLC and ocular tissues.

Table 13. Retention within fresh porcine tissues after 24 h contact at 37 °C in Franz-cells with DexAc-NLC and Dex-NLC (S = sclera; Ch = choroid; SCh = sclera + choroid). Data for DexAc-NLC are presented as DexAc+Dex, DexAc and Dex. Sample "S" refers to the experiment performed in absence of choroid.

		DexAc-NLC (230 µg/mL = 529 µM) (n = 8)			**Dex-NLC (141 µg/mL = 360 µM) (n = 4)**
Sample	Tissue	DexAc+Dex (nmol/g tissue)	DexAc (nmol/g tissue)	Dex (nmol/g tissue)	Dex (nmol/g tissue)
S	S	139.9 ± 35.6	91.8 ± 34.8	48.1 ± 19.5	Not studied
SCh	S	98.9 ± 19.9	50.6 ± 13.4	48.4 ± 13.2	83.4 ± 8.1
	Ch	30.9 ± 9.3	0.00 ± 0.00	30.9 ± 9.3	80.7 ± 12.6
	SCh	92.8 ± 19.0	45.9 ± 12.1	46.9 ± 12.7	83.3 ± 8.3

While Dex was retained in both sclera and choroid, DexAc was retrieved essentially from sclera. Since the NLC present an excessively large size to permeate intact through the sclera, and DexAc has a high LogP, it cannot be ruled out that further structures, such as tyloxapol micelles, might be instantly formed with the degradation products of the NLC. This hypothesis has been further assessed in the next section.

5.3.2.2. Spectroscopic studies of NR-NLC

NR is a hydrophobic heterotetracyclic fluorescent probe, which is used in bioimaging due to its high affinity for nonpolar media [332]. In addition, NR is a solvatochromic dye, *i.e.*, its absorption and emission spectra are sensitive to the polarity of the surroundings, making it a useful fluorescent probe for different local environments [333,334].

Blank NLC were fluorescent in the UV region, as reported in Figure 53. This weak fluorescence is attributed to the tyloxapol surfactant, which has the same emission profile. However, the emission of tyloxapol did not affect MPM experiments, since it falls in a spectral region that cannot be detected with the applied MPM setup.

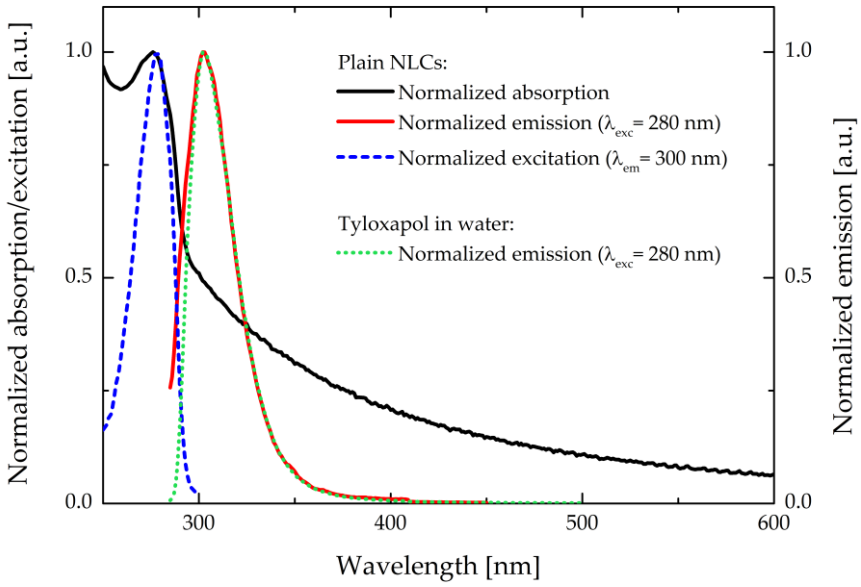

Figure 53. Normalized absorption, excitation, and emission spectra of a diluted blank (plain) NLC aqueous suspension and normalized emission spectrum of tyloxapol. The excitation and emission wavelengths are reported in the legend.

The produced NR-NLC were purified from unencapsulated Nile red *via* size exclusion chromatography, with the help of desalting columns from which several fractions were collected (Table 14).

Table 14. DLS characterization of the eight fractions collected after separation in desalting column.

Collected 1mL Fraction	Z-Average Size (nm)	PDI
Unfiltered	106.9 ± 1.2	0.104 ± 0.019
Fraction 1	1042 ± 282.1	0.916 ± 0.118
Fraction 2	669 ± 213.5	0.67 ± 0.16
Fraction 3	109.3 ± 1.5	0.126 ± 0.007
Fraction 4	108.2 ± 1.8	0.114 ± 0.007
Fraction 5	110.5 ± 1.4	0.133 ± 0.008
Fraction 6	118.8 ± 3.1	0.207 ± 0.064
Fraction 7	367.8 ± 124.2	0.412 ± 0.126
Fraction 8	354.0 ± 126.9	0.401 ± 0.076

Data reported are mean ± standard deviation (n = 3)

No differences have been observed between the emission (and excitation) spectra of the unseparated sample and of the filtered fractions, suggesting that NR is probably embedded in a similar environment (Figure 54).

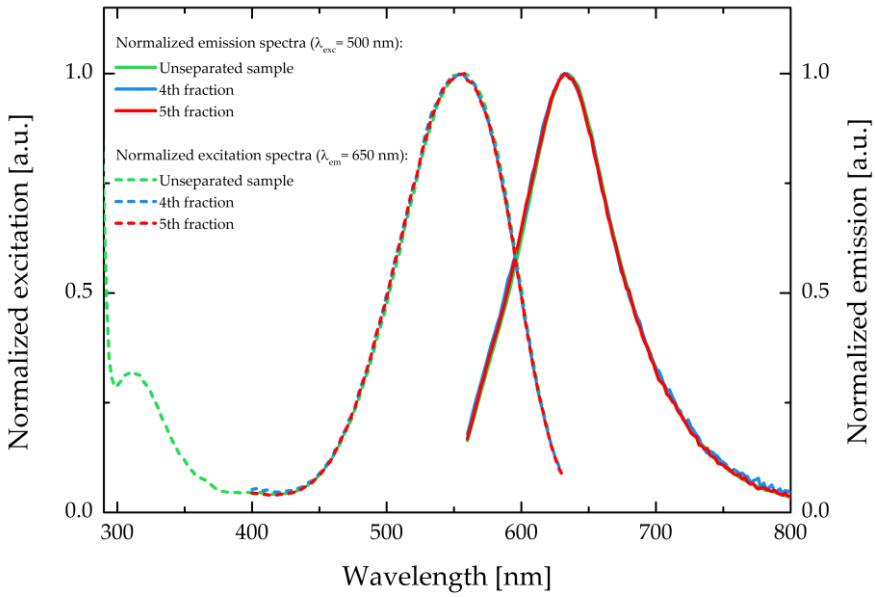

Figure 54. Comparison between the excitation and emission spectra of the unseparated sample and the two separated fractions of NR-loaded NLC. The emission and excitation spectra have been acquired using appropriate longpass filters with 550 and 645 nm cut-off wavelengths, respectively.

The successful encapsulation of NR inside the NLC is evident from the comparison between emission spectra in different media reported in Figure 55a and the MPM images reported in Figures 55b and 55c.

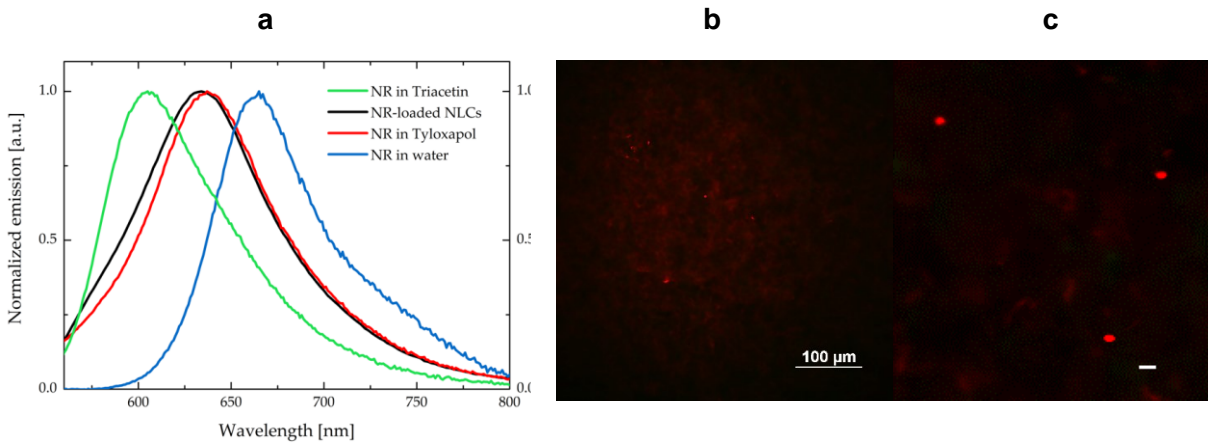

Figure 55. (a) Comparison between emission spectra of NR in triacetin, NLC, tyloxapol (2.7 mg/mL in water), and water (with < 1% DMSO). The spectra have been collected exciting at 500 nm and (b, c) MPM images obtained from NR-loaded NLC with an excitation wavelength of 1100 nm. Images size: 512 µm x 512 µm (left) and 101 µm x 94 µm (right, white bar length: 5 µm).

The emission spectrum of the NR-NLC is very similar to the one collected from NR at a concentration of 1 µM in *approx.* 2.7 mg/mL tyloxapol aqueous solution (corresponding to tyloxapol concentration in the NLC formulation). Emission spectra suggest that NR is entrapped between the polyoxyethylene chains of the surfactant, *i.e.*, in the surface layer of the NLC. The similarity of the emission spectra of NR collected in tyloxapol and NLC does not exclude the presence of some NR-loaded tyloxapol micelles in the suspension, which could be in thermodynamic equilibrium with the NLC and thus, not completely removed by the size exclusion chromatography. This assumption is further supported by the presence of a non-negligible background emission signal in the MPM images reported in Figures 55b and 55c, that could stem from the presence of NR-loaded tyloxapol micelles.

5.3.2.3. MPM on isolated sclera

To further investigate the behaviour of the NLC once in contact with porcine sclera, NR distribution from NR-NLC was studied by multiphoton microscopy, following the same experimental approach that has been recently proposed [41]. The NR-NLC (0.1 µg/mg triacetin) were in contact with the scleral tissue, previously mounted on a Franz-type cell, for 2 hours. Figure 56 reports images acquired at 40 and 150 µm depth from the episclera.

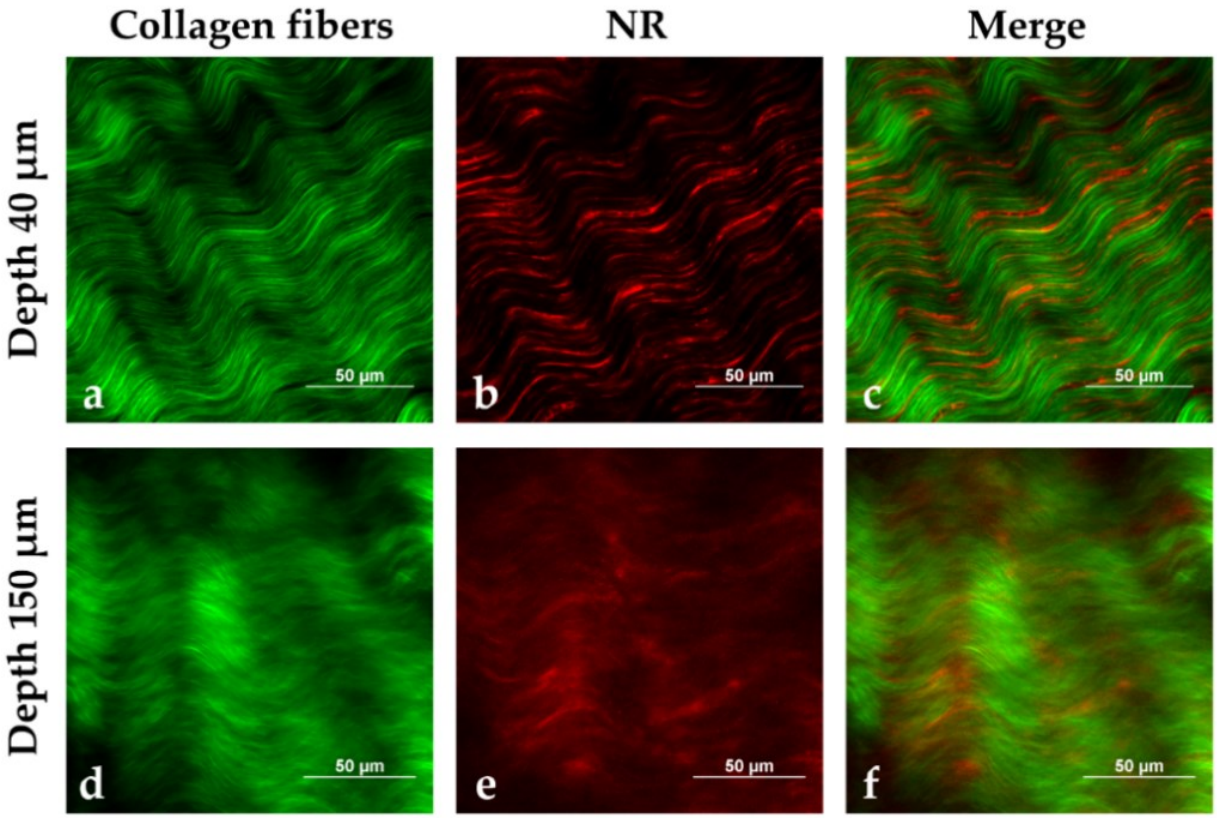

Figure 56. MPM images of porcine sclera (excitation wavelength: 1100 nm) after 2 h contact with NR-loaded NLC (0.1 µg/mg triacetin), at a depth of 40 µm (a, b, c) and 150 µm (d, e, f) from the tissue surface, respectively. Panels a and d report the signal detected in the green channel, mainly due to the SHG of collagen fibres; panels b and e show the signal collected in the red channel, which is attributed to NR emission. Panels c and f report the corresponding channels overlay, showing NR distribution (red) between collagen fibres (green). Images size: 170 µm x 170 µm.

The green signal is mainly attributed to the SHG of collagen fibres; the black spaces among green fibres are aqueous pores (Figure 56a, d), since sclera is composed by 70% water [87]. Collagen fibres appear thicker in the outermost scleral layers (Figure 56a) than in the innermost ones (Figure 56d), as previously observed with a different technique [335]. NR emission, collected in the red channel (Figures 56b, e), was detected between the collagen fibres, as clearly observed in panels c and f of Figure 56. Figure 57 reports both a volume rendering and bidimensional images of the permeated sample with NR-loaded NLC.

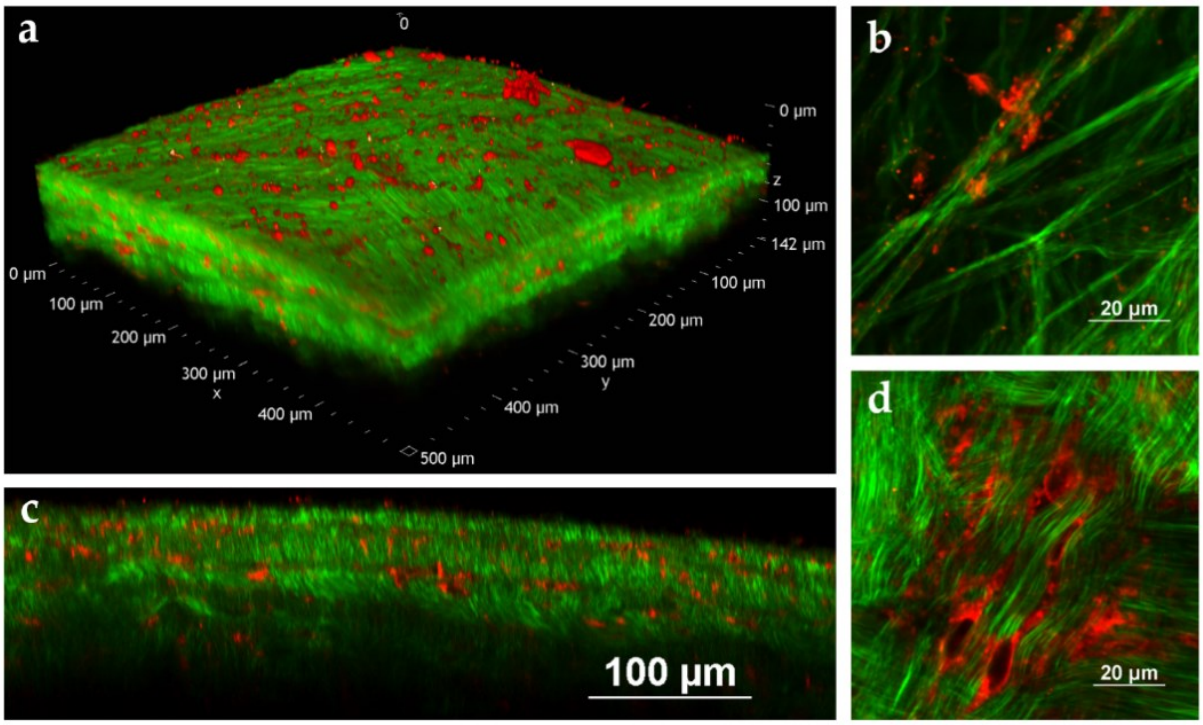

Figure 57. MPM images of porcine sclera after 2 h contact with NR-loaded NLC (0.1 µg/mg triacetin). (a) Volume rendering of the tissue reconstructed from the Z-stack (Z-step: 1 µm, total depth: 142 µm), (b) image of the tissue surface (size: 82 µm x 82 µm), (c) YZ slice extracted from the Z-stack reported in panel a (image size: 512 µm x 142 µm), (d) image acquired 30 µm below the surface of the tissue (size: 92 µm x 92 µm). The excitation wavelength was set to 1100 nm for all the collected images.

On the surface of the tissue (Figure 57 panels a, b), some fluorescent particles and big aggregates were present, adhered to the most externals collagen fibres.

The emission signal of NR was detected from scleral porosities up to the innermost tissue layers that have been visualized, 142 µm from the surface. NR is a hydrophobic probe characterized by very weak emission in aqueous environments, primarily due to aggregation phenomena [336,337]. The bright emission observed in the red channel suggests that NR is well solubilized even after the permeation in the tissue.

The emission spectra of the tissue after the permeation of NLC both loaded with NR (starting from two different concentrations of NR in triacetin, namely 0.1 µg/mg and 0.5 µg/mg) and without dye were also recorded. The three emission profiles obtained are reported in Figure 58 together with the MPM images collected in correspondence of the same focal planes (a comparison between the corresponding Z-stacks is reported in Figure 59).

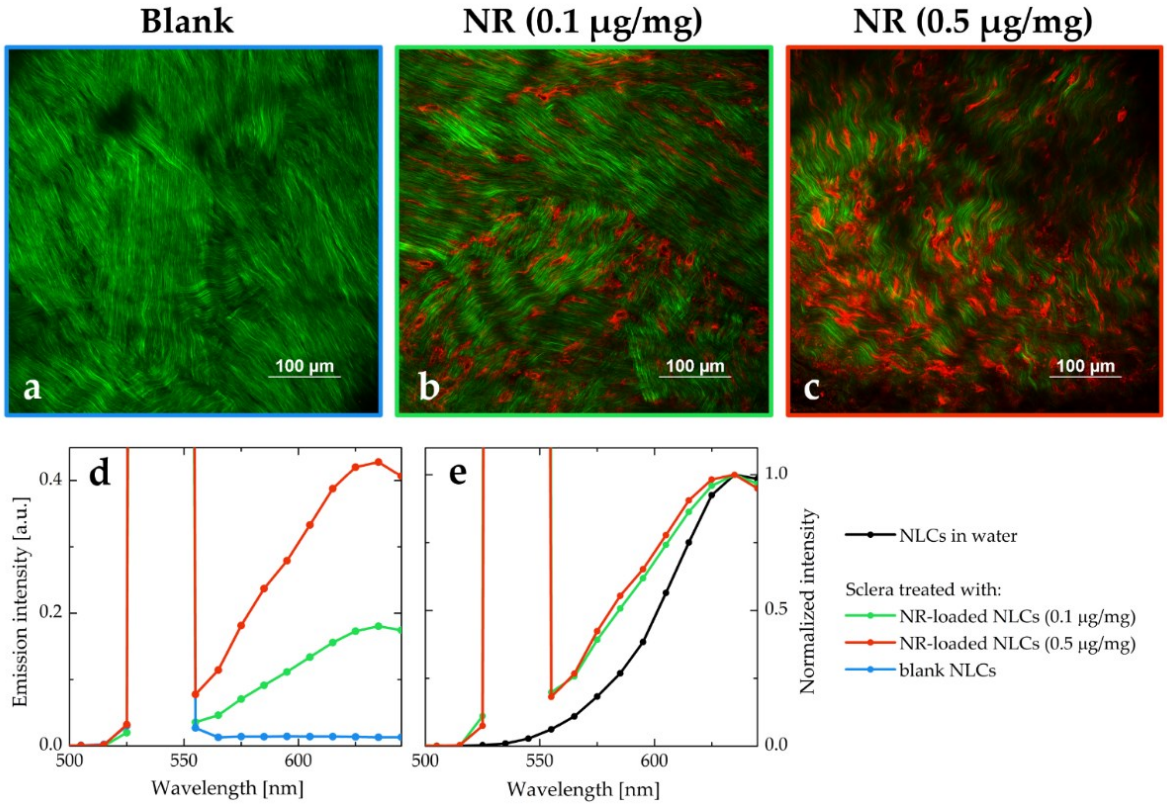

Figure 58. MPM images of porcine sclera (depth of 40 µm, image size: 512 µm x 512 µm and excitation wavelength of 1100 nm) after 2 h contact with NLC: a) blank NLC, b) NR-loaded NLC (starting from 0.1 µg/mg NR), c) NR-loaded NLC (starting from 0.5 µg/mg NR). Panels d and e report the TPEF (broad band) /SHG (intense sharp peak; peak maximum is not shown) profiles obtained with the spectral detector in correspondence of images a, b, and c focal planes, exciting at 1080 nm. The spectra in panel e have been normalized and compared to the emission signal collected with the microscope from a NR-loaded NLC aqueous suspension. Images were acquired in the same experimental conditions (detector gains and laser power), as well as emission spectra.

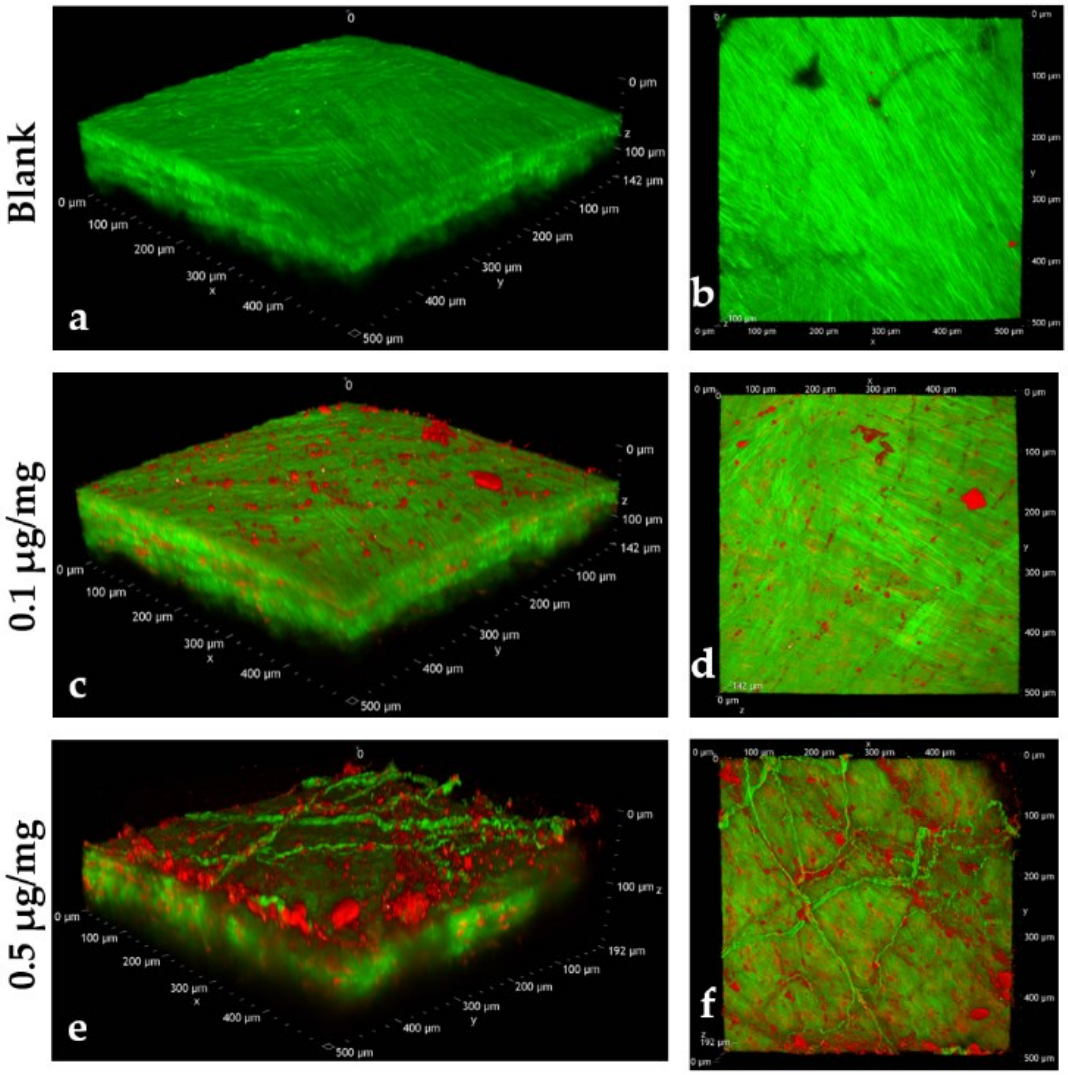

Figure 59. Volume renderings reconstructed from the Z-stacks of the scleral tissues treated with blank NLC (Z-step: 1 µm, total depth: 142 µm, panel a and b), 0.1 µg/mg triacetin NR-loaded NLC (Z-step: 1 µm, total depth: 142 µm, panel c and d), 0.5 µg/mg triacetin NR-loaded NLC (Z-step: 1 µm, total depth: 192 µm, panel e and f). Panels a, c and e report the volume overviews while in panels b, d, and f the XY views can be observed. The same experimental conditions were used to acquire the three Z-stacks: laser power, detectors gain and excitation wavelength (1100 nm).

All the emission profiles were characterized by a strong and sharp peak centered at 540 nm, due to the SHG process promoted by the collagen fibres. The spectrum collected from the tissue permeated with blank NLC (blue line in Figure 58d) has a very intense SHG signal, and very weak autofluorescence. The spectra obtained from the tissues treated with NR-NLC were broadened when compared to the emission recorded from plain NLC (Figure 58e). The broadening of spectra is often associated with an increase of the disorder in the local environment [338]. As hypothesized in Section 5.3.2.1., it is likely that the NLC do not permeate intact within the tissue: in this case, a redistribution of the NR molecules would be expected, exposing the dye to the lipophilic components of the nanocarriers, as well as to the hydrophilic surfactant and

the scleral fibroblasts. The resulting emission spectrum is characterized by an overall broadening since it originates from the superposition of emission spectra of NR in different environments.

5.3.3. Dex-ieNLC *ex vivo* evaluation

The dexamethasone acetate loaded NLC presented in the previous Section, although leading to promising results, presented the main drawback of containing a drug that is subject to the natural esterase activity present in the swine sclera. These results further ratify the value of porcine ocular *ex vivo* models for formulation screening purposes and offer good predicting capabilities, up to a certain level, of the *in vivo* fate of the developed nanosystems. Nonetheless, the observed metabolism did hinder a straightforward interpretation of the permeation and retention results since data had to be interpreted in molar units and not in mass units. In addition, the limiting step of the process towards permeation was not only the physical barrier effect of the tissues studied (sclera and choroid), but also their metabolic activity. Therefore, the decision of producing the same nanoparticulate systems with plain dexamethasone was taken, as described in Chapter 3. This would simplify data interpretation in view of a further application of the formulations on the newly developed *ex vivo* whole porcine eye model presented in Chapter 4.

5.3.3.1. Permeation and retention on isolated Sclera-Choroid

Permeation profiles of dexamethasone across the double barrier sclera-choroid over a 24 hour time period from Dex-ieNLC and a triacetin solution are reported in Figure 60.

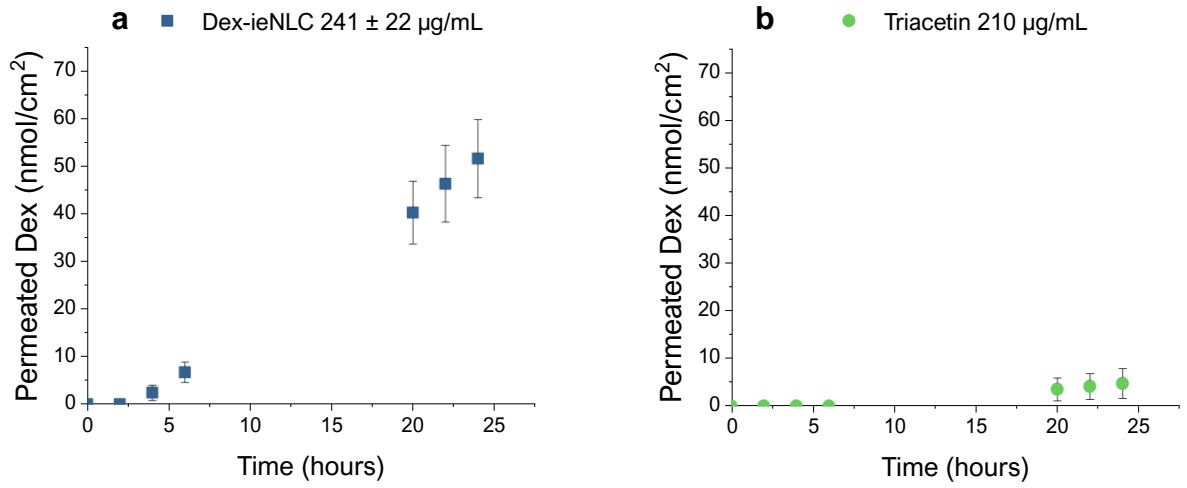

Figure 60. (a) Permeation profiles across sclera-choroid (SCh) of Dex from Dex-ieNLC, donor concentration 241 ± 22 µg/mL (corresponding to 614 ± 57 µM) and (b) Dex diffusion across sclera-choroid when a 210 µg/mL solution in triacetin (corresponding to 535 µM) is used as donor.

The ieNLC confirmed their ability to improve Dex delivery across sclera-choroid. When Dex was applied as a solution in triacetin the calculated P_{app} was of only 1.5 ± 0.9 * 10^{-7} cm/s, one order of magnitude lower than the obtained value when dexamethasone is contained inside the ieNLC (1.1 ± 0.2 * 10^{-6} cm/s). The percentage of drug permeated, in relation to the applied dose, was of 25.2 ± 4.1%.

This result finds an explanation in the different affinity of the drug for the ieNLC with respect to the oil. Following the solubility screening methodology described in Section 3.2.2.2., solubility of plain dexamethasone in triacetin is approximately 1 mg/mL, lower than the solubility of dexamethasone acetate (≥ 10 mg/mL, as calculated from Figure 5, being 1.16 g/ml the density of triacetin [339]), but enough to justify a limited trans-scleral diffusion in comparison to ieNLC encapsulated drug. The affinity for triacetin was confirmed also by retention data, shown in Table 15.

Table 15. Retention within fresh porcine tissues after 24 h contact at 37 °C in Franz-cells with Dex-ieNLC and Dex dissolved in triacetin (S = sclera; Ch = choroid; SCh = sclera + choroid).

		Dex-ieNLC (241 µg/mL = 614 µM)* (n = 8)	**Triacetin (210 µg/mL = 535 µM) (n = 4)**
Sample	Tissue	Dex (nmol/g tissue)	Dex (nmol/g tissue)
	S	132.2 ± 27.7	11.6 ± 1.8
SCh	Ch	101.1 ± 21.1	0.0 ± 0.0
	SCh	129.7 ± 26.0	10.8 ± 1.6

*Average donor concentration

As previously observed for Dex-NLC, Dex is significantly retained within both sclera and choroid, suggesting a reservoir and thus a sustained drug release over time. Unfortunately, a direct comparison between Dex-NLC and Dex-ieNLC is not possible since donor concentrations were different (141 *vs* 241 µg/mL). However, in both cases the NLC demonstrated their ability to sustain the delivery of dexamethasone across the sclera.

5.3.3.2. Retention on whole porcine eye (Ocudonor-Ocutainer)

Dex-ieNLC were further tested *ex vivo* on whole porcine eyes using the Ocudonor-Ocutainer setup. Dexamethasone was retrieved from ocular tissues after 6 and 18 hours contact, and the obtained data are presented in Figure 61.

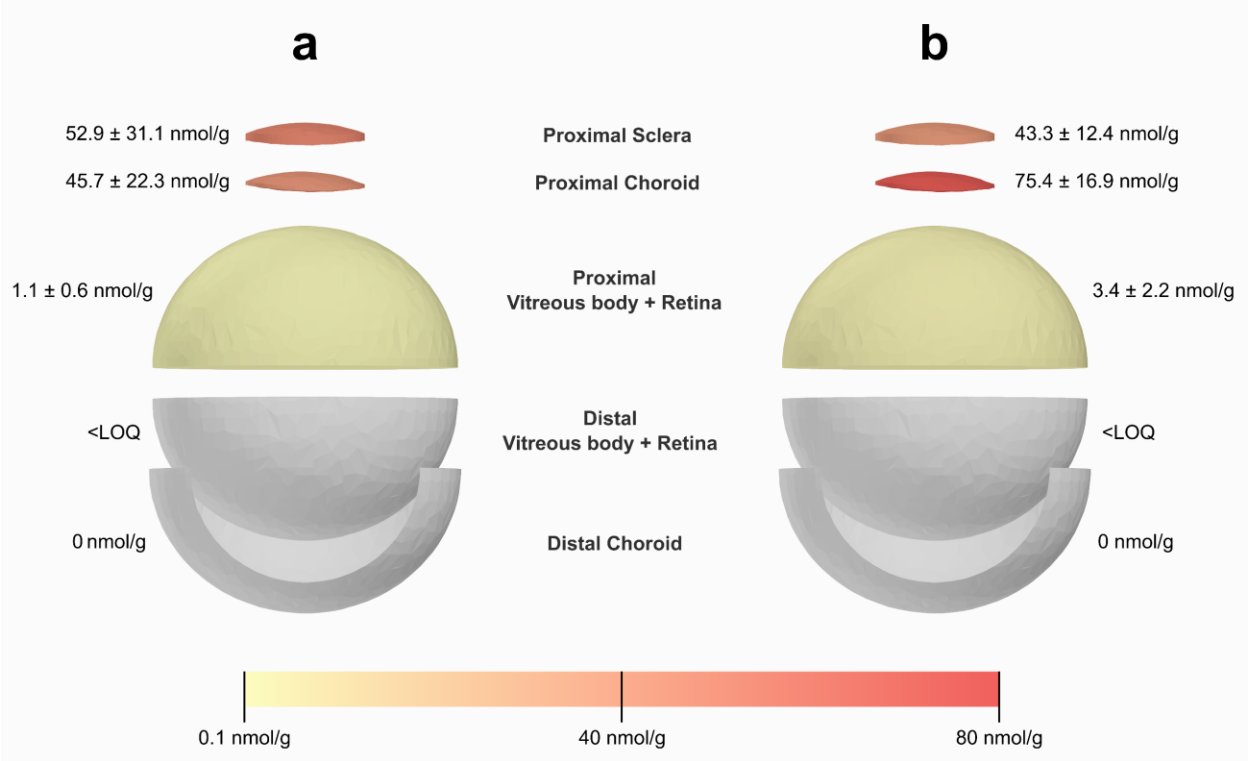

Figure 61. Dexamethasone retained within different ocular tissues (reported as mass of drug per mass of tissue) in *ex vivo* whole-eye using the Ocudonor-Ocutainer setup (Figure 47). Data were collected after a contact of 6 h (n = 9, panel a) and 18 h (n = 6, panel b) of Dex-ieNLC (580.83 ± 31.86 μM).

After 6 hours, a gradient is clearly observable for dexamethasone concentration following the order: proximal S > proximal Ch > proximal Vitreous > distal Vitreous > distal Ch. When increasing the contact time to 18 hours, the sclera in direct contact with the formulation appears to reduce its drug content and a “switch” between sclera and proximal choroid is observed.

The reported values refer only to a small portion of sclera and proximal choroid corresponding to the permeation area, that is the 0.6 cm^2 circular area delimited by the Ocudonor, which is the same permeation area of the Franz-type cells previously used. The Dex detected concentration within sclera after 18 h in the whole-eye *ex vivo* model (Figure 61) is considerably lower than after 24 h using the Franz-cell setup (Table 15), being 43.3 μg/g vs 132 μg/g, respectively. These results can be mainly attributed to a lateral diffusion of dexamethasone occurring in both sclera and choroid. In a Franz-cell, lateral diffusion is not feasible and the drug flux, driven by the concentration gradient, necessarily follows a single direction. On the contrary, when the whole ocular bulb is used, diffusion can occur in multiple directions which explains thus the concentration in the permeation area progressively decreases.

Dexamethasone concentration inside the proximal vitreous body is three times higher after 18 h, indicating a continuative progress of the diffusion across tissues, and

corresponds to 3.4 nmol/g. This value is consistent with the drug concentration required for producing a therapeutic effect in the back of the eye and corresponding to 2.5 nmol/g [340]. Even so, it is necessary to underline that the present ocular model is devoid of dynamic barriers and therefore collected data might not necessarily correlate to *in vivo* conditions. In fact, the strength of the model lies on the possibility to screen different formulation candidates with respect to their behaviour towards static and, even if only in a certain amount, metabolic barriers.

5.3.4. Dex Microemulsions *ex vivo* evaluation

Among the lipid-based nanocarriers, microemulsions are promising formulations widely studied in skin delivery [341] that only in recent times got the attention of the ophthalmic field researchers [342-346]. The developed microemulsions were formulated with ocular compatible surfactants, namely tyloxapol and polysorbate 60, consistently reported in literature for ocular formulations [219,342,347,348].

As discussed in section 3.4.2.4., the microemulsion composition strongly influenced maximal drug loading capabilities, while the microemulsion globule diameter hardly changed. Maximal drug loading remained ≥ 0.8 mg/mL for any formulation within the microemulsion region, higher than the observed values for NLC. Consequently, three microemulsion candidates (F'80, G77.5 and G'75) were selected on the principles of reducing the surfactant concentration (potentially toxic for ocular tissues) and increasing the triacetin content and tested on Franz-cell and on the Ocudonor-Ocutainer setup.

5.3.4.1. Permeation and retention on isolated Sclera-Choroid

Dexamethasone concentration of 1 mg/ml was selected for *ex vivo* experiments. This concentration is relatively far from the solubility (Table 11) and higher enough to allow for a drug quantification within ocular tissues considering the sensitivity of the analytical method. Permeation profiles obtained across the double barrier sclera-choroid are reported in Figure 62.

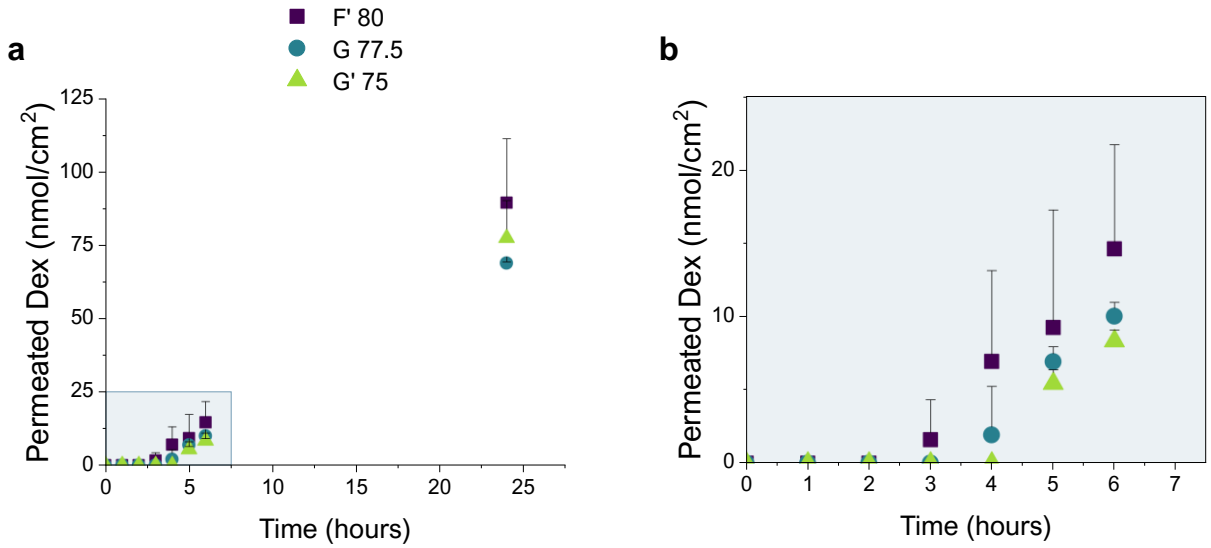

Figure 62. Permeation profiles across sclera-choroid (SCh) of Dex from F'80 (n=3), G77.5 (n=3) and G'75 (n=4). In all formulations, Dex concentration was 1 mg/ml (corresponding to 2547.8 μM). Panel (a) 24 h and (b) 6 h.

No differences could be detected among F'80, G77.5 and G'75, indicating that the different excipients quantitative composition does not impact on formulation behaviour once placed in biorelevant conditions. Permeability coefficients were not calculable, since collected data points were insufficient. However, permeation studies were conducted for screening purposes, in order to compare the three formulation and select the best performing in view of an application on the Ocudonor-Ocutainer setup.

A similar scenario also occurred for retention studies. No differences among microemulsions were detected as reported in Table 16.

Table 16. Dexamethasone extracted from sclera and choroid after 24 h contact with the three tested microemulsions. The total amount of drug retained within the entire sample SCh is also reported.

		F'80	**G77.5**	**G'75**
Sample	Tissue	Dex (nmol/g tissue)	Dex (nmol/g tissue)	Dex (nmol/g tissue)
SCh	S	371.7 ± 44.3	295.7 ± 25.0	275.2 ± 117.0
	Ch	147.6 ± 42.8	97.7 ± 7.0	116.4 ± 39.5
	SCh	358.4 ± 44.6	284.5 ± 24.3	265.7 ± 110.9

It is observed that for all three formulations tested, dexamethasone retention in the sclera was higher than in the choroid. Having observed that the formulations are comparable to each other both in terms of permeation and accumulation data, to carry out the accumulation studies in the whole-eye model, the formulation with the lower surfactant (S_{mix}) content, namely F'80, was selected.

5.3.4.2. Retention on whole porcine eye (Ocudonor-Ocutainer)

After a 6-hours contact of F'80 in the whole-eye Ocudonor-Ocutainer setup, tissues were retrieved, and the retained dexamethasone was quantified (Figure 63).

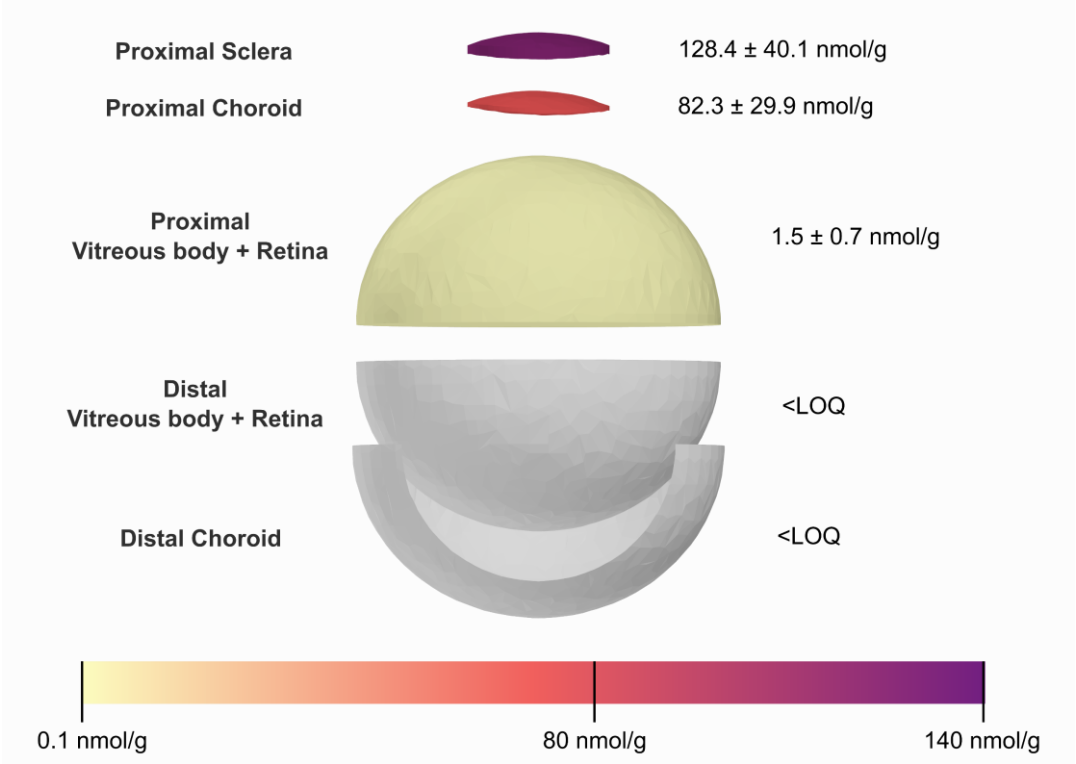

Figure 63. Dexamethasone retained within different ocular tissues (reported as mass of drug per mass of tissue) in ex vivo whole porcine eye using the Ocudonor-Ocutainer setup (Figure 47). Data were collected after a contact of 6 h (n = 5) of F'80 (1 mg/ml corresponding to 2547.8 µM).

Increasing the donor concentration (four times with respect to the ieNLC, Table 16 and Figure 61) translated into an increase in the amount of dexamethasone retained within sclera and proximal choroid.

However, the amount retained inside the proximal vitreous body appears comparable since the concentration of dexamethasone is *approx.* 1 nmol/g in both ieNLC and F'80 experiments. This result can be mainly explained by the expected differences in the releasing mechanism of the drug from the two different colloidal nanocarriers.

Chapter 6

Conclusions

The research work described in the present doctoral thesis pursued three main goals: i) the development of corticosteroid-loaded lipid nanoformulations for periocular administration, ii) the setup of an *ex vivo* model consisting of porcine whole-eye for studying drug retention within ocular tissues, and iii) the *ex vivo* study of the developed colloidal formulations, also by implementing the new whole-eye setup.

The preparation of corticosteroid-loaded NLC and microemulsions was preceded by pre-formulation studies and design of experiments which, by creating mathematical models that are able to predict physicochemical characteristics, allowed to fine-tune the colloidal nanocarriers. All three formulations shared in their composition ocular-compatible excipients such as triacetin (oil) and tyloxapol (surfactant). The latter, owing to its peculiar properties, allowed to produce co-surfactant free NLC. The production method for DexAc-NLC was similar to other previously methods reported in literature and required a 1:10 dilution step in cold water for globule solidification. Under these circumstances, a tangential flow filtration step was required to reconcentrate the NLC which hampered standardization of the formulation drug loading values. Thereupon, Dex-ieNLC were developed. The new production method (hence the “ie” designation) allowed to obtain more reproducible nanoparticle populations in terms of stability and drug loading, since the dilution happens at a 1:1 ratio and thus no reconcentration step is required. In addition, loading of dexamethasone instead of the prodrug facilitated the interpretation of permeation and retention *ex vivo* results, considering that dexamethasone acetate is a substrate for ocular esterases.

A porcine whole-eye *ex vivo* setup was developed with the help of 3D printing by which two tailor-made devices, namely Ocudonor and Ocutainer, were designed and optimized. The former allowed to maintain the contact between formulation and scleral surface, mimicking a periocular administration, and the latter allowed maintain the

ocular bulb in a fixed position at constant temperature and humidity rates, throughout the whole time of the experiment. The whole-eye model can be considered as a natural evolution of Franz-type cells: drug multidirectional diffusion within all ocular tissues takes place and therefore precious information about the static and, to a certain extent, metabolic barriers in trans-scleral drug delivery can be collected and used for the optimization of the formulations. In fact, as a significant part of the development process, adequate methods for tissue retrieval and drug extraction were established.

Drug permeation and retention studies in sclera and choroid were conducted on a classical Franz-cell setup and the newly developed whole-eye *ex vivo* model. Both NLC and microemulsions demonstrated their ability to enhance trans-scleral delivery of dexamethasone and valuable information about dexamethasone distribution within ocular tissues was further collected. In addition, the NLC fate once in contact with sclera (*i.e.*, in biorelevant conditions) was studied with the multiphoton microscopy.

The developed formulations could be used as a delivery platform for other drugs with a therapeutic rationale in the ophthalmic drug delivery. Important parameters such as dosage, dose frequency and release rate are to be established in further research steps (*i.e., in vivo* studies). The implementation of the whole-eye *ex vivo* models will allow to collect crucial information during the development and optimization of ophthalmic formulations.

A summary of the main findings is presented in Table 17.

Table 17. Key highlights of the current PhD thesis.

Section	Aim of Chapter	Main findings / conclusions	Strengths / limitations
Chapter 3	Development of lipid-based formulations for the transscleral delivery of corticosteroids (DexAc and Dex)	· Two production methods for NLC were developed and two different NLC were produced (NLC and ieNLC) with a drug loading of 0.2 mg/mL of either dexamethasone or dexamethasone acetate. · A microemulsion was produced following a DoE approach and a drug loading of 1 mg/mL was achieved.	· NLC were obtained avoiding organic solvents or cosurfactants in the production process. · The DoE approach allowed to fully characterize the microemulsion region. · DoE was unsuccessful for the optimization of the NLC

Chapter 4	Development of an *ex vivo* ocular model based on freshly excised whole porcine ocular bulbs	· Following a 3D printing approach, two devices were designed and printed, namely Ocudonor and Ocutainer, that allow to perform retention experiments on whole porcine bulbs for up to 24 hours. · Tissue and drug retrieval methodologies for sclera, choroid and vitreous body were established.	· The Ocudonor and Ocutainer devices were obtained thanks to the highly tunable and precise MSLA 3D printing approach. · Addition of preservative agents might allow to extend the experimental time.
Chapter 5	*Ex vivo* evaluation of lipid-based nanocarriers	· Permeation and retention experiments on isolated sclera and sclera+choroid demonstrated a better performance of the NLC and/or microemulsions in relation to a drug solution. · NLC loading with Nile Red allowed to acquire valuable information on the fate of the nanoparticles once applied to isolated porcine sclera. · The whole-eye *ex vivo* setup allowed to create a three-dimensional map of the distribution of dexamethasone within the ocular tissues.	· The whole-eye *ex vivo* model setup is adequate for a plethora of liquid or semisolid formulations. · The setup offers the ability to determine lateral drug diffusion which cannot be evaluated on classical Franz-type cells. · The retina is hardly detachable from the frozen vitreous body and thus both tissues are evaluated as a whole.

References

1. Hutmacher, F. Why Is There So Much More Research on Vision Than on Any Other Sensory Modality? Frontiers in psychology 2019, 10, 2246, 10.3389/fpsyg.2019.02246.
2. Schifferstein, H.N.J.; Otten, J.J.; Thoolen, F.; Hekkert, P. The experimental assessment of sensory dominance in a product development context. J. of Design Research 2010, 8, 119-144, 10.1504/JDR.2010.032074.
3. World Health Organization World Report on Vision; World Health Organization: Geneva, 2019; ISBN 978-92-4-151657-0.
4. Wong, W.L.; Su, X.; Li, X.; Cheung, C.M.G.; Klein, R.; Cheng, C.; Wong, T.Y. Global prevalence of age-related macular degeneration and disease burden projection for 2020 and 2040: a systematic review and meta-analysis. The Lancet Global Health 2014, 2, e106-e116, 10.1016/S2214-109X(13)70145-1.
5. Tham, Y.; Li, X.; Wong, T.Y.; Quigley, H.A.; Aung, T.; Cheng, C. Global Prevalence of Glaucoma and Projections of Glaucoma Burden through 2040: A Systematic Review and Meta-Analysis. Ophthalmology 2014, 121, 2081-2090, 10.1016/j.ophtha.2014.05.013.
6. Teo, Z.L.; Tham, Y.; Yan Yu, M.C.; Chee, M.L.; Rim, T.H.; Cheung, N.; Bikbov, M.M.; Wang, Y.X.; Tang, Y.; Lu, Y.; et al. Global Prevalence of Diabetic Retinopathy and Projection of Burden through 2045: Systematic Review and Meta-analysis. Ophthalmology (Rochester, Minn.) 2021, 128, 1580-1591, 10.1016/j.ophtha.2021.04.027.
7. Kontis, V., PhD; Bennett, J.E., PhD; Mathers, C.D., PhD; Li, G., PhD; Foreman, K., PhD; Ezzati, M., Prof Future life expectancy in 35 industrialised countries: projections with a Bayesian model ensemble. The Lancet 2017, 389, 1323-1335, 10.1016/S0140-6736(16)32381-9.
8. Bourne, R.R.A.; Flaxman, S.R.; Braithwaite, T.; Cicinelli, M.V.; Das, A.; Jonas, J.B.; Keeffe, J.; Kempen, J.H.; Leasher, J.; Limburg, H.; et al. Magnitude, temporal trends, and projections of the global prevalence of blindness and distance and near vision impairment: a systematic review and meta-analysis. The Lancet global health 2017, 5, e888-e897, 10.1016/S2214-109X(17)30293-0.
9. Urtti, A. Challenges and obstacles of ocular pharmacokinetics and drug delivery. Adv. Drug Deliv. Rev. 2006, 58, 1131-1135, 10.1016/j.addr.2006.07.027.
10. Gaudana, R.; Ananthula, H.K.; Parenky, A.; Mitra, A.K. Ocular Drug Delivery. The AAPS Journal 2010, 12, 348-360, 10.1208/s12248-010-9183-3.
11. Riordan-Eva, P. In Anatomy & Embryology of the Eye; Riordan-Eva, P., Augsburger, J.J., Eds.; Vaughan & Asbury's General Ophthalmology, 19e; McGraw-Hill Education: New York, NY, 2017; , ISBN 9780071843539.
12. Souto, E.B.; Dias-Ferreira, J.; López-Machado, A.; Ettcheto, M.; Cano, A.; Camins Espuny, A.; Espina, M.; Garcia, M.L.; Sánchez-López, E. Advanced Formulation Approaches for Ocular Drug Delivery: State-Of-The-Art and Recent Patents. Pharmaceutics 2019, 11, 460, 10.3390/pharmaceutics11090460.
13. Järvinen, K.; Järvinen, T.; Urtti, A. Ocular absorption following topical delivery. Adv. Drug Deliv. Rev. 1995, 16, 3-19, 10.1016/0169-409X(95)00010-5.
14. Willoughby, C.E.; Ponzin, D.; Ferrari, S.; Lobo, A.; Landau, K.; Omidi, Y. Anatomy and physiology of the human eye: effects of mucopolysaccharidoses disease on structure and function - a review: Anatomy and physiology of the eye. Clin. Experiment. Ophthalmol. 2010, 38, 2-11, 10.1111/j.1442-9071.2010.02363.x.
15. Remington, L.A. In Chapter 2 - Cornea and Sclera; Remington, L.A., Ed.; Clinical Anatomy and Physiology of the Visual System; Butterworth-Heinemann: Saint Louis, 2012; pp 10-39, ISBN 9781437719260.
16. Toffoletto, N.; Chauhan, A.; Alvarez-Lorenzo, C.; Saramago, B.; Serro, A.P. Asymmetry in Drug Permeability through the Cornea. Pharmaceutics 2021, 13, 694, 10.3390/pharmaceutics13050694.
17. Schoenwald, R.D.; Deshpande, G.S.; Rethwisch, D.G.; Barfknecht, C.F. Penetration into the Anterior Chamber Via the Conjunctival/Scleral Pathway. Journal of Ocular Pharmacology and Therapeutics 1997, 13, 41-59, 10.1089/jop.1997.13.41.

18. del Amo, E.M.; Rimpelä, A.; Heikkinen, E.; Kari, O.K.; Ramsay, E.; Lajunen, T.; Schmitt, M.; Pelkonen, L.; Bhattacharya, M.; Richardson, D.; et al. Pharmacokinetic aspects of retinal drug delivery. Prog. Retin. Eye Res. 2017, 57, 134-185, 10.1016/j.preteyeres.2016.12.001.

19. Bhatt, P.; Kelly, S.; Sutariya, V. Nanoscale delivery systems in treatment of posterior ocular neovascularization: strategies and potential applications. Therapeutic Delivery 2019, 10, 737-747, 10.4155/tde-2019-0025.

20. Amadio, M.; Govoni, S.; Pascale, A. Targeting VEGF in eye neovascularization: What's new?: A comprehensive review on current therapies and oligonucleotide-based interventions under development. Pharmacological Research 2016, 103, 253-269, 10.1016/j.phrs.2015.11.027.

21. Nelson, M.L.; Tennant, M.T.S.; Sivalingam, A.; Regillo, C.D.; Belmont, J.B.; Martidis, A. Infectious and presumed noninfectious endophthalmitis after intravitreal triamcinolone acetonide injection. Retina 2003, 23, 686-691, 10.1097/00006982-200310000-00014.

22. Ozkiriş, A.; Erkiliç, K. Complications of intravitreal injection of triamcinolone acetonide. Canadian Journal of Ophthalmology.Journal Canadien D'ophtalmologie 2005, 40, 63-68, 10.1016/S0008-4182(05)80119-X.

23. Shah, C.P.; Hsu, J.; Garg, S.J.; Fischer, D.H.; Kaiser, R. Retinal pigment epithelial tear after intravitreal bevacizumab injection. Am. J. Ophthalmol. 2006, 142, 1070-1072, 10.1016/j.ajo.2006.07.037.

24. Kidron, H.; Del Amo, E.M.; Vellonen, K.; Urtti, A. Prediction of the vitreal half-life of small molecular drug-like compounds. Pharm. Res. 2012, 29, 3302-3311, 10.1007/s11095-012-0822-5.

25. Xu, Q.; Boylan, N.J.; Suk, J.S.; Wang, Y.; Nance, E.A.; Yang, J.; McDonnell, P.J.; Cone, R.A.; Duh, E.J.; Hanes, J. Nanoparticle diffusion in, and microrheology of, the bovine vitreous ex vivo. Journal of controlled release 2013, 167, 76-84, 10.1016/j.jconrel.2013.01.018.

26. Tavakoli, S.; Kari, O.K.; Turunen, T.; Lajunen, T.; Schmitt, M.; Lehtinen, J.; Tasaka, F.; Parkkila, P.; Ndika, J.; Viitala, T.; et al. Diffusion and Protein Corona Formation of Lipid-Based Nanoparticles in the Vitreous Humor: Profiling and Pharmacokinetic Considerations. Molecular pharmaceutics 2021, 18, 699-713, 10.1021/acs.molpharmaceut.0c00411.

27. del Amo, E.M.; Vellonen, K.; Kidron, H.; Urtti, A. Intravitreal clearance and volume of distribution of compounds in rabbits: In silico prediction and pharmacokinetic simulations for drug development. European Journal of Pharmaceutics and Biopharmaceutics 2015, 95, 215-226, 10.1016/j.ejpb.2015.01.003.

28. Subrizi, A.; del Amo, E.M.; Korzhikov-Vlakh, V.; Tennikova, T.; Ruponen, M.; Urtti, A. Design principles of ocular drug delivery systems: importance of drug payload, release rate, and material properties. Drug discovery today 2019, 24, 1446-1457, 10.1016/j.drudis.2019.02.001.

29. Amrite, A.C.; Edelhauser, H.F.; Singh, S.R.; Kompella, U.B. Effect of circulation on the disposition and ocular tissue distribution of 20 nm nanoparticles after periocular administration. Molecular vision 2008, 14, 150-160.

30. Wan, C.; Muya, L.; Kansara, V.; Ciulla, T.A. Suprachoroidal Delivery of Small Molecules, Nanoparticles, Gene and Cell Therapies for Ocular Diseases. Pharmaceutics 2021, 13, 288, 10.3390/pharmaceutics13020288.

31. Ghate, D.; Brooks, W.; McCarey, B.E.; Edelhauser, H.F. Pharmacokinetics of Intraocular Drug Delivery by Periocular Injections Using Ocular Fluorophotometry. Investigative ophthalmology & visual science 2007, 48, 2230-2237, 10.1167/iovs.06-0954.

32. Kim, S.H.; Lutz, R.J.; Wang, N.S.; Robinson, M.R. Transport Barriers in Transscleral Drug Delivery for Retinal Diseases. Ophthalmic Res. 2007, 39, 244-254, 10.1159/000108117.

33. Molokhia, S.A.; Jeong, E.; Higuchi, W.I.; Kevin Li, S. Examination of Barriers and Barrier Alteration in Transscleral Iontophoresis. Journal of pharmaceutical sciences 2008, 97, 831-844, 10.1002/jps.21003.

34. Cruysberg, L.P.J.; Nuijts, R.M.M.A.; Geroski, D.H.; Koole, L.H.; Hendrikse, F.; Edelhauser, H.F. In Vitro Human Scleral Permeability of Fluorescein, Dexamethasone-Fluorescein, Methotrexate-Fluorescein and Rhodamine 6G and the Use of a Coated Coil as a New Drug Delivery System. Journal of ocular pharmacology and therapeutics 2002, 18, 559-569, 10.1089/108076802321021108.

35. Grimaudo, M.A.; Tratta, E.; Pescina, S.; Padula, C.; Santi, P.; Nicoli, S. Parameters affecting the transscleral delivery of two positively charged proteins of comparable size. International journal of pharmaceutics 2017, 521, 214-221, 10.1016/j.ijpharm.2017.02.044.

36. Tratta, E.; Pescina, S.; Padula, C.; Santi, P.; Nicoli, S. In vitro permeability of a model protein across ocular tissues and effect of iontophoresis on the transscleral delivery. European journal of pharmaceutics and biopharmaceutics 2014, 88, 116-122, 10.1016/j.ejpb.2014.04.018.

37. Kim, E.S.; Durairaj, C.; Kadam, R.S.; Lee, S.J.; Mo, Y.; Geroski, D.H.; Kompella, U.B.; Edelhauser, H.F. Human Scleral Diffusion of Anticancer Drugs from Solution and Nanoparticle Formulation. Pharm Res 2009, 26, 1155-1161, 10.1007/s11095-009-9835-0.

38. Kalita, D.; Shome, D.; Jain, V.G.; Chadha, K.; Bellare, J.R. In Vivo Intraocular Distribution and Safety of Periocular Nanoparticle Carboplatin for Treatment of Advanced Retinoblastoma in Humans. American journal of ophthalmology 2014, 157, 1109-1115.e2, 10.1016/j.ajo.2014.01.027.

39. Pandit, J.; Sultana, Y.; Aqil, M. Chitosan-coated PLGA nanoparticles of bevacizumab as novel drug delivery to target retina: optimization, characterization, and in vitro toxicity evaluation. Artificial cells, nanomedicine, and biotechnology 2017, 45, 1397-1407, 10.1080/21691401.2016.1243545.

40. Pescina, S.; Sonvico, F.; Clementino, A.; Padula, C.; Santi, P.; Nicoli, S. Preliminary Investigation on Simvastatin-Loaded Polymeric Micelles in View of the Treatment of the Back of the Eye. Pharmaceutics 2021, 13, 855, 10.3390/pharmaceutics13060855.

41. Ghezzi, M.; Ferraboschi, I.; Delledonne, A.; Pescina, S.; Padula, C.; Santi, P.; Sissa, C.; Terenziani, F.; Nicoli, S. Cyclosporine-loaded micelles for ocular delivery: Investigating the penetration mechanisms. Journal of controlled release 2022, 349, 744-755, 10.1016/j.jconrel.2022.07.019.

42. Jumelle, C.; Gholizadeh, S.; Annabi, N.; Dana, R. Advances and limitations of drug delivery systems formulated as eye drops. J. Controlled Release 2020, 321, 1-22, 10.1016/j.jconrel.2020.01.057.

43. Medzhitov, R. Origin and physiological roles of inflammation. Nature 2008, 454, 428-435, 10.1038/nature07201.

44. Owsley, C. Aging and vision. Vision research (Oxford) 2011, 51, 1610-1622, 10.1016/j.visres.2010.10.020.

45. Curcio, C.A.; Millican, C.L.; Allen, K.A.; Kalina, R.E. Aging of the human photoreceptor mosaic: evidence for selective vulnerability of rods in central retina. Investigative ophthalmology & visual science 1993, 34, 3278-3296.

46. Xu, H.; Chen, M.; Forrester, J.V. Para-inflammation in the aging retina. Progress in retinal and eye research 2009, 28, 348-368, 10.1016/j.preteyeres.2009.06.001.

47. Fung, A.T.; Tran, T.; Lim, L.L.; Samarawickrama, C.; Arnold, J.; Gillies, M.; Catt, C.; Mitchell, L.; Symons, A.; Buttery, R.; et al. Local delivery of corticosteroids in clinical ophthalmology: A review. Clinical & Experimental Ophthalmology 2020, 48, 366-401, 10.1111/ceo.13702.

48. Gaballa, S.A.; Kompella, U.B.; Elgarhy, O.; Alqahtani, A.M.; Pierscionek, B.; Alany, R.G.; Abdelkader, H. Corticosteroids in ophthalmology: drug delivery innovations, pharmacology, clinical applications, and future perspectives. Drug Deliv. and Transl. Res 2021, 11, 866-893, 10.1007/s13346-020-00843-z.

49. Villanueva, J.R.; Villanueva, L.R.; Navarro, M.G. Pharmaceutical technology can turn a traditional drug, dexamethasone into a first-line ocular medicine. A global perspective and future trends. International journal of pharmaceutics 2017, 516, 342-351, 10.1016/j.ijpharm.2016.11.053.

50. Usayapant, A.; Karana, A.H.; Narurkar, M.M. Effect of 2-hydroxypropyl-β-cyclodextrin on the ocular absorption of dexamethasone and dexamethasone acetate. Pharmaceutical research 1991, 8, 1495-1499, 10.1023/A:1015838215268.

51. Leibowitz, H.M.; Kupferman, A.; Stewart, R.H.; Kimbrough, R.L. Evaluation of Dexamethasone Acetate as a Topical Ophthalmic Formulation. American journal of ophthalmology 1978, 86, 418-423, 10.1016/0002-9394(78)90249-0.

52. Sherif, Z.; Pleyer, U. Corticosteroids in Ophthalmology: Past – Present – Future. Ophthalmologica 2002, 216, 305-315, 10.1159/000066189.

53. Arakawa, Y.; Hashida, N.; Ohguro, N.; Yamazaki, N.; Onda, M.; Matsumoto, S.; Ohishi, M.; Yamabe, K. Eye-concentrated distribution of dexamethasone carried by sugar-chain modified liposome in experimental autoimmune uveoretinitis mice. Biomedical Research 2007, 28, 331-334, 10.2220/biomedres.28.331.

54. Lee, J.; Goh, U.; Park, J.H.; Park, S.W.; Heo, H. Effective Delivery of Exogenous Compounds to the Optic Nerve by Intravitreal Injection of Liposome. Korean Journal of Ophthalmology 2018, 32, 417-423, 10.3341/kjo.2017.0128.

55. Di Prima, G.; Licciardi, M.; Bongiovì, F.; Pitarresi, G.; Giammona, G. Inulin-Based Polymeric Micelles Functionalized with Ocular Permeation Enhancers: Improvement of Dexamethasone Permeation/Penetration through Bovine Corneas. Pharmaceutics 2021, 13, 1431, 10.3390/pharmaceutics13091431.

56. Pescina, S.; Leticia Grolli Lucca; Govoni, P.; Padula, C.; Elena Del Favero; Cantù, L.; Santi, P.; Nicoli, S. Ex Vivo Conjunctival Retention and Transconjunctival Transport of Poorly Soluble Drugs Using Polymeric Micelles. Pharmaceutics 2019, 11, 476, 10.3390/pharmaceutics11090476.

57. L Kiss, E.; Berkó, S.; Gácsi, A.; Kovács, A.; Katona, G.; Soós, J.; Csányi, E.; Gróf, I.; Harazin, A.; Deli, M.A.; et al. Design and Optimization of Nanostructured Lipid Carrier Containing Dexamethasone for Ophthalmic Use. Pharmaceutics 2019, 11, 679, 10.3390/pharmaceutics11120679.

58. Kumari, S.; Dandamudi, M.; Rani, S.; Behaeghel, E.; Behl, G.; Kent, D.; O'Reilly, N.J.; O'Donovan, O.; McLoughlin, P.; Fitzhenry, L. Dexamethasone-Loaded Nanostructured Lipid Carriers for the Treatment of Dry Eye Disease. Pharmaceutics 2021, 13, 905, 10.3390/pharmaceutics13060905.

59. Coursey, T.G.; Henriksson, J.T.; Marcano, D.C.; Shin, C.S.; Isenhart, L.C.; Ahmed, F.; De Paiva, C.S.; Pflugfelder, S.C.; Acharya, G. Dexamethasone nanowafer as an effective therapy for dry eye disease. Journal of controlled release 2015, 213, 168-174, 10.1016/j.jconrel.2015.07.007.

60. Shin, C.S.; Marcano, D.C.; Park, K.; Acharya, G. In Application of Hydrogel Template Strategy in Ocular Drug Delivery; Biomedical Nanotechnology; Springer New York: New York, NY, 2017; Vol. 1570, pp 279-285, ISBN 1493968386.

61. Rodríguez Villanueva, J.; Bravo Osuna, I.; Herrero Vanrell, R.; Molina Martínez, I.T.; Guzmán Navarro, M. Optimising the controlled release of dexamethasone from a new generation of PLGA-based microspheres intended for intravitreal administration. European journal of pharmaceutical sciences 2016, 92, 287-297, 10.1016/j.ejps.2016.03.012.

62. Xu, J.; Wang, Y.; Li, Y.; Yang, X.; Zhang, P.; Hou, H.; Shi, Y.; Song, C. Inhibitory Efficacy of Intravitreal Dexamethasone Acetate-Loaded PLGA Nanoparticles on Choroidal Neovascularization in a Laser-Induced Rat Model. Journal of ocular pharmacology and therapeutics 2007, 23, 527-539, 10.1089/jop.2007.0002.

63. Gómez-Gaete, C.; Fattal, E.; Silva, L.; Besnard, M.; Tsapis, N. Dexamethasone acetate encapsulation into Trojan particles. Journal of controlled release 2008, 128, 41-49, 10.1016/j.jconrel.2008.02.008.

64. Li, X.; Müller, R.H.; Keck, C.M.; Bou-Chacra, N.A. Mucoadhesive dexamethasone acetate-polymyxin B sulfate cationic ocular nanoemulsion - novel combinatorial formulation concept. Pharmazie 2016, 71, 327-333, 10.1691/ph.2016.5190.

65. Da Silva, G.R.; Lima, T.H.; Fernandes-Cunha, G.M.; Oréfice, R.L.; Da Silva-Cunha, A.; Zhao, M.; Behar-Cohen, F. Ocular biocompatibility of dexamethasone acetate loaded poly(ε-caprolactone) nanofibers. European journal of pharmaceutics and biopharmaceutics 2019, 142, 20-30, 10.1016/j.ejpb.2019.05.010.

66. Rocha, E.D.; Ferreira, M.R.S.; dos Santos Neto, E.; Barbosa, E.J.; Löbenberg, R.; Lourenço, F.R.; Bou-Chacra, N. Enhanced In Vitro Antimicrobial Activity of Polymyxin B–Coated Nanostructured Lipid Carrier Containing Dexamethasone Acetate. J Pharm Innov 2021, 16, 125-135, 10.1007/s12247-020-09427-3.

67. Khiev, D.; Mohamed, Z.A.; Vichare, R.; Paulson, R.; Bhatia, S.; Mohapatra, S.; Lobo, G.P.; Valapala, M.; Kerur, N.; Passaglia, C.L.; et al. Emerging Nano-Formulations and Nanomedicines Applications for Ocular Drug Delivery. Nanomaterials 2021, 11, 173, 10.3390/nano11010173.

68. Brown, C.K.; Friedel, H.D.; Barker, A.R.; Buhse, L.F.; Keitel, S.; Cecil, T.L.; Kraemer, J.; Morris, J.M.; Reppas, C.; Stickelmeyer, M.P.; et al. FIP/AAPS Joint Workshop Report: Dissolution/In Vitro Release Testing of Novel/Special Dosage Forms. AAPS PharmSciTech 2011, 12, 782-794, 10.1208/s12249-011-9634-x.

69. ⟨1092⟩ The Dissolution Procedure: Development and Validation In The United States Pharmacopeia and National Formulary USP 29–NF 24, Second Supplement; United States Pharmacopeial Convention Inc.: Rockville, MD, USA, 2009; .

70. Baranowski, P.; Karolewicz, B.; Gajda, M.; Pluta, J. Ophthalmic Drug Dosage Forms: Characterisation and Research Methods. The Scientific World Journal 2014, 2014, 861904-14, 10.1155/2014/861904.

71. Pescina, S.; Macaluso, C.; Gioia, G.A.; Padula, C.; Santi, P.; Nicoli, S. Mydriatics release from solid and semi-solid ophthalmic formulations using different in vitro methods. Drug development and industrial pharmacy 2017, 43, 1472-1479, 10.1080/03639045.2017.1318910.

72. Bao, Q.; Newman, B.; Wang, Y.; Choi, S.; Burgess, D.J. In vitro and ex vivo correlation of drug release from ophthalmic ointments. Journal of controlled release 2018, 276, 93-101, 10.1016/j.jconrel.2018.03.003.

73. Adrianto, M.F.; Annuryanti, F.; Wilson, C.G.; Sheshala, R.; Thakur, R.R.S. In vitro dissolution testing models of ocular implants for posterior segment drug delivery. Drug Deliv. and Transl. Res 2022, 12, 1355-1375, 10.1007/s13346-021-01043-z.

74. Pereira-da-Mota, A.F.; Phan, C.; Concheiro, A.; Jones, L.; Alvarez-Lorenzo, C. Testing drug release from medicated contact lenses: The missing link to predict in vivo performance. Journal of controlled release 2022, 343, 672-702, 10.1016/j.jconrel.2022.02.014.

75. Awwad, S.; Henein, C.; Ibeanu, N.; Khaw, P.T.; Brocchini, S. Preclinical challenges for developing long acting intravitreal medicines. European journal of pharmaceutics and biopharmaceutics 2020, 153, 130-149, 10.1016/j.ejpb.2020.05.005.

76. Scholz, M.; Lin, J.C.; Lee, V.H.L.; Keipert, S. Pilocarpine Permeability across Ocular Tissues and Cell Cultures: Influence of Formulation Parameters. Journal of ocular pharmacology and therapeutics 2002, 18, 455-468, 10.1089/10807680260362731.

77. Pepić, I.; Lovrić, J.; Cetina-Čižmek, B.; Reichl, S.; Filipović-Grčić, J. Toward the practical implementation of eye-related bioavailability prediction models. Drug discovery today 2014, 19, 31-44, 10.1016/j.drudis.2013.08.002.

78. Oliveira, A.V.; Sarmento, B. Establishment of a multilayered 3D cellular model of the retinal-blood barrier. International journal of pharmaceutics 2019, 572, 118811, 10.1016/j.ijpharm.2019.118811.

79. Souto, E.B.; Campos, J.R.; Da Ana, R.; Martins-Gomes, C.; Silva, A.M.; Souto, S.B.; Lucarini, M.; Durazzo, A.; Santini, A. Ocular Cell Lines and Genotoxicity Assessment. International Journal of Environmental Research and Public Health 2020, 17, 2046, 10.3390/ijerph17062046.

80. Hornof, M.; Toropainen, E.; Urtti, A. Cell culture models of the ocular barriers. European journal of pharmaceutics and biopharmaceutics 2005, 60, 207-225, 10.1016/j.ejpb.2005.01.009.

81. Koeberle, M.J.; Hughes, P.M.; Skellern, G.G.; Wilson, C.G. Pharmacokinetics and Disposition of Memantine in the Arterially Perfused Bovine Eye. Pharmaceutical research 2006, 23, 2781-2798, 10.1007/s11095-006-9106-2.

82. Pescina, S.; Govoni, P.; Potenza, A.; Padula, C.; Santi, P.; Nicoli, S. Development of a Convenient ex vivo Model for the Study of the Transcorneal Permeation of Drugs: Histological and Permeability Evaluation. Journal of pharmaceutical sciences 2015, 104, 63-71, 10.1002/jps.24231.

83. Pescina, S.; Santi, P.; Ferrari, G.; Padula, C.; Cavallini, P.; Govoni, P.; Nicoli, S. Ex vivo models to evaluate the role of ocular melanin in trans-scleral drug delivery. European journal of pharmaceutical sciences 2012, 46, 475-483, 10.1016/j.ejps.2012.03.013.

84. Missel, P.; Chastain, J.; Mitra, A.; Kompella, U.; Kansara, V.; Duvvuri, S.; Amrite, A.; Cheruvu, N. In Vitro Transport and Partitioning of AL-4940, Active Metabolite of Angiostatic Agent Anecortave Acetate, in Ocular Tissues of the Posterior Segment. Journal of ocular pharmacology and therapeutics 2010, 26, 137-146, 10.1089/jop.2009.0132.

85. Tavakoli, S.; Peynshaert, K.; Lajunen, T.; Devoldere, J.; del Amo, E.M.; Ruponen, M.; De Smedt, S.C.; Remaut, K.; Urtti, A. Ocular barriers to retinal delivery of intravitreal liposomes: Impact of vitreoretinal interface. Journal of controlled release 2020, 328, 952-961, 10.1016/j.jconrel.2020.10.028.

86. Gogola, A.; Jan, N.; Lathrop, K.L.; Sigal, I.A. Radial and Circumferential Collagen Fibers Are a Feature of the Peripapillary Sclera of Human, Monkey, Pig, Cow, Goat, and Sheep. Investigative Ophthalmology & Visual Science 2018, 59, 4763-4774, 10.1167/iovs.18-25025.

87. Nicoli, S.; Ferrari, G.; Quarta, M.; Macaluso, C.; Govoni, P.; Dallatana, D.; Santi, P. Porcine sclera as a model of human sclera for in vitro transport experiments: histology, SEM, and comparative permeability. Molecular Vision 2009, 15, 259-266.

88. Schnichels, S.; Paquet-Durand, F.; Löscher, M.; Tsai, T.; Hurst, J.; Joachim, S.C.; Klettner, A. Retina in a dish: Cell cultures, retinal explants and animal models for common diseases of the retina. Progress in retinal and eye research 2021, 81, 100880, 10.1016/j.preteyeres.2020.100880.

89. del Amo, E.M.; Urtti, A. Rabbit as an animal model for intravitreal pharmacokinetics: Clinical predictability and quality of the published data. Experimental eye research 2015, 137, 111-124, 10.1016/j.exer.2015.05.003.

90. Battaglia, L.; Ugazio, E. Lipid Nano- and Microparticles: An Overview of Patent-Related Research. Journal of nanomaterials 2019, 2019, 1-22, 10.1155/2019/2834941.

91. Morrison, P.W.J.; Khutoryanskiy, V.V. Advances in ophthalmic drug delivery. Therapeutic Delivery 2014, 5, 1297-1315, 10.4155/tde.14.75.

92. Srinivasarao, D.A.; Lohiya, G.; Katti, D.S. Fundamentals, challenges, and nanomedicine-based solutions for ocular diseases. WIREs Nanomedicine and Nanobiotechnology 2019, 11, e1548, 10.1002/wnan.1548.

93. U.S. Food and Drug Administration (FDA). Center for Drug Evaluation and Research. Approval Package for Restasis (cyclosporine ophthalmic emulsion). Application Number: 021023. Available online: https://www.accessdata.fda.gov/drugsatfda_docs/nda/2003/21-023_Restasis.cfm (accessed on December 2022).

94. European Medicines Agency EMEA/H/C/002066 - Human medicine European public assessment report (EPAR): Ikervis (ciclosporin). Available online: https://www.ema.europa.eu/en/medicines/human/EPAR/ikervis (accessed on December 2022).

95. U.S. Food and Drug Administration (FDA). Center for Drug Evaluation and Research. Approval Package for Cequa (cyclosporine ophthalmic solution) 0.09%. Application Number: 210913. Available online: https://www.accessdata.fda.gov/drugsatfda_docs/nda/2018/210913Orig1s000TOC.cfm (accessed on December 2022).

96. Mehnert, W.; Mäder, K. Solid lipid nanoparticles: Production, characterization and applications. Advanced drug delivery reviews 2001, 47, 165-196, 10.1016/S0169-409X(01)00105-3.

97. Mehnert, W.; Mäder, K. Solid lipid nanoparticles. Adv. Drug Deliv. Rev. 2012, 64, 83-101, 10.1016/j.addr.2012.09.021.

98. Gan, L.; Wang, J.; Jiang, M.; Bartlett, H.; Ouyang, D.; Eperjesi, F.; Liu, J.; Gan, Y. Recent advances in topical ophthalmic drug delivery with lipid-based nanocarriers. Drug Discov. Today 2013, 18, 290-297, 10.1016/j.drudis.2012.10.005.

99. Acosta, E. Bioavailability of nanoparticles in nutrient and nutraceutical delivery. Current opinion in colloid & interface science 2009, 14, 3-15, 10.1016/j.cocis.2008.01.002.

100. McClements, D.J. Nanoemulsions versus microemulsions: terminology, differences, and similarities. Soft matter 2012, 8, 1719-1729, 10.1039/c2sm06903b.

101. Ammar, H.O.; Salama, H.A.; Ghorab, M.; Mahmoud, A.A. Nanoemulsion as a potential ophthalmic delivery system for dorzolamide hydrochloride. AAPS PharmSciTech 2009, 10, 808-819, 10.1208/s12249-009-9268-4.

102. Tayel, S.A.; El-Nabarawi, M.; Tadros, M.I.; Abd-Elsalam, W. Promising ion-sensitive in situ ocular nanoemulsion gels of terbinafine hydrochloride: Design, in vitro characterization and in vivo estimation of the ocular irritation and drug pharmacokinetics in the aqueous humor of rabbits. Int. J. Pharm. 2013, 443, 293-305, 10.1016/j.ijpharm.2012.12.049.

103. Morsi, N.; Ibrahim, M.; Refai, H.; El Sorogy, H. Nanoemulsion-based electrolyte triggered in situ gel for ocular delivery of acetazolamide. European Journal of Pharmaceutical Sciences 2017, 104, 302-314, 10.1016/j.ejps.2017.04.013.

104. Salvat. A Phase 3, Multicenter, Randomized, Double-Masked Clinical Trial to Assess the Efficacy and Safety of Clobetasol Propionate Ophthalmic Nanoemulsion 0.05% Compared to Placebo in the Treatment of

Inflammation and Pain Associated With Cataract Surgery. Available online: https://clinicaltrials.gov/ct2/show/NCT04246801 (accessed on December 2022).

105. U.S. Food and Drug Administration (FDA). Center for Drug Evaluation and Research. Approval Package for Durezol (difluprednate) ophthalmic emulsion. Application Number: 022212. Available online: https://www.accessdata.fda.gov/drugsatfda_docs/nda/2008/022212s000TOC.cfm (accessed on December 2022).

106. Mehta, S.; Kaur, G. In Microemulsions: Thermodynamic and Dynamic Properties; Tadashi, M., Ed.; Thermodynamics; InTech: Rijeka, 2011; pp 381-406, ISBN 978-953-307-544-0.

107. Peng, C.C.; Bengani, L.C.; Jung, H.J.; Leclerc, J.; Gupta, C.; Chauhan, A. Emulsions and microemulsions for ocular drug delivery. Journal of Drug Delivery Science and Technology 2011, 21, 111-121, 10.1016/S1773-2247(11)50010-3.

108. Westesen, K.; Bunjes, H.; Koch, M.H.J. Physicochemical characterization of lipid nanoparticles and evaluation of their drug loading capacity and sustained release potential. Journal of controlled release 1997, 48, 223-236, 10.1016/S0168-3659(97)00046-1.

109. de Oliveira, I.F.; Barbosa, E.J.; Peters, M.C.C.; Henostroza, M.A.B.; Yukuyama, M.N.; dos Santos Neto, E.; Löbenberg, R.; Bou-Chacra, N. Cutting-edge advances in therapy for the posterior segment of the eye: Solid lipid nanoparticles and nanostructured lipid carriers. Int. J. Pharm. 2020, 589, 119831, 10.1016/j.ijpharm.2020.119831.

110. Himawan, C.; Starov, V.M.; Stapley, A.G.F. Thermodynamic and kinetic aspects of fat crystallization. Adv. Colloid Interface Sci. 2006, 122, 3-33, 10.1016/j.cis.2006.06.016.

111. Helgason, T.; Awad, T.; Kristbergsson, K.; McClements, D.; Weiss, J. Influence of Polymorphic Transformations on Gelation of Tripalmitin Solid Lipid Nanoparticle Suspensions. J Am Oil Chem Soc 2008, 85, 501-511, 10.1007/s11746-008-1219-9.

112. Sonoda, T.; Takata, Y.; Ueno, S.; Sato, K. Effects of Emulsifiers on Crystallization Behavior of Lipid Crystals in Nanometer-Size Oil-in-Water Emulsion Droplets. Crystal growth & design 2006, 6, 306-312, 10.1021/cg050045h.

113. Awad, T.; Hamada, Y.; Sato, K. Effects of addition of diacylglycerols on fat crystallization in oil-in-water emulsion. European journal of lipid science and technology 2001, 103, 735-741, 10.1002/1438-9312(200111)103:113.0.CO;2-X.

114. Khosa, A.; Reddi, S.; Saha, R.N. Nanostructured lipid carriers for site-specific drug delivery. Biomedicine & Pharmacotherapy 2018, 103, 598-613, 10.1016/j.biopha.2018.04.055.

115. Beloqui, A.; Solinís, M.Á; Rodríguez-Gascón, A.; Almeida, A.J.; Préat, V. Nanostructured lipid carriers: Promising drug delivery systems for future clinics. Nanomedicine: Nanotechnology, Biology and Medicine 2016, 12, 143-161, 10.1016/j.nano.2015.09.004.

116. Müller, R.H.; Radtke, M.; Wissing, S.A. Solid lipid nanoparticles (SLN) and nanostructured lipid carriers (NLC) in cosmetic and dermatological preparations. Advanced drug delivery reviews 2002, 54, S131-S155, 10.1016/S0169-409X(02)00118-7.

117. Sánchez-López, E.; Espina, M.; Doktorovova, S.; Souto, E.B.; García, M.L. Lipid nanoparticles (SLN, NLC): Overcoming the anatomical and physiological barriers of the eye – Part II - Ocular drug-loaded lipid nanoparticles. European Journal of Pharmaceutics and Biopharmaceutics 2017, 110, 58-69, 10.1016/j.ejpb.2016.10.013.

118. Lalu, L.; Tambe, V.; Pradhan, D.; Nayak, K.; Bagchi, S.; Maheshwari, R.; Kalia, K.; Tekade, R.K. Novel nanosystems for the treatment of ocular inflammation: Current paradigms and future research directions. J. Controlled Release 2017, 268, 19-39, 10.1016/j.jconrel.2017.07.035.

119. Bastogne, T. Quality-by-design of nanopharmaceuticals – a state of the art. Nanomedicine: Nanotechnology, Biology and Medicine 2017, 13, 2151-2157, 10.1016/j.nano.2017.05.014.

120. Vo, A.; Feng, X.; Patel, D.; Mohammad, A.; Kozak, D.; Choi, S.; Ashraf, M.; Xu, X. Factors affecting the particle size distribution and rheology of brinzolamide ophthalmic suspensions. Int. J. Pharm. 2020, 586, 119495, 10.1016/j.ijpharm.2020.119495.

121. Li, J.; Qiao, Y.; Wu, Z. Nanosystem trends in drug delivery using quality-by-design concept. J. Controlled Release 2017, 256, 9-18, 10.1016/j.jconrel.2017.04.019.

122. Korakianiti, E.; Rekkas, D. Statistical thinking and knowledge management for quality-driven design and manufacturing in pharmaceuticals. Pharm. Res. 2011, 28, 1465-1479, 10.1007/s11095-010-0315-3.

123. Negi, P.; Singh, B.; Sharma, G.; Beg, S.; Katare, O.P. Biocompatible lidocaine and prilocaine loaded-nanoemulsion system for enhanced percutaneous absorption: QbD-based optimisation, dermatokinetics and in vivo evaluation. J. Microencapsul. 2015, 32, 419-431, 10.3109/02652048.2015.1046513.

124. Zidan, A.S.; Sammour, O.A.; Hammad, M.A.; Megrab, N.A.; Habib, M.J.; Khan, M.A. Quality by design: Understanding the formulation variables of a cyclosporine A self-nanoemulsified drug delivery systems by Box-Behnken design and desirability function. Int. J. Pharm. 2007, 332, 55-63, 10.1016/j.ijpharm.2006.09.060.

125. Kelmann, R.G.; Kuminek, G.; Teixeira, H.F.; Koester, L.S. Carbamazepine parenteral nanoemulsions prepared by spontaneous emulsification process. Int. J. Pharm. 2007, 342, 231-239, 10.1016/j.ijpharm.2007.05.004.

126. Yu, L.X. Pharmaceutical Quality by Design: Product and Process Development, Understanding, and Control. Pharm. Res. 2008, 25, 781-791, 10.1007/s11095-007-9511-1.

127. International Council for Harmonisation of Technical Requirements for Pharmaceuticals for Human Use. ICH. Harmonised Tripartite Guideline: Pharmaceutical DevelopmentH Q8(R2). Available online: https://www.ich.org/page/quality-guidelines (accessed on December 2022).

128. Yu, L.X. Pharmaceutical Quality by Design: Product and Process Development, Understanding, and Control. Pharm. Res. 2008, 25, 781-791, 10.1007/s11095-007-9511-1.

129. Zhang, L.; Mao, S. Application of quality by design in the current drug development. Asian Journal of Pharmaceutical Sciences 2017, 12, 1-8, 10.1016/j.ajps.2016.07.006.

130. Cunha, S.; Costa, C.P.; Moreira, J.N.; Sousa Lobo, J.M.; Silva, A.C. Using the quality by design (QbD) approach to optimize formulations of lipid nanoparticles and nanoemulsions: A review. Nanomedicine: Nanotechnology, Biology and Medicine 2020, 28, 102206, 10.1016/j.nano.2020.102206.

131. Frey, D.D.; Engelhardt, F.; Greitzer, E.M. A role for "one-factor-at-a-time" experimentation in parameter design. Research in Engineering Design 2003, 14, 65-74, 10.1007/s00163-002-0026-9.

132. Bolton, S.; Bon, C. Pharmaceutical statistics: practical and clinical applications; Drugs and the pharmaceutical sciences; CRC Press: New York, USA, 2003; Vol. 135ISBN 0824746953.

133. Antony, J. Design of Experiments for Engineers and Scientists; Elsevier: Jordan Hill, 2003; ISBN 9780750647090.

134. Eriksson, L.; Johansson, E.; Kettaneh-Wold, N.; Wikström, C.; Wold, S. Design of experiments: principles and applications; Umetrics: Umeå, 2008; ISBN 9789197373043 9197373044.

135. Montgomery, D.C. Design and analysis of experiments; John Wiley: New York, 2001; , pp 684 ISBN 978-0-471-31649-7.

136. Box, G.E.P.; Meyer, R.D. An Analysis for Unreplicated Fractional Factorials. Technometrics 1986, 28, 11-18, 10.1080/00401706.1986.10488093.

137. Dupuy, D.; Corre, B.; Claeys-Bruno, M.; Sergent, M. Comparison of different screening methods. Case Studies in Business, Industry & Government Statistics 2014, 5, 115-125.

138. Danaei, M.; Dehghankhold, M.; Ataei, S.; Hasanzadeh Davarani, F.; Javanmard, R.; Dokhani, A.; Khorasani, S.; Mozafari, M.R. Impact of Particle Size and Polydispersity Index on the Clinical Applications of Lipidic Nanocarrier Systems. Pharmaceutics 2018, 10, 57, 10.3390/pharmaceutics10020057.

139. Mun, E.A.; Morrison, P.W.J.; Williams, A.C.; Khutoryanskiy, V.V. On the Barrier Properties of the Cornea: A Microscopy Study of the Penetration of Fluorescently Labeled Nanoparticles, Polymers, and Sodium Fluorescein. Molecular Pharmaceutics 2014, 11, 3556-3564, 10.1021/mp500332m.

140. Honary, S.; Zahir, F. Effect of Zeta Potential on the Properties of Nano-Drug Delivery Systems - A Review (Part 2). Tropical Journal of Pharmaceutical Research 2013, 12, 265-273, 10.4314/tjpr.v12i2.20.

141. Hanaor, D.; Michelazzi, M.; Leonelli, C.; Sorrell, C.C. The effects of carboxylic acids on the aqueous dispersion and electrophoretic deposition of ZrO2. Journal of the European Ceramic Society 2012, 32, 235-244, 10.1016/j.jeurceramsoc.2011.08.015.

142. Pignatello, R.; Leonardi, A.; Fuochi, V.; Petronio Petronio, G.; Greco, A.S.; Furneri, P.M. A Method for Efficient Loading of Ciprofloxacin Hydrochloride in Cationic Solid Lipid Nanoparticles: Formulation and Microbiological Evaluation. Nanomaterials 2018, 8, 304, 10.3390/nano8050304.

143. Silva, A.M.; Martins-Gomes, C.; Coutinho, T.E.; Fangueiro, J.F.; Sanchez-Lopez, E.; Pashirova, T.N.; Andreani, T.; Souto, E.B. Soft Cationic Nanoparticles for Drug Delivery: Production and Cytotoxicity of Solid Lipid Nanoparticles (SLNs). Applied Sciences 2019, 9, 4438, 10.3390/app9204438.

144. Hagigit, T.; Abdulrazik, M.; Orucov, F.; Valamanesh, F.; Lambert, M.; Lambert, G.; Behar-Cohen, F.; Benita, S. Topical and intravitreous administration of cationic nanoemulsions to deliver antisense oligonucleotides directed towards VEGF KDR receptors to the eye. J. Controlled Release 2010, 145, 297-305, 10.1016/j.jconrel.2010.04.013.

145. Lakhani, P.; Patil, A.; Taskar, P.; Ashour, E.; Majumdar, S. Curcumin-loaded Nanostructured Lipid Carriers for ocular drug delivery: Design optimization and characterization. Journal of Drug Delivery Science and Technology 2018, 47, 159-166, 10.1016/j.jddst.2018.07.010.

146. Gonzalez-Mira, E.; Egea, M.A.; Garcia, M.L.; Souto, E.B. Design and ocular tolerance of flurbiprofen loaded ultrasound-engineered NLC. Colloids and Surfaces B: Biointerfaces 2010, 81, 412-421, 10.1016/j.colsurfb.2010.07.029.

147. Kiss, E.L.; Berkó, S.; Gácsi, A.; Kovács, A.; Katona, G.; Soós, J.; Csányi, E.; Gróf, I.; Harazin, A.; Deli, M.A.; et al. Development and Characterization of Potential Ocular Mucoadhesive Nano Lipid Carriers Using Full Factorial Design. Pharmaceutics 2020, 12, 682, 10.3390/pharmaceutics12070682.

148. Kiss, E.L.; Berkó, S.; Gácsi, A.; Kovács, A.; Katona, G.; Soós, J.; Csányi, E.; Gróf, I.; Harazin, A.; Deli, M.A.; et al. Development and Characterization of Potential Ocular Mucoadhesive Nano Lipid Carriers Using Full Factorial Design. Pharmaceutics 2020, 12, 682, 10.3390/pharmaceutics12070682.

149. Plackett, R.L.; Burman, J.P. The Design of Optimum Multifactorial Experiments. Biometrika 1946, 33, 305-325, 10.2307/2332195.

150. Guthrie, W.F. NIST/SEMATECH e-Handbook of Statistical Methods (NIST Handbook 151). Available online: https://www.itl.nist.gov/div898/handbook/index.htm (accessed on December 2022).

151. Rathod, V.R.; Shah, D.A.; Dave, R.H. Systematic implementation of quality-by-design (QbD) to develop NSAID-loaded nanostructured lipid carriers for ocular application: preformulation screening studies and statistical hybrid-design for optimization of variables. Drug Dev. Ind. Pharm. 2020, 46, 443-455, 10.1080/03639045.2020.1724135.

152. Bohanec, S.; Peterka, T.R.; Blažič, P.; Jurečič, R.; Grmaš, J.; Krivec, A.; Zakrajšek, J. Using different experimental designs in drug-excipient compatibility studies during the preformulation development of a stable solid dosage formulation. Acta chimica Slovenica 2010, 57, 895-903.

153. Morris, M.D. A Class of Three-Level Experimental Designs for Response Surface Modeling. Technometrics 2000, 42, 111-121, 10.1080/00401706.2000.10485990.

154. Youshia, J.; Kamel, A.O.; El Shamy, A.; Mansour, S. Design of cationic nanostructured heterolipid matrices for ocular delivery of methazolamide. International Journal of Nanomedicine 2012, 7, 2483-2496, 10.2147/IJN.S28307.

155. Fangueiro, J.F.; Andreani, T.; Egea, M.A.; Garcia, M.L.; Souto, S.B.; Silva, A.M.; Souto, E.B. Design of cationic lipid nanoparticles for ocular delivery: Development, characterization and cytotoxicity. Int. J. Pharm. 2014, 461, 64-73, 10.1016/j.ijpharm.2013.11.025.

156. Rimple; Newton, M.J. Impact of Ocular Compatible Lipoids and Castor Oil in Fabrication of Brimonidine Tartrate Nanoemulsions by 33 Full Factorial Design. Recent Patents on Inflammation & Allergy Drug Discovery 2018, 12, 169-183, 10.2174/1872213X12666180730115225.

157. Wadetwar, R.N.; Agrawal, A.R.; Kanojiya, P.S. In situ gel containing Bimatoprost solid lipid nanoparticles for ocular delivery: In-vitro and ex-vivo evaluation. Journal of Drug Delivery Science and Technology 2020, 56, 101575, 10.1016/j.jddst.2020.101575.

158. Fangueiro, J.F.; Andreani, T.; Fernandes, L.; Garcia, M.L.; Egea, M.A.; Silva, A.M.; Souto, E.B. Physicochemical characterization of epigallocatechin gallate lipid nanoparticles (EGCG-LNs) for ocular instillation. Colloids and Surfaces B: Biointerfaces 2014, 123, 452-460, 10.1016/j.colsurfb.2014.09.042.

159. Yadav, M.; Schiavone, N.; Guzman-Aranguez, A.; Giansanti, F.; Papucci, L.; Perez de Lara, M.J.; Singh, M.; Kaur, I.P. Atorvastatin-loaded solid lipid nanoparticles as eye drops: proposed treatment option for age-related macular degeneration (AMD). Drug delivery and translational research 2020, 10, 919-944, 10.1007/s13346-020-00733-4.

160. Gonzalez-Mira, E.; Egea, M.A.; Souto, E.B.; Calpena, A.C.; García, M.L. Optimizing flurbiprofen-loaded NLC by central composite factorial design for ocular delivery. Nanotechnology 2011, 22, 045101, 10.1088/0957-4484/22/4/045101.

161. Gonzalez-Mira, E.; Nikolić, S.; Calpena, A.C.; Egea, M.A.; Souto, E.B.; García, M.L. Improved and Safe Transcorneal Delivery of Flurbiprofen by NLC and NLC-Based Hydrogels. J. Pharm. Sci. 2012, 101, 707-725, 10.1002/jps.22784.

162. Araújo, J.; Gonzalez-Mira, E.; Egea, M.A.; Garcia, M.L.; Souto, E.B. Optimization and physicochemical characterization of a triamcinolone acetonide-loaded NLC for ocular antiangiogenic applications. Int. J. Pharm. 2010, 393, 168-176, 10.1016/j.ijpharm.2010.03.034.

163. Araújo, J.; Nikolic, S.; Egea, M.A.; Souto, E.B.; Garcia, M.L. Nanostructured lipid carriers for triamcinolone acetonide delivery to the posterior segment of the eye. Colloids and Surfaces B: Biointerfaces 2011, 88, 150-157, 10.1016/j.colsurfb.2011.06.025.

164. Yu, Y.; Feng, R.; Yu, S.; Li, J.; Wang, Y.; Song, Y.; Yang, X.; Pan, W.; Li, S. Nanostructured lipid carrier-based pH and temperature dual-responsive hydrogel composed of carboxymethyl chitosan and poloxamer for drug delivery. Int. J. Biol. Macromol. 2018, 114, 462-469, 10.1016/j.ijbiomac.2018.03.117.

165. Box, G.E.P.; Behnken, D.W. Some New Three Level Designs for the Study of Quantitative Variables. Technometrics 1960, 2, 455-475, 10.2307/1266454.

166. Ferreira, S.L.C.; Bruns, R.E.; Ferreira, H.S.; Matos, G.D.; David, J.M.; Brandão, G.C.; da Silva, E.G.P.; Portugal, L.A.; dos Reis, P.S.; Souza, A.S.; et al. Box-Behnken design: An alternative for the optimization of analytical methods. Anal. Chim. Acta 2007, 597, 179-186, 10.1016/j.aca.2007.07.011.

167. Kincl, M.; Turk, S.; Vrečer, F. Application of experimental design methodology in development and optimization of drug release method. Int. J. Pharm. 2005, 291, 39-49, 10.1016/j.ijpharm.2004.07.041.

168. Baig, M.S.; Owida, H.; Njoroge, W.; Siddiqui, A.; Yang, Y. Development and evaluation of cationic nanostructured lipid carriers for ophthalmic drug delivery of besifloxacin. Journal of Drug Delivery Science and Technology 2020, 55, 101496, 10.1016/j.jddst.2019.101496.

169. Lakhani, P.; Patil, A.; Wu, K.; Sweeney, C.; Tripathi, S.; Avula, B.; Taskar, P.; Khan, S.; Majumdar, S. Optimization, stabilization, and characterization of amphotericin B loaded nanostructured lipid carriers for ocular drug delivery. Int. J. Pharm. 2019, 572, 118771, 10.1016/j.ijpharm.2019.118771.

170. Patil, A.; Lakhani, P.; Taskar, P.; Wu, K.; Sweeney, C.; Avula, B.; Wang, Y.; Khan, I.A.; Majumdar, S. Formulation Development, Optimization, and In Vitro–In Vivo Characterization of Natamycin-Loaded PEGylated Nano-Lipid Carriers for Ocular Applications. J. Pharm. Sci. 2018, 107, 2160-2171, 10.1016/j.xphs.2018.04.014.

171. Khames, A.; Khaleel, M.A.; El-Badawy, M.; El-Nezhawy, A. Natamycin solid lipid nanoparticles – sustained ocular delivery system of higher corneal penetration against deep fungal keratitis: preparation and optimization. International Journal of Nanomedicine 2019, 14, 2515-2531, 10.2147/IJN.S190502.

172. Baig, M.S.; Ahad, A.; Aslam, M.; Imam, S.S.; Aqil, M.; Ali, A. Application of Box–Behnken design for preparation of levofloxacin-loaded stearic acid solid lipid nanoparticles for ocular delivery: Optimization, in vitro release, ocular tolerance, and antibacterial activity. Int. J. Biol. Macromol. 2016, 85, 258-270, 10.1016/j.ijbiomac.2015.12.077.

173. Kalam, M.A.; Sultana, Y.; Ali, A.; Aqil, M.; Mishra, A.K.; Aljuffali, I.A.; Alshamsan, A. Part I: Development and optimization of solid-lipid nanoparticles using Box–Behnken statistical design for ocular delivery of gatifloxacin. Journal of Biomedical Materials Research Part A 2013, 101A, 1813-1827, 10.1002/jbm.a.34453.

174. U.S. Food and Drug Administration (FDA). Center for Drug Evaluation and Research. Approval Package for Besivance (Besifloxacin). Application Number: 022308. Available online: https://www.accessdata.fda.gov/drugsatfda_docs/nda/2009/022308s000TOC.cfm (accessed on December 2022).

175. Scheffé, H. Experiments With Mixtures. Journal of the Royal Statistical Society.Series B (Methodological) 1958, 20, 344-360.

176. Cornell, J.A. Experiments with Mixtures: A Review. Technometrics 1973, 15, 437-455, 10.1080/00401706.1973.10489071.

177. Cornell, J.A. Experiments with mixtures: designs, models, and the analysis of mixture data; Wiley: New York, 1990; , pp 632 ISBN 978-0-471-52221-8.

178. Perez-Roman, I.; Kiekens, F.; Cordoba-Diaz, D.; Garcia-Rodriguez, J.; Cordoba-Diaz, M. Development of a Solid Formulation Containing a Microemulsion of a Novel Artemisia Extract with Nematocidal Activity for Oral Administration. Pharmaceutics 2020, 12, 873, 10.3390/pharmaceutics12090873.

179. Alhakamy, N.A.; Fahmy, U.A.; Ahmed, O.A.A. Attenuation of Benign Prostatic Hyperplasia by Optimized Tadalafil Loaded Pumpkin Seed Oil-Based Self Nanoemulsion: In Vitro and In Vivo Evaluation. Pharmaceutics 2019, 11, 640, 10.3390/pharmaceutics11120640.

180. Jeirani, Z.; Mohamed Jan, B.; Si Ali, B.; Mohd. Noor, I.; Chun Hwa, S.; Saphanuchart, W. The optimal mixture design of experiments: Alternative method in optimizing the aqueous phase composition of a microemulsion. Chemometrics Intellig. Lab. Syst. 2012, 112, 1-7, 10.1016/j.chemolab.2011.10.008.

181. Snee, R.D.; Marquardt, D.W. Screening Concepts and Designs for Experiments with Mixtures. Technometrics 1976, 18, 19-29, 10.1080/00401706.1976.10489396.

182. Piepel, G.F.; Cornell, J.A. Designs for Mixture-Amount Experiments. Journal of Quality Technology 1987, 19, 11-28, 10.1080/00224065.1987.11979029.

183. Shah, J.; Nair, A.B.; Jacob, S.; Patel, R.K.; Shah, H.; Shehata, T.M.; Morsy, M.A. Nanoemulsion Based Vehicle for Effective Ocular Delivery of Moxifloxacin Using Experimental Design and Pharmacokinetic Study in Rabbits. Pharmaceutics 2019, 11, 230, 10.3390/pharmaceutics11050230.

184. Hibbert, D.B. Experimental design in chromatography: A tutorial review. Journal of Chromatography B 2012, 910, 2-13, 10.1016/j.jchromb.2012.01.020.

185. Langsrud, Ø; Ellekjaer, M.R.; Naes, T. Identifying significant effects in fractional factorial experiments. J. Chemometrics 1994, 8, 205-219, 10.1002/cem.1180080304.

186. Derringer, G.; Suich, R. Simultaneous Optimization of Several Response Variables. Journal of Quality Technology 1980, 12, 214-219, 10.1080/00224065.1980.11980968.

187. Del Castillo, E.; Montgomery, D.C.; McCarville, D.R. Modified Desirability Functions for Multiple Response Optimization. Journal of Quality Technology 1996, 28, 337-345, 10.1080/00224065.1996.11979684.

188. Bhandari, S.; Gabrielle, P.; Nguyen, V.; Daien, V.; Viola, F.; Bougamha, W.; Young, S.; Romero-Nuñez, B.; Figueras-Roca, M.; Zarranz-Ventura, J.; et al. Dexamethasone Implant for Diabetic Macular Oedema: 1-Year Treatment Outcomes from the Fight Retinal Blindness! Registry. Ophthalmol Ther 2022, 11, 797-810, 10.1007/s40123-022-00473-3.

189. Amrite, A.C.; Edelhauser, H.F.; Singh, S.R.; Kompella, U.B. Effect of circulation on the disposition and ocular tissue distribution of 20 nm nanoparticles after periocular administration. Molecular vision 2008, 14, 150-160.

190. Chemical Abstracts Service Scifinder-n: Dexamethasone acetate CAS Registry Number: 1177-87-3: Available online: https://scifinder-n.cas.org/searchDetail/substance/63ce9c5aa8718f29bd45c6b4/substanceDetails (accessed on December 2022).

191. National Center for Biotechnology Information PubChem Compound Summary for CID 5743, Dexamethasone. Available online: https://pubchem.ncbi.nlm.nih.gov/compound/Dexamethasone (accessed on December 2022).

192. Rathod, V.R.; Shah, D.A.; Dave, R.H. Systematic implementation of quality-by-design (QbD) to develop NSAID-loaded nanostructured lipid carriers for ocular application: preformulation screening studies and statistical hybrid-design for optimization of variables. Drug Dev. Ind. Pharm. 2020, 46, 443-455, 10.1080/03639045.2020.1724135.

193. Cavalli, R.; Caputo, O.; Gasco, M.R. Preparation and characterization of solid lipid nanospheres containing paclitaxel. European journal of pharmaceutical sciences 2000, 10, 305-309, 10.1016/S0928-0987(00)00081-6.

194. Sandri, G.; Motta, S.; Bonferoni, M.C.; Brocca, P.; Rossi, S.; Ferrari, F.; Rondelli, V.; Cantù, L.; Caramella, C.; Del Favero, E. Chitosan-coupled solid lipid nanoparticles: Tuning nanostructure and mucoadhesion. European journal of pharmaceutics and biopharmaceutics 2017, 110, 13-18, 10.1016/j.ejpb.2016.10.010.

195. Bonilla, L.; Espina, M.; Severino, P.; Cano, A.; Ettcheto, M.; Camins, A.; García, M.L.; Souto, E.B.; Sánchez-López, E. Lipid Nanoparticles for the Posterior Eye Segment. Pharmaceutics 2021, 14, 90, 10.3390/pharmaceutics14010090.

196. Jarvinen, T.; Jarvinen, K. .Prodrugs for improved ocular drug delivery. Advanced Drug Delivery Reviews . 1996, 19, 203-224.

197. Dai, W.; Dong, L.C.; Li, S.; Pollock-Dove, C.; Chen, J.; Mansky, P.; Eichenbaum, G. Parallel screening approach to identify solubility-enhancing formulations for improved bioavailability of a poorly water-soluble compound using milligram quantities of material. International journal of pharmaceutics 2007, 336, 1-11, 10.1016/j.ijpharm.2006.11.034.

198. Kovačević, A.B.; Müller, R.H.; Keck, C.M. Formulation development of lipid nanoparticles: Improved lipid screening and development of tacrolimus loaded nanostructured lipid carriers (NLC). International journal of pharmaceutics 2020, 576, 118918, 10.1016/j.ijpharm.2019.118918.

199. IOI Oleo GmbH O/W Emusifiers: Imwitor® 491. Available online: https://www.ioioleo.de/produkte/pharma/imwitor-491/ (accessed on December 2022).

200. IOI Oleo GmbH O/W Emusifiers: Imwitor® 900 K. Available online: https://www.ioioleo.de/produkte/pharma/imwitor-900-k/ (accessed on December 2022).

201. Krog, N.J.; Sparsø, F.V. In Food Emulsifiers: Their Chemical and Physical Properties; Friberg, S., Larsson, K., Eds.; Food emulsions 3rd ed., rev. and expanded; Marcel Dekker: New York, 1997; pp 582.

202. Fiume, M.Z. Final Report on the Safety Assessment of Triacetin. International journal of toxicology 2003, 22, 1-10, 10.1080/10915810390204845.

203. Himawan, C.; Starov, V.M.; Stapley, A.G.F. Thermodynamic and kinetic aspects of fat crystallization. Advances in colloid and interface science 2006, 122, 3-33, 10.1016/j.cis.2006.06.016.

204. Salminen, H.; Helgason, T.; Aulbach, S.; Kristinsson, B.; Kristbergsson, K.; Weiss, J. Influence of co-surfactants on crystallization and stability of solid lipid nanoparticles. Journal of colloid and interface science 2014, 426, 256-263, 10.1016/j.jcis.2014.04.009.

205. Jenning, V.; Schäfer-Korting, M.; Gohla, S. Vitamin A-loaded solid lipid nanoparticles for topical use: drug release properties. Journal of controlled release 2000, 66, 115-126, 10.1016/S0168-3659(99)00223-0.

206. Windbergs, M.; Strachan, C.J.; Kleinebudde, P. Understanding the solid-state behaviour of triglyceride solid lipid extrudates and its influence on dissolution. European journal of pharmaceutics and biopharmaceutics 2009, 71, 80-87, 10.1016/j.ejpb.2008.05.015.

207. Himawan, C.; Starov, V.M.; Stapley, A.G.F. Thermodynamic and kinetic aspects of fat crystallization. Adv. Colloid Interface Sci. 2006, 122, 3-33, 10.1016/j.cis.2006.06.016.

208. Windbergs, M.; Strachan, C.J.; Kleinebudde, P. Investigating the Principles of Recrystallization from Glyceride Melts. AAPS PharmSciTech 2009, 10, 1224-1233, 10.1208/s12249-009-9311-5.

209. Ali, H.; Singh, S.K.; Verma, P.R.P. Preformulation and physicochemical interaction study of furosemide with different solid lipids. Journal of Pharmaceutical Investigation 2015, 45, 385-398, 10.1007/s40005-015-0191-2.

210. Goto, M.; Kozawa, K.; Uchida, T. The Crystal Structure of the β′1 Form of Optically Active α-Monostearin. Bulletin of the Chemical Society of Japan 1988, 61, 1434-1436, 10.1246/bcsj.61.1434.

211. Yajima, T.; Itai, S.; Takeuchi, H.; Kawashima, Y. Determination of Optimum Processing Temperature for Transformation of Glyceryl Monostearate. Chemical & pharmaceutical bulletin 2002, 50, 1430-1433, 10.1248/cpb.50.1430.

212. Bertoni, S.; Passerini, N.; Albertini, B. Liquid Lipids Act as Polymorphic Modifiers of Tristearin-Based Formulations Produced by Melting Technologies. Pharmaceutics 2021, 13, 1089, 10.3390/pharmaceutics13071089.

213. Pattarino, F.; Bettini, R.; Foglio Bonda, A.; Della Bella, A.; Giovannelli, L. Polymorphism and kinetic behavior of binary mixtures of triglycerides. International journal of pharmaceutics 2014, 473, 87-94, 10.1016/j.ijpharm.2014.06.042.

214. Gasco, M.R. Method for producing solid lipid microspheres having a narrow size distribution. US Patent 5250236A, 1993.

215. Haider, M.; Abdin, S.M.; Kamal, L.; Orive, G. Nanostructured Lipid Carriers for Delivery of Chemotherapeutics: A Review. Pharmaceutics 2020, 12, 288, 10.3390/pharmaceutics12030288.

216. Zana, R. Dimeric and oligomeric surfactants. Behavior at interfaces and in aqueous solution: a review. Advances in colloid and interface science 2002, 97, 205-253, 10.1016/S0001-8686(01)00069-0.

217. Regev, O.; Zana, R. Aggregation Behavior of Tyloxapol, a Nonionic Surfactant Oligomer, in Aqueous Solution. Journal of colloid and interface science 1999, 210, 8-17, 10.1006/jcis.1998.5776.

218. Jiao, J. Polyoxyethylated nonionic surfactants and their applications in topical ocular drug delivery. Advanced drug delivery reviews 2008, 60, 1663-1673, 10.1016/j.addr.2008.09.002.

219. Juretić, M.; Cetina-Čižmek, B.; Filipović-Grčić, J.; Hafner, A.; Lovrić, J.; Pepić, I. Biopharmaceutical evaluation of surface active ophthalmic excipients using in vitro and ex vivo corneal models. European journal of pharmaceutical sciences 2018, 120, 133-141, 10.1016/j.ejps.2018.04.032.

220. Krog, N.; Larsson, K. Phase behaviour and rheological properties of aqueous systems of industrial distilled monoglycerides. Chemistry and physics of lipids 1968, 2, 129-143, 10.1016/0009-3084(68)90038-8.

221. Krog, N.; Borup, A.P. Swelling behaviour of lamellar phases of saturated monoglycerides in aqueous systems. Journal of the science of food and agriculture 1973, 24, 691-701, 10.1002/jsfa.2740240609.

222. Cerqueira, M.A.; Fasolin, L.H.; Picone, C.S.F.; Pastrana, L.M.; Cunha, R.L.; Vicente, A.A. Structural and mechanical properties of organogels: Role of oil and gelator molecular structure. Food research international 2017, 96, 161-170, 10.1016/j.foodres.2017.03.021.

223. Rane, S.S.; Anderson, B.D. What determines drug solubility in lipid vehicles: Is it predictable? Advanced drug delivery reviews 2008, 60, 638-656, 10.1016/j.addr.2007.10.015.

224. Constantinides, P.P. Lipid Microemulsions for Improving Drug Dissolution and Oral Absorption: Physical and Biopharmaceutical Aspects. Pharm. Res. 1995, 12, 1561-1572, 10.1023/A:1016268311867.

225. Zetzl, A.; Ollivon, M.; Marangoni, A. A Coupled Differential Scanning Calorimetry and X-ray Study of the Mesomorphic Phases of Monostearin and Stearic Acid in Water. Crystal growth & design 2009, 9, 3928-3933, 10.1021/cg9000285.

226. Morley, W.G.; Tiddy, G.J.T. Phase behaviour of monoglyceride/water systems. Faraday Transactions 1993, 89, 2823-2831, 10.1039/FT9938902823.

227. Skibell, B.C.; Soparkar, C.N.S.; Tower, R.N.; Patrinely, J.R. Periocular Anesthesia in Aesthetic Surgery. Seminars in plastic surgery 2007, 21, 37, 10.1055/s-2007-967746.

228. Souto, E.B.; Doktorovova, S.; Gonzalez-Mira, E.; Egea, M.A.; Garcia, M.L. Feasibility of Lipid Nanoparticles for Ocular Delivery of Anti-Inflammatory Drugs. Current eye research 2010, 35, 537-552, 10.3109/02713681003760168.

229. Boafo, G.F.; Magar, K.T.; Ekpo, M.D.; Qian, W.; Tan, S.; Chen, C. The Role of Cryoprotective Agents in Liposome Stabilization and Preservation. International journal of molecular sciences 2022, 23, 12487, 10.3390/ijms232012487.

230. Konan, Y.N.; Gurny, R.; Allémann, E. Preparation and characterization of sterile and freeze-dried sub-200 nm nanoparticles. International journal of pharmaceutics 2002, 233, 239-252, 10.1016/S0378-5173(01)00944-9.

231. Lim, S.; Kim, C. Formulation parameters determining the physicochemical characteristics of solid lipid nanoparticles loaded with all-trans retinoic acid. International journal of pharmaceutics 2002, 243, 135-146, 10.1016/S0378-5173(02)00269-7.

232. Unione Galenisti Italiani Calcolo dell'isosmolarità. Available online: http://www.ugiweb.it/wp-content/uploads/2016/06/CALCOLO-DELL%E2%80%99ISOSMOLARITA%E2%80%99.pdf (accessed on December 2022).

233. Alany, R.G.; Rades, T.; Agatonovic-Kustrin, S.; Davies, N.M.; Tucker, I.G. Effects of alcohols and diols on the phase behaviour of quaternary systems. International journal of pharmaceutics 2000, 196, 141-145, 10.1016/S0378-5173(99)00408-1.

234. Graciaa, A.; Lachaise, J.; Cucuphat, C.; Bourrel, M.; Salager, J.L. Improving solubilization in microemulsions with additives. 2. Long chain alcohols as lipophilic linkers. Langmuir 1993, 9, 3371-3374, 10.1021/la00036a008.

235. Westesen, K. Phase diagram of tyioxapol and water — I. International journal of pharmaceutics 1994, 102, 91-100, 10.1016/0378-5173(94)90043-4.

236. Shen, H.; Zhong, M. Preparation and evaluation of self-microemulsifying drug delivery systems (SMEDDS) containing atorvastatin. Journal of pharmacy and pharmacology 2006, 58, 1183-1191, 10.1211/jpp.58.9.0004.

237. Khoo, S.; Humberstone, A.J.; Porter, C.J.H.; Edwards, G.A.; Charman, W.N. Formulation design and bioavailability assessment of lipidic self-emulsifying formulations of halofantrine. International journal of pharmaceutics 1998, 167, 155-164, 10.1016/S0378-5173(98)00054-4.

238. Date, A.A.; Nagarsenker, M.S. Design and evaluation of self-nanoemulsifying drug delivery systems (SNEDDS) for cefpodoxime proxetil. International journal of pharmaceutics 2007, 329, 166-172, 10.1016/j.ijpharm.2006.08.038.

239. R Core Team. (2022). R: A language and environment for statistical computing. R Foundation for Statistical Computing, Vienna, Austria. https://www.R-project.org/.

240. Lawson, J.; Willden, C. Mixture Experiments in R Using mixexp. Journal of Statistical Software 2016, 72, 1-20, 10.18637/jss.v072.c02.

241. D. Robinson, A. Hayes and S. Couch, (2022). broom: Convert Statistical Objects into Tidy Tibbles. https://broom.tidymodels.org/.

242. H. Wickham, R. François, L. Henry and K. Müller, (2022). dplyr: A Grammar of Data Manipulation. https://dplyr.tidyverse.org.

243. RStudio Team. (2020). RStudio: Integrated Development Environment for R. http://www.rstudio.com/.

244. Butt, U.; ElShaer, A.; Snyder, L.A.S.; Al-Kinani, A.A.; Le Gresley, A.; Alany, R.G. Fatty Acid Based Microemulsions to Combat Ophthalmia Neonatorum Caused by Neisseria gonorrhoeae and Staphylococcus aureus. Nanomaterials 2018, 8, 51, 10.3390/nano8010051.

245. Dhaval, M.; Devani, J.; Parmar, R.; Soniwala, M.M.; Chavda, J. Formulation and optimization of microemulsion based sparfloxacin in-situ gel for ocular delivery: In vitro and ex vivo characterization. Journal of drug delivery science and technology 2020, 55, 101373, 10.1016/j.jddst.2019.101373.

246. Liu, Z.; Nie, S.; Guo, H.; Pan, W.; Li, J. Effects of Transcutol P on the corneal permeability of drugs and evaluation of its ocular irritation of rabbit eyes. Journal of pharmacy and pharmacology 2006, 58, 45-50, 10.1211/jpp.58.1.0006.

247. Lv, F.; Zheng, L.; Tung, C. Phase behavior of the microemulsions and the stability of the chloramphenicol in the microemulsion-based ocular drug delivery system. International journal of pharmaceutics 2005, 301, 237-246, 10.1016/j.ijpharm.2005.06.006.

248. Singh-Joy, S.D.; McLain, V.C. Safety Assessment of Poloxamers 101, 105, 108, 122, 123, 124, 181, 182, 183, 184, 185, 188, 212, 215, 217, 231, 234, 235, 237, 238, 282, 284, 288, 331, 333, 334, 335, 338, 401, 402, 403, and 407, Poloxamer 105 Benzoate, and Poloxamer 182 Dibenzoate as Used in Cosmetics. International journal of toxicology 2008, 27, 93-128, 10.1080/10915810802244595.

249. Mashal, M.; Attia, N.; Puras, G.; Martínez-Navarrete, G.; Fernández, E.; Pedraz, J.L. Retinal gene delivery enhancement by lycopene incorporation into cationic niosomes based on DOTMA and polysorbate 60. Journal of controlled release 2017, 254, 55-64, 10.1016/j.jconrel.2017.03.386.

250. Naz, T.; Nazir, S.; Rashid, M.A.; Akhtar, M.N.; Usman, M.; Abbas, M.; Abbas, G. The Study of Stability and Location of Chloramphenicol in Newly Formed Microemulsion Based Ocular Drug Delivery System. Pharm Chem J 2020, 53, 1047-1052, 10.1007/s11094-020-02120-2.

251. Rashid, M.A.; Naz, T.; Abbas, M.; Nazir, S.; Younas, N.; Majeed, S.; Qureshi, N.; Akhtar, M.N. Chloramphenicol Loaded Microemulsions: Development, Characterization and Stability. Colloid and interface science communications 2019, 28, 41-48, 10.1016/j.colcom.2018.11.006.

252. Pasquali, R.C.; Taurozzi, M.P.; Bregni, C. Some considerations about the hydrophilic–lipophilic balance system. International journal of pharmaceutics 2008, 356, 44-51, 10.1016/j.ijpharm.2007.12.034.

253. Winsor, P.A. Solvent properties of amphiphilic compounds; Butterworths Scientific Publ. Ltd: London, 1954; , pp 202 .

254. Binks, B.P.; Fletcher, P.D.I.; Tian, L. Influence of nanoparticle addition to Winsor surfactant microemulsion systems. Colloids and surfaces. A, Physicochemical and engineering aspects 2010, 363, 8-15, 10.1016/j.colsurfa.2010.03.045.

255. Salager, J.; Antón, R.E.; Sabatini, D.A.; Harwell, J.H.; Acosta, E.J.; Tolosa, L.I. Enhancing solubilization in microemulsions—State of the art and current trends. Journal of surfactants and detergents 2005, 8, 3-21, 10.1007/s11743-005-0328-4.

256. Carreón Hidalgo, J.P. R in the Lab: Design of Experiments with Mixtures and their Analysis with R. Available online: https://r-inthelab.net/2022/07/01/design-of-experiments-with-mixtures-and-their-analysis-with-r/ (accessed on December 2022).

257. Myers, R.H.; Montgomery, D.C.; Anderson-Cook, C.M. Response surface methodology: process and product optimization using designed experiments; 2009; ISBN 0470174463.

258. Lawson, J. Chapter 11: Mixture Experiments; Chapman and Hall/CRC: Boca Raton, 2015; Vol. 115ISBN 9780429154522.

259. Nobbman, U. Malvern Panalytical Materials Talks blog: Polydispersity – what does it mean for DLS and chromatography? Available online: https://www.materials-talks.com/polydispersity-what-does-it-mean-for-dls-and-chromatography/ (accessed on December 2022).

260. Organisation for Economic Cooperation and Development, (OECD) Test No. 428: Skin Absorption: In Vitro Method; OECD Guidelines for the Testing of Chemicals, Section 4; OECD Publishing: Paris, 2004; ISBN 9789264071087.

261. Charles, D.D.; Fisher, J.R.; Hoskinson, S.M.; Medina-Colorado, A.A.; Shen, Y.C.; Chaaban, M.R.; Widen, S.G.; Eaves-Pyles, T.D.; Maxwell, C.A.; Miller, A.L.; et al. Development of a Novel ex vivo Nasal Epithelial Cell Model Supporting Colonization With Human Nasal Microbiota. Frontiers in Cellular and Infection Microbiology 2019, 9, 165, 10.3389/fcimb.2019.00165.

262. Xu, Y.; Shrestha, N.; Préat, V.; Beloqui, A. An overview of in vitro, ex vivo and in vivo models for studying the transport of drugs across intestinal barriers. Advanced drug delivery reviews 2021, 175, 113795, 10.1016/j.addr.2021.05.005.

263. Agarwal, P.; Rupenthal, I.D. In vitro and ex vivo corneal penetration and absorption models. Drug Deliv. and Transl. Res 2016, 6, 634-647, 10.1007/s13346-015-0275-6.

264. Ng, S.; Rouse, J.J.; Sanderson, F.D.; Meidan, V.; Eccleston, G.M. Validation of a Static Franz Diffusion Cell System for In Vitro Permeation Studies. AAPS PharmSciTech 2010, 11, 1432-1441, 10.1208/s12249-010-9522-9.

265. European Commission Environment - Animals used for scientific purposes. Available online: https://ec.europa.eu/environment/chemicals/lab_animals/3r/alternative_en.htm (accessed on December 2022).

266. Kirk, R.G.W. Recovering The Principles of Humane Experimental Technique. Science, technology, & human values 2018, 43, 622-648, 10.1177/0162243917726579.

267. Begum, G.; Leigh, T.; Courtie, E.; Moakes, R.; Butt, G.; Ahmed, Z.; Rauz, S.; Logan, A.; Blanch, R.J. Rapid assessment of ocular drug delivery in a novel ex vivo corneal model. Scientific reports 2020, 10, 11754, 10.1038/s41598-020-68254-1.

268. Hemmilä, S.; Ruponen, M.; Toropainen, E.; Tengvall-Unadike, U.; Urtti, A.; Kallio, P. Microflow-Based Device for In Vitro and Ex Vivo Drug Permeability Studies. SLAS technology 2020, 25, 455-462, 10.1177/2472630320916190.

269. Shafaie, S.; Hutter, V.; Brown, M.B.; Cook, M.T.; Chau, D.Y.S. Diffusion through the ex vivo vitreal body – Bovine, porcine, and ovine models are poor surrogates for the human vitreous. International journal of pharmaceutics 2018, 550, 207-215, 10.1016/j.ijpharm.2018.07.070.

270. Christensen, G.; Barut, L.; Urimi, D.; Schipper, N.; Paquet-Durand, F. Investigating Ex Vivo Animal Models to Test the Performance of Intravitreal Liposomal Drug Delivery Systems. Pharmaceutics 2021, 13, 1013, 10.3390/pharmaceutics13071013.

271. Rousou, C.; Hoogenboom, P.; van Overdam, K.A.; Storm, G.; Dorrestijn, J.; Mastrobattista, E. A technical protocol for an experimental ex vivo model using arterially perfused porcine eyes. Experimental eye research 2019, 181, 171-177, 10.1016/j.exer.2019.02.003.

272. Pescina, S.; Padula, C.; Santi, P.; Nicoli, S. Effect of formulation factors on the trans-scleral iontophoretic and post-iontophoretic transports of a 40 kDa dextran in vitro. European journal of pharmaceutical sciences 2011, 42, 503-508, 10.1016/j.ejps.2011.02.008.

273. Bartholomew, L.R. (W.K. Kellogg Eye Center, Ann Arbor, MI.); Pang, D.X.; Sam, D.A.; Cavender, J.C. Ultrasound biomicroscopy of globes from young adult pigs. American journal of veterinary research 1997, 58, 942-948.

274. Bekerman, I.; Gottlieb, P.; Vaiman, M. Variations in Eyeball Diameters of the Healthy Adults. Journal of Ophthalmology 2014, 2014, 503645-5, 10.1155/2014/503645.

275. Sanchez, I.; Martin, R.; Ussa, F.; Fernandez-Bueno, I. The parameters of the porcine eyeball. Graefes Arch Clin Exp Ophthalmol 2011, 249, 475-482, 10.1007/s00417-011-1617-9.

276. Nambiar, M.H.; Liechti, L.; Müller, F.; Bernau, W.; Studer, H.; Roy, A.S.; Seiler, T.G.; Büchler, P. Orientation and depth dependent mechanical properties of the porcine cornea: Experiments and parameter identification. Experimental eye research 2022, 224, 109266, 10.1016/j.exer.2022.109266.

277. Crespo-Moral, M.; García-Posadas, L.; López-García, A.; Diebold, Y. Histological and immunohistochemical characterization of the porcine ocular surface. PLoS ONE 2020, 15, e0227732, 10.1371/journal.pone.0227732.

278. Tan, P.E.Z.; Yu, P.K.; Cringle, S.J.; Morgan, W.H.; Yu, D. Regional heterogeneity of endothelial cells in the porcine vortex vein system. Microvascular research 2013, 89, 70-79, 10.1016/j.mvr.2013.06.004.

279. Ninomiya, H.; Inomata, T. Microvascular anatomy of the pig eye: Scanning electron microscopy of vascular corrosion casts. Journal of veterinary medical science 2006, 68, 1149-1154, 10.1292/jvms.68.1149.

280. Olsen, T.W.; Sanderson, S.; Feng, X.; Hubbard, W.C. Porcine Sclera: Thickness and Surface Area. Investigative ophthalmology & visual science 2002, 43, 2529-2532.

281. Remington, L.A. Clinical anatomy and physiology of the visual system; Elsevier/Butterworth Heinemann: St. Louis, Mo, 2012; ISBN 9781437719260.

282. Wakamatsu, K.; Hu, D.; McCormick, S.A.; Ito, S. Characterization of melanin in human iridal and choroidal melanocytes from eyes with various colored irides. Pigment cell and melanoma research 2008, 21, 97-105, 10.1111/j.1755-148X.2007.00415.x.

283. Stein, S.; Hadlich, S.; Langner, S.; Biesenack, A.; Zehm, N.; Kruschke, S.; Oelze, M.; Grimm, M.; Mahnhardt, S.; Weitschies, W.; et al. 7.1 T MRI and T2 mapping of the human and porcine vitreous body post mortem. European journal of pharmaceutics and biopharmaceutics 2018, 131, 82-91, 10.1016/j.ejpb.2018.07.021.

284. Lossi, L.; D'Angelo, L.; De Girolamo, P.; Merighi, A. Anatomical features for an adequate choice of experimental animal model in biomedicine: II. Small laboratory rodents, rabbit, and pig. Annals of anatomy 2016, 204, 11-28, 10.1016/j.aanat.2015.10.002.

285. Vrolyk, V.; Desmarais, M.; Lambert, D.; Haruna, J.; Benoit-Biancamano, M. Neonatal and Juvenile Ocular Development in Göttingen Minipigs and Domestic Pigs: A Histomorphological and Immunohistochemical Study. Veterinary pathology 2020, 57, 889-914, 10.1177/0300985820954551.

286. Middleton, S. Porcine Ophthalmology. The Veterinary clinics of North America. Food animal practice 2010, 26, 557-572, 10.1016/j.cvfa.2010.09.002.

287. Lunney, J.K.; Van Goor, A.; Walker, K.E.; Hailstock, T.; Franklin, J.; Dai, C. Importance of the pig as a human biomedical model. Science translational medicine 2021, 13, eabd5758, 10.1126/scitranslmed.abd5758.

288. van Kooten, T.G.; Koopmans, S.; Terwee, T.; Norrby, S.; Hooymans, J.M.M.; Busscher, H.J. Development of an accommodating intra-ocular lens—In vitro prevention of re-growth of pig and rabbit lens capsule epithelial cells. Biomaterials 2006, 27, 5554-5560, 10.1016/j.biomaterials.2006.06.026.

289. Goole, J.; Amighi, K. 3D printing in pharmaceutics: A new tool for designing customized drug delivery systems. International journal of pharmaceutics 2016, 499, 376-394, 10.1016/j.ijpharm.2015.12.071.

290. Jamróz, W.; Szafraniec, J.; Kurek, M.; Jachowicz, R. 3D Printing in Pharmaceutical and Medical Applications – Recent Achievements and Challenges. Pharm Res 2018, 35, 176-22, 10.1007/s11095-018-2454-x.

291. Seoane-Viaño, I.; Trenfield, S.J.; Basit, A.W.; Goyanes, A. Translating 3D printed pharmaceuticals: From hype to real-world clinical applications. Advanced drug delivery reviews 2021, 174, 553-575, 10.1016/j.addr.2021.05.003.

292. Jeong, H.Y.; Lee, E.; An, S.; Lim, Y.; Jun, Y.C. 3D and 4D printing for optics and metaphotonics. Nanophotonics (Berlin, Germany) 2020, 9, 1139-1160, 10.1515/nanoph-2019-0483.

293. Xu, X.; Awad, A.; Robles-Martinez, P.; Gaisford, S.; Goyanes, A.; Basit, A.W. Vat photopolymerization 3D printing for advanced drug delivery and medical device applications. Journal of controlled release 2021, 329, 743-757, 10.1016/j.jconrel.2020.10.008.

294. Larochelle, R.D.; Mann, S.E.; Ifantides, C. 3D Printing in Eye Care. Ophthalmol Ther 2021, 10, 733-752, 10.1007/s40123-021-00379-6.

295. Garg, U.; Jain, N.; Kaul, S.; Rai, V.K.; Pandey, M.; Nagaich, U.; Dua, K. The emerging role of 3D-printing in ocular drug delivery: Challenges, current status, and future prospects. Journal of drug delivery science and technology 2022, 76, 103798, 10.1016/j.jddst.2022.103798.

296. Xu, X.; Awwad, S.; Diaz-Gomez, L.; Alvarez-Lorenzo, C.; Brocchini, S.; Gaisford, S.; Goyanes, A.; Basit, A.W. 3D Printed Punctal Plugs for Controlled Ocular Drug Delivery. Pharmaceutics 2021, 13, 1421, 10.3390/pharmaceutics13091421.

297. Tagami, T.; Goto, E.; Kida, R.; Hirose, K.; Noda, T.; Ozeki, T. Lyophilized ophthalmologic patches as novel corneal drug formulations using a semi-solid extrusion 3D printer. International journal of pharmaceutics 2022, 617, 121448, 10.1016/j.ijpharm.2022.121448.

298. Alam, F.; Salih, A.E.; Elsherif, M.; Yetisen, A.K.; Butt, H. 3D printed contact lenses for the management of color blindness. Additive manufacturing 2022, 49, 102464, 10.1016/j.addma.2021.102464.

299. Zhang, Y.; Wu, L.; Zou, M.; Zhang, L.; Song, Y. Suppressing the Step Effect of 3D Printing for Constructing Contact Lenses. Advanced materials (Weinheim) 2022, 34, e2107249-n/a, 10.1002/adma.202107249.

300. Ko, J.; Kim, S.H.; Baek, S.W.; Chae, M.K.; Yoon, J.S. Semi-automated fabrication of customized ocular prosthesis with three–dimensional printing and sublimation transfer printing technology. Scientific Reports 2019, 9, 2968, 10.1038/s41598-019-38992-y.

301. Ruiters, S.; Mombaerts, I. Applications of three-dimensional printing in orbital diseases and disorders. Current opinion in ophthalmology 2019, 30, 372-379, 10.1097/ICU.0000000000000586.

302. Ruiters, S.; Shujaat, S.; Faria Vasconcelos, K.; Shaheen, E.; Jacobs, R.; Mombaerts, I. Three-dimensional design of a geometric model for an ocular prosthesis in ex vivo anophthalmic socket models. Acta ophthalmologica (Oxford, England) 2021, 99, 221-226, 10.1111/aos.14549.

303. Scawn, R.L.; Foster, A.; Lee, B.W.; Kikkawa, D.O.; Korn, B.S. Customised 3D Printing: An Innovative Training Tool for the Next Generation of Orbital Surgeons. Orbit (Amsterdam) 2015, 34, 216-219, 10.3109/01676830.2015.1049367.

304. Pereira, D.D.; Cardoso, S.C.; Batista, D.V.S.; de Souza, F.M.L.; de Sousa, J.V.M.; Gonçalves, O.D.; da Rosa, L.A.R. Development of an anthropomorphic phantom based on 3D printing for assessment of dose delivered to the eye and adjacent tissues. Radiation physics and chemistry (Oxford, England : 1993) 2022, 199, 110292, 10.1016/j.radphyschem.2022.110292.

305. Riva, L.; Mazzoldi, E.L.; Ginestra, P.S.; Ceretti, E.; Giliani, S.C. Eye model for floaters' studies: production of 3D printed scaffolds. Prog Addit Manuf 2022, 7, 1127-1140, 10.1007/s40964-022-00288-5.

306. Sil, B.C.; Alvarez, M.P.; Zhang, Y.; Kung, C.; Hossain, M.; Iliopoulos, F.; Luo, L.; Crowther, J.M.; Moore, D.J.; Hadgraft, J.; et al. 3D-printed Franz type diffusion cells. International journal of cosmetic science 2018, 40, 604-609, 10.1111/ics.12504.

307. Stein, S.; Auel, T.; Kempin, W.; Bogdahn, M.; Weitschies, W.; Seidlitz, A. Influence of the test method on in vitro drug release from intravitreal model implants containing dexamethasone or fluorescein sodium in poly (d,l-lactide-co-glycolide) or polycaprolactone. European journal of pharmaceutics and biopharmaceutics 2018, 127, 270-278, 10.1016/j.ejpb.2018.02.034.

308. Chang, W.; Liu, P.; Lin, D.; Jiang, Y.; Lu, C.; Hsu, Y.H. Dynamic Protein Adsorption-Desorption Analysis of Contact Lenses in a Three-Dimensional-Printed Eye Model. Macromol. Res 2022, 30, 6-15, 10.1007/s13233-022-0003-2.

309. Dixon, P.; Christopher, K.; Jovic, N.; Chauhan, A. Spectroscopy of Oxygen-Sensitive Material for Measuring Contact Lens Oxygen Transmissibility. Current eye research 2019, 44, 514-521, 10.1080/02713683.2018.1559335.

310. Phan, C.; Walther, H.; Qiao, H.; Shinde, R.; Jones, L. Development of an Eye Model With a Physiological Blink Mechanism. Translational Vision Science & Technology 2019, 8, 1, 10.1167/tvst.8.5.1.

311. Phan, C.; Shukla, M.; Walther, H.; Heynen, M.; Suh, D.; Jones, L. Development of an In Vitro Blink Model for Ophthalmic Drug Delivery. Pharmaceutics 2021, 13, 300, 10.3390/pharmaceutics13030300.

312. Auel, T.; Großmann, L.; Schulig, L.; Weitschies, W.; Seidlitz, A. The EyeFlowCell: Development of a 3D-Printed Dissolution Test Setup for Intravitreal Dosage Forms. Pharmaceutics 2021, 13, 1394, 10.3390/pharmaceutics13091394.

313. Jang, J.; Yi, H.; Cho, D. 3D Printed Tissue Models: Present and Future. ACS biomaterials science & engineering 2016, 2, 1722-1731, 10.1021/acsbiomaterials.6b00129.

314. Isaacson, A.; Swioklo, S.; Connon, C.J. 3D bioprinting of a corneal stroma equivalent. Experimental Eye Research 2018, 173, 188-193, 10.1016/j.exer.2018.05.010.

315. Masaeli, E.; Forster, V.; Picaud, S.; Karamali, F.; Nasr-Esfahani, M.H.; Marquette, C. Tissue engineering of retina through high resolution 3-dimensional inkjet bioprinting. Biofabrication 2020, 12, 025006, 10.1088/1758-5090/ab4a20.

316. Shi, P.; Edgar Yong Sheng Tan; Yeong, W.; Laude, A. Hybrid three-dimensional (3D) bioprinting of retina equivalent for ocular research. International Journal of Bioprinting 2017, 3, 008, 10.18063/IJB.2017.02.008.

317. Bartholomew, L.R.; Pang, D.X.; Sam, D.A.; Cavender, J.C. Ultrasound biomicroscopy of globes from young adult pigs. American journal of veterinary research 1997, 58, 942-948.

318. Petriceks, A.H.; Peterson, A.S.; Angeles, M.; Brown, W.P.; Srivastava, S. Photogrammetry of Human Specimens: An Innovation in Anatomy Education. Journal of Medical Education and Curricular Development 2018, 5, 2382120518799356, 10.1177/2382120518799356.

319. Duffin, R.M.; Olson, R.J.; Ohrloff, C. Analysis of the Hessburg-Barron vacuum trephine. Ophthalmic surgery 1984, 15, 51-54.

320. Larsson, R.; Selén, G.; Björklund, H.; Fagerholm, P. Intraocular PMMA lenses modified with surface-immobilized heparin: evaluation of biocompatibility in vitro and in vivo. Biomaterials 1989, 10, 511-516, 10.1016/0142-9612(89)90055-0.

321. Cai, C.; Tey, W.S.; Chen, J.; Zhu, W.; Liu, X.; Liu, T.; Zhao, L.; Zhou, K. Comparative study on 3D printing of polyamide 12 by selective laser sintering and multi jet fusion. Journal of materials processing technology 2021, 288, 116882, 10.1016/j.jmatprotec.2020.116882.

322. Parodi, V.; Jacchetti, E.; Osellame, R.; Cerullo, G.; Polli, D.; Raimondi, M.T. Nonlinear Optical Microscopy: From Fundamentals to Applications in Live Bioimaging. Frontiers in bioengineering and biotechnology 2020, 8, 585363, 10.3389/fbioe.2020.585363.

323. Vargas-Nadal, G.; Köber, M.; Nsamela, A.; Terenziani, F.; Sissa, C.; Pescina, S.; Sonvico, F.; Gazzali, A.M.; Wahab, H.A.; Grisanti, L.; et al. Fluorescent Multifunctional Organic Nanoparticles for Drug Delivery and Bioimaging: A Tutorial Review. Pharmaceutics 2022, 14, 2498, 10.3390/pharmaceutics14112498.

324. Han, M.; Giese, G.; Bille, J. Second harmonic generation imaging of collagen fibrils in cornea and sclera. Optics express 2005, 13, 5791-5797, 10.1364/OPEX.13.005791.

325. Webb, W.W.; Zipfel, W.R.; Williams, R.M. Nonlinear magic: multiphoton microscopy in the biosciences. Nature biotechnology 2003, 21, 1369-1377, 10.1038/nbt899.

326. Stracke, F.; Weiss, B.; Lehr, C.; König, K.; Schaefer, U.F.; Schneider, M. Multiphoton Microscopy for the Investigation of Dermal Penetration of Nanoparticle-Borne Drugs. Journal of Investigative Dermatology 2006, 126, 2224-2233, 10.1038/sj.jid.5700374.

327. Ghezzi, M.; Pescina, S.; Delledonne, A.; Ferraboschi, I.; Sissa, C.; Terenziani, F.; Remiro, P.D.F.R.; Santi, P.; Nicoli, S. Improvement of Imiquimod Solubilization and Skin Retention via TPGS Micelles: Exploiting the Co-Solubilizing Effect of Oleic Acid. Pharmaceutics 2021, 13, 1476, 10.3390/pharmaceutics13091476.

328. Nakano, M.; Lockhart, C.M.; Kelly, E.J.; Rettie, A.E. Ocular cytochrome P450s and transporters: roles in disease and endobiotic and xenobiotic disposition. Drug metabolism reviews 2014, 46, 247-260, 10.3109/03602532.2014.921190.

329. Heikkinen, E.M.; Del Amo, E.M.; Ranta, V.; Urtti, A.; Vellonen, K.; Ruponen, M. Esterase activity in porcine and albino rabbit ocular tissues. European journal of pharmaceutical sciences 2018, 123, 106-110, 10.1016/j.ejps.2018.07.034.

330. Pescina, S.; Govoni, P.; Antopolsky, M.; Murtomaki, L.; Padula, C.; Santi, P.; Nicoli, S. Permeation of Proteins, Oligonucleotide and Dextrans Across Ocular Tissues: Experimental Studies and a Literature Update. Journal of pharmaceutical sciences 2015, 104, 2190-2202, 10.1002/jps.24465.

331. Grimaudo, M.A.; Pescina, S.; Padula, C.; Santi, P.; Concheiro, A.; Alvarez-Lorenzo, C.; Nicoli, S. Poloxamer 407/TPGS Mixed Micelles as Promising Carriers for Cyclosporine Ocular Delivery. Molecular pharmaceutics 2018, 15, 571-584, 10.1021/acs.molpharmaceut.7b00939.

332. Kucherak, O.A.; Oncul, S.; Darwich, Z.; Yushchenko, D.A.; Arntz, Y.; Didier, P.; Mély, Y.; Klymchenko, A.S. Switchable Nile Red-Based Probe for Cholesterol and Lipid Order at the Outer Leaflet of Biomembranes. Journal of the American Chemical Society 2010, 132, 4907-4916, 10.1021/ja100351w.

333. Greenspan, P.; Fowler, S.D. Spectrofluorometric studies of the lipid probe, nile red. Journal of Lipid Research 1985, 26, 781-789, 10.1016/S0022-2275(20)34307-8.

334. Boldrini, B.; Cavalli, E.; Painelli, A.; Terenziani, F. Polar Dyes in Solution: A Joint Experimental and Theoretical Study of Absorption and Emission Band Shapes. The journal of physical chemistry A 2002, 106, 6286-6294, 10.1021/jp020031b.

335. Murtomäki, L.; Vainikka, T.; Pescina, S.; Nicoli, S. Drug Adsorption on Bovine and Porcine Sclera Studied with Streaming Potential. Journal of pharmaceutical sciences 2013, 102, 2264-2272, 10.1002/jps.23585.

336. Ray, A.; Das, S.; Chattopadhyay, N. Aggregation of Nile Red in Water: Prevention through Encapsulation in β Cyclodextrin. ACS Omega 2019, 4, 15-24, 10.1021/acsomega.8b02503.

337. Golini, C.M.; Williams, B.W.; Foresman, J.B. Further solvatochromic, thermochromic, and theoretical studies on Nile Red. Journal of Fluorescence 1998, 8, 395-404, 10.1023/A:1020584801600.

338. Terenziani, F.; Painelli, A.; Comoretto, D. Solvation Effects and Inhomogeneous Broadening in Optical Spectra of Phenol Blue. The journal of physical chemistry A 2000, 104, 11049-11054, 10.1021/jp001608x.

339. International Labour Organization. International Chemical Safety Card 1203 - Triacetin. Available online: https://www.ilo.org/dyn/icsc/showcard.display?p_version=2&p_card_id=1203 (accessed on December 2022).

340. Barcia, E.; Herrero-Vanrell, R.; Díez, A.; Alvarez-Santiago, C.; López, I.; Calonge, M. Downregulation of endotoxin-induced uveitis by intravitreal injection of polylactic-glycolic acid (PLGA) microspheres loaded with dexamethasone. Experimental eye research 2009, 89, 238-245, 10.1016/j.exer.2009.03.012.

341. Nastiti, C.M.R.R.; Ponto, T.; Abd, E.; Grice, J.E.; Benson, H.A.E.; Roberts, M.S. Topical Nano and Microemulsions for Skin Delivery. Pharmaceutics 2017, 9, 37, 10.3390/pharmaceutics9040037.

342. Vandamme, T.F. Microemulsions as ocular drug delivery systems: recent developments and future challenges. Progress in retinal and eye research 2002, 21, 15-34, 10.1016/S1350-9462(01)00017-9.

343. López-Cano, J.J.; González-Cela-Casamayor, M.A.; Andrés-Guerrero, V.; Vicario -de-la-Torre, M.; Benítez del Castillo, J.M.; Herrero-Vanrell, R.; Molina-Martínez, I.T. Development of an osmoprotective microemulsion as a therapeutic platform for ocular surface protection. International journal of pharmaceutics 2022, 623, 121948, 10.1016/j.ijpharm.2022.121948.

344. Ma, Y.; Yang, J.; Zhang, Y.; Zheng, C.; Liang, Z.; Lu, P.; Song, F.; Wang, Y.; Zhang, J. Development of a naringenin microemulsion as a prospective ophthalmic delivery system for the treatment of corneal neovascularization: in vitro and in vivo evaluation. Drug delivery 2022, 29, 111-127, 10.1080/10717544.2021.2021323.

345. Rupenthal, I.D.; Agarwal, P.; Uy, B.; Kim, J.; Cunningham, A.A.; Seyfoddin, A.; Swift, S.; Craig, J.P. Preparation and Characterisation of a Cyclodextrin-Complexed Mānuka Honey Microemulsion for Eyelid Application. Pharmaceutics 2022, 14, 1493, 10.3390/pharmaceutics14071493.

346. Cardoso, C.O.; Ferreira-Nunes, R.; Cunha-Filho, M.; Gratieri, T.; Gelfuso, G.M. In situ gelling microemulsion for topical ocular delivery of moxifloxacin and betamethasone. Journal of molecular liquids 2022, 360, 119559, 10.1016/j.molliq.2022.119559.

347. Jansook, P.; Muankaew, C.; Stefánsson, E.; Loftsson, T. Development of eye drops containing antihypertensive drugs: formulation of aqueous irbesartan/γCD eye drops. Pharmaceutical development and technology 2015, 20, 626-632, 10.3109/10837450.2014.910811.

348. Gugleva, V.; Titeva, S.; Rangelov, S.; Momekova, D. Design and in vitro evaluation of doxycycline hyclate niosomes as a potential ocular delivery system. International journal of pharmaceutics 2019, 567, 118431, 10.1016/j.ijpharm.2019.06.022.

Acknowledgments

The author kindly thanks all the ORBITAL consortium members, especially the hosting institutions of the ESR 13 project (University of Parma and Nanovector Srl) and the seconding institutions (South East Technological University and Ocupharm Diagnostics SL) for their continuous support on producing the data hereby presented.

A considerable amount of the results would not be possible without the inestimable contribution of Prof Daniele Alessandro Cauzzi, Prof Cristina Sissa and Andrea Delledonne which made every trip to the Department of Chemistry, Life Sciences and Environmental Sustainability a new opportunity to learn and broaden our research into new fields.

Some sections are here presented only because of the (maybe) short but surely impactful contributions of Dr Ana González-Paredes (CSIC) on lipid-based nanocarriers production, Madhuri and Sreeraj (SETU) for their teachings in *in vitro* cytotoxicity assays and Salvatore Guastella for kindly providing the FEG-SEM images. The gratitude is further extended to Pierugo Cavallini and Macello Annoni SpA for kindly providing the valuable *ex vivo* tissues and to Prof Annalisa Bianchera and Nicoletta Bertani for sharing their time and knowledge in cytotoxicity assays and design of experiments.

Finally, the author would like to state that:

This project is funded by the European Union's Horizon 2020 research and innovation programme under the Marie Skłodowska-Curie Actions (grant agreement - No 813440).